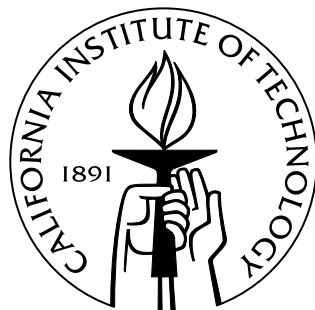


Chemical-Scale Studies of G Protein-Coupled Receptors and Ligand-Gated Ion Channels

Thesis by

Ethan Buggie Van Arnam

In Partial Fulfillment of the
Requirements for the Degree of
Doctor of Philosophy



California Institute of Technology

Pasadena, California

2014

(Defended December 12, 2013)

UMI Number: 3613569

All rights reserved

INFORMATION TO ALL USERS

The quality of this reproduction is dependent upon the quality of the copy submitted.

In the unlikely event that the author did not send a complete manuscript and there are missing pages, these will be noted. Also, if material had to be removed, a note will indicate the deletion.



UMI 3613569

Published by ProQuest LLC (2014). Copyright in the Dissertation held by the Author.

Microform Edition © ProQuest LLC.

All rights reserved. This work is protected against unauthorized copying under Title 17, United States Code



ProQuest LLC.
789 East Eisenhower Parkway
P.O. Box 1346
Ann Arbor, MI 48106 - 1346

© 2014

Ethan Buggie Van Arnam

All Rights Reserved

Dedicated to my parents:
Jean and Peter Van Arnam

Acknowledgements

I expected a rich scientific experience at Caltech, but never imagined how personally fulfilling my time here would be. For that I have a great number of people to thank. First and foremost, I want to extend heartfelt thanks to my graduate advisor Dennis Dougherty. I appreciate the extensive freedom he gives his students and yet the compassion and personal dedication he devotes to each one of us. Dennis is a supremely talented communicator, and I especially value the lessons I've learned about speaking, writing, and teaching from him. I also appreciate the support he has given me and the confidence he has instilled in me to tackle hard scientific problems and to explore a new field after Caltech.

Henry Lester, a longtime collaborator of the Dougherty group, is an inexhaustible source of suggestions for new experiments and novel approaches to scientific problems. I value his scientific rigor and his dedication to his students. I also want to thank the members of my thesis committee, Peter Dervan, Doug Rees, and David Tirrell for their support and suggestions, both with regards to my graduate research and my career.

The Dougherty group has been a fantastic place to work (and a fantastic place at times to hang out and not work too). I really look forward to keeping in touch with everyone I overlapped with in the group. When I first arrived in lab, Ariele Hanek, Kiowa Bower, and Kristin Gleitsman had saintly patience while I was learning the ropes, passed on endless sage advice, and made me feel welcome. I'm very glad I got to know Jai Shanata, who always brought a valuable quantitative rigor to scientific discussions and whose worldview is refreshingly optimistic. Sean Kedrowski answered so, so, many of my chemistry questions and put up with all assortment of canned fish and other exciting

lunch items that I brought in. I really enjoyed sitting next to him for three years. Angela Blum and Nyssa Puskar, with whom I overlapped for a good deal of grad school, have great integrity and are supremely capable researchers. Kay Limapichat helped me immensely to get started on fluorescence experiments and was generous with time and with materials she worked long to prepare. Noah Duffy is a hell of a human being. He always has an open mind, really thinks things through, and can fix absolutely anything.

Kristina Daeffler, Ximena da Silva, Maggie Thompson, and I all entered Caltech together and had the wisdom to join the Dougherty group. Maggie has remained a good friend and I deeply admire her bravery to teach middle school science. Ximena (da Silva Tavares Bongoll de Rossi) has the longest name of anyone I know. Kristina and I both cut our teeth on GPCR projects and have commiserated on more than one topic on more than one occasion.

Tim Miles knows how to chart his own path and excel at it. I've appreciated his friendship and look forward to watching what he does in the future. We were ever so fortunate to land Michael Post in the group. He's carrying the nicotinic receptor torch forward and smiles seem to erupt everywhere he goes. Oliver Shafaat and Fan Liu have orders of magnitude more mathematical competence than I do. I really enjoyed my GPCR collaborations with Fan and all of our conversations. The future involves photons for Kayla Busby, Matt (Jefferson) Davis, and Paul (David?) Walton. These folks are breaking new ground, which made my last year in the group a lot more intellectually stimulating. They made it a whole lot more fun too. Betty Wong is bravely taking on some fluorescence work, and is more than up to the task. She hasn't been in the group long, but everybody agrees she's a force for good.

Finally, Matt Rienzo and Clint Regan were my companions in the south bay of desks for the last few years and I'll deeply miss them. Clint is steering the photochemistry ship – making good progress and knowing the right questions to ask. Matt can do very hard chemistry and very hard biology and is a very good person as well.

I had the privilege of working with three truly outstanding undergraduates in lab during my graduate career: Jessica Swallow, Emily Blythe, and Jessica Hsu. All learned the ropes in lab effortlessly and accomplished much, were great to work with, and were often many steps ahead of me.

Friends in the Los Angeles area showed me that this is an awesome place to live and is going to be an especially hard place to leave. Michael Van Vliet has been a fantastic friend and a much needed beacon of normalcy beyond the Caltech community. All of my cycling friends gave me a window into this city I would never have seen otherwise and are all fantastic people. My roommates Alex Goldberg, James McKone, and Judy Lattimer have been great friends and deserve a medal for putting up with my eccentricities.

Finally, I want to thank my family, who I don't thank nearly enough. My parents have always supported me unconditionally and serve as the strongest role models I could ever ask for.

Abstract

This dissertation describes studies of G protein-coupled receptors (GPCRs) and ligand-gated ion channels (LGICs) using unnatural amino acid mutagenesis to gain high precision insights into the function of these important membrane proteins.

Chapter 2 considers the functional role of highly conserved proline residues within the transmembrane helices of the D2 dopamine GPCR. Through mutagenesis employing unnatural α -hydroxy acids, proline analogs, and N-methyl amino acids, we find that lack of backbone hydrogen bond donor ability is important to proline function. At one proline site we additionally find that a substituent on the proline backbone N is important to receptor function.

In Chapter 3, side chain conformation is probed by mutagenesis of GPCRs and the muscle-type nAChR. Specific side chain rearrangements of highly conserved residues have been proposed to accompany activation of these receptors. These rearrangements were probed using conformationally-biased β -substituted analogs of Trp and Phe and unnatural stereoisomers of Thr and Ile. We also modeled the conformational bias of the unnatural Trp and Phe analogs employed.

Chapters 4 and 5 examine details of ligand binding to nAChRs. Chapter 4 describes a study investigating the importance of hydrogen bonds between ligands and the complementary face of muscle-type and $\alpha 4\beta 4$ nAChRs. A hydrogen bond involving the agonist appears to be important for ligand binding in the muscle-type receptor but not the $\alpha 4\beta 4$ receptor. Chapter 5 describes a study characterizing the binding of varenicline, an actively prescribed smoking cessation therapeutic, to the $\alpha 7$ nAChR. Additionally,

binding interactions to the complementary face of the $\alpha 7$ binding site were examined for a small panel of agonists. We identified side chains important for binding large agonists such as varenicline, but dispensable for binding the small agonist ACh.

Chapter 6 describes efforts to image nAChRs site-specifically modified with a fluorophore by unnatural amino acid mutagenesis. While progress was hampered by high levels of fluorescent background, improvements to sample preparation and alternative strategies for fluorophore incorporation are described.

Chapter 7 describes efforts toward a fluorescence assay for G protein association with a GPCR, with the ultimate goal of probing key protein-protein interactions along the G protein/receptor interface. A wide range of fluorescent protein fusions were generated, expressed in *Xenopus* oocytes, and evaluated for their ability to associate with each other.

Table of Contents

Chapter 1: Introduction

1.1 Signaling across a membrane: the chemical underpinning of neuroscience.....	1
1.2 Ligand-gated ion channels	1
1.3 G protein-coupled receptors.....	5
1.4 Methods for interrogating ion channel and GPCR function	7
1.4.1 <i>Electrophysiology as an assay for ion channels and GPCRs</i>	7
1.4.2 <i>Unnatural amino acid mutagenesis</i>	9
1.4.3 <i>Probing receptor function with fluorescence</i>	12
1.5 Summary of dissertation work	13
1.6 References.....	14

Chapter 2: Dissecting the functions of conserved prolines within transmembrane helices of the D2 dopamine receptor

2.1 Abstract	16
2.2 Introduction.....	16
2.3 Results.....	20
2.3.1 <i>Experimental approach</i>	20
2.3.2 <i>Strategy and general observations</i>	20
2.3.3 <i>169^{4,59}, 388^{6,50}, 423^{7,50}: Importance of lacking a backbone hydrogen bond donor</i>	24
2.3.4 <i>201^{5,50}: N-substitution as well as lack of a hydrogen bond donor are important</i>	25
2.4 Discussion	26
2.5 Conclusions.....	29
2.6 Experimental	30
2.6.1 <i>Molecular biology</i>	30
2.6.2 <i>Oocyte preparation and RNA injection</i>	31

2.6.3 Electrophysiology	32
2.7 References	33

Chapter 3: Probing side chain conformations and rearrangements in receptor binding sites

3.1 Abstract	36
3.2 Introduction	37
3.2.1 GPCR activation	37
3.2.2 nAChR activation	40
3.2.3 Probing side chain conformation by mutagenesis	42
3.3 Results and Discussion	44
3.3.1 Mutagenesis probing conformational rearrangements of C6.47 upon D2 dopamine receptor activation	44
3.3.2 Investigating the role of a F6.44/I3.40 switch in activation of the D2 dopamine receptor	46
3.3.3 Synthesis and use of 5-aminomethyltryptophan to probe the W6.48 site in GPCRs	49
3.3.4 Synthesis, mutagenesis, and modeling of β -methyltryptophan and β -methylphenylalanine	53
3.3.4.1 Synthesis	53
3.3.4.2 Mutagenesis	54
3.3.4.3 Conformational effects	56
3.3.4.4 Double mutant cycle analysis to probe steric effects of β -methyl substituents	66
3.4 Conclusions	72
3.5 Experimental	73
3.5.1 Molecular biology	73
3.5.2 Microinjection	74
3.5.3 Electrophysiology	75
3.5.4 Energy calculations	76

3.5.5 <i>Synthesis</i>	77
3.6 References.....	89

Chapter 4: Binding interactions to the complementary subunit of the $\alpha 4\beta 4$ receptor

4.1 Abstract.....	92
4.2 Introduction.....	93
4.3 Results.....	96
4.3.1 <i>General strategy</i>	96
4.3.2 <i>Mutagenesis studies of the Leu NH</i>	100
4.3.3 <i>Mutagenesis studies of the Asn CO</i>	101
4.4 Discussion.....	102
4.5 Experimental	107
4.5.1 <i>Mutagenesis</i>	107
4.5.2 <i>Microinjection</i>	108
4.5.3 <i>Electrophysiology</i>	109
4.6 References.....	109

Chapter 5: An unusual pattern of ligand-receptor interactions for the $\alpha 7$ nicotinic acetylcholine receptor, with implications for the binding of varenicline

5.1 Abstract.....	112
5.2 Introduction.....	113
5.3 Results.....	117
5.3.1 <i>Experimental design</i>	117
5.3.2 <i>Unnatural amino acid mutagenesis to probe cation-π interactions and hydrogen bonds to the protein backbone</i>	119
5.3.3 <i>Varenicline interactions with the binding site's principal face</i>	121
5.3.4 <i>Probing the canonical hydrogen bond of the nicotinic pharmacophore between agonists and the complementary subunit</i>	125

<i>5.3.5 Functional importance of side chains on the complementary face of the binding site</i>	125
5.4 Discussion	126
<i> 5.4.1 Cation-π interactions to the “aromatic box” residues of the principal face</i>	127
<i> 5.4.2 Hydrogen bonding and steric effects on the principal face.....</i>	128
<i> 5.4.3 Hydrogen bonding to the complementary face.....</i>	129
<i> 5.4.4 Interactions with complementary face side chains.....</i>	132
5.5 Conclusions.....	133
5.6 Experimental	133
<i> 5.6.1 Molecular biology</i>	133
<i> 5.6.2 Microinjection</i>	134
<i> 5.6.3 Electrophysiology</i>	135
5.7 References.....	135

Chapter 6: Efforts toward single molecule fluorescence imaging of nAChRs

6.1 Abstract.....	139
6.2 Introduction.....	139
6.3 Results and Discussion	142
<i> 6.3.1 Background fluorescence from tRNA-BODIPY</i>	142
<i> 6.3.2 Optimization of vitelline membrane removal</i>	149
<i> 6.3.3 Two-color imaging and single puncta analysis.....</i>	153
<i> 6.3.4 Attempts at fluorophore conjugation by azide-alkyne cycloaddition</i>	159
<i> 6.3.5 Design and synthesis of a fluorescence-quenched tRNA.....</i>	161
6.4 Conclusions.....	168
6.5 Experimental	169
<i> 6.5.1 Molecular biology and <i>in vivo</i> expression</i>	169

6.5.2 <i>Electrophysiology</i>	169
6.5.3 <i>Oocyte membrane preparation</i>	169
6.5.4 <i>Total internal reflection fluorescence (TIRF) imaging</i>	170
6.5.5 <i>Azido dye labeling under copper-catalyzed click conditions</i>	171
6.5.6 <i>Two-color TIRF imaging and image analysis</i>	171
6.5.7 <i>tRNA synthesis and characterization</i>	172
6.6 References.....	174

Chapter 7: Attempts to develop a FRET assay for the GPCR-G protein interaction

7.1 Abstract.....	177
7.2 Introduction.....	177
7.3 Results and Discussion	183
7.3.1 <i>Construction of fluorescent protein fusions</i>	183
7.3.2 <i>Tests of construct function in vivo</i>	185
7.3.3 <i>Formation and fluorescence imaging of plasma membrane sheets</i> 188	188
7.3.4 <i>Attempts to measure FRET between G protein and receptor</i>	188
7.4 Conclusions.....	192
7.5 Experimental	193
7.5.1 <i>Molecular biology and in vivo expression</i>	193
7.5.2 <i>Electrophysiology</i>	193
7.5.3 <i>Membrane preparation</i>	194
7.5.4 <i>FLIM imaging</i>	194
7.6 References.....	194

Chapter 1: Introduction*

1.1 Signaling across a membrane: the chemical underpinning of neuroscience

Nature has evolved exquisite mechanisms for cells to sense the world beyond the boundaries of their plasma membranes. Small molecule chemical signals are recognized by a broad array of membrane-spanning receptor proteins, which couple an extracellular ligand binding event to an intracellular response. Such proteins enable communication among adjacent cells, within tissues, and across organisms. Cellular communication mediated by membrane receptors is played out on the grandest scale in the human brain, which comprises 10^{12} highly interconnected neurons. There, neurotransmitters relay across synapses to bind receptors, which initiate signal propagation to the next neuron: this is the basic chemical underpinning of thought, emotion, and awareness. Myriad receptors and neurotransmitters play roles in synaptic transmission. Key families of membrane receptors are the ligand-gated ion channels (LGICs) and G protein-coupled receptors (GPCRs).

1.2 Ligand-gated ion channels

Ligand-gated ion channels are multimeric membrane-spanning proteins that open a transmembrane ion-conducting pore upon binding their cognate ligand. A key family of these proteins involved in synaptic transmission is the nicotinic acetylcholine receptors (nAChRs), cation-selective channels gated by the neurotransmitter acetylcholine (ACh). These receptors are pentamers and can be comprised of a wide range of subunits, either in a homomeric or heteromeric fashion. The prototypical nAChR, the muscle-type receptor,

* Portions of this chapter are adapted from a review article in preparation (Van Arnam, E. B. and Dougherty, D. A.)

assembles with a fixed subunit composition of $(\alpha 1)_2 \beta 1 \gamma \delta$ (fetal form: in adults the ϵ subunit substitutes for γ). The remainder of the nAChRs, the neuronal receptors, can be found throughout the central and peripheral nervous systems, though some have been found in non-neuronal cells as well. Neuronal nAChRs can be comprised of the subunits $\alpha 2-\alpha 10$ and $\beta 2-\beta 4$, of which homomeric $\alpha 7$ receptors and receptors containing $\alpha 4$ and $\beta 2$ subunits are the dominant subtypes expressed in the brain.¹⁴

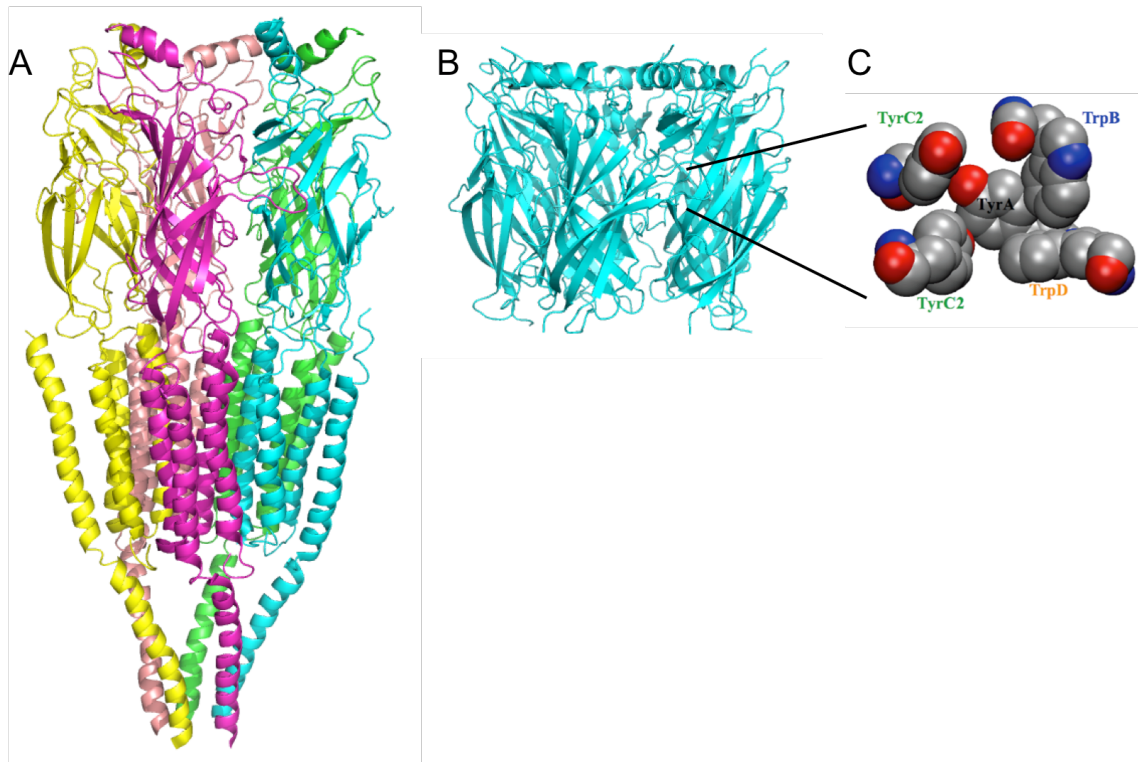


Figure 1.1. (A) *Torpedo* nAChR cryo-EM structure.¹ (B) Acetylcholine binding protein structure.² (C) Aromatic box residues of the nAChR binding site.

In these pentameric receptors, each subunit contains four membrane-spanning α -helices and a large, primarily β -sheet, N-terminal extracellular domain. The five subunits arrange pseudo-symmetrically around a pore lined by the second transmembrane helix, and ligand-binding sites are found at subunit interfaces in the extracellular domain. While we lack a nAChR crystal structure, the global architecture of these proteins is now

well established from a wealth of biochemical studies and from several informative model structures. A cryo-EM structure of the *Torpedo* ray nAChR is available at 4 Å resolution for the closed receptor (Figure 1.1A).¹ Crystal structures of homologs within the same superfamily of pentameric receptors corroborate the global architecture, including structures of the *C. elegans* channel GluCl and the bacterial channels ELIC and GLIC.³⁻⁶ Comparison of structures thought to represent an open pore conformation (GluCl, GLIC) to those in closed-channel conformations (ELIC, nAChR cryo-EM) support a gating model^{7,8} in which twisting of the extracellular domain modulates the tilt of the second and third transmembrane helices to open the ion-conducting pore.

Our knowledge of nAChR ligand-binding sites has been buoyed by structures of invertebrate acetylcholine binding proteins (AChBPs) (Figure 1.1B). These soluble proteins have proven amenable to crystallization, and share structural homology and 20 – 25% sequence identity with the nAChR extracellular domain. AChBP structures reveal that binding site aromatic residues conserved across nAChRs are arranged into an “aromatic box” (Figure 1.1C). Components of this box are contributed from four different structural loops (named loop A through loop D) and also from both subunits that meet at the binding site. This box comprises a pocket for ligand binding, and numerous AChBP structures have been reported in complex with pharmacologically-relevant ligands, suggesting specific ligand-binding interactions (Figure 1.2).¹⁰ One key ligand-binding interaction suggested by AChBP and corroborated by mutagenesis studies is a cation-π interaction between an agonist cationic group and the side chain of a tryptophan on loop B (TrpB).^{7,8} Additionally, agonists that have a N⁺H group can form a hydrogen bond to the backbone carbonyl of TrpB.⁹ Finally, AChBP structures suggest that the

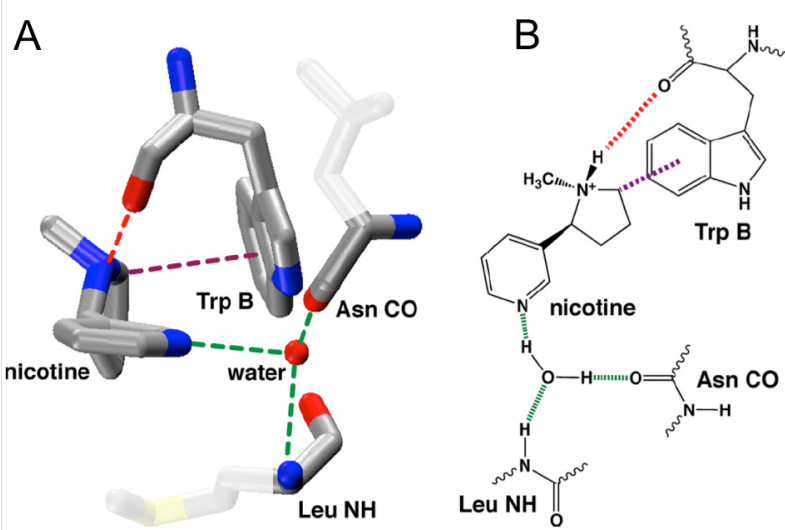


Figure 1.2. A binding model for nicotine at nAChRs. **(A)** Crystal structure of nicotine bound to AChBP. **(B)** Schematic of the binding model. Reproduced with permission from reference 11.

hydrogen bond-accepting group common to most nAChR agonists interacts with a water molecule held between backbone groups of a conserved Leu and a conserved Asn that lie across the subunit interface from TrpB. Mutagenesis confirms that the Leu backbone NH can be important for ligand binding.^{10,11}

However, functional studies reveal that these ligand-receptor interactions can be variable across receptor subtypes. For example, the muscle-type receptor and the $\alpha 4\beta 2$ and $\alpha 4\beta 4$ neuronal receptors typically utilize a cation- π interaction to TrpB. The $\alpha 7$ neuronal nAChR, however, binds agonists through cation- π interactions to a tyrosine on loop A (TyrA) and a tyrosine on loop C (TyrC2).¹² The Leu backbone NH is important to ligand binding in $\alpha 4\beta 2$ and muscle-type receptors, but appears dispensable to ligand binding in $\alpha 4\beta 4$ and $\alpha 7$ receptors.^{10,11,13} Such distinctions likely contribute to the unique pharmacology of different nAChRs and could help guide rational design of subtype-selective pharmaceuticals targeting these receptors.

1.3 G protein-coupled receptors

The largest family of membrane receptors (and indeed the largest class of membrane proteins in humans) are the G protein-coupled receptors, of which an estimated 720 – 800 are encoded in the human genome.¹⁴ While GPCRs comprise a sprawling class of proteins responding to diverse stimuli and inducing varied downstream responses, several structural features and principles of signaling are common among all GPCRs. All are characterized by a bundle of seven transmembrane helices and (with the exception of the receptor rhodopsin, which responds to light) are activated by ligand binding. GPCR activation begins with ligand binding to a pocket in the extracellular half of the transmembrane helical core (Figure 1.3A), which induces a conformational change in the receptor. This new receptor conformation modulates an associated guanine nucleotide-binding protein (G protein), causing the G protein to exchange bound GDP for GTP and assume its active, signaling state. The activated G protein dissociates into its G α and G $\beta\gamma$ subunits (Figure 1.3B), which can affect various cellular targets (Figure 1.3C), such as

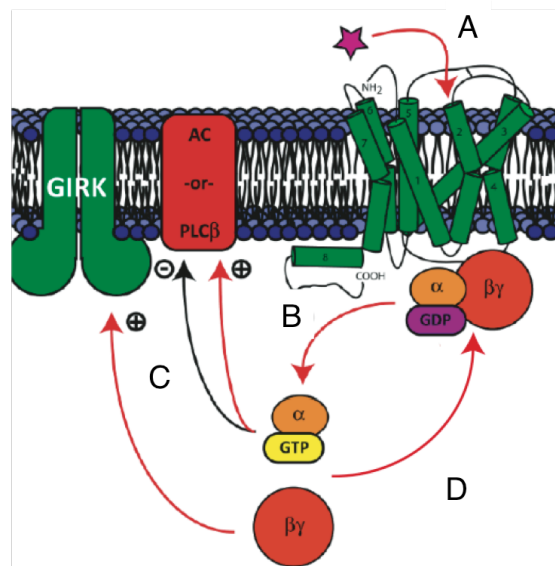


Figure 1.3. Schematic of GPCR signaling. **(A)** Ligand binding initiates GPCR signaling. **(B)** Activation of the G protein by GDP/GTP exchange induces dissociation of G α and G $\beta\gamma$ subunits. **(C)** G α and G $\beta\gamma$ subunits can activate cellular signaling partners. **(D)** GTP hydrolysis terminates signaling by inducing reassociation of G α and G $\beta\gamma$.

adenylate cyclase, phospholipase C β , or potassium channels, inducing complex signaling pathways. GTP hydrolysis causes the G α and G $\beta\gamma$ subunits to reassociate, ending signaling (Figure 1.3D).

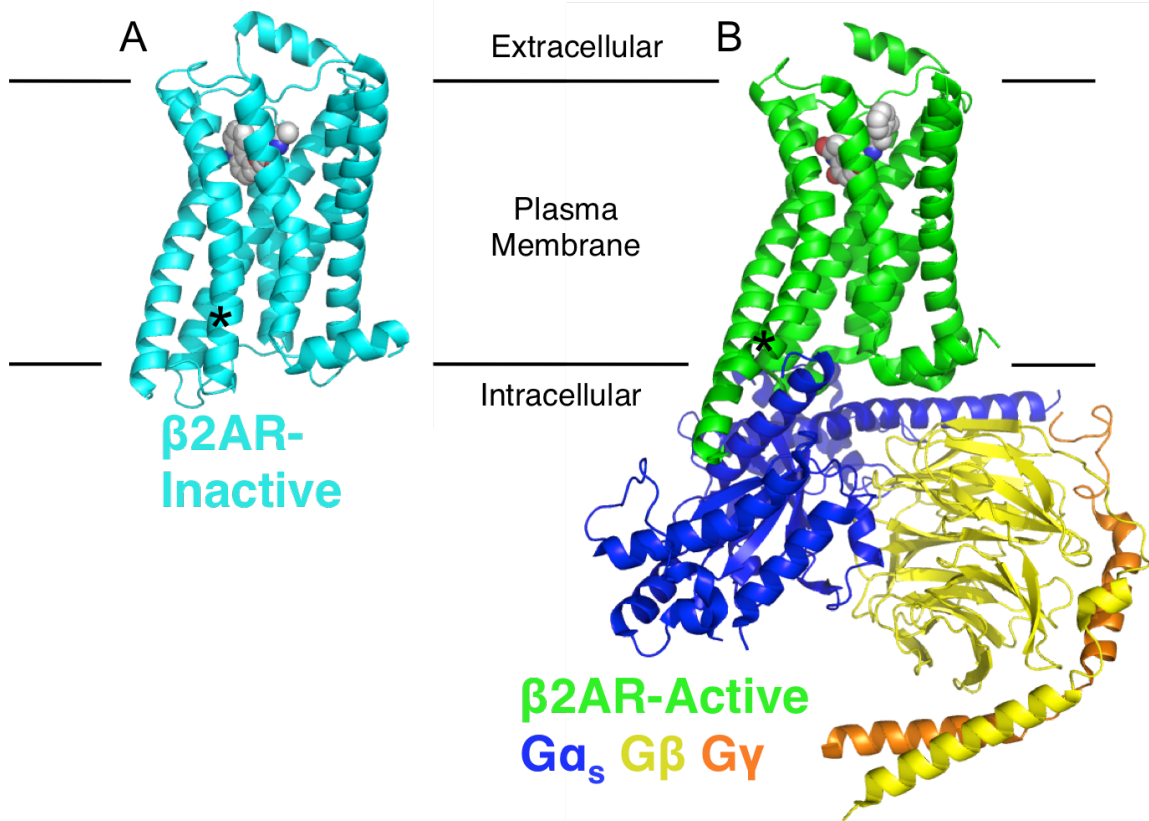


Figure 1.4. (A) Structure of the inactive β2 adrenergic GPCR (β2AR) bound to an antagonist.¹⁵ (B) Structure of the β2AR in its active conformation bound to an agonist and its cognate G protein, Gs.¹⁶ TM6, the helix that undergoes the most dramatic conformational rearrangement upon activation, is denoted with an asterisk in both structures.

Since the seminal crystal structure of rhodopsin in 2000,¹⁷ considerable structural information has emerged for GPCRs, including structures of over 15 distinct receptors and structures capturing different conformational states.¹⁸ In a landmark achievement, a crystal structure was obtained for the β2 adrenergic GPCR in an active conformation in complex with its cognate G protein, Gs (Figure 1.4).¹⁶ All GPCRs share the same general topology with an extracellular N-terminus, intracellular C-terminus, and seven

intervening transmembrane helices (TMs) in a roughly counterclockwise arrangement when viewed from the extracellular face, numbered TM1 – TM7. The main ligand-binding pocket typically sits between TMs 3, 5, and 6 on the extracellular half of the receptor, beneath extracellular loop 2 (EL2).

While the specifics of ligand binding vary from receptor to receptor, mounting evidence from both crystallography and from biochemical studies suggests that receptor activation among the various classes of GPCRs involves common conformational changes in the transmembrane helical bundle, allowing for activation of the G protein at the receptor's intracellular face.^{18,19} Briefly, agonist binding induces subtle changes at the extracellular half of the helical bundle, accompanied by more marked spreading of the intracellular end, most notably of TM6 and TM7. Outward displacement of the intracellular end of TM6 is critical to expose an important G protein binding site (Figure 1.4).¹⁸

1.4 Methods for interrogating ion channel and GPCR function

1.4.1 Electrophysiology as an assay for ion channels and GPCRs

The studies described in this dissertation probe the function of ion channels and GPCRs *in vivo* using *Xenopus laevis* oocytes as an expression system. These physically large (~ 1 mm diameter) cells can be readily injected with mRNA or other material. In this eukaryotic *in vivo* expression system, complex membrane proteins are competently translated, folded, modified, and trafficked to the plasma membrane.

These cells provide a convenient vehicle in which to assay surface-expressed membrane proteins by electrophysiology. Using two-electrode voltage clamp electrophysiology, passage of ions across the plasma membrane through ion channels can be recorded as an electrical current. Hence, we can directly assay ligand-gated ion channels by applying agonist to cells and recording responses from open channels. For GPCRs, we use an indirect assay that relies on G protein activation of an ion channel. $G_{i/o}$ -type G proteins are activated by select GPCRs (including the D2 dopamine and M2 acetylcholine receptors considered in this dissertation) and can in turn activate G protein-coupled inwardly rectifying potassium (GIRK) channels (Figure 1.3C).²⁰ Coexpression of GIRK with the GPCR of interest thus enables a straightforward assay for these receptors by electrophysiology via GIRK activation.

For both GPCRs and ligand-gated ion channels, we assay receptor function by assembling a dose-response curve from current responses to progressively greater concentrations of agonist (Figure 1.5A, B). This curve is fit to the Hill equation (Figure 1.5C), which gives an EC_{50} , the dose that affording a half-maximal response, and the Hill coefficient, n_H , which represents ligand binding cooperativity. The EC_{50} is a metric of receptor function; mutations that increase EC_{50} relative to the wild-type receptor (Figure 1.5B, red curve) are referred to as a “loss of function,” since a larger agonist concentration is required to give the same response, while those that lower the EC_{50} (Figure 1.5B, green curve) are referred to as “gain of function” mutations.

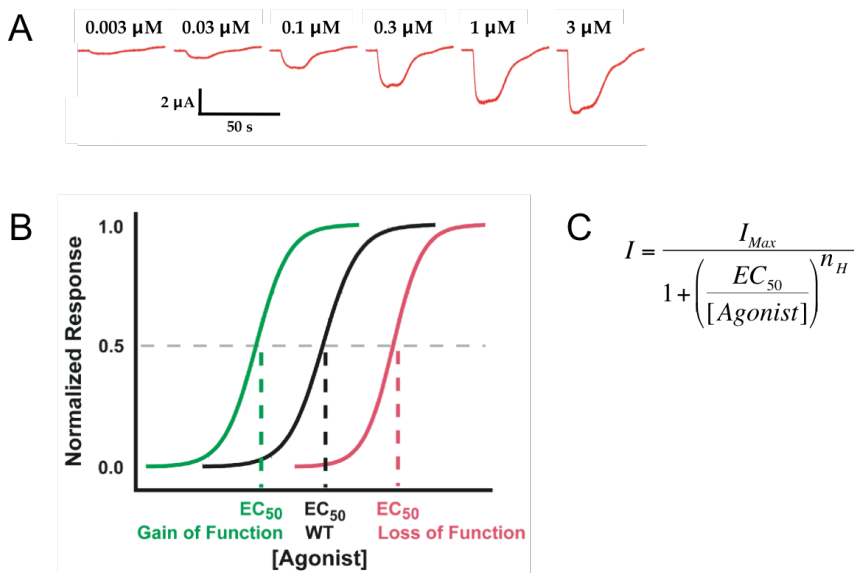


Figure 1.5. (A) Current responses to a range of agonist concentrations. (B) Dose-response curves. The black curve represents the wild-type receptor while the red curve represents a loss-of-function mutant and the green curve a gain-of-function mutant. (C) Hill equation. I_{max} is the maximal current response to agonist, EC_{50} is the agonist concentration that gives half-maximal current response, and n_H is the Hill coefficient.

1.4.2 Unnatural amino acid mutagenesis

Unnatural amino acid mutagenesis expands the palette of amino acids available for structure-function studies. Through site-specific incorporation of unnatural amino acids, we can engineer novel functionalities into proteins or introduce much more subtle modifications to protein structure than are possible from the 20 naturally occurring residues, including modifications to the protein backbone. This powerful tool allows us to bring a physical organic chemistry problem solving approach to the study of complex membrane proteins. Unnatural amino acids can serve as highly specific probes of ligand binding interactions such as hydrogen bonds, cation-π interactions, and ion pairs, can serve as probes of local conformational changes, and can act as site-specific biophysical probes such as fluorophores.

To site-specifically incorporate unnatural amino acids, we use the nonsense suppression method for ribosomal incorporation.²¹ The mRNA codon corresponding to the amino acid of interest is replaced with a nonsense (stop) codon and a suppressor tRNA with the corresponding anticodon is supplied. This tRNA is acylated with the desired unnatural amino acid, which gets incorporated into the protein at the site of interest (Figure 1.6). tRNA acylation is typically accomplished in two steps. A dinucleotide corresponding to the last two positions of the complete 76mer tRNA's 3' terminus is chemically acylated with the amino acid of interest. This acylated dinucleotide is then ligated a truncated 74mer tRNA to yield the desired complete acylated tRNA. To discourage hydrolysis of the amino acid off of the tRNA, the unnatural amino acid typically bears a photolabile protecting group on its α -amino group, which is cleaved immediately before use of the tRNA.

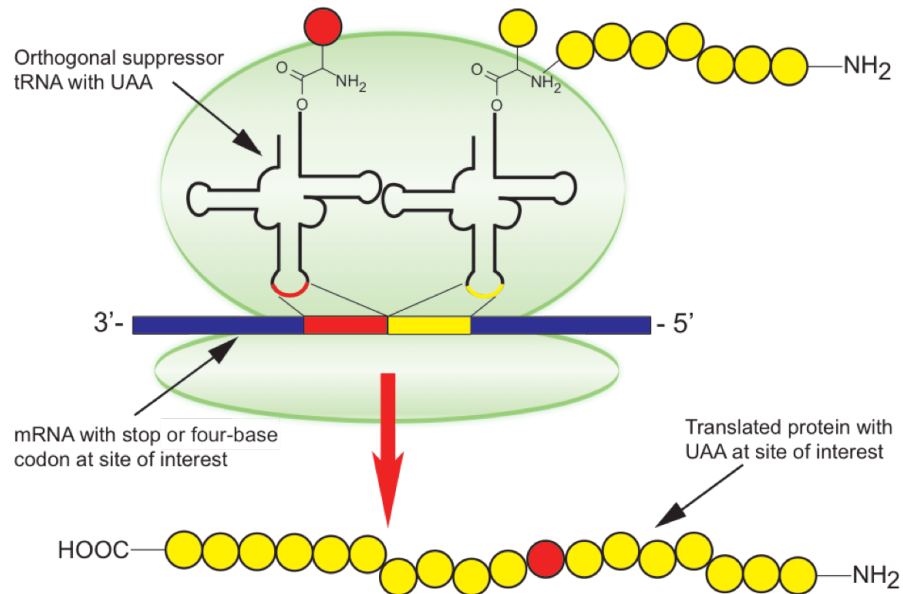


Figure 1.6. Nonsense suppression method for ribosomal incorporation of an unnatural amino acid into a protein.

For unnatural amino acid mutagenesis *in vivo*, we simply inject *Xenopus* oocytes with the appropriate mRNA and suppressor tRNA. The native translational machinery of the cell accepts these components to translate the protein of interest bearing the unnatural residue (Figure 1.7). It should be noted that the suppressor tRNA has been engineered to be orthogonal to cellular aminoacyl-tRNA synthetases, to limit *in vivo* reacylation of the tRNA with a natural amino acid.^{22,23}

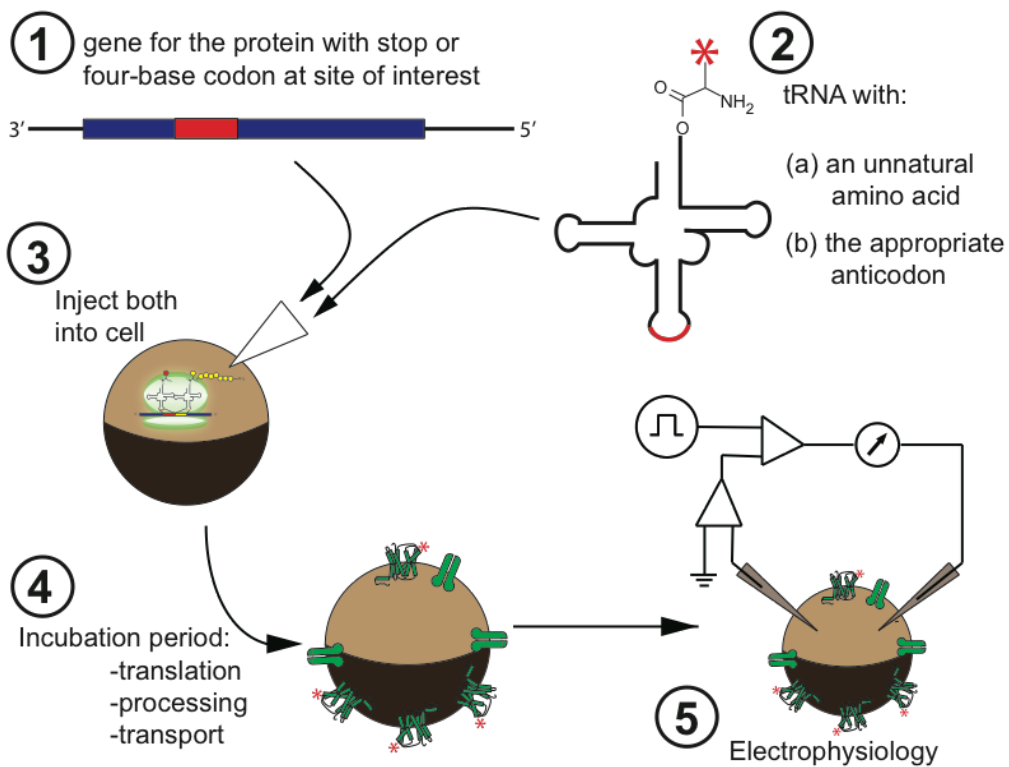


Figure 1.7. Unnatural amino acid mutagenesis by nonsense suppression applied to receptors expressed in *Xenopus* oocytes.

1.4.3 Probing receptor function with fluorescence

Fluorescent probes are incredibly powerful tools for the study of biological systems, allowing for location and conformation of biomolecules to be interrogated. While crystallography has clarified the structure of GPCRs and ligand-gated ion channels and suggested both inactive and active conformations of some of these proteins, many questions remain with regard to conformational changes involved in the activation of these receptors. Fluorescence is an ideal tool to probe the conformational repertoire of these proteins and its kinetics. Specifically, Förster resonance energy transfer (FRET) can monitor conformation by serving as a “molecular ruler” between two appropriate fluorophores. Fluorescence energy from a donor dye is transferred nonradiatively to an acceptor dye with an efficiency that depends sharply on the separation of these fluorophores, r , (FRET efficiency is proportional to $1/r^6$).

A major challenge for FRET studies is the selective incorporation of fluorophores into the protein(s) of interest in a nonperturbing fashion. Fluorescent proteins have the advantage of facile genetic incorporation into a protein of interest, but have relatively low brightness and photostability and are very large (~27 kDa), so they may perturb function.²⁴ Small molecule fluorophores have the advantage of smaller size and can have high brightness and photostability, but are generally more difficult to incorporate site-specifically. Unnatural amino acid mutagenesis by nonsense suppression offers an attractive option for site-selective fluorophore incorporation as an amino acid side chain. Both small molecule fluorophores incorporated as unnatural amino acid side chains and genetically encoded fluorescent proteins are applied to the study of membrane receptors in this dissertation.

1.5 Summary of dissertation work

This dissertation describes six studies on GPCRs and ligand-gated ion channels, primarily structure-function analyses of these proteins using unnatural amino acid probes.

Chapter 2 describes a study investigating the functional role of highly conserved proline residues within the transmembrane helices of the D2 dopamine GPCR. Through mutagenesis employing unnatural α -hydroxy acids, proline analogs, and N-methyl amino acids, we find that lack of backbone hydrogen bond donor ability is important to proline function. At one proline site we additionally find that a substituent on the proline backbone N is important to function.

Chapter 3 describes studies that probe side chain conformation by mutagenesis of GPCRs and the muscle-type nAChR. Specific side chain rearrangements have been proposed to accompany activation of these receptors. These rearrangements were probed using conformationally-biased β -substituted analogs of Trp and Phe and unnatural stereoisomers of Thr and Ile. We also modeled the conformational bias of the unnatural Trp and Phe analogs employed.

Chapters 4 and 5 examine details of ligand binding to nAChRs. Chapter 4 describes a study investigating the importance of hydrogen bonds to the complementary face of the muscle-type and $\alpha 4\beta 4$ nAChRs. A hydrogen bond involving the agonist appears to be important for ligand binding in the muscle-type receptor, but not the $\alpha 4\beta 4$ receptor. Chapter 5 describes a study characterizing the binding of varenicline, an actively prescribed smoking cessation therapeutic, to the $\alpha 7$ nAChR. Additionally, binding interactions to the complementary face of the $\alpha 7$ binding site were examined for a small

panel of agonists. We identified side chains important for binding large agonists such as varenicline, but dispensable for binding the small agonist ACh.

Chapter 6 describes efforts to image nAChRs site-specifically modified with a fluorophore by unnatural amino acid mutagenesis. Progress was hampered by high levels of fluorescent background. Improvements to sample preparation and alternative strategies for fluorophore incorporation are described.

Chapter 7 describes attempted development of a fluorescence assay for G protein association with a GPCR, with the ultimate goal of probing key protein-protein interactions along the G protein/receptor interface. A wide range of fluorescent protein fusions were generated, expressed in *Xenopus* oocytes, and evaluated for their ability to associate with each other using a FRET assay.

1.6 References

1. Unwin, N. Refined structure of the nicotinic acetylcholine receptor at 4 Å resolution. *Journal of Molecular Biology* **346**, 967–989 (2005).
2. Celie, P. H. *et al.* Nicotine and carbamylcholine binding to nicotinic acetylcholine receptors as studied in AChBP crystal structures. *Neuron* **41**, 907–914 (2004).
3. Bocquet, N. *et al.* X-ray structure of a pentameric ligand-gated ion channel in an apparently open conformation. *Nature* **457**, 111–114 (2009).
4. Hilf, R. J. C. & Dutzler, R. Structure of a potentially open state of a proton-activated pentameric ligand-gated ion channel. *Nature* **457**, 115–118 (2009).
5. Hilf, R. J. C. & Dutzler, R. X-ray structure of a prokaryotic pentameric ligand-gated ion channel. *Nature* **452**, 375–379 (2008).
6. Hibbs, R. E. & Gouaux, E. Principles of activation and permeation in an anion-selective Cys-loop receptor. *Nature* **474**, 54–60 (2011).
7. Zhong, W. *et al.* From ab initio quantum mechanics to molecular neurobiology: a cation-π binding site in the nicotinic receptor. *Proc. Natl. Acad. Sci. U.S.A.* **95**, 12088–12093 (1998).
8. Xiu, X., Puskar, N. L., Shanata, J. A., Lester, H. A. & Dougherty, D. A. Nicotine binding to brain receptors requires a strong cation-π interaction. *Nature* **458**, 534–537 (2009).

9. Cashin, A. L., Petersson, E. J., Lester, H. A. & Dougherty, D. A. Using physical chemistry to differentiate nicotinic from cholinergic agonists at the nicotinic acetylcholine receptor. *J. Am. Chem. Soc.* **127**, 350–356 (2005).
10. Blum, A. P., Lester, H. A. & Dougherty, D. A. Nicotinic pharmacophore: the pyridine N of nicotine and carbonyl of acetylcholine hydrogen bond across a subunit interface to a backbone NH. *Proc. Natl. Acad. Sci. U.S.A.* **107**, 13206–13211 (2010).
11. Blum, A. P., Van Arnam, E. B., German, L. A., Lester, H. A. & Dougherty, D. A. Binding interactions to the complementary subunit of nicotinic receptors. *J. Biol. Chem.* **288**, 6991–6997 (2013).
12. Puskar, N. L., Xiu, X., Lester, H. A. & Dougherty, D. A. Two neuronal nicotinic acetylcholine receptors, alpha4beta4 and alpha7, show differential agonist binding modes. *J. Biol. Chem.* **286**, 14618–14627 (2011).
13. Van Arnam, E. B., Blythe, E. E., Lester, H. A. & Dougherty, D. A. An Unusual Pattern of Ligand-Receptor Interactions for the alpha7 Nicotinic Acetylcholine Receptor, with Implications for the Binding of Varenicline. *Molecular Pharmacology* **84**, 201–207 (2013).
14. Jacoby, E., Bouhelal, R., Gerspacher, M. & Seuwen, K. The 7 TM G-protein-coupled receptor target family. *ChemMedChem* **1**, 761–782 (2006).
15. Cherezov, V. *et al.* High-resolution crystal structure of an engineered human beta2-adrenergic G protein-coupled receptor. *Science* **318**, 1258–1265 (2007).
16. Rasmussen, S. G. *et al.* Crystal structure of the beta2 adrenergic receptor-Gs protein complex. *Nature* **477**, 549–555 (2011).
17. Palczewski, K. *et al.* Crystal structure of rhodopsin: A G protein-coupled receptor. *Science* **289**, 739–745 (2000).
18. Katritch, V., Cherezov, V. & Stevens, R. C. Structure-Function of the G Protein-Coupled Receptor Superfamily. *Annu. Rev. Pharmacol. Toxicol.* **53**, 531–556 (2013).
19. Schwartz, T. W., Frimurer, T. M., Holst, B., Rosenkilde, M. M. & Elling, C. E. Molecular mechanism of 7TM receptor activation—a global toggle switch model. *Annu. Rev. Pharmacol. Toxicol.* **46**, 481–519 (2006).
20. Lüscher, C. & Slesinger, P. A. Emerging roles for G protein-gated inwardly rectifying potassium (GIRK) channels in health and disease. 1–15 (2010). doi:10.1038/nrn2834
21. Nowak, M. W. *et al.* In vivo incorporation of unnatural amino acids into ion channels in Xenopus oocyte expression system. *Meth. Enzymol.* **293**, 504–529 (1998).
22. Saks, M. E. *et al.* An engineered Tetrahymena tRNAGln for in vivo incorporation of unnatural amino acids into proteins by nonsense suppression. *J. Biol. Chem.* **271**, 23169–23175 (1996).
23. Rodriguez, E. A., Lester, H. A. & Dougherty, D. A. Improved amber and opal suppressor tRNAs for incorporation of unnatural amino acids in vivo. Part 1: Minimizing misacylation. *Rna* **13**, 1703–1714 (2007).
24. Shaner, N. C., Steinbach, P. A. & Tsien, R. Y. A guide to choosing fluorescent proteins. *Nat Methods* **2**, 905–909 (2005).

Chapter 2: Dissecting the functions of conserved prolines within transmembrane helices of the D2 dopamine receptor*

2.1 Abstract

G protein-coupled receptors (GPCRs) contain a number of conserved proline residues in their transmembrane helices, and it is generally assumed these play important functional and/or structural roles. Here we use unnatural amino acid mutagenesis, employing α -hydroxy acids and proline analogs, to examine the functional roles of five proline residues in the transmembrane helices of the D2 dopamine receptor. The well-known tendency of proline to disrupt helical structure is important at all sites, while we find no evidence for a functional role for backbone amide *cis-trans* isomerization, another feature associated with proline. At most proline sites, the loss of the backbone NH is sufficient to explain the role of the proline. However, at one site – P210^{5,50} – a substituent on the backbone N appears to be essential for proper function. Interestingly, the pattern in functional consequences that we see is mirrored in the pattern of structural distortions seen in many GPCR crystal structures.

2.2 Introduction

Proline stands apart from the other 19 canonical amino acids. Its cyclic side chain uniquely shapes protein structure and facilitates protein dynamics. As proline's side chain substantially restricts its backbone psi angle and removes a backbone hydrogen bond donor, proline disrupts the regular structures of both α -helices and β -sheets and can

*This chapter is adapted with permission from: Van Arnam, E. B., Lester, H. A., and Dougherty, D. A. Dissecting the functions of conserved prolines within transmembrane helices of the D2 dopamine receptor. *ACS Chem Biol* (2011) **6**, 1063-1068. Copyright © 2011 American Chemical Society.

introduce flexibility into these structures.¹⁻⁴ Further, proline's backbone N–substitution biases its peptide bonds to the *cis* conformer, relative to other peptide bonds. The *cis*–*trans* isomerization of proline peptide bonds is well documented to mediate protein folding and mature protein function.⁵ Here we examine which of the above properties contribute to function of the D2 dopamine G protein–coupled receptor (GPCR) at conserved proline sites within its transmembrane α -helices (TMs), using conventional and unnatural amino acid mutagenesis.

Transmembrane proline residues are a characteristic feature of GPCRs and are found in five of the D2 receptor's seven TMs. These prolines are also highly conserved; three (P201^{5.50}, P388^{6.50}, and P423^{7.50}) are the most conserved residue of their respective helix among Class A GPCRs and the remaining two (P89^{2.59}, P169^{4.59}) are conserved among aminergic GPCRs. (Superscripts refer to Ballesteros–Weinstein numbering, in which the most conserved residue of helix X is denoted X.50).⁶ A wealth of conventional mutagenesis studies has already established that these prolines play some significant functional role in GPCRs.⁷⁻¹⁴ Proline kinks have long been hypothesized to mediate the helical movements involved in GPCR activation, acting as pivot points, hinges, and/or swivels to expose a G protein binding site at the intracellular end of the helical bundle.^{15,16} A recent crystal structure of the closely related D3 dopamine receptor confirms that the prolines investigated here are associated with helical kinks, especially prominent in TMs 2, 6, and 7 (Figure 2.1).¹⁷ P169^{4.59} sits only one helical turn from the N–terminus of TM4, although the pre–proline turn is indeed kinked relative to the rest of the helix. Interestingly in the D3 and other GPCR crystal structures, TM5 is only slightly kinked, but instead possesses a prominent bulge in the helical turn preceding P201^{5.50}.¹⁷⁻²²

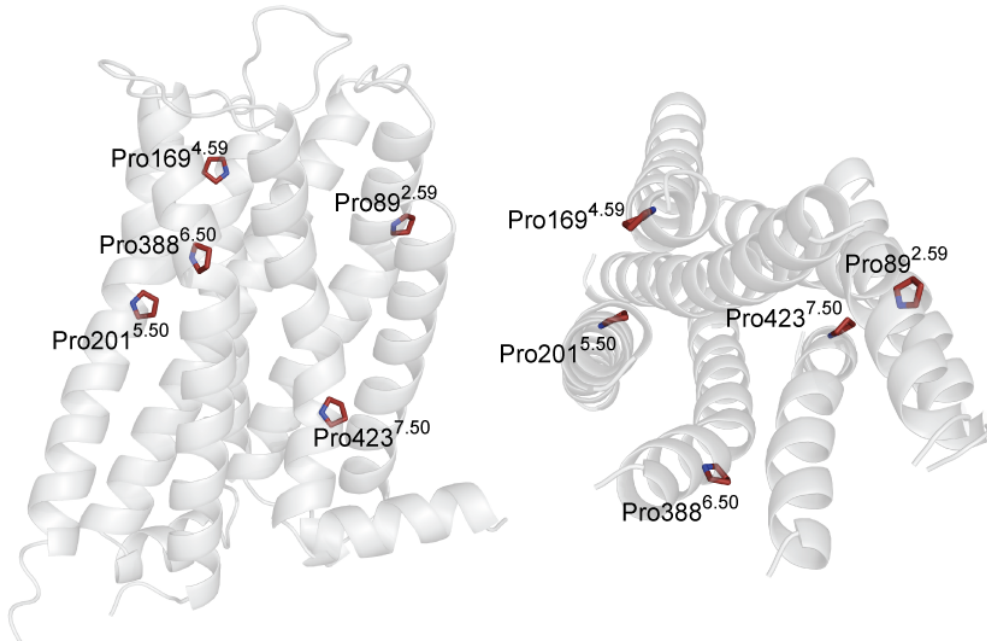


Figure 2.1. Two views of the crystal structure of the D3 dopamine receptor (PDB: 3PBL), highlighting the prolines considered here.¹⁷ Numbering is for the corresponding residues in the D2 receptor.

Proline's ability to distort helices most obviously comes from its lack of backbone hydrogen bond donor ability, which frees its would-be hydrogen bond acceptor, the backbone carbonyl of the residue $i-4$ from proline (Figure 2.2). Additionally, the proline side chain introduces a steric clash with the $i-4$ carbonyl. The net effect is usually manifested as a kink, which often frees the carbonyl $i-3$ to proline as well.^{2,5,23,24}

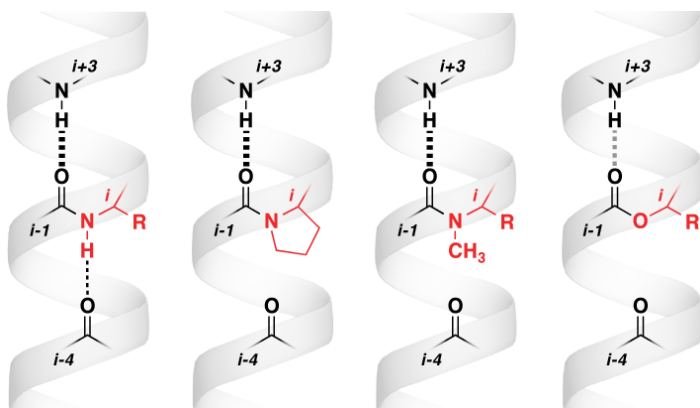


Figure 2.2. Hydrogen bonding patterns in an α -helix for (left to right) a typical amino acid; proline; an N-methyl amino acid; and an α -hydroxy acid.

Since the 19 other canonical amino acids are ill suited to probe the unique properties of proline, unnatural amino acid mutagenesis is an especially valuable tool to dissect the basis for a given proline's functional importance. As structural information on GPCRs continues to accrue, the subtle and high precision probes provided by unnatural residues will become increasingly valuable. Tests of detailed structural environments and specific functional roles are significantly facilitated by the unnatural amino acid methodology.

Here we compare the effect of replacing each of 5 TM prolines of the D2 receptor with unnatural α -hydroxy acids, and an N-methyl amino acid (Figure 2.2). We also consider cyclic proline analogs and conventional amino acids that correspond to the α -hydroxy acids. Unnatural α -hydroxy acids introduce a backbone ester that, like the proline peptide bond it replaces, is not a hydrogen bond donor (Figure 2.2). N-Me-Ala, effectively proline lacking its side chain C _{γ} , shares N-substitution (and thus lack of hydrogen bond donor ability) with proline, but has greater conformational freedom. Finally, proline analogs (Figure 2.3) that vary the size of the ring or introduce substituents can probe tolerance for subtle changes to the proline side chain as well as *cis-trans* isomerization. Pipecolic acid (Pip) and azetidine-2-carboxylic acid (Aze), six- and four-membered ring analogs of proline, respectively, have a greater *cis* bias relative to proline, while 2-methylproline (2-Me-Pro) is substantially more *trans*-biased.^{5,6}

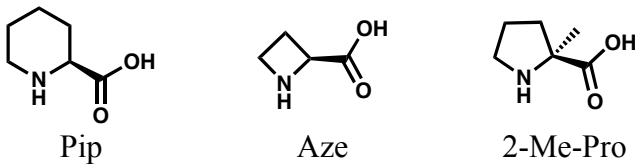


Figure 2.3. Unnatural proline analogs employed in this study

2.3 Results

2.3.1 Experimental approach

We utilized a recently optimized electrophysiological readout of the D2 receptor that yields quantitative dose–response relationships from receptor activation of coexpressed GIRK1/4 channels in *Xenopus laevis* oocytes and is amenable to unnatural amino acid mutagenesis by nonsense suppression.^{7-14,25} All unnatural amino acid and hydroxy acid mutations, as well as the valine mutants noted, were generated by nonsense suppression, while all other mutants were expressed conventionally. A wild-type rescue experiment (incorporating Pro by nonsense suppression) at each proline site yields an EC₅₀ within two-fold of the wild-type value, validating the ability to perform nonsense suppression at all residues considered here.

Because of the indirect nature of the measurement, interpretation of EC₅₀ requires some caution. A detailed discussion of this issue has been presented elsewhere.^{15,16,26} For present purposes, we consider EC₅₀ values that differ by a factor of greater than 2 to be distinguishable in this assay.

2.3.2 Strategy and general observations

Previously, we have characterized three distinct phenotypes for functionally important proline residues in ligand–gated ion channels. In the M1 transmembrane helix of both the α subunit of the muscle–type nicotinic acetylcholine receptor and the 5-HT_{3A} receptor, a conserved proline in the middle of the helix can be replaced by a range of α –hydroxy acids, giving essentially wild-type behavior.^{17,27,28} In contrast, incorporating any canonical amino acid other than proline gave a nonfunctional receptor. A second phenotype was seen in the M2–M3 loop of the 5-HT_{3A} receptor.^{17-22,29} In this system,

cis-trans isomerization of a proline peptide bond is critical for receptor gating, as revealed by a series of cyclic proline analogs with varying *cis* preferences. Finally, we have characterized an important proline–aromatic interaction in the Cys loop of the muscle–type nicotinic acetylcholine receptor, in which the hydrophobicity of a Phe side chain preceding proline is important for receptor function.³⁰ We seek to determine which of these phenotypes is most applicable to the transmembrane prolines of the D2 receptor, and we began by incorporating α -hydroxy acids at each site.

For the most part, incorporation of an α -hydroxy residue is not strongly perturbing; all but one of the hydroxy acid mutants we could characterize gave EC₅₀s within 5-fold of wild type (Figure 2.4, Table 2.1). In addition, each conventional amino acid residue is typically much more perturbing than its unnatural α -hydroxy acid analog. This trend suggests the importance of lacking a hydrogen bond donor at these sites. N-Me-Ala provides an alternative way to remove the backbone NH group, and it is also well-tolerated at all sites. Given the results for α -hydroxy residues and N-Me-Ala, it is not surprising that various cyclic proline analogs, which are much more similar to proline, are well-tolerated at all transmembrane proline sites, yielding EC₅₀s within 5-fold of wild type.

Mutations of proline to the conventional amino acids Ala, Val, and Leu range from modestly perturbing to dramatically perturbing (EC₅₀ shifts of 3.5-fold to >2000-fold from wild type), with the exception of P89^{2,59}, discussed below. Generally, Gly is less perturbing than the other natural amino acids, with the glaring exception of P201^{5,50}G. These conventional mutants provide a useful reference to which we can compare the α -hydroxy mutants.

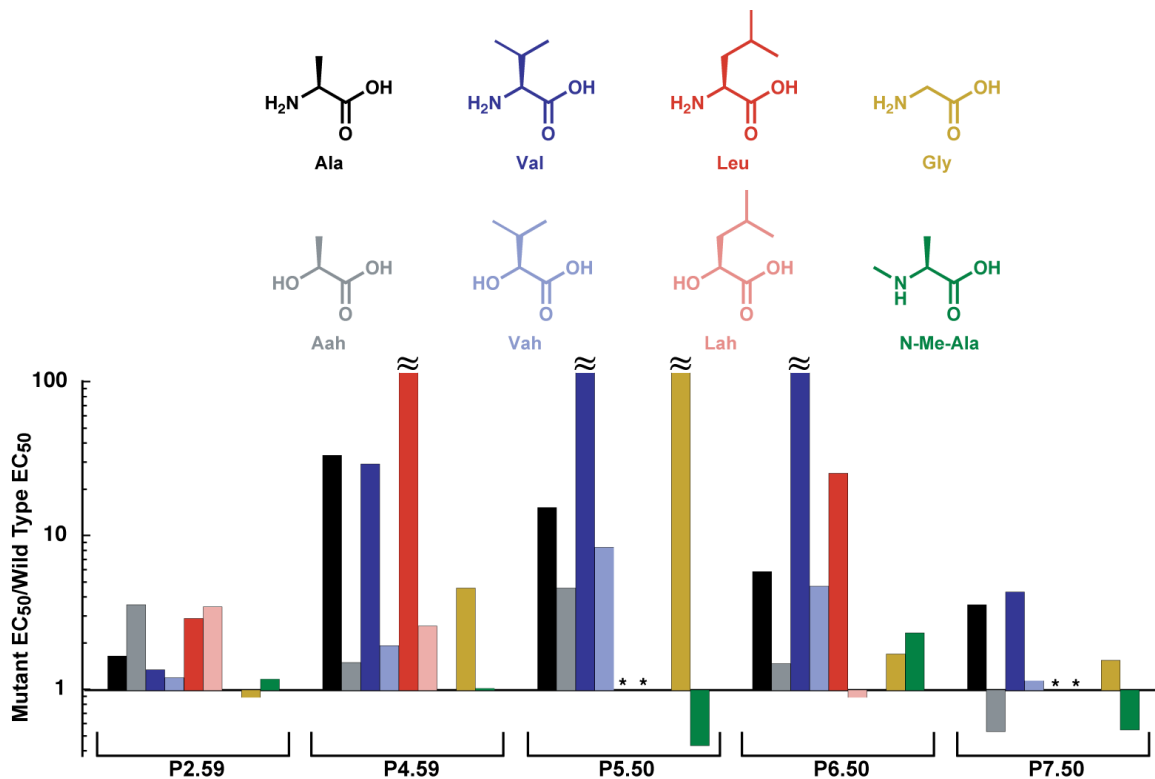


Figure 2.4. Results for incorporating α -hydroxy acids; their amino acid analogs; Gly; and N-Me-Ala. At four sites, indicated by a \approx , EC₅₀ is too large to determine accurately. * = no current detected.

The P89^{2,59} site, despite >70% conservation among aminergic receptors, accepts diverse mutations with only modest functional consequences. All mutations made, including conventional mutations, give wild-type EC₅₀s or relatively small shifts from wild type. Evidently, this site does not require the unique side chain and hydrogen bonding properties conferred by proline, and we will not consider it further here.

Table 2.1. Conventional amino acid, hydroxy acid, and N-Me-Ala mutations. EC₅₀ and Hill coefficient (n_H) are ± SEM for goodness of fit to the Hill equation.

Site	Mutation	EC ₅₀ (nM)	n _H	n
wild type		39 ± 1	1.12 ± 0.03	71
Pro89 ^{2,59}	Pro ^a	24 ± 1	1.14 ± 0.04	30
	Gly	35 ± 3	1.3 ± 0.1	12
	Ala	65 ± 4	1.32 ± 0.08	10
	Val ^b	53 ± 7	1.2 ± 0.2	11
	Leu	114 ± 5	1.33 ± 0.07	10
	Aah	140 ± 10	0.94 ± 0.05	12
	Vah	47 ± 1	1.20 ± 0.02	13
	Lah	136 ± 4	1.19 ± 0.03	13
	N-Me-Ala	46 ± 2	1.11 ± 0.04	19
Pro169 ^{4,59}	Pro ^a	41 ± 2	1.17 ± 0.05	49
	Gly	180 ± 10	1.00 ± 0.06	14
	Ala	1310 ± 80	1.12 ± 0.06	12
	Val ^b	1150 ± 70	1.03 ± 0.05	12
	Leu	>2000 ^c		14
	Aah	59 ± 3	1.20 ± 0.07	15
	Vah	76 ± 4	1.42 ± 0.09	14
	Lah	102 ± 2	1.27 ± 0.03	27
	N-Me-Ala	40 ± 2	1.22 ± 0.06	11
Pro201 ^{5,50}	Pro ^a	24 ± 1	1.07 ± 0.04	37
	Gly	>2000 ^c		17
	Ala	600 ± 50	1.09 ± 0.09	17
	Val	>2000 ^c		20
	Leu	ND ^d		
	Aah	180 ± 10	1.3 ± 0.1	9
	Vah	330 ± 10	1.01 ± 0.04	14
	Lah	ND ^d		
	N-Me-Ala	16 ± 1	1.15 ± 0.08	14
Pro388 ^{6,50}	Pro ^a	46 ± 2	1.18 ± 0.04	34
	Gly	67 ± 3	1.24 ± 0.06	9
	Ala	230 ± 10	1.25 ± 0.06	14
	Val ^b	>2000 ^c		15
	Leu	1000 ± 100	0.87 ± 0.07	10
	Aah	58 ± 2	1.43 ± 0.07	15
	Vah	185 ± 6	1.31 ± 0.05	9
	Lah	35 ± 2	1.12 ± 0.07	25
	N-Me-Ala	92 ± 4	1.26 ± 0.06	12
Pro423 ^{7,50}	Pro ^a	35 ± 2	1.13 ± 0.06	43
	Gly	61 ± 5	1.19 ± 0.09	16
	Ala	140 ± 10	1.4 ± 0.1	10
	Val ^b	170 ± 8	1.01 ± 0.04	16
	Leu	ND ^d		
	Aah	21 ± 2	1.4 ± 0.1	8
	Vah	45 ± 3	1.10 ± 0.05	16
	Lah	ND ^d		
	N-Me-Ala	21.5 ± 1	1.25 ± 0.06	10

^aExpression of the wild type receptor with the natural amino acid incorporated by nonsense suppression

^bConventional mutant generated by nonsense suppression

^cResponse of naïve oocytes to dopamine doses ≥ 100 μM obscures complete dose-response data

^dNo dopamine-induced current detected for dopamine concentrations up to 1 mM

2.3.3 $169^{4.59}$, $388^{6.50}$, $423^{7.50}$: Importance of lacking a backbone hydrogen bond donor

For the TM4, 6, and 7 proline sites, we observe hydroxy acid mutations (to Aah, Vah, or Lah; “ah” signifying α -hydroxy) in all cases to be less perturbing than the corresponding conventional amino acid mutations (to Ala, Val, or Leu) (Figure 2.4, Table 2.1). In fact, most of the hydroxy acid mutants for these sites ($P169^{4.59}$ Aah, $P169^{4.59}$ Vah, $P388^{6.50}$ Aah, $P388^{6.50}$ Lah, $P423^{7.50}$ Aah, and $P423^{7.50}$ Vah) have EC_{50} s that are not meaningfully different from wild type (i.e., within the margin of error we can expect from this assay). As hydroxy acids and proline both lack backbone hydrogen bond donors, this property alone may account for proline’s functional role at these sites. However, hydroxy acids do introduce additional perturbations, including weakening the hydrogen bond acceptor strength of the preceding residue’s backbone carbonyl, and an electrostatic repulsion by the introduced main chain oxygen with the $i-4$ carbonyl.

An alternative way to remove the backbone NH of a peptide bond is with N-Me-Ala, which contains a fragment of the proline ring and does not significantly perturb the backbone carbonyl. At the helix 4, 6, and 7 prolines, N-Me-Ala is not largely perturbing, being essentially equivalent to Aah and producing EC_{50} s within 2.5-fold of wild type. This suggests that the carbonyl mutation associated with α -hydroxy residues is not a large factor in these helices.

Given the tolerance for α -hydroxy and N-methyl residues, it is not surprising that the proline analogs Aze and Pip are also well tolerated in helices 4, 6, and 7 (Table 2.2). As described in previous work, Aze and Pip show different intrinsic *cis-trans* preferences than Pro.⁵ The minimal impact of these mutations at these sites indicates that *cis-trans* isomerization is not an essential component of receptor function. While varying ring size

does not substantially alter function, introducing a methyl substituent at proline's α carbon (2-Me-Pro) does produce measurable EC₅₀ shifts at the 388^{6.50} and 423^{7.50} sites, but not at 169^{4.59}.

Table 2.2. Proline analog mutations. EC₅₀ and Hill coefficient (n_H) are \pm SEM for goodness of fit to the Hill equation.

Site	Mutation	EC ₅₀ (nM)	n _H	n
Pro89 ^{2.59}	Pip	26 \pm 2	1.04 \pm 0.04	11
	Aze	26 \pm 3	1.3 \pm 0.1	11
	2-Me-Pro	64 \pm 3	1.25 \pm 0.05	9
Pro169 ^{4.59}	Pip	19 \pm 2	1.00 \pm 0.09	12
	Aze	25 \pm 3	1.1 \pm 0.1	17
	2-Me-Pro	37 \pm 3	1.3 \pm 0.1	18
Pro201 ^{5.50}	Pip	34 \pm 2	1.14 \pm 0.06	21
	Aze	41 \pm 2	0.90 \pm 0.03	10
	2-Me-Pro	160 \pm 10	0.95 \pm 0.07	15
Pro388 ^{6.50}	Pip	82 \pm 5	1.12 \pm 0.07	17
	Aze	47 \pm 3	1.26 \pm 0.07	11
	2-Me-Pro	131 \pm 5	0.77 \pm 0.02	15
Pro423 ^{7.50}	Pip	80 \pm 5	1.27 \pm 0.09	10
	Aze	15 \pm 2	1.1 \pm 0.1	12
	2-Me-Pro	128 \pm 7	0.95 \pm 0.04	12

Interestingly, Gly is less perturbing than the other conventional amino acids at these sites. We do note, however, that the P423^{7.50}G mutant gave currents that were generally small, suggesting either poor expression or diminished receptor efficacy. While no P423^{7.50} mutants produced dramatic EC₅₀ shifts, cells injected with appropriate mRNA and tRNA for the Leu and Lah mutants gave no response in our assay; evidently the leucine side chain is not tolerated.

2.3.4 201^{5.50}: N-substitution as well as lack of a hydrogen bond donor are important

The 201^{5.50} site shows a qualitatively distinct pattern from the other prolines considered here. As before, α -hydroxy residues are less perturbing than their α -amino analogs. Unlike the other proline sites, however, no hydroxy acid mutation to P201^{5.50}

yields a wild-type EC₅₀. P201^{5.50}Aah and P201^{5.50}Vah are loss of function by 4– and 8-fold, respectively, while we were unable to characterize the P201^{5.50}Lah mutant (though the same was true of the Leu mutant). Interestingly, N–Me–Ala is minimally perturbing, perhaps even gain of function, and the proline analogs Pip and Aze are wild type. Taken together, these data suggest that simply deleting the hydrogen bonding ability of the backbone NH is not sufficient to produce a functional receptor. A substituent on the N is also necessary, and it can be either a ring (Pro, Pip, Aze) or a methyl (N–Me–Ala). Also in contrast to the TM4, 6, and 7 sites, Gly is highly disruptive at 201^{5.50}, more so than Ala. Together with the fact that no hydroxy acid tested gave a wild-type EC₅₀ at this site, these findings suggests a more specific need for proline here, not merely a generic requirement for a helix–breaking residue.

2.4 Discussion

In the present work, we have used nonsense suppression techniques and the assay system we recently developed to evaluate an array of unnatural residues at five new sites of the D2 dopamine receptor. Our results establish the generality of this protocol for evaluating GPCR function with unnatural residues.

In particular, we have probed five conserved proline sites located in the transmembrane region of the D2 receptor. Transmembrane prolines are not uncommon, and are frequently considered to play important functional roles by introducing structural perturbations and/or increased conformational flexibility to the helix.^{4,15} In previous work we established several types of unnatural residues to probe proline function: α -

hydroxy acids to evaluate the role of backbone hydrogen bonding,^{27,28} and a series of proline analogs to evaluate any role for *cis–trans* isomerization around the proline peptide bond.²⁹ In many ways, the prolines considered here respond to our various mutations in a common fashion, although we find that P201^{5,50} shows a functional phenotype that is distinct from the other residues.

Not surprisingly, P89^{2,59}, which is located in a helix that is not intimately involved in ligand binding nor conformational changes, is generally tolerant of mutations and does not show any obvious trends in the mutagenesis data.

Three prolines on more critical helices – P169^{4,59}, P388^{6,50}, and P423^{7,50} – share a functional phenotype. Conventional amino acids are modestly to substantially disruptive, but their corresponding α -hydroxy acids significantly restore function. N-Me-Ala and the proline analogs Pip and Aze are also well tolerated. Taken together, these results indicate that the key function of proline at these sites is to disrupt the α helix by removing the key backbone NH. Any strategy that accomplishes this, including cyclic residues, α -hydroxy residues, or N-methyl residues, produces receptors with essentially wild type function. Interestingly, glycine is also well tolerated. Glycine is well known to have an especially low propensity for helical structures relative to other amino acids (second-lowest only to proline),^{31,32} a property believed to stem both from its high conformational entropy and from its minimal burial of solvent accessible surface area in helices.³³ The good tolerance of Gly at these sites suggests a generic functional requirement for a helix breaker at these sites. Proline appears to accomplish this by lack of a backbone hydrogen bond donor, but Gly can achieve the same end by different means.

Structurally, all three prolines seem to play a similar role also. In various structures of GPCRs, helices 4, 6, and 7 all display a significant kink associated with the proline.¹⁷⁻²¹ Movements of helices 6 and 7 are considered to be critical to receptor activation, with the kinks playing a prominent role.¹⁶ Indeed, a recent crystal structure thought to represent an active conformation of the β 2 adrenergic receptor shows displacement of TM6 accomplished by a slight “unwinding” of the helical turn preceding the proline at position 6.50.³⁴ The movement originates at residue 6.46, the would-be backbone hydrogen bond acceptor to position 6.50, potentially providing a direct link between proline 6.50’s lack of hydrogen bond donor ability and functionally important helix flexibility.

Because the α -hydroxy residues do not seriously compromise receptor function at these sites (the way their α -amino analogs do), we can use the α -hydroxy data to consider the effects of side chain variation. The largest perturbations are seen for Lah at P169^{4,59} and Vah at P388^{6,50}. This suggests that the 169^{4,59} site is sensitive to size, while 388^{6,50} is sensitive to β -branching. No response was detected for cells injected with appropriate mRNA and tRNA for P423^{7,50}L and P423^{7,50}Lah mutations, suggesting this site is especially sensitive to steric bulk. Supporting this notion, in the D3 receptor crystal structure, the P423^{7,50} side chain points directly at TM1, while P169^{4,59} and P388^{6,50} are directed more toward the lipid bilayer.¹⁷ Curiously, the P423^{7,50}G mutant gives small signals (though a near-wild-type EC₅₀), suggesting this site may play an important role in GPCR folding, transport, and/or function, possibilities we cannot differentiate with our assay.

P201^{5,50} shows a different pattern in response to the array of mutations considered here. α -Hydroxy residues are more strongly perturbing, while N-Me-Ala and the cyclic proline analogs Pip and Aze are wild type. This suggests that simply removing the NH is not enough to achieve the function of the native proline residue. There must be a substituent on the backbone N. Consistent with this, glycine is highly perturbing at P201^{5,50}, in contrast to the other sites.

It is clear from Figure 2.1 that the structural perturbation associated with the proline of helix 5 is distinct from what is seen in helices 2, 4, 6, and 7. Instead of a prominent kink, helix 5 has a bulge. It has been proposed that this bulge is functionally significant, as residues in the bulge directly contact ligands in the agonist binding site. Specifically, the side chain of S197^{5,46}, which is *i*-4 relative to P201^{5,50} and located at the center of the bulge, is thought to contribute a hydrogen bond that is important to agonist binding.^{35,36} Evidently, the steric effect of proline's N-substitution is key to producing this bulge.

2.5 Conclusions

In all functionally important transmembrane proline sites we have investigated to date – the TM 4, 5, 6, and 7 prolines in this study and the M1 transmembrane proline of two different ligand-gated ion channels – we find that lack of a backbone hydrogen bond donor is important for function.^{27,28} A general phenotype has emerged in which loss of function mutations to conventional amino acids are mitigated by the corresponding α -hydroxy acids. In contrast, α -hydroxy residues produced nonfunctional human 5-HT₃

receptors when replacing a proline that appears to undergo *cis–trans* isomerization.²⁹ This proline lies not in an α –helix, but in a loop/turn region, where *cis–trans* isomerization seems much more plausible.

We do observe variations on the general transmembrane proline phenotype. Unlike the D2 receptor’s TM4, 6, and 7 prolines, the requirement for lacking a backbone hydrogen bond donor is absolute at the ion channel M1 proline sites; conventional amino acids, including glycine, produced completely nonfunctional channels.^{27,28} The TM5 proline of the D2 receptor additionally requires N–substitution for fully wild-type function. Taken together, these studies establish the power of unnatural amino acid methodology for dissecting out the various consequences of the proline residue’s unique structural features.

2.6 Experimental

2.6.1 Molecular biology

In these experiments, the cDNA for GIRK1 and GIRK4 was in pBSMXT plasmids and for the D2 receptor (human long form) was in the pGEMhe plasmid. Site-directed mutagenesis was performed using the Stratagene QuikChange protocol to generate the appropriate codon. For unnatural amino acid mutants and conventional mutants generated by nonsense suppression, the site of interest was mutated to the TAG stop codon. Plasmids were linearized with the appropriate restriction enzymes (the GIRK plasmids with SalI and the D2 receptor with NheI or SbfI). Receptor mRNA was

prepared by *in vitro* runoff transcription using the Ambion T7 mMessage mMachine kit and GIRQ1 and GIRQ4 mRNA was prepared with the T3 kit.

Hydroxy or amino acids, all commercially available, were appended to the dinucleotide dCA and enzymatically ligated to truncated 74mer THG73 tRNA as previously described.^{37,38} The 74mer tRNA was prepared using the Ambion T7 MEGAshortscript™ kit by transcription from a DNA oligonucleotide template with its 5' terminal two nucleotides bearing methoxy groups at the ribose C2' position to enhance RNA transcript homogeneity, as described in the literature.³⁹ Crude tRNA–amino acid or tRNA–hydroxy acid product was used without desalting, and the product was confirmed by matrix–assisted laser desorption ionization time–of–flight mass spectrometry on a 3–hydroxypicolinic acid matrix. Deprotection of the NVOC group on the tRNA–amino acids or NB group on tRNA–Aah was carried out by 5–min photolysis on a 1 kW xenon lamp with WG–335 and UG–11 filters immediately prior to injection. tRNA–Vah and –Lah were unprotected and were injected directly.

2.6.2 Oocyte preparation and RNA injection

Stage V–VI oocytes of *Xenopus laevis* were harvested and injected with RNAs as described previously.³⁷ For nonsense suppression experiments, each cell was injected with 15 ng each of GIRQ1 and GIRQ4 mRNA approximately 64 hours before recording, then 4 – 30 ng receptor mRNA and approximately 25 – 60 ng appropriate tRNA approximately 48 hours before recording. Mutants yielding small responses required a second injection of receptor mRNA and appropriate tRNA 24 hours before recording.

For wild type experiments, each cell received a single injection of 0.16 ng receptor mRNA and 10 ng each of GIRK1 and GIRK4 mRNA approximately 48 hrs before recording. Conventional amino acid mutants (except those generated by nonsense suppression) were prepared identically, except 1 ng receptor mRNA was required. Small responses were obtained for P423^{7,50}G, which required 10 ng receptor mRNA. Injection volumes for each injection session were 25 – 75 nL per cell.

As a negative control for suppression experiments at each site, unacylated full length tRNA was co-injected with mRNA in the same manner as charged tRNA. These experiments yielded negligible responses for all sites. Wild-type recovery conditions (injecting tRNA-Pro and appropriate mRNA) were injected alongside mutant nonsense suppression conditions to control for data variability.

2.6.3 Electrophysiology

Oocyte recordings were made in two-electrode voltage clamp mode using the OpusXpress™ 6000A (Axon Instruments). Recording buffers were ND96 (96 mM NaCl, 2 mM KCl, 1 mM MgCl₂, 5 mM HEPES, 1.8 mM CaCl₂, pH 7.5) and high K⁺ ringer (96 mM NaCl, 24 mM KCl, 1 mM MgCl₂, 5 mM HEPES, 1.8 mM CaCl₂, pH 7.5). Solution flow rates were 2 mL min⁻¹ and drug application flow rates were 2.5 mL min⁻¹. Initial holding potential was -60 mV. Data were sampled at 125 Hz and filtered at 50 Hz. Cells were subjected to a ND96 pre-wash for 10 s, a high K⁺ application for 50 s to establish basal currents, and dopamine application in high K⁺ ringer for 25 s, followed by high K⁺ and ND96 washings for 45 s and 90 s in duration, respectively. Dopamine-induced currents were measured over the basal K⁺ current as described previously.²⁵ Dopamine (Sigma-Aldrich) solutions in high K⁺ ringer were prepared immediately before recording

by dilutions from a 1 M stock in ddi water. Dose–response data were obtained for a minimum of eight concentrations of dopamine, for a minimum of two cell batches, and for a minimum of 8 cells total. Dose–response relations were fitted to the Hill equation, $I_{Norm} = 1/(1+(EC_{50}/A))^{nH}$, where I_{Norm} is the normalized current peak at [dopamine] = A , EC_{50} is the concentration of agonist that elicits a half–maximum response, and n_H is the Hill coefficient. EC_{50} values were obtained by averaging the I_{Norm} values for each cell at a given dose and fitting those averaged I_{Norm} data to the Hill equation.

2.7 References

1. Barlow, D. J. & Thornton, J. M. Helix geometry in proteins. *J Mol Biol* **201**, 601–619 (1988).
2. Woolfson, D. N. & Williams, D. H. The influence of proline residues on alpha-helical structure. *FEBS Lett.* **277**, 185–188 (1990).
3. Reiersen, H. & Rees, A. R. The hunchback and its neighbours: proline as an environmental modulator. *Trends Biochem. Sci.* **26**, 679–684 (2001).
4. Cordes, F. S., Bright, J. N. & Sansom, M. S. Proline-induced distortions of transmembrane helices. *J Mol Biol* **323**, 951–960 (2002).
5. Dugave, C. & Demange, L. Cis-trans isomerization of organic molecules and biomolecules: implications and applications. *Chem. Rev.* **103**, 2475–2532 (2003).
6. Ballesteros, J. A. & Weinstein, H. Integrated Methods for the Construction of Three-Dimensional Models and Computational Probing of Structure-Function Relations in G Protein-Coupled Receptors. *Methods in Neurosciences* **25**, 366–428 (1995).
7. Wess, J., Nanavati, S., Vogel, Z. & Maggio, R. Functional role of proline and tryptophan residues highly conserved among G protein-coupled receptors studied by mutational analysis of the m3 muscarinic receptor. *EMBO J* **12**, 331–338 (1993).
8. Kolakowski, L. F. J., Lu, B., Gerard, C. & Gerard, N. P. Probing the ‘message:address’ sites for chemoattractant binding to the C5a receptor. Mutagenesis of hydrophilic and proline residues within the transmembrane segments. *J. Biol. Chem.* **270**, 18077–18082 (1995).
9. Hong, S., Ryu, K. S., Oh, M. S., Ji, I. & Ji, T. H. Roles of transmembrane prolines and proline-induced kinks of the lutropin/choriogonadotropin receptor. *J. Biol. Chem.* **272**, 4166–4171 (1997).
10. Knudsen, S. M., Tams, J. W. & Fahrenkrug, J. Functional roles of conserved transmembrane prolines in the human VPAC(1) receptor. *FEBS Lett.* **503**, 126–

- 130 (2001).
11. Stitham, J., Martin, K. A. & Hwa, J. The critical role of transmembrane prolines in human prostacyclin receptor activation. *Mol Pharmacol* **61**, 1202–1210 (2002).
 12. Conner, A. C. *et al.* A key role for transmembrane prolines in calcitonin receptor-like receptor agonist binding and signalling: implications for family B G-protein-coupled receptors. *Mol Pharmacol* **67**, 20–31 (2005).
 13. Haffemayer, B., Richard, E., Mattras, H. & Marie, J. Functional role of the conserved proline in helix 6 of the human bradykinin B2 receptor. *Biochem Biophys Res Commun* **366**, 1001–1006 (2008).
 14. Mazna, P. *et al.* The role of proline residues in the structure and function of human MT2 melatonin receptor. *J. Pineal Res.* **45**, 361–372 (2008).
 15. Sansom, M. S. & Weinstein, H. Hinges, swivels and switches: the role of prolines in signalling via transmembrane alpha-helices. *Trends in Pharmacological Sciences* **21**, 445–451 (2000).
 16. Schwartz, T. W., Frimurer, T. M., Holst, B., Rosenkilde, M. M. & Elling, C. E. Molecular mechanism of 7TM receptor activation—a global toggle switch model. *Annu Rev Pharmacol Toxicol* **46**, 481–519 (2006).
 17. Chien, E. Y. *et al.* Structure of the human dopamine D3 receptor in complex with a D2/D3 selective antagonist. *Science* **330**, 1091–1095 (2010).
 18. Palczewski, K. *et al.* Crystal structure of rhodopsin: A G protein-coupled receptor. *Science* **289**, 739–745 (2000).
 19. Cherezov, V. *et al.* High-resolution crystal structure of an engineered human beta2-adrenergic G protein-coupled receptor. *Science* **318**, 1258–1265 (2007).
 20. Warne, T. *et al.* Structure of a beta1-adrenergic G-protein-coupled receptor. *Nature* **454**, 486–491 (2008).
 21. Jaakola, V. P. *et al.* The 2.6 angstrom crystal structure of a human A2A adenosine receptor bound to an antagonist. *Science* **322**, 1211–1217 (2008).
 22. Wu, B. *et al.* Structures of the CXCR4 chemokine GPCR with small-molecule and cyclic peptide antagonists. *Science* **330**, 1066–1071 (2010).
 23. Heijne, von, G. Proline kinks in transmembrane alpha-helices. *J Mol Biol* **218**, 499–503 (1991).
 24. MacArthur, M. W. & Thornton, J. M. Influence of proline residues on protein conformation. *J Mol Biol* **218**, 397–412 (1991).
 25. Torrice, M. M., Bower, K. S., Lester, H. A. & Dougherty, D. A. Probing the role of the cation-pi interaction in the binding sites of GPCRs using unnatural amino acids. *Proc. Natl. Acad. Sci. U.S.A.* **106**, 11919–11924 (2009).
 26. Torrice, M. M. Chemical-Scale Studies of the Nicotinic and Muscarinic Acetylcholine Receptors. (2009).
 27. England, P. M., Zhang, Y., Dougherty, D. A. & Lester, H. A. Backbone mutations in transmembrane domains of a ligand-gated ion channel: implications for the mechanism of gating. *Cell* **96**, 89–98 (1999).
 28. Dang, H., England, P. M., Farivar, S. S., Dougherty, D. A. & Lester, H. A. Probing the role of a conserved M1 proline residue in 5-hydroxytryptamine(3) receptor gating. *Mol Pharmacol* **57**, 1114–1122 (2000).
 29. Lummis, S. C. *et al.* Cis-trans isomerization at a proline opens the pore of a neurotransmitter-gated ion channel. *Nature* **438**, 248–252 (2005).

30. Limapichat, W., Lester, H. A. & Dougherty, D. A. Chemical scale studies of the Phe-Pro conserved motif in the cys loop of Cys loop receptors. *J. Biol. Chem.* **285**, 8976–8984 (2010).
31. Pace, C. N. & Scholtz, J. M. A helix propensity scale based on experimental studies of peptides and proteins. *Biophys J* **75**, 422–427 (1998).
32. Moreau, R. J. *et al.* Context-independent, temperature-dependent helical propensities for amino acid residues. *J. Am. Chem. Soc.* **131**, 13107–13116 (2009).
33. Scott, K. A., Alonso, D. O., Sato, S., Fersht, A. R. & Daggett, V. Conformational entropy of alanine versus glycine in protein denatured states. *Proc. Natl. Acad. Sci. U.S.A.* **104**, 2661–2666 (2007).
34. Rasmussen, S. G. *et al.* Structure of a nanobody-stabilized active state of the beta(2) adrenoceptor. *Nature* **469**, 175–180 (2011).
35. Floresca, C. Z. & Schetz, J. A. Dopamine receptor microdomains involved in molecular recognition and the regulation of drug affinity and function. *J Recept Signal Transduct Res* **24**, 207–239 (2004).
36. Warne, T. *et al.* The structural basis for agonist and partial agonist action on a beta(1)-adrenergic receptor. *Nature* **469**, 241–244 (2011).
37. Nowak, M. W. *et al.* In vivo incorporation of unnatural amino acids into ion channels in Xenopus oocyte expression system. *Meth. Enzymol.* **293**, 504–529 (1998).
38. England, P. M., Lester, H. A. & Dougherty, D. A. Incorporation of esters into proteins: Improved synthesis of hydroxyacyl tRNAs. *Tetrahedron Lett* **40**, 6189–6192 (1999).
39. Kao, C., Zheng, M. & Rudisser, S. A simple and efficient method to reduce nontemplated nucleotide addition at the 3 terminus of RNAs transcribed by T7 RNA polymerase. *Rna* **5**, 1268–1272 (1999).

Chapter 3: Probing side chain conformations and rearrangements in receptor binding sites

3.1 Abstract

The large-scale gating motions of ligand-activated transmembrane receptors are likely correlated with motions at the ligand binding site, such as side chain rearrangements upon ligand binding. In GPCRs and in nAChRs, the nature of these conformational changes, and the precise orientation of side chains in the ligand-bound, active state, have been widely debated. Activation models have been proposed, such as the rotamer toggle switch model for GPCR activation, though there is little experimental evidence to support them. Crystallography and molecular dynamics of these systems have offered some insight, though have largely complicated, rather than clarified, models of gating at the binding site. Here we present several mutagenesis approaches to study side chain conformations and rearrangements. Rotamer-biased β -methyl analogs of Trp and Phe, and other unnatural analogs, were employed at several sites in the muscle-type nAChR and in the D2 dopamine and M2 acetylcholine GPCRs. These data provide some suggestive evidence for specific side chain geometries, corroborated by modeling of the conformational bias of these unnatural side chains. However, much of the data cannot be reconciled with proposed steric clashes or activation models, underscoring the difficulty of rationalizing conformation by mutagenesis.

3.2 Introduction

Gating of GPCRs and nAChRs is initiated by ligand binding, and ultimately results in substantial conformational changes of the receptor that enable association with a G protein (in the case of GPCRs) or opening of an ion-conducting pore (in the case of nAChRs). Presumably these large-scale gating motions are coupled to smaller scale rearrangements of the binding site, which also assumes active and inactive states. The structural details of these active and inactive states of the binding site are debated in both of these systems.

3.2.1 GPCR activation

In GPCRs, receptor activation is characterized by an outward displacement of the intracellular end of transmembrane helix 6 (TM6), which creates a binding site for the G protein.¹ This is thought to be a conserved mode of activation among GPCRs and was originally proposed on the basis of site-directed spin labeling,² disulfide crosslinking,³ and fluorescence experiments.⁴ TM6 displacement upon activation has also been borne out by crystallography of Rhodopsin and of the $\beta 2$ adrenergic receptor, both of which have been captured in both inactive and active states, the latter in complex with its cognate G protein.⁵⁻⁸ These structures also indicate more subtle movements of the intracellular ends of TM5 and TM7.

Presumably, a local rearrangement in TM6 at or near the ligand-binding site gets propagated into the larger conformational changes observed. Much attention has been focused on the highly conserved CWxPx(Y/F) motif in the middle of TM6, centered around the helical kink associated with P6.50 (residue numbering follows the Ballesteros-Weinstein scheme, in which the most conserved residue of helix X is denoted X.50).⁹

Based on biased Monte Carlo simulations and mutagenesis of the $\beta 2$ adrenergic receptor, Javitch and co-workers (expanding upon a proposal by Weinstein and co-workers¹⁰) proposed that the binding site residues C6.47, W6.48, and F6.52 form a rotamer toggle switch, in which receptor activation involves a correlated “switch” of these residues’ sidechain χ^1 rotamers (Figures 3.1 and 3.2).¹¹ The authors further propose that the rotamer switching, including a *gauche(-)* to *trans* transition of the W6.48 χ^1 angle, increases the TM6 kink angle, inducing the key displacement of the intracellular end of TM6. These residues line the binding site and ligand binding would presumably induce the rotamer switching.

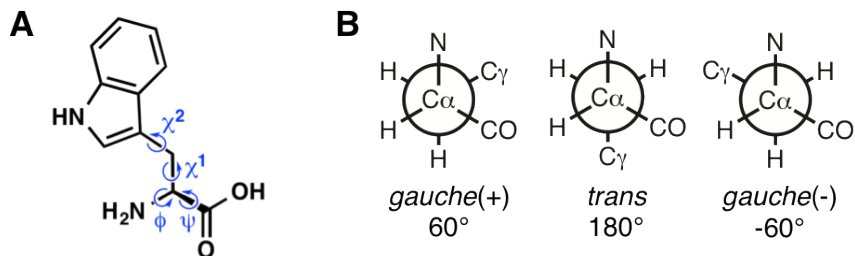


Figure 3.1. (A) Angles describing a residue’s conformation, shown for Trp. (B) χ^1 rotamer definitions

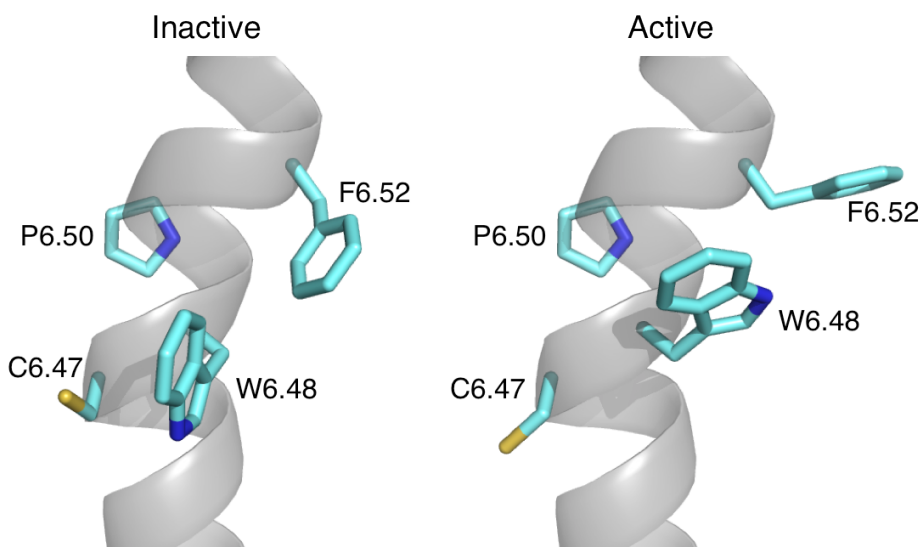


Figure 3.2. The TM6 rotamer toggle switch model for GPCR activation, involving changes in χ^1 for residues C6.47, W6.48, and F6.52.

NMR and fluorescence experiments on rhodopsin suggest rotamer switching or some other local rearrangement of the W6.48 side chain upon receptor activation,^{12,13} and molecular dynamics simulations of rhodopsin show rotamer switching of W6.48.¹⁴ In detailed molecular dynamics experiments on the A2A receptor that draw upon multiple ligand-bound crystal structures, Voth and co-workers have proposed a model in which receptor activation is intimately connected to rotamer transitions of W6.48. The proposed rotamer transitions are the same as those suggested by Javitch: a *gauche(-)* to *trans* switch in χ^1 and a 180° flip in χ^2 .¹⁵

However, crystal structures that are thought to represent active GPCR conformations consistently show binding sites essentially unchanged from the putative inactive structures (Figure 3.3).^{8,16,17} A slight lateral displacement of W6.48 toward TM5 has been observed, especially in rhodopsin structures (Figure 3.3B), but no rotamer changes are seen. A different orientation of the W6.48 side chain is observed in a structure of the M2 acetylcholine receptor (Figure 3.3D), but this is an antagonist-bound, inactive structure.¹⁸ Thus the role of TM6 side chain rearrangements in GPCR activation remains unresolved. Interestingly, a different “switch” was observed one helical turn below W6.48 in crystal structures of the β2 adrenergic receptor. F6.44 moves laterally past the I3.40 side chain “gate” (I3.40 undergoes a rotamer transition). The experiments described in this chapter interrogate the rotamer toggle switch and the F6.44/I3.40 switch in the D2 dopamine receptor and also interrogate W6.48 in the M2 muscarinic acetylcholine receptor.

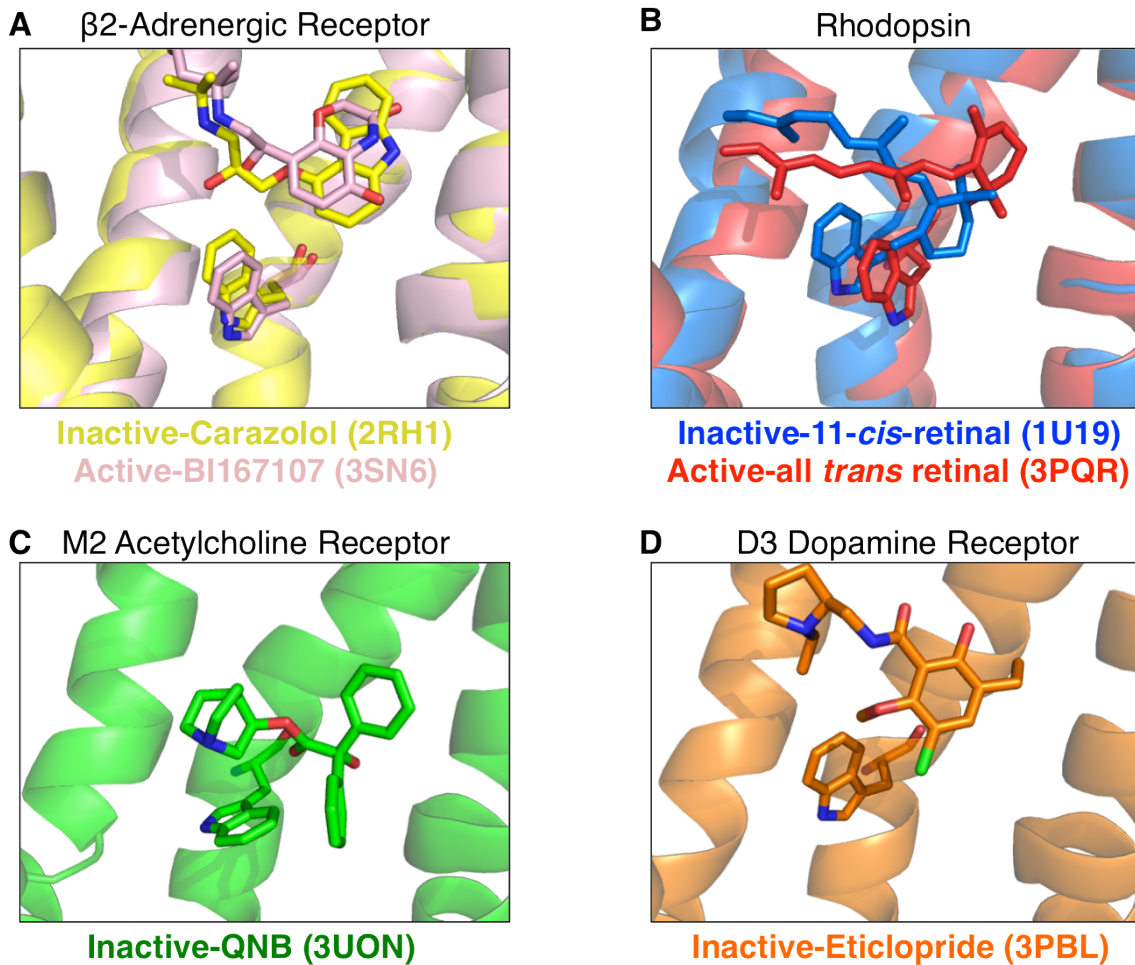


Figure 3.3. W6.48 conformations seen in GPCR crystal structures. Binding sites are shown with W6.48 and co-crystallized ligand.

3.2.2 *nAChR activation*

Activation of nAChRs and other pentameric receptors opens the ion-conducting transmembrane pore approximately 60 Å away from the ligand binding site. This is thought to occur through a twisting of the extracellular domain, which induces a tilting of TM2 and TM3 to open the pore. This general gating mechanism has been borne out both computationally, through normal mode analysis of an $\alpha 7$ receptor model,¹⁹ and by crystallography, through structures of pentameric bacterial channels in open and closed pore conformations.²⁰⁻²²

Other structural data have guided our understanding of gating motions at the ligand binding site. Mollusc-derived acetylcholine binding proteins (AChBPs) with homology to the extracellular domain of nAChRs have been crystallized at high resolution, offering a structural template for the ligand binding region of these receptors. Structures of several variants of this protein are available, in complex with antagonists, partial agonists, and full agonists.²³ A consensus model has emerged in which agonist binding induces closure of the C loop around the ligand binding site. Very subtle changes have been observed for ligand binding residues, for example, in apo versus agonist-bound structures of an AChBP/α7 receptor chimera: subtle side chain displacements are seen for TyrC1, TyrA, and TrpD.²⁴ However, as AChBPs simply bind acetylcholine and do not open a transmembrane pore, it is unclear how well, if at all, these binding site “gating” motions are applicable to nAChRs.

Other insights into nAChR gating have come from cryo-EM structures of the *Torpedo* nAChR in native membrane. One recent structure obtained from rapid freezing after exposure to acetylcholine corroborates some gating motions, including C loop closure and pore opening (though these changes were not observed in all subunits).²⁵ The resolution of this structure (~6 Å) is too low for insight into side chain geometry. A higher resolution (4 Å) structure is available for the closed, ligand-free receptor.²⁶ This structure reveals an extended C loop and a more open binding site, relative to AChBP structures, suggesting side chain rearrangements that must occur upon ligand binding (Figure 3.4). In particular, TrpD is seen in a different side chain rotamer, and the critical cation-π binding residue TrpB shows a displacement as well. The nAChR experiments in

this chapter interrogate the mouse muscle-type nAChR ($\alpha_2\beta\gamma\delta$), which has very high homology to the *Torpedo* nAChR.

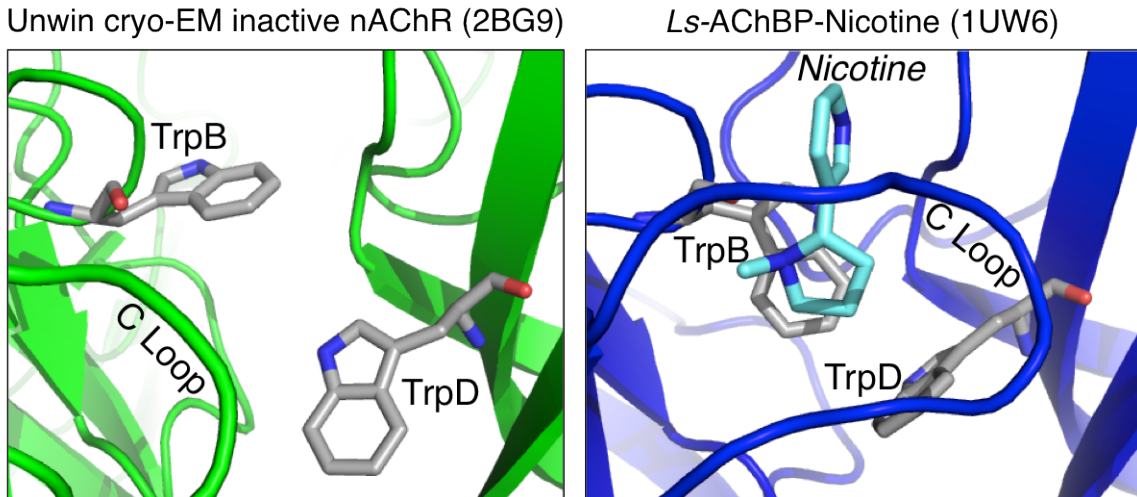


Figure 3.4. The nAChR binding site in a cryo-EM structure of the inactive receptor shows different side chain conformations for TrpB and TrpD, compared to an agonist-bound AChBP structure.

3.2.3 Probing side chain conformation by mutagenesis

Here we use mutagenesis to probe side chain conformation in these transmembrane receptor systems. In one approach, we assess the effect of appending a charged amine to the Trp side chain using 5-aminomethyltryptophan, a novel amino acid that was synthesized for these experiments. The tolerance of this significant structural and electrostatic perturbation helps inform the positioning of the W6.48 side chain within GPCR binding sites. In another approach, we employ conformationally-biased unnatural side chains to probe for rotameric transitions upon receptor activation. For Phe and Trp, we use conformationally constrained β -methyl analogs – a method introduced by Victor Hruby to study the orientation of aromatic side chains.²⁷ The β -methyl group (in either (R) or (S) stereochemistry, Figure 3.5) alters the conformational landscape of these amino acids, changing their side chain rotamer preferences. This reshaping of the χ^1 , χ^2

conformational landscape was modeled by Hruby using molecular mechanics calculations on a model peptide,²⁷ and we performed similar calculations here to produce energy maps for these unnatural side chains.

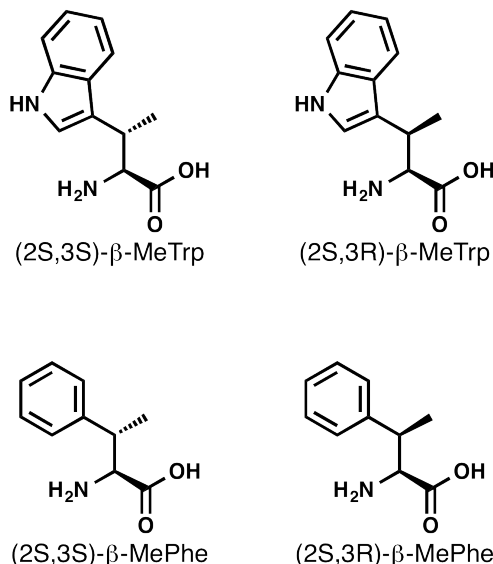


Figure 3.5. β -methyl amino acids employed in this chapter

We probed the W6.48 site of the M2 muscarinic GPCR and the W6.48, F6.51, and F6.52 sites of the D2 dopamine GPCR to test the rotamer toggle switch hypothesis. We also used β -methyltryptophan to probe the TrpB and TrpD sites of the muscle-type nAChR, to test for rotamer transitions of these residues. To explore possible steric effects of the introduced methyl groups with adjacent residues, we performed double mutants of the β -methyl analog and potentially clashing side chains. Finally, a similar approach was applied using the *allo* isomers of β -branched amino acids Thr and Ile – unnatural analogs with inverted stereochemistry at the β carbon. These were used as probes of Thr and Ile rotamer transitions.

3.3 Results and Discussion

3.3.1 Mutagenesis probing conformational rearrangements of C6.47 upon D2 dopamine receptor activation

In their study proposing the rotamer toggle switch model for GPCR activation, Javitch and co-workers supported their model through mutagenesis of the $\beta 2$ adrenergic receptor.¹¹ In their model (Figure 3.2), C6.47 adopts the *trans* rotamer in the inactive state, contacting W6.48, and switches to the *gauche(-)* rotamer in the active state. Mutation of C6.47 to Ser, which has a similar rotamer distribution to Cys in an α -helix, largely preserved wild type function in the $\beta 2$ receptor. They rationalized that since the “inactive” *trans* rotamer is highly disfavored for Thr, a C6.47T mutation would promote receptor activation. Indeed, the C6.47T mutant of the $\beta 2$ receptor showed enhanced constitutive activity (basal signaling in the absence of agonist) and a reduced EC₅₀. We sought to test these and other mutations in the D2 dopamine receptor to probe the proposed rotamer toggle switch in that system.

In the D2 dopamine receptor we also observe a small gain of function for the C6.47T mutant and a borderline loss of function for C6.47S (Table 3.1) – consistent with the Javitch results for the $\beta 2$ receptor. To test the hypothesis that the C6.47T mutation causes a gain of function because it favors the “active” *gauche(-)* rotamer, we evaluated *allo*-threonine (*a*Thr) at this position, which has opposite stereochemistry at the β carbon. On the basis of simple conformational analysis (Figure 3.6), the “inactive” *trans* rotamer of *a*Thr should be favored and the active *gauche(-)* rotamer disfavored, relative to Thr. Surprisingly, the *a*Thr mutation gives an even larger gain of function than C6.47T, inconsistent with this model. C6.47A, which removes all side chain functionality, also gives a gain of function. This latter observation could be consistent with the Javitch

model, in that no interaction with W6.48 is possible to stabilize the inactive state.

Overall, this data set does not lend strong support for the Javitch model of C6.47's role in activation. The nature of an interaction between C6.47 and the W6.48 side chain is unclear. While the native Cys would be anticipated to undergo a sulfur- π -type interaction, a comparable interaction is not very favorable for the -OH of Ser and Thr. As such, it is difficult to anticipate how these mutants would adapt to the toggle switch model.

Table 3.1. C6.47 mutations in the D2 dopamine receptor. Dopamine EC₅₀ and Hill coefficient (n_H) are \pm SEM for goodness of fit to the Hill equation.

	EC ₅₀ (μ M Dopamine)	Fold Shift	n _H	n
wt	0.043 \pm 0.001		1.13 \pm 0.02	57
C6.47S	0.072 \pm 0.002	1.7	1.17 \pm 0.04	20
C6.47A	0.010 \pm 0.002	1 / 4.3	1.1 \pm 0.1	5
C6.47T	0.0152 \pm 0.0009	1 / 2.8	1.07 \pm 0.06	28
C6.47Thr ^a	0.014 \pm 0.001	1 / 3.1	1.12 \pm 0.08	11
C6.47aThr	0.0082 \pm 0.0004	1 / 5.2	1.21 \pm 0.06	14

^aExpression of the wild type receptor with the natural amino acid incorporated by nonsense suppression

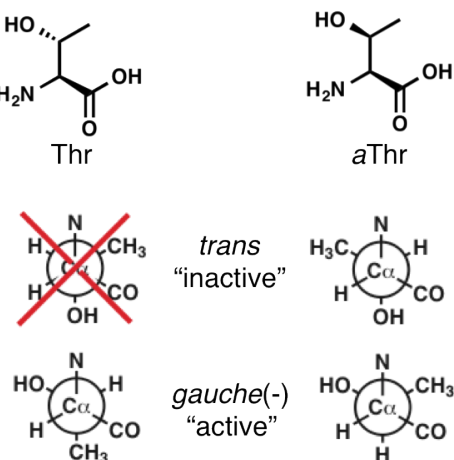


Figure 3.6. Conformational analysis indicates that the putative “inactive” *trans* χ^1 rotamer will be more accessible to aThr than to Thr.

Also casting doubt on this model, C6.47 is found in the “inactive” *trans* rotamer in the crystal structure of rhodopsin in the inactive state (the structural template for the Javitch study), but is actually found in the putative “active” *gauche(-)* rotamer (pointing away from W6.48) in many other “inactive” GPCR crystal structures. These include antagonist-bound structures of the β 2 adrenergic receptor and the D3 dopamine receptor.^{5,7,28} As such, the role of C6.47 in activation of the D2 receptor and other GPCRs remains unclear.

3.3.2 Investigating the role of a F6.44/I3.40 switch in activation of the D2 dopamine receptor

GPCR crystal structures thought to represent active conformations have not shown any of the side chain transitions predicted by the rotamer toggle switch model. However, for the β 2 adrenergic receptor, the closest homolog to the D2 receptor for which we have an active state crystal structure, another switch was found. One turn below W6.48, F6.44 was observed to slide laterally, with the lower half of TM6 following it. This rigid body rotation contributes to the large displacement of TM6 to accommodate the G protein. The F6.44 side chain does not undergo a conformational change, but rather moves past I3.40, which serves as a “swinging gate,” adopting a new side chain rotamer to follow the Phe side chain in the active state (Figure 3.7). These residues, especially F6.44, are highly conserved. Previous mutagenesis studies have pointed to the importance of F6.44 for receptor activation in the β 2 adrenergic receptor, among other systems, and computational work has supported the idea of a F6.44/I3.40 activation “switch.”²⁹⁻³¹ In particular, previous studies in the M3 muscarinic receptor, the β 2 adrenergic receptor, and the α 1B-adrenergic receptor have shown that mutating F6.44

to smaller side chains such as Leu, Val, or Ala results in a gain of receptor function and/or an increase in constitutive activity.^{29,31,32}

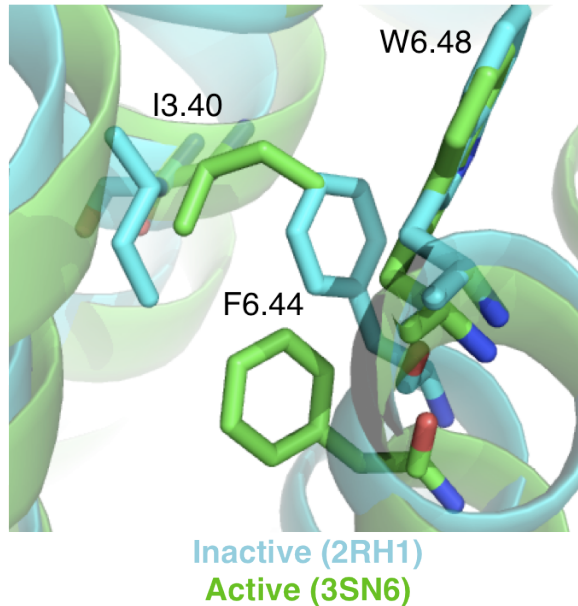


Figure 3.7. F6.44/I3.40 activation switch revealed by structures of the β 2-adrenergic receptor. Inactive (blue) and active (green) structures are overlaid.

To investigate the role of these residues in the D2 dopamine receptor, we also characterized the F6.44L mutant, for which a gain of function was observed, consistent with the results described above from other systems (Table 3.2). This could reflect a weakening of the inactive state “lock” imposed by the interaction of F6.44 with I3.40. We saw no EC₅₀ shift for the 3,4,5-trifluorophenylalanine mutant of F6.44, indicating that side chain electrostatics are unimportant and suggesting no involvement in significant aromatic-aromatic interactions with F5.47, W6.48, or other nearby residues.

At the I3.40 site, we observed a significant loss of function for the I3.40V mutant – simply a methyl group deletion from the native Ile side chain. Such sensitivity confirms the importance of this side chain, but as this methyl contacts F6.44 in both active and

Table 3.2. Mutations to F6.44 and I3.40 in the D2 dopamine receptor. Dopamine EC₅₀ and Hill coefficient (n_H) are \pm SEM for goodness of fit to the Hill equation.

	EC ₅₀ (μ M Dopamine)	Fold Shift	Hill	n
wt	0.043 \pm 0.001		1.13 \pm 0.02	57
F6.44L	0.013 \pm 0.001	1 / 3.3	1.3 \pm 0.1	5
F6.44Phe ^a	0.047 \pm 0.005		1.0 \pm 0.1	5
F6.44F ₃ -Phe	0.046 \pm 0.003	1.0	1.3 \pm 0.1	4
I3.40V	0.280 \pm 0.020	6.5	1.10 \pm 0.08	5
I3.40A	ND ^b			
I3.40Ile ^a	0.034 \pm 0.002		1.13 \pm 0.09	9
I3.40alle	0.059 \pm 0.007	1.7	0.95 \pm 0.10	10

^aExpression of the wild type receptor with the natural amino acid incorporated by nonsense suppression

^bNo dopamine-induced current detected

inactive states of the putative “switch,” it is difficult to ascribe these data a mechanistic significance. No response was detected from the I3.40A mutant (Table 3.2). Finally, to probe the potential role of a rotamer switch, Ile was mutated to *allo*-isoleucine (*a*Ile), the Ile analog with inverted stereochemistry at the β carbon. I3.40 undergoes a *trans* to *gauche*(-) rotamer transition upon activation in the β 2 receptor crystal structures. *a*Ile is expected to favor the *trans* rotamer and disfavor *gauche*(-), by the same logic applied to *a*Thr in section 3.3.1 above, and thus should be deleterious to receptor function. A very small loss of function was measured, below the 2-fold threshold we typically consider to be meaningful for this assay, so it is difficult to rule on the importance of the rotamer transition based on this data point. Of course, the stereochemistry inversion also alters the packing of this side chain with its neighbors.

Overall, these various mutagenesis results could be consistent with a F6.44/I3.40 rotamer switch, and indicate some functional importance of these residues. However, our observations are certainly insufficient to confirm the presence of this “switch” in the D2 dopamine receptor.

3.3.3 Synthesis and use of 5-aminomethyltryptophan to probe the W6.48 site in GPCRs

It remains unclear what conformation W6.48 assumes in the active state of various GPCRs, and whether rotamer switching has a role in activation. We reasoned that we could learn about the Trp's orientation by measuring the tolerance for a significant structural perturbation added to the W6.48 side chain. We chose to introduce an aminomethyl group at the 5-position of the indole, a group that will be positively charged at physiological pH. We further envisioned that by also introducing a negative charge in the receptor (i.e., Asp or Glu) near the Trp side chain, we might create a salt bridge involving W6.48 (Figure 3.8). If such a salt bridge could be engineered and was functionally tolerated, this would help inform the preferred orientation of the W6.48 side chain.

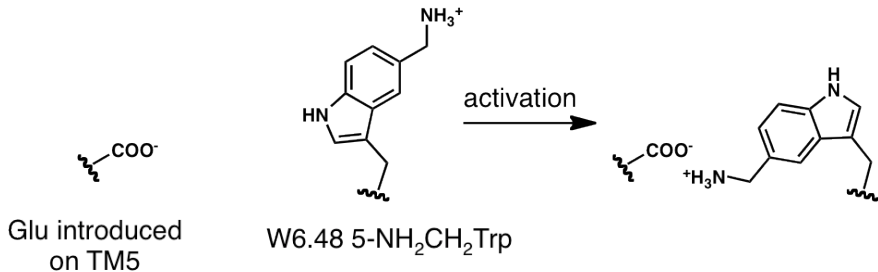


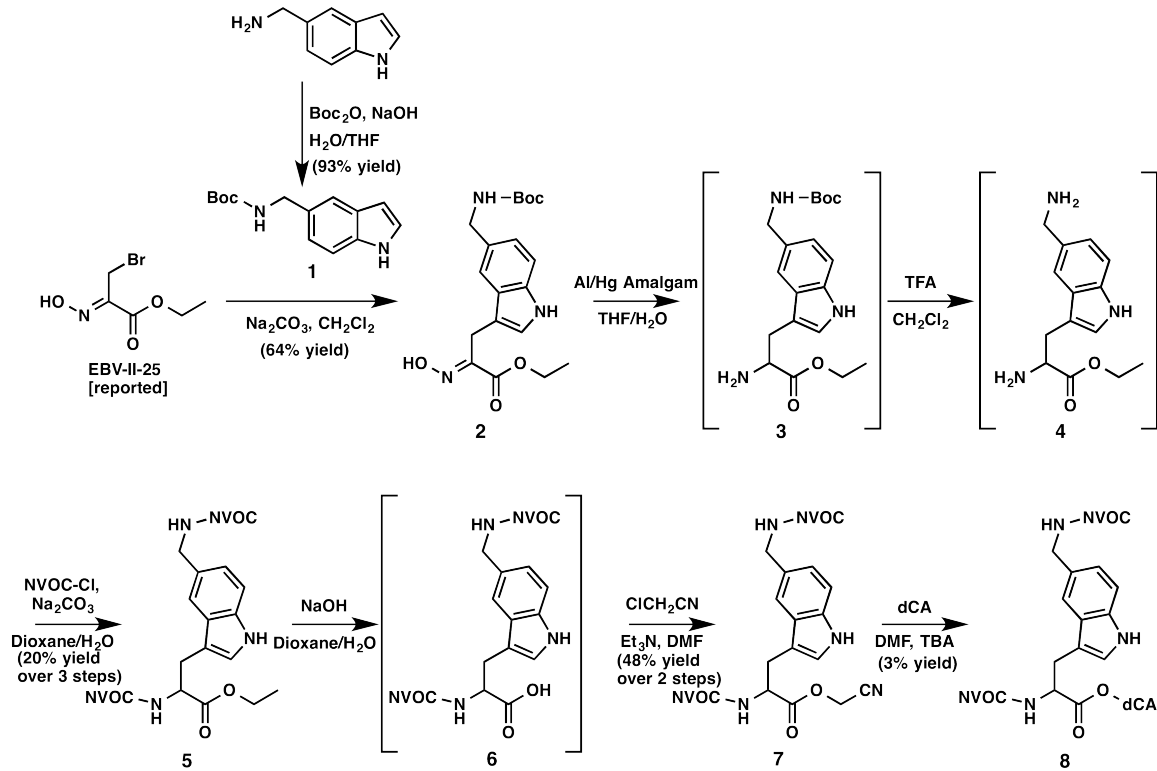
Figure 3.8. Scheme for an engineered salt bridge involving 5-aminomethyltryptophan to test for W6.48 rotamer switching

In particular, we were interested in probing W6.48 in the M2 muscarinic acetylcholine receptor and in the D2 dopamine receptor. Inactive, antagonist-bound crystal structures are available for the M2 receptor and for the D3 dopamine receptor, a very close homolog to the D2 receptor.^{18,28} Interestingly, these structures show different orientations of W6.48: the usual “vertical” Trp orientation in the D3 structure, and a “tilted” orientation with a different χ^2 rotamer in the M2 structure (Figure 3.3, C and D).

We wondered whether these different orientations seen by crystallography would be reflected in different functional tolerance for 5-aminomethyltryptophan ($5\text{-NH}_2\text{CH}_2\text{Trp}$).

$5\text{-NH}_2\text{CH}_2\text{Trp}$ was synthesized employing a Friedel-Crafts-type indole coupling (Scheme 3.1).³³ 5-Aminomethyl-indole was Boc protected, and this species (**1**), was coupled to ethyl 3-bromo-2-hydroxyiminopropanoate.³³ The hydroximine (**2**) was reduced by an aluminum/mercury amalgam, and the Boc group removed by trifluoroacetic acid. This racemic diamine (**4**) was protected with nitroveratryloxycarbonyl (NVOC) groups and the ester was hydrolyzed. Reaction with chloroacetonitrile gave the cyanomethyl ester **7**, which was coupled to dCA and ligated to tRNA by standard methods.

Scheme 3.1. Synthesis of 5-aminomethyltryptophan



5-NH₂CH₂Trp was surprisingly well tolerated at the W6.48 site in the M2 receptor, giving an EC₅₀ less than 2-fold shifted from wild type (Table 3.3). In contrast, no response was detected from efforts to incorporate W6.48[5-NH₂CH₂Trp] in the D2 receptor under otherwise identical conditions. It is unclear whether the mutation rendered the receptor nonfunctional or reduced receptor expression levels. The salt bridge conceived for W6.48 in the “active” conformation (Figure 3.8) suggested by the rotamer toggle switch pairs 5-NH₂CH₂Trp with Y5.48E. No response was detected for this double mutant either, and again, it is unclear whether low expression or lack of receptor function is the reason, though the Y5.48E single mutant gave a very large loss of function.

Table 3.3. 5-Aminomethyltryptophan mutations to W6.48 in the M2 acetylcholine and D2 dopamine receptors. EC₅₀ and Hill coefficient (n_H) are ± SEM for goodness of fit to the Hill equation.

M2 Acetylcholine Receptor	EC ₅₀ (μM ACh)	Fold Shift	n _H	n
W6.48Trp ^a	0.27 ± 0.01		1.32 ± 0.06	7
W6.48[5-NH ₂ CH ₂ Trp]	0.47 ± 0.09	1.7	1.5 ± 0.4	4
D2 Dopamine Receptor	EC ₅₀ (μM Dopamine)	Fold Shift	n _H	n
W6.48Trp ^a	0.025 ± 0.002		1.00 ± 0.06	8
W6.48[5-NH ₂ CH ₂ Trp]	ND ^b			
Y5.48E	6 ± 2	240	0.56 ± 0.05	4
Y5.48E W6.48[5-NH ₂ CH ₂ Trp]	ND ^b			

^aExpression of the wild type receptor with the natural amino acid incorporated by nonsense suppression

^bNo dopamine-induced current detected

In the speculative case that the D2 W6.48[5-NH₂CH₂Trp] mutant expresses but is nonfunctional, an interesting contrast emerges with the M2 receptor. If W6.48 does not move upon activation, as suggested by crystallography, 5-NH₂CH₂Trp is expected to be especially deleterious in the D2 receptor, for which the D3 structure suggests a “vertical”

orientation. The cationic amine of dopamine is expected to meet steric and electrostatic repulsion from the introduced aminomethyl substituent (Figure 3.9).

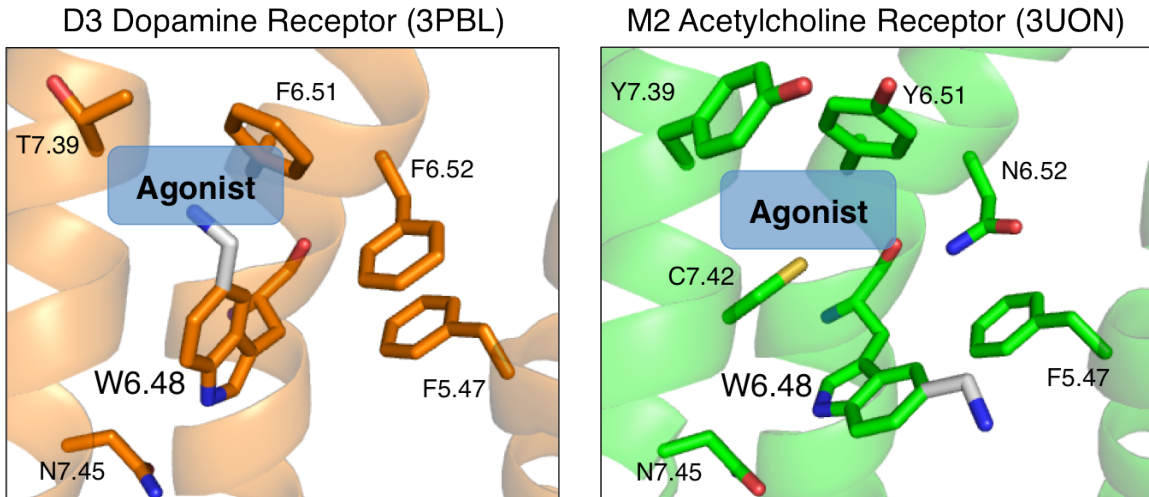


Figure 3.9. Structures of GPCR binding sites with the 5-aminomethyl substituent modeled onto the W6.48 side chain. The approximate predicted location of agonist binding is noted.

Also supporting this “vertical” tryptophan conformation in the active D2 receptor, a functionally important sulfur- π interaction between W6.48 and C3.36 has been identified.³⁴ Weakening this interaction by indole fluorination is detrimental to receptor function, suggesting that the interaction is present in the active receptor, which would require the Trp to maintain its “vertical” conformation. In contrast, the “tilted” orientation of W6.48 in the M2 structure would place the aminomethyl group clear of the agonist in a pocket between helices 3, 4, and 5 (Figure 3.9). This could account for the surprisingly good tolerance for this side chain in the M2 receptor. These data are consistent with a lack of Trp movement upon activation, and with different Trp conformations in the D2 and M2 receptors, as suggested by crystallography.

3.3.4 Synthesis, mutagenesis, and modeling of β -methyltryptophan and β -methylphenylalanine

β -methyl analogs of Phe and Trp were employed to probe the conformation of aromatic side chains within nAChR and GPCR binding sites. β -methyl substituents introduce conformational constraints to the side chain and have been employed to study the conformation of aromatic amino acids in various peptide contexts by Hruby and co-workers.²⁷

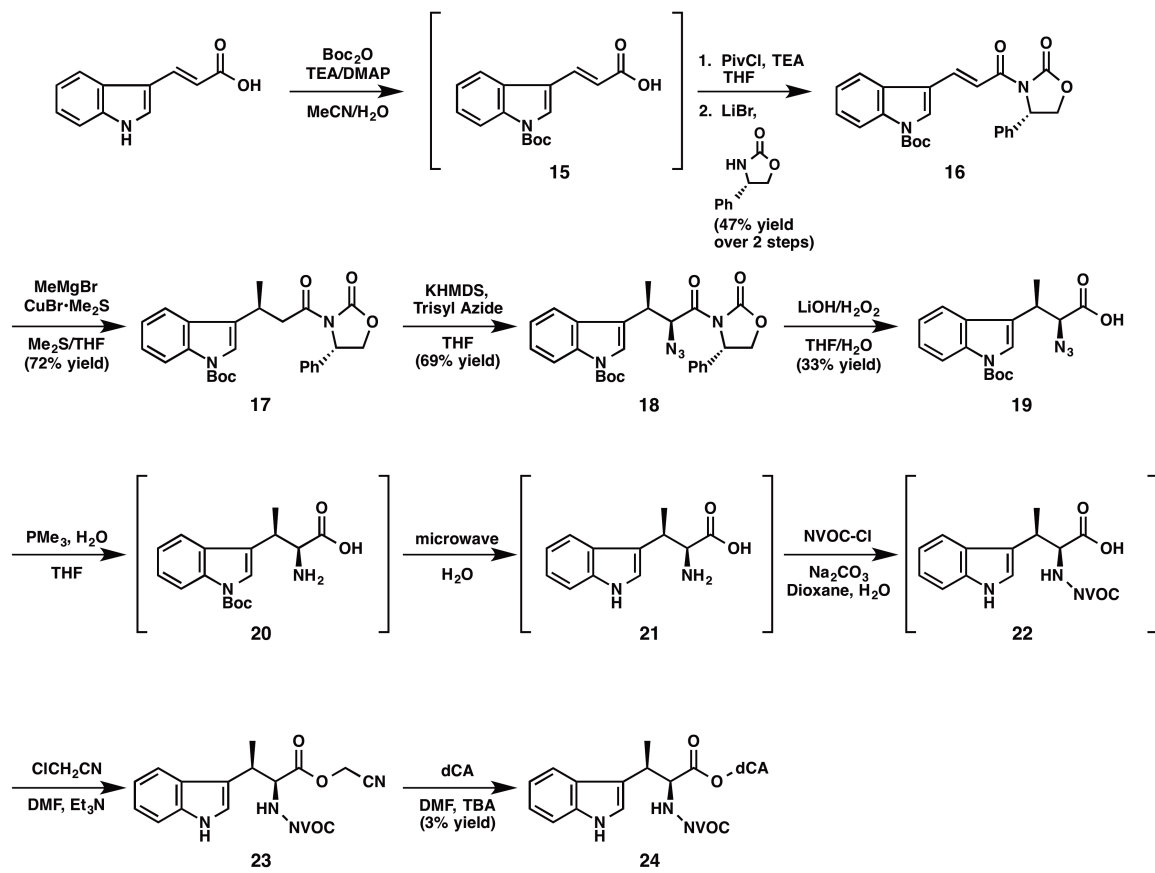
3.3.4.1 Synthesis

In these studies, we employed (2S, 3S) and (2S, 3R) stereoisomers of both β -methyltryptophan and β -methylphenylalanine. (2S, 3S)- β -methylphenylalanine [hereafter (S)- β -MePhe] was obtained from a commercial supplier (Chem-Impex). (2S, 3R)- β -methylphenylalanine [(R)- β -MePhe] and (2S, 3S)- β -methyltryptophan [(S)- β -MeTrp] were generous gifts from Victor Hruby. These three compounds were NVOC-protected, activated as cyanomethyl esters, and coupled to dCA by standard methods (compounds **9-14**). (2S, 3R)- β -methyltryptophan [(R)- β -MeTrp] was synthesized by a route drawing upon two previously reported syntheses by Hruby (Scheme 3.2).^{35,36}

Indoleacrylic acid was Boc-protected and the resulting compound (**15**) was coupled to the (S)-4-phenyl-2-oxazolidinone chiral auxiliary via a pivalate ester to yield compound **16**. The chiral auxiliary directs installation of the methyl and amine groups with good stereoselectivity. Conjugate cuprate addition of methyl Grignard installed the β -methyl group (**17**). The azide precursor to the amine was installed via deprotonation and electrophilic azide addition with trisyl azide to yield compound **18**. The chiral auxiliary was removed via hydrogen peroxide-mediated hydrolysis, and the azide of this

compound (**19**) was reduced to the amine (compound **20**) via a Staudinger reduction. Removal of the Boc group yielded the amino acid (**21**), which was NVOC protected (compound **22**), activated as a cyanomethyl ester (compound **23**), and coupled to dCA (**24**) by standard methods.

Scheme 3.2. Synthesis of (2S,3R)- β -methyltryptophan



3.3.4.2 Mutagenesis

(R) and (S) β -methyl analogs of both Phe and Trp proved viable for incorporation by nonsense suppression; robust currents were measured from receptors expressing these unnatural amino acid analogs in both GPCRs and in the muscle-type nAChR. While very large losses of receptor function were recorded for the β -MeTrp analogs at the W6.48 site

of the D2 dopamine and M2 acetylcholine GPCRs, these side chains caused little, or no, perturbation to nAChR function at the TrpB (α W149) and TrpD (γ W55/ δ W57) sites (Table 3.4). The β -MePhe analogs were well-tolerated at the F6.52 site in the D2 dopamine receptor. Additionally, both β -MePhe analogs were incorporated at the TrpD site, which interestingly yielded equivalent losses of function, in contrast to the β -MeTrp derivatives. Both conformational and steric effects could contribute to the EC₅₀ shifts observed in Table 3.4. Conformational (rotamer-bias) effects are considered in section 3.3.4.3 and steric effects are considered in section 3.3.4.4.

Table 3.4. β -methyl mutations to W6.48 of the M2 acetylcholine receptor, W6.48 and F6.52 of the D2 dopamine receptor, and TrpB (α W149) and TrpD (γ W55/ δ W57) of the muscle-type nAChR. EC₅₀ and Hill coefficient (n_H) are \pm SEM for goodness of fit to the Hill equation.

M2 Acetylcholine Receptor	EC ₅₀ (μ M ACh)	Fold Shift	n _H	n
W6.48Trp ^a	0.27 \pm 0.01		1.32 \pm 0.06	7
W6.48(R)- β -MeTrp	54 \pm 1	200	0.95 \pm 0.02	7
W6.48(S)- β -MeTrp	73 \pm 2	270	0.91 \pm 0.02	7
D2 Dopamine Receptor	EC ₅₀ (μ M Dopamine)	Fold Shift	n _H	n
W6.48Trp ^a	0.025 \pm 0.002		1.00 \pm 0.06	8
W6.48(R)- β -MeTrp	4.3 \pm 0.4	170	0.70 \pm 0.03	5
W6.48(S)- β -MeTrp	0.69 \pm 0.10	28	1.18 \pm 0.16	7
F6.52Phe ^a	0.052 \pm 0.003		1.44 \pm 0.08	5
F6.52(R)- β -MePhe	0.067 \pm 0.007	1.3	1.19 \pm 0.05	10
F6.52(S)- β -MePhe	0.127 \pm 0.008	2.4	1.12 \pm 0.07	7
Muscle-Type nAChR	EC ₅₀ (μ M ACh)	Fold Shift	n _H	n
α W149Trp ^a	22 \pm 2		1.5 \pm 0.1	6
α W149(R)- β -MeTrp	22 \pm 1	1.0	1.6 \pm 0.1	4
α W149(S)- β -MeTrp	17.1 \pm 0.4	1 / 1.3	1.39 \pm 0.04	7
γ W55/ δ W57Trp ^a	23.4 \pm 0.7		1.35 \pm 0.05	3
γ W55/ δ W57(R)- β -MeTrp	95 \pm 3	4.0	1.44 \pm 0.05	4
γ W55/ δ W57(S)- β -MeTrp	23.6 \pm 0.8	1.0	1.30 \pm 0.05	5
γ W55/ δ W57Phe	271 \pm 7	12	1.51 \pm 0.05	4
γ W55/ δ W57(R)- β -MePhe	330 \pm 20	14	1.35 \pm 0.09	4
γ W55/ δ W57(S)- β -MePhe	290 \pm 30	12	1.2 \pm 0.1	6

^aExpression of the wild type receptor with the natural amino acid incorporated by nonsense suppression

3.3.4.3 Conformational effects

To gain insight into the conformational bias of these β -methyl analogs relative to the native Phe and Trp side chains, we performed calculations to map the energy landscape of these amino acids as a function of χ^1 and χ^2 . Using a protocol similar to that previously employed by Hruby,²⁷ molecular mechanics calculations (MMFF) were performed for each amino acid, capped in the form: Ac-Xaa-NH-Me (where Xaa is the β -methyl amino acid). Energies were determined at all angles of χ^1 and χ^2 , in 10° increments. The angles ϕ and ψ were constrained to either the β -sheet values observed for TrpD in the nicotine-bound *Ls*-AChBP crystal structure³⁷ ($\phi = -86^\circ$, $\psi = 120^\circ$), or to idealized α -helix values ($\phi = -48^\circ$, $\psi = -57^\circ$) which are closer to the appropriate angles for TrpB and for W6.48. The plots (Figures 3.10 through 3.12) show the same general shape as those previously constructed by Hruby,²⁷ and the location of wells in these plots generally (though not perfectly) corresponds to the predominant rotamers represented in the PDB for Phe and Trp.³⁸

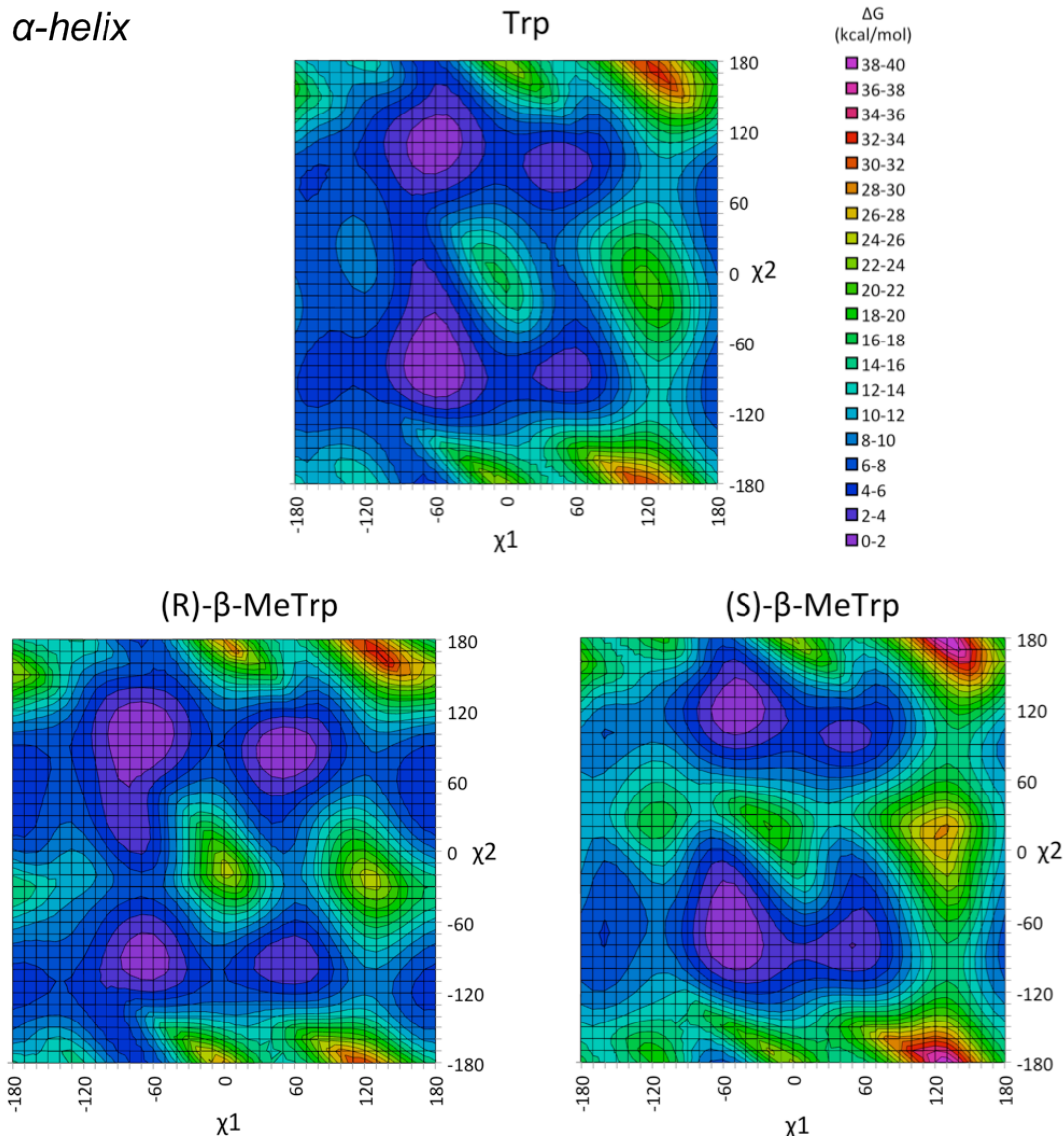


Figure 3.10. Energy maps for Trp, (R)- β -MeTrp, and (S)- β -MeTrp as a function of the side chain dihedrals χ^1 and χ^2 , with the backbone constrained to idealized α -helix dihedral values ($\phi = -48^\circ$, $\psi = -57^\circ$).

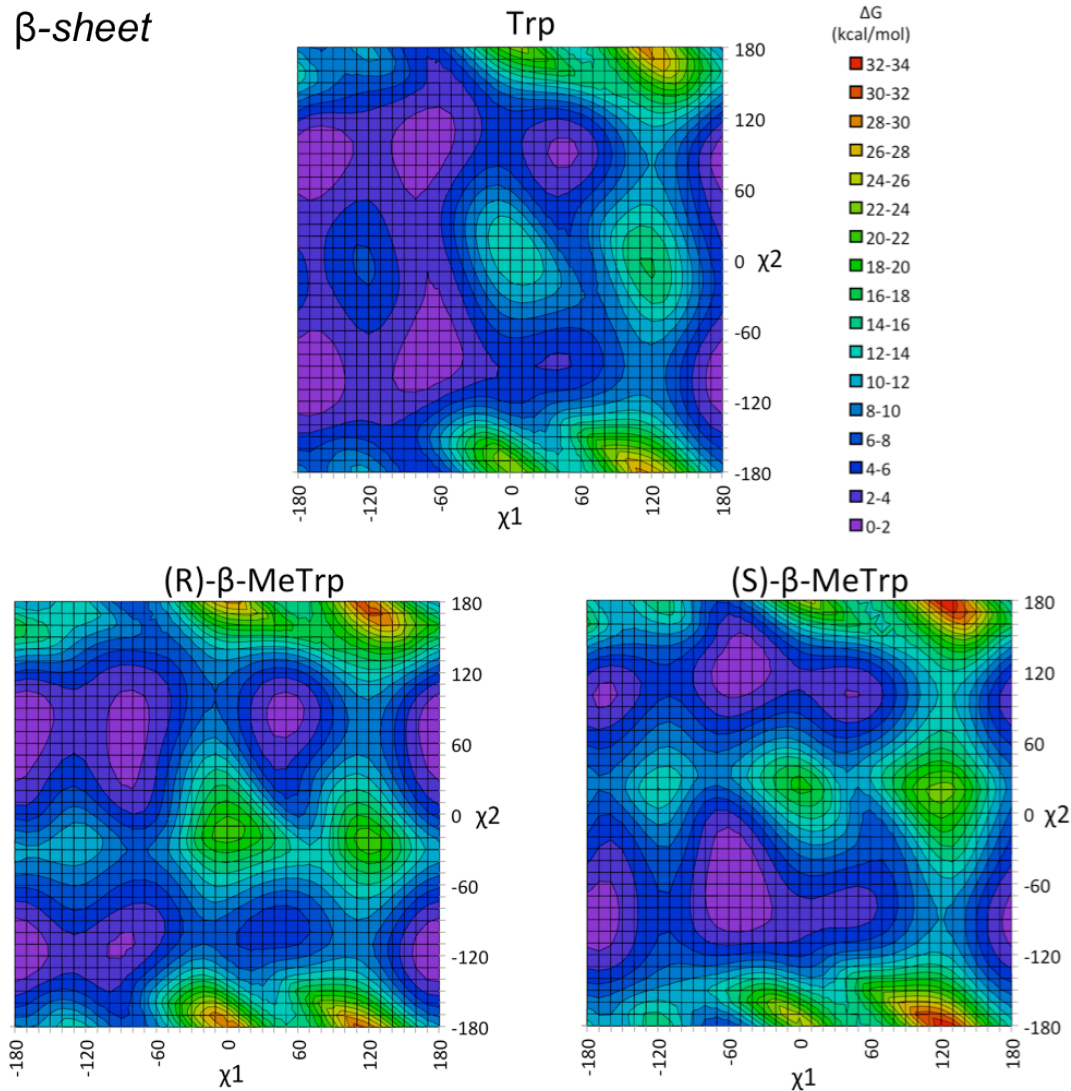


Figure 3.11. Energy maps for Trp, (R)- β -MeTrp, and (S)- β -MeTrp as a function of the side chain dihedrals χ^1 and χ^2 , with the backbone constrained to the β -sheet dihedral values observed for TrpD in the nicotine-bound *Ls*-AChBP crystal structure³⁷ ($\varphi = -86^\circ$, $\psi = 120^\circ$).

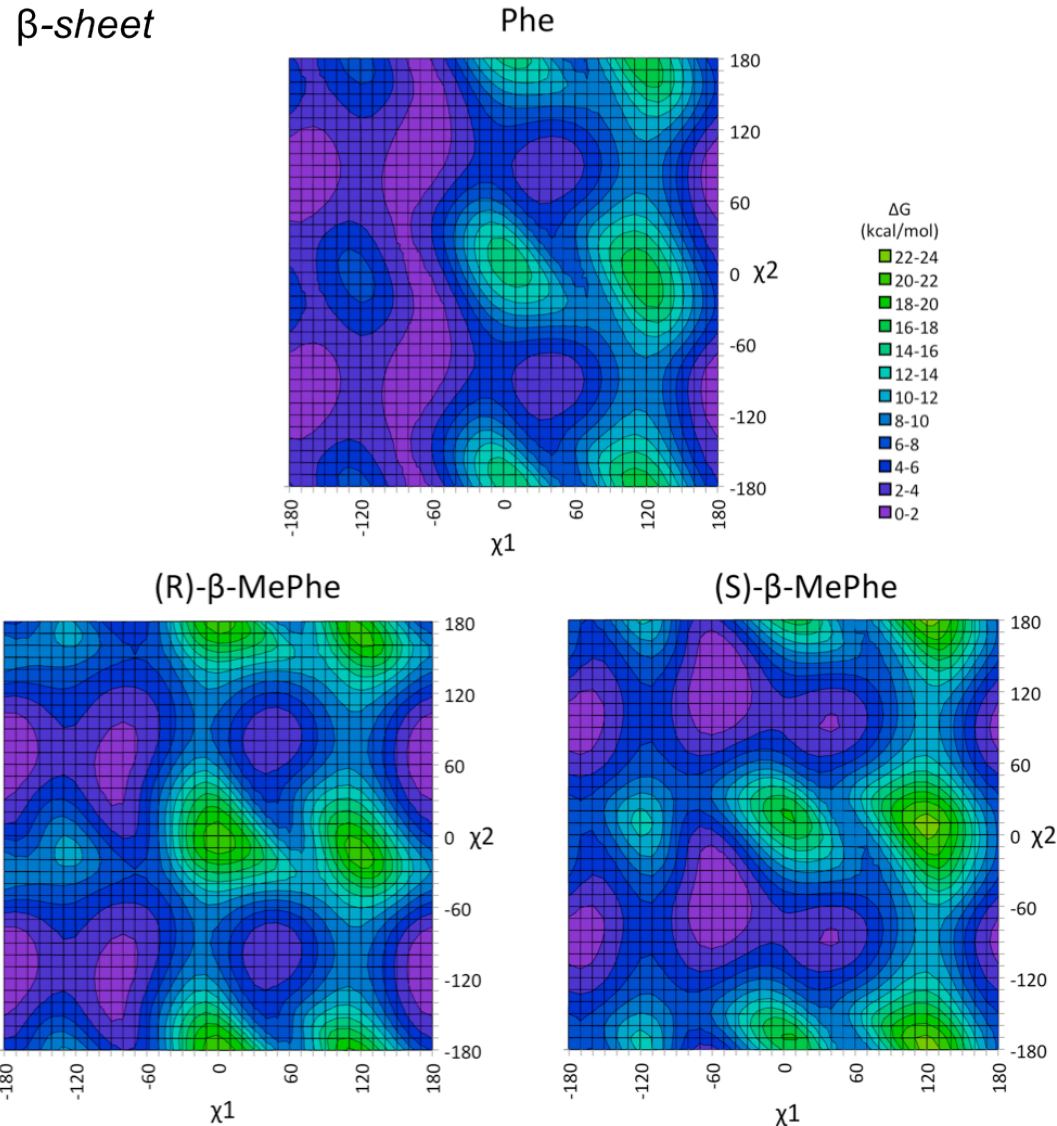


Figure 3.12. Energy maps for Phe, (R)- β -MePhe, and (S)- β -MePhe as a function of the side chain dihedrals χ^1 and χ^2 , with the backbone constrained to the β -sheet dihedral values observed for TrpD in the nicotine-bound *Ls*-AChBP crystal structure³⁷ ($\varphi = -86^\circ$, $\psi = 120^\circ$).

To evaluate the effect of a β -methyl mutation on the conformational landscape of a Trp or Phe side chain, we created “ β -methyl effect” plots, in which the plot for the parent side chain (Trp or Phe) is subtracted from the plot for one of its β -methyl analogs (Figures 3.13 through 3.16). Note that the two plots from which the difference is taken are for different compounds and have different global minima, so the value $\Delta\Delta G = 0$ should not be ascribed special significance.

We can use these plots to make predictions about how β -methyl mutations should affect receptor activation on the basis of specific activation models. We first consider the “rotamer toggle switch” activation model for W6.48 in GPCR binding sites (Figure 3.13). As W6.48 in the inactive M2 acetylcholine receptor structure was observed in a noncanonical conformation unaccounted for in models of GPCR activation, the M2 receptor is not included in this analysis. Instead, we consider the D3 dopamine receptor structure as a model for the inactive D2 dopamine receptor. The Javitch/Voth “rotamer toggle switch” model for GPCR activation posits a W6.48 χ^1 rotamer change from *gauche(-)* to *trans* and a 180° flip in χ^2 .^{11,15} On Figure 3.13A, this is a transition from the black \times (χ^1, χ^2 for the canonical inactive W6.48 rotamer seen in the D3 structure) to the purple \times . The difference in energy between these two (χ^1, χ^2) points is 0.3 kcal/mol greater for (R)- β -MeTrp than for Trp and 0.4 kcal/mol less for (S)- β -MeTrp than for Trp (Figure 3.13B, blue values). Thus, β -methyl substitutions are expected to have modest but opposite effects for the two stereoisomers. This stands in stark contrast to the large losses of function recorded for both stereoisomers in the D2 dopamine receptor. Steric effects, discussed in section 3.3.4.4, most likely dominate.

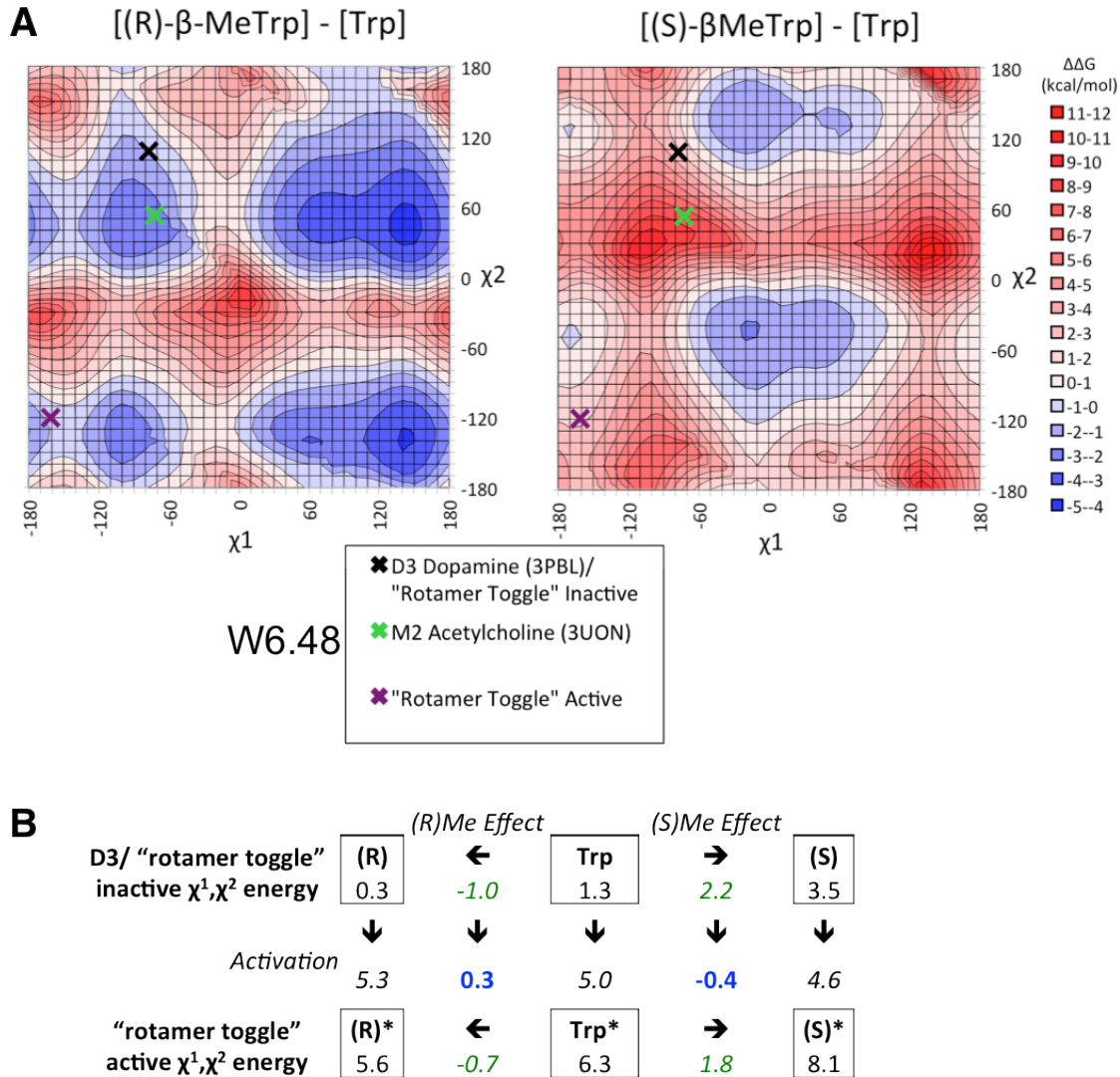


Figure 3.13. (A) “ β -methyl effect” difference plots for (R) and (S) β -methyls of tryptophan with α -helix backbone dihedral constraints. χ^1, χ^2 values for W6.48 observed in crystal structures and predicted for the active state are denoted with an \times . (B) Conformational energy analysis. Boxed values are energies (in kcal/mol) calculated for the indicated χ^1, χ^2 , taken from the corresponding plot in Figure 3.10. Values associated with arrows are energy differences. Note that the green “methyl effect” values correspond to $\Delta\Delta G$ values at the appropriate \times in part A. Blue values are the differential effect of the methyl on activation.

In an alternative model, W6.48 does not move upon activation, as suggested by crystal structures of active GPCRs, mutagenesis suggesting a sulfur- π interaction between W6.48 and C3.36,³⁴ and perhaps consistent with the 5-NH₂CH₂Trp results in section 3.3.3. In this scenario, β -methyl groups could conceivably have a functional effect if they

destabilize the W6.48 conformation observed in inactive GPCR crystal structures (which is also the active conformation). Note that the different W6.48 conformations (specifically, different χ^2 values) seen in the D3 and M2 structures are indeed differentially affected by the β -methyl analogs (Figure 3.13A, black X and green X). While (R)- β -MeTrp should have a similar effect on both receptors, (S)- β -MeTrp will significantly destabilize the M2 tryptophan conformation. This effect could in part be responsible for the larger loss of function observed for (S)- β -MeTrp in the M2 acetylcholine receptor, compared to the D2 dopamine receptor (Table 3.4).

In the nAChR, a speculative gating model emerges by comparing agonist-bound AChBP structures (presumably the active conformation) to Unwin's cryo-EM structure of the inactive nAChR (Figure 3.4). An analysis of predicted β -methyl effects for this Unwin cryo-EM-to-AChBP activation model is presented in Figures 3.14 through 3.16 using the same approach applied to GPCR W6.48 activation in Figure 3.13. For TrpB, the inactive to active energy gap is predicted to be 3.4 kcal/mol larger for (R)- β -MeTrp than for Trp and 3.4 kcal/mol smaller for (S)- β -MeTrp than for Trp (blue values, Figure 3.14B). However, both of these analogs gave wild type function at TrpB (Table 3.4), calling into question the validity of this activation model and/or energy analysis. For TrpD, smaller but still significant β -methyl perturbations are predicted (+1.5 kcal/mol for (R)- β -MeTrp and -2.2 kcal/mol for (S)- β -MeTrp) (Figure 3.15). (R)- β -MeTrp did indeed give a loss of function for TrpD, as predicted, while the (S) analog was wild type (Table 3.4). Interestingly, the loss of function for the (R) analog was not observed for the series Phe, (S)- β -MePhe, and (R)- β -MePhe. However, the energy analysis for the β -methyl Phe analogs suggests that (R)- β -MePhe should destabilize activation by 2.6 kcal/mol, even

more than (R)- β -MeTrp (Figure 3.16). Clearly, the predictions made by computational work on model systems are inconsistent with our mutagenesis results. This could reflect incorrect assignment of inactive and active Trp conformations, certainly possible for the inactive state given the low resolution of the Unwin structure. Alternatively, steric effects in the actual protein are unaccounted for in the model system used for the calculations. We consider the latter possibility in the following section.

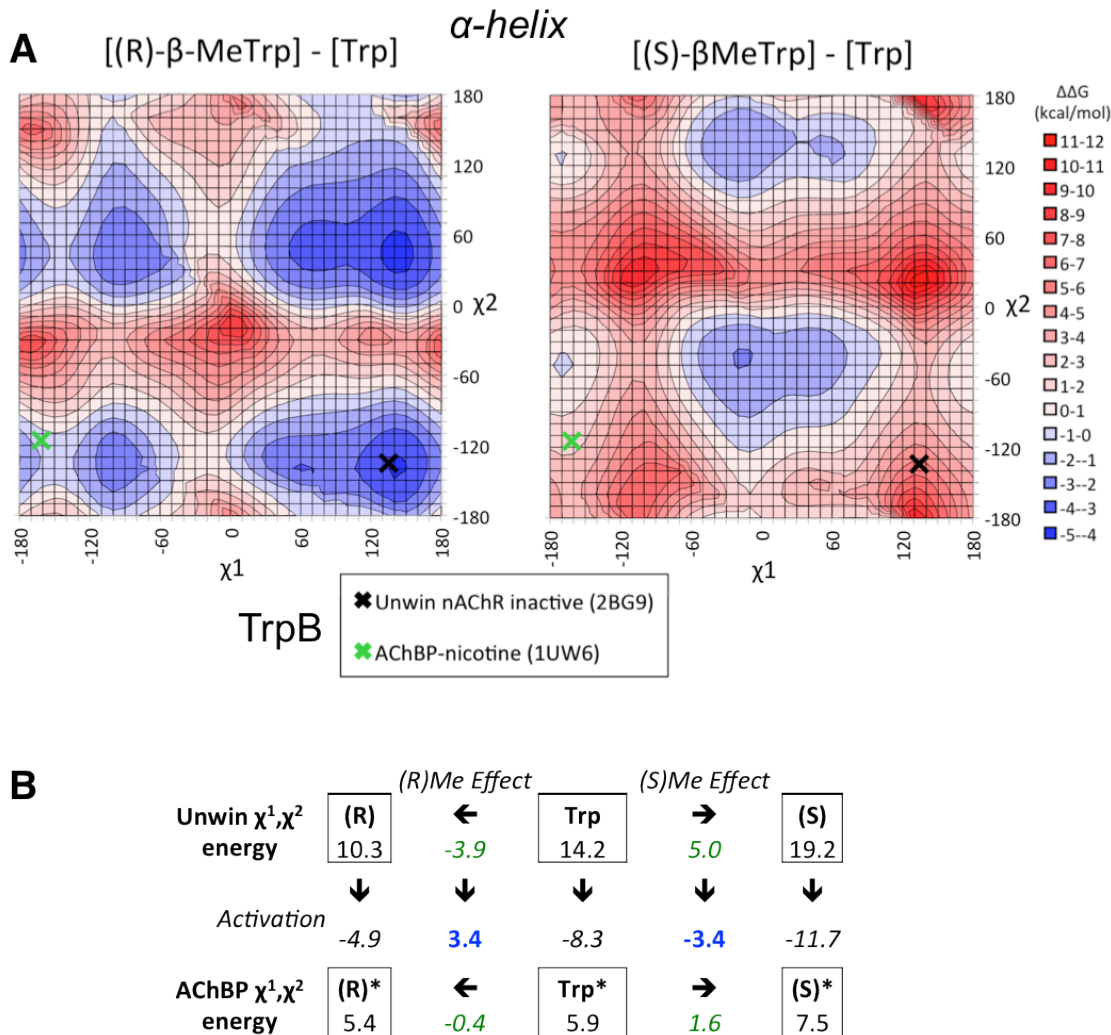


Figure 3.14. (A) “ β -methyl effect” difference plots for (R) and (S) β -methyls of tryptophan with α -helix backbone dihedral constraints (note that these are the same plots as in Figure 3.13A). χ^1, χ^2 values for TrpB observed in cryo-EM and crystal structures are denoted with an \times . (B) Conformational energy analysis. Boxed values are energies (in kcal/mol) calculated for the indicated χ^1, χ^2 , taken from the corresponding plot in Figure 3.10. Values associated with arrows are energy differences. Note that the green “methyl effect” values correspond to $\Delta\Delta G$ values at the appropriate \times in part A. Blue values are the differential effect of the methyl on activation.

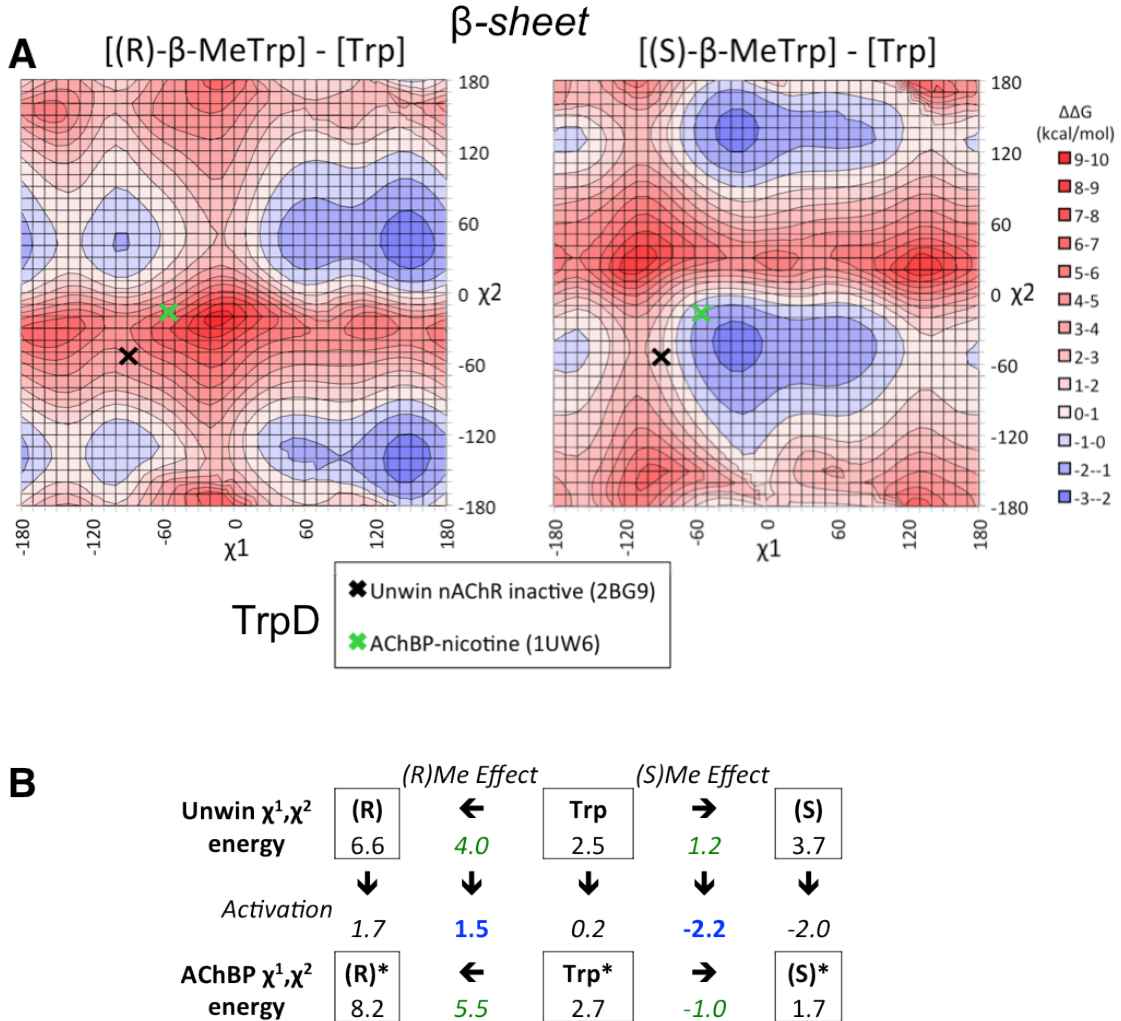


Figure 3.15. (A) “ β -methyl effect” difference plots for (R) and (S) β -methyls of tryptophan with β -sheet backbone dihedral constraints. χ^1, χ^2 values for TrpD observed in cryo-EM and crystal structures are denoted with an X. (B) Conformational energy analysis. Boxed values are energies (in kcal/mol) calculated for the indicated χ^1, χ^2 , taken from the corresponding plot in Figure 3.11. Values associated with arrows are energy differences. Note that the green “methyl effect” values correspond to $\Delta\Delta G$ values at the appropriate X in part A. Blue values are the differential effect of the methyl on activation.

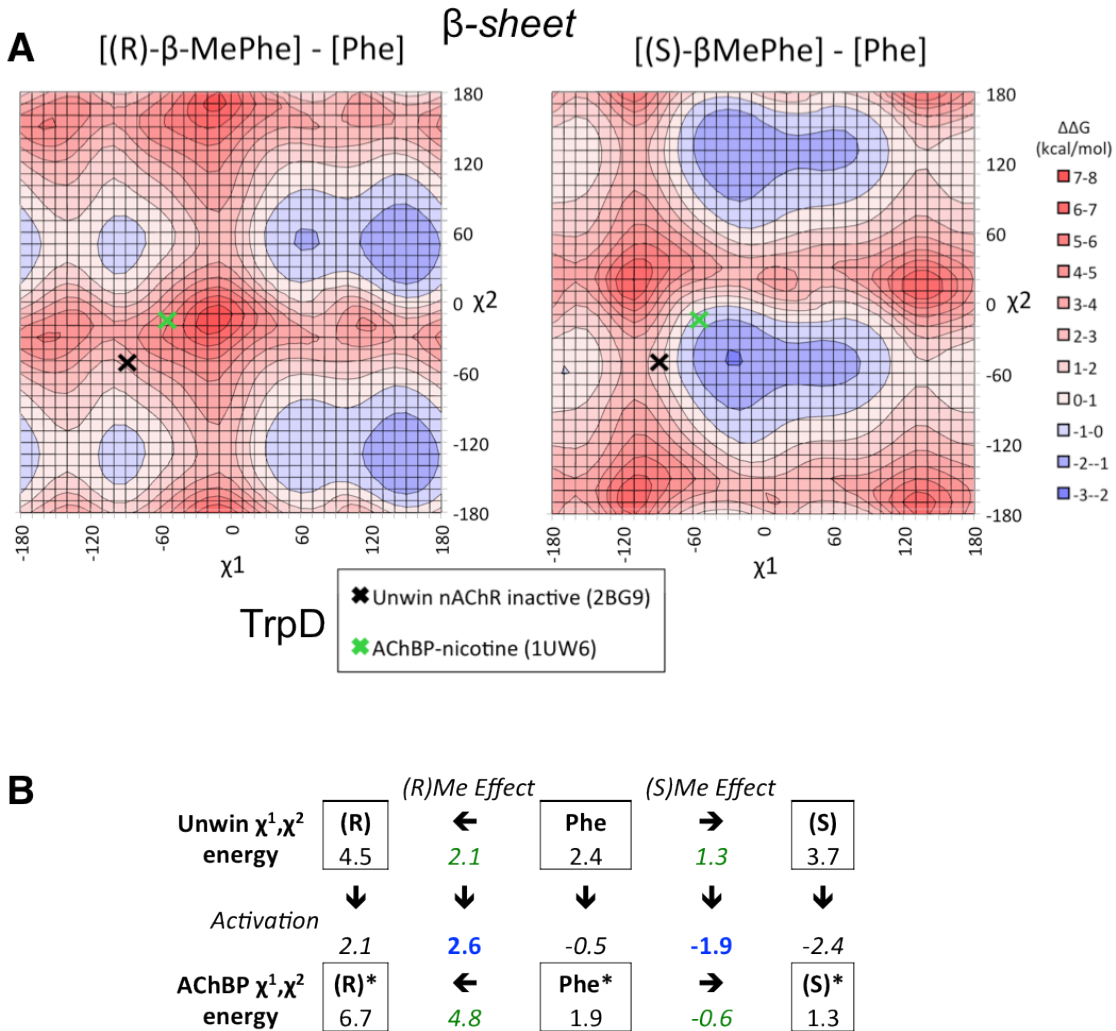


Figure 3.16. (A) “ β -methyl effect” difference plots for (R) and (S) β -methyls of phenylalanine with β -sheet backbone dihedral constraints. χ^1, χ^2 values for TrpD observed in cryo-EM and crystal structures are denoted with an X. (B) Conformational energy analysis. Boxed values are energies (in kcal/mol) calculated for the indicated χ^1, χ^2 , taken from the corresponding plot in Figure 3.12. Values associated with arrows are energy differences. Note that the green “methyl effect” values correspond to $\Delta\Delta G$ values at the appropriate X in part A. Blue values are the differential effect of the methyl on activation.

3.3.4.4 Double mutant cycle analysis to probe steric effects of β -methyl substituents

To probe for steric effects of the introduced β -methyl substituents, we made β -methyl mutations in combination with mutations to adjacent side chains. Double mutant cycle analyses could then be used to test for interactions, and perhaps clarify why energy analyses in the preceding section failed. Mutant cycle analysis can determine whether two single mutants' perturbations are functionally coupled or act independently. This is done by calculating a coupling coefficient $\{\Omega = [\text{EC}_{50}(\text{mut}_{1,2}) \times \text{EC}_{50}(\text{WT})]/[\text{EC}_{50}(\text{mut}_1) \times \text{EC}_{50}(\text{mut}_2)]\}$, which can in turn be converted to a coupling energy [$\Delta\Delta G = -RT\ln(\Omega)$]. If the two mutations are independent of each other, $\Omega \sim 1$. A "compensatory" coupling, in which the double mutant is less deleterious than the effect of the two single mutants multiplied, will yield $\Omega < 1$ and a positive $\Delta\Delta G$. By defining specific steric clashes, we can place constraints on the side chain χ^1 angle (i.e., in which direction the β -methyl group is pointing).

In the D3 and M2 GPCR crystal structures, the F5.47 side chain is expected to clash with both (R) and (S) β -methyl substituents on W6.48, and a clash between the (S)- β -methyl and the F6.52 side chain is anticipated in the D3 structure (Figure 3.17). No clash with the ligand is predicted for either receptor (neither for the antagonist co-crystallized in each structure nor for the agonist used to probe each receptor).

The F5.47L mutation in the M2 receptor, which reduces the size of the side chain, caused a large loss of function (Table 3.5). The EC_{50} estimates for the double mutants of F5.47L with the β -MeTrp analogs predictably indicate large losses of function, though a strong "compensatory" coupling is seen: +1.8 kcal/mol with the (S)- β -methyl and +2.4 kcal/mol with the (R)- β -methyl. The compensatory nature of the coupling ($\Omega < 1$,

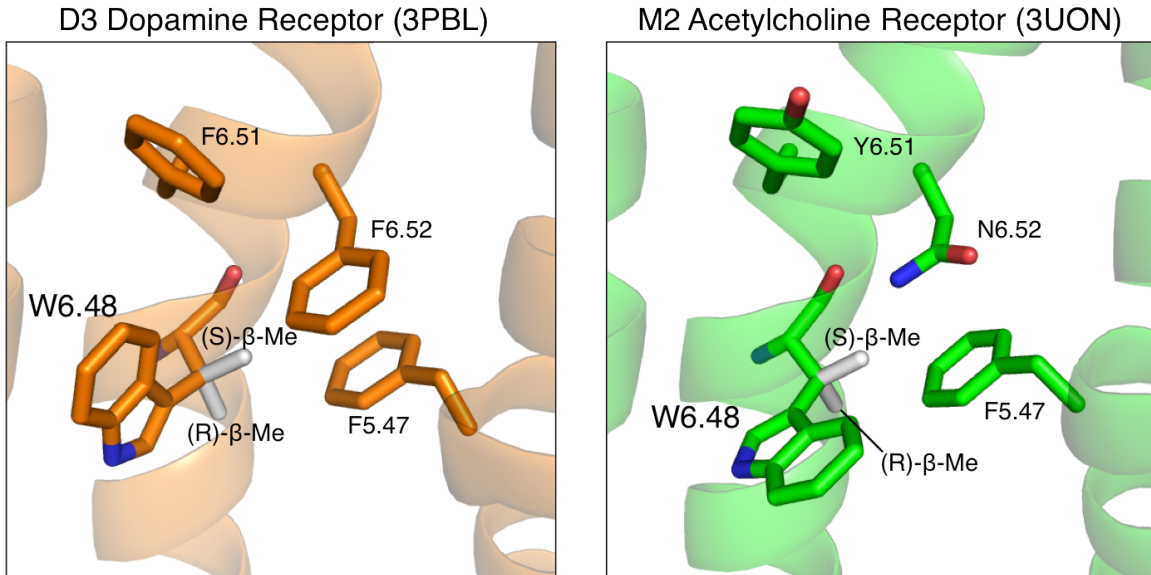


Figure 3.17. Structures of GPCR binding sites with β -methyl substituents modeled onto the W6.48 side chain

Table 3.5. W6.48/F5.47 double mutants of the M2 acetylcholine receptor. EC₅₀ and Hill coefficient (n_H) are \pm SEM for goodness of fit to the Hill equation.

	EC ₅₀ (μ M ACh)	Fold Shift	n _H	n	Ω	$\Delta\Delta G$ (kcal/mol)
W6.48Trp ^{a,b}	0.27 \pm 0.01		1.32 \pm 0.06	7		
W6.48(R)- β -MeTrp ^a	54 \pm 1	200	0.95 \pm 0.02	7		
W6.48(S)- β -MeTrp ^a	73 \pm 2	270	0.91 \pm 0.02	7		
F5.47L	25 \pm 2	93	1.2 \pm 0.1	4		
F5.47L W6.48Trp	Low Currents					
F5.47L W6.48(R)- β -MeTrp	80 \pm 10 ^c	300	1.1 \pm 0.1	6	1 / 62.5	+2.4
F5.47L W6.48(S)- β -MeTrp	310 \pm 70 ^c	1100	0.67 \pm 0.05	4	1 / 21.8	+1.8

^aData reproduced from Table 3.4

^bExpression of the wild type receptor with the natural amino acid incorporated by nonsense suppression

^cEC₅₀ estimate from truncated dose-response data

positive $\Delta\Delta G$) is consistent with the envisioned “bump-hole” pair created in the double mutant. The fact that both methyls couple strongly with the 5.47 side chain suggests that the *gauche(-)* χ^1 angle seen for W6.48 in the crystal structure may indeed be the approximate χ^1 angle of the active receptor, as both proposed steric clashes are evidently detrimental to receptor activation. Further, W6.48 and F5.47 move slightly closer to one

another in crystal structures of the active $\beta 2$ adrenergic receptor and of rhodopsin: the $\text{Ca}-\text{C}\alpha$ distance decreases by 1.2 Å for the $\beta 2$ receptor and by 2.5 Å for rhodopsin. Thus, the β -methyl perturbation might be telling us more about subtle repacking upon activation rather than about side chain rotamer changes.

A similar approach to study steric interactions with F5.47 in the D2 dopamine receptor was attempted, but the F5.47L mutant gave too large of a loss of function to accurately measure an EC_{50} . However, previously published results for single mutants in this region are consistent with a similar steric clash as seen in the M2 receptor. A 14-fold loss of function was recorded for mutation of F5.47 to the bulkier 3,5-dimethylphenylalanine analog, and an extremely large 1300-fold loss of function was recorded for the same mutation to F6.52.^{34,39} These results are consistent with tight packing in this region where the β -methyls were introduced.

In the muscle-type nAChR, we have identified several potential steric clashes between adjacent side chains and the β -methyl groups introduced, using a homology model of this receptor based on AChBP that should represent the active state (Figure 3.18). Steric clashes in this active conformation of the receptor are predicted to give a loss of function. Little, if any, steric clash is predicted for either β -methyl introduced to TrpB, in keeping with the wild type EC_{50} values measured for both (R) and (S) analogs at this site (Figure 3.18A).

However, it is predicted that extra bulk at the α V91 site will result in a steric clash with the (R) β -methyl. In an effort to verify the χ^1 rotamer of TrpB in the active receptor, double mutants of α V91 with (R)- β -MeTrp were made, with (S)- β -MeTrp mutations serving as controls (Table 3.6). Lengthening the α 91 side chain from Val to Leu had no

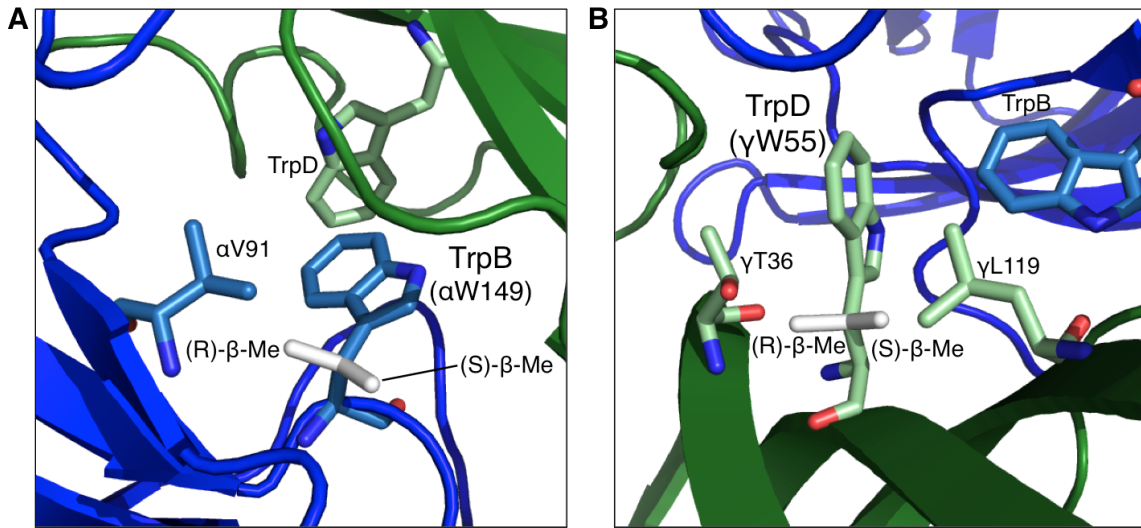


Figure 3.18. Two views of the α/γ binding site of the muscle-type nAChR in the presumed active conformation from a homology model based on AChBP by Kristin Rule Gleitsman,⁴⁰ with β -methyl substituents modeled onto the side chains of TrpB and TrpD. Similar conformations are seen at the α/δ binding site. Corresponding residues in the δ subunit are T38, W57, and L121.

Table 3.6. TrpB (α W149) double mutants of the muscle-type nAChR. EC₅₀ and Hill coefficient (n_H) are \pm SEM for goodness of fit to the Hill equation.

	EC ₅₀ (μ M ACh)	Fold Shift	n _H	n	Ω	$\Delta\Delta G$ (kcal/mol)
α W149Trp ^{a,b}	22 \pm 2		1.5 \pm 0.1	6		
α W149(R)- β -MeTrp ^a	22 \pm 1	1.0	1.6 \pm 0.1	4		
α W149(S)- β -MeTrp ^a	17.1 \pm 0.4	1 / 1.3	1.39 \pm 0.04	7		
α V91L α W149Trp	23 \pm 1	1.0	1.4 \pm 0.1	7		
α V91L α W149(R)- β -MeTrp	63 \pm 2	2.9	1.52 \pm 0.06	4	2.74	-0.60
α V91L α W149(S)- β -MeTrp	57 \pm 3	2.6	1.46 \pm 0.08	4	3.19	-0.69
α V91I α W149Trp	33 \pm 1	1.5	1.39 \pm 0.07	7		
α V91I α W149(R)- β -MeTrp	38 \pm 2	1.7	1.20 \pm 0.05	5	1.15	-0.084
α V91I α W149(S)- β -MeTrp	108 \pm 2	4.9	1.43 \pm 0.04	4	4.21	-0.85
α V91Val α W149Trp ^b	22.5 \pm 0.3		1.57 \pm 0.03	8		
α V91Tle α W149Trp	93 \pm 2	4.1	1.55 \pm 0.05	7		
α V91Tle α W149(S)- β -MeTrp	260 \pm 10	12	1.6 \pm 0.1	7	3.59	-0.76
α V91Tle α W149(R)- β -MeTrp	ND ^c					

^aData reproduced from Table 3.4

^bExpression of the wild type receptor with the natural amino acid(s) incorporated by nonsense suppression

^cNo current detected from identical expression conditions as α V91Tle α W149(S)- β -MeTrp

effect on the wild type receptor, and unexpectedly gave a similar modest coupling energy for both (R) and (S) β -methyl analogs. Also unexpectedly, the larger Ile side chain had a meaningful coupling with the (S) β -methyl, but not the (R). Finally, α V91 was mutated to *tert*-leucine (Tle), which adds an additional methyl group to the β carbon (Figure 3.19) that is expected to clash significantly with an (R) β -methyl on TrpB. The α V91Tle single mutant itself gave a modest loss of function and a measurable +0.76 kcal/mol coupling energy was calculated for the Tle/(S)- β -MeTrp double mutant cycle. The (R)- β -MeTrp/Tle double mutant gave very little, if any, detectable currents (*versus* average currents of 1.3 μ A for the Tle/(S)- β -MeTrp double mutant also measured at 24 hrs post-injection). This observation could be consistent with a major perturbation to this key residue of the ligand binding site, which would confirm the proposed TrpB χ^1 rotamer, though it is unknown whether the deficit is in ligand binding, activation, or expression.

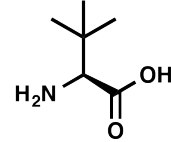


Figure 3.19.
Tert-leucine (Tle)

At the TrpD site, steric clashes are predicted for the (R) β -methyl with the γ T36/ δ T38 side chain and for the (S) β -methyl with the γ L119/ δ L121 side chain (Figure 3.18B). We wondered whether the loss of function recorded for the (R) β -methyl analog was due to a clash with the adjacent Thr. In support of this hypothesis, double mutant cycles with (R)- β -MeTrp in which the Thr side chain was made progressively smaller – to Ser, to Ala, and to Gly – gave progressively larger “compensatory” coupling energies of +0.069, +0.50, and +0.72 kcal/mol (Table 3.7). However, moderate coupling energies (also positive in sign) were also observed for the same Thr mutations in conjunction with (S)- β -MeTrp. As this β -methyl should not interact with the Thr side chain, the trend

described above cannot reasonably be attributed to a specific interaction between the (R) β -methyl and the Thr.

Table 3.7. TrpD (γ W55/ δ W57) double mutants of the muscle-type nAChR. EC₅₀ and Hill coefficient (n_H) are \pm SEM for goodness of fit to the Hill equation.

	EC ₅₀ (μ M ACh)	Fold Shift	n _H	n	Ω	$\Delta\Delta G$ (kcal/mol)
γ W55/ δ W57Trp ^{a,b}	23.4 \pm 0.7		1.35 \pm 0.05	3		
γ W55/ δ W57(R)- β -MeTrp ^a	95 \pm 3	4.0	1.44 \pm 0.05	4		
γ W55/ δ W57(S)- β -MeTrp ^a	23.6 \pm 0.8	1.0	1.30 \pm 0.05	5		
γ T36/ δ T38S γ W55/ δ W57Trp	44 \pm 1	1.9	1.24 \pm 0.04	5		
γ T36/ δ T38S γ W55/ δ W57(R) β -MeTrp	160 \pm 3	6.8	1.40 \pm 0.03	6	1 / 1.13	+0.069
γ T36/ δ T38S γ W55/ δ W57(S) β -MeTrp	22.0 \pm 0.6	1 / 1.1	1.32 \pm 0.04	4	1 / 2.07	+0.43
γ T36/ δ T38A γ W55/ δ W57Trp	63 \pm 1	2.7	1.35 \pm 0.03	5		
γ T36/ δ T38A γ W55/ δ W57(R) β -MeTrp	112 \pm 3	4.8	1.45 \pm 0.05	4	1 / 2.34	+0.5
γ T36/ δ T38A γ W55/ δ W57(S) β -MeTrp	40.1 \pm 0.8	1.7	1.28 \pm 0.03	5	1 / 1.66	+0.29
γ T36/ δ T38G γ W55/ δ W57Trp	192 \pm 3	8.2	1.43 \pm 0.03	5		
γ T36/ δ T38G γ W55/ δ W57(R) β -MeTrp	230 \pm 10	9.8	1.34 \pm 0.07	5	1 / 3.41	+0.72
γ T36/ δ T38G γ W55/ δ W57(S) β -MeTrp	117 \pm 3	5.0	1.27 \pm 0.03	5	1 / 1.70	+0.31
γ L119/ δ L121F γ W55/ δ W57Trp	86 \pm 3	3.7	1.73 \pm 0.09	3		
γ L119/ δ L121F γ W55/ δ W57(R) β -MeTrp	390 \pm 10	17	1.36 \pm 0.05	4	1.12	-0.066
γ L119/ δ L121F γ W55/ δ W57(S) β -MeTrp	142 \pm 5	6.1	1.17 \pm 0.04	4	1.63	-0.29

^aData reproduced from Table 3.4

^bExpression of the wild type receptor with the natural amino acid incorporated by nonsense suppression

While the TrpD mutation to (S)- β -MeTrp gave a wild type EC₅₀, a modest steric clash is predicted with the γ L119/ δ L121 side chain. We wondered if mutation to a larger Phe side chain at this site might induce a functionally significant clash. The (S)- β -MeTrp/Phe double mutant cycle indeed yields a coupling (-0.29 kcal/mol), though modest, and the sign (negative $\Delta\Delta G$, $\Omega > 1$) is consistent with an engineered clash. Reassuringly, the (R)- β -MeTrp/Phe double mutant cycle has a negligible coupling energy.

While a sensible result emerges from this series of mutations of TrpD with γ L119/ δ L121, the majority of these nAChR double mutants probing sterics (Tables 3.6 and 3.7) give unexpected results. Overall, the lack of predictability suggests that either our model of the active receptor's binding site is incorrect, or that the mutations designed to simply alter sterics have unforeseen consequences.

3.4 Conclusions

The experiments described in this chapter use mutagenesis to probe side chain conformation in receptor binding sites, and changes to side chain conformation upon receptor activation. The D2 and M2 GPCR results are most consistent with a model in which the W6.48 side chain does not change its conformation upon activation, and suggest different χ^2 rotamers for W6.48 in the D2 and M2 receptors, consistent with crystallography. However, no definitive conclusions emerge. The nAChR results are largely inconclusive. Thus, even very subtle mutations like those considered here can produce ambiguous results when used to probe the complex motions associated with integral membrane receptors.

To be able to interpret the effect of a mutation on a conformational change, there are two requirements. First, a fairly precise description of the protein's inactive and active conformations is necessary (if indeed a two-state model adequately describes the system). From the current limited body of structural data and of proposed activation mechanisms for GPCRs and nAChRs, this requirement is a significant challenge.

Second, the energetic consequence of the mutation on each state must be accurately predicted. On this point, it is hard to know the true energetic consequence of a mutation in the actual receptor. Steric and electrostatic impacts of the local protein environment certainly complicate the simple conformational analysis applied to Thr/*a*Thr or Ile/*a*Ile or the more sophisticated χ^1 , χ^2 energy analysis applied to the β -methyl analogs in this chapter. Recently developed molecular dynamics approaches termed “metadynamics” allow the energy of an entire system to be determined as a function of a set of collective variables, such as χ^1 , χ^2 of a specific residue.⁴¹ This effectively allows for the construction of plots such as those in Figures 3.10 through 3.12 for a given side chain in its actual protein context. Such an approach has been used by Voth and co-workers to suggest χ^1 , χ^2 rearrangements of W6.48 in the A2A adenosine GPCR.¹⁵ If extended to unnatural amino acid analogs at W6.48 or other protein sites, this approach could aid the interpretation of experimental data to inform activation mechanisms.

3.5 Experimental

3.5.1 Molecular biology

cDNA for the mouse muscle nAChR α 1, β 1, γ , and δ subunits was in the pAMV plasmid, the human D2 dopamine receptor (long isoform) was in the pGEMhe plasmid, the human M2 muscarinic acetylcholine receptor was in the pGEM3 plasmid, GIRK1 and GIRK4 were in pBSMXT plasmids, and RGS4 was in the pcDNA3.1 plasmid. Site-directed mutagenesis was performed using the QuikChange protocol (Agilent Technologies). For nonsense suppression experiments, the site of interest was mutated to the amber stop codon, with the exception of muscle-type nAChR α V91, which was

mutated to the opal stop codon. Circular DNA was linearized with the appropriate restriction enzyme (NotI for nAChR subunits, NheI or SbfI for the D2 receptor, HindIII for the M2 receptor, SalI for GIRQ1 and GIRQ4, and StuI for RGS4). After purification (Qiagen), linearized DNA was used as a template for runoff *in vitro* transcription using the T7 mMessage mMachine kit (Life Technologies). The amber suppressor tRNA THG73⁴² was used for nonsense suppression at all sites except α V91 in the muscle-type nAChR, for which the opal suppressor TQOpS^{43,44} was used.

Amino acids were appended to the dinucleotide dCA and enzymatically ligated to the appropriate truncated 74mer suppressor tRNA as previously described.⁴⁵ Crude tRNA-amino acid product was used without desalting, and the product was confirmed by MALDI-TOF MS on a 3-hydropicolinic acid matrix. tRNA-amino acids bearing a 6-nitroveratryloxycarbonyl protecting group were deprotected prior to injection *via* irradiation with a 500 W Hg/Xe arc lamp, filtered with WG-334 and UG-11 filters prior to injection.

3.5.2 Microinjection

Stage V–VI *Xenopus laevis* oocytes were harvested and injected with RNAs as described previously.⁴⁵ For the muscle-type nAChR, oocytes were injected with 10 - 20 ng mRNA in a 10:1:1:1 ratio of α 1: β 1: γ : δ for nonsense suppression in the α 1 subunit or in a 1:1:5:5 ratio for nonsense suppression in the γ and δ subunits, together with ~25 ng of the appropriate tRNA. Oocytes were incubated 18 - 24 hrs before recording.

For the M2 acetylcholine receptor, approximately 10 ng M2 receptor mRNA (2 ng for conventional mutagenesis experiments), 10 ng each of GIRQ1 and GIRQ4 mRNA,

and ~25 ng of the appropriate tRNA (for nonsense suppression) were injected 48 hrs prior to recording. An additional ~25 ng tRNA (for nonsense suppression) and 10 ng of RGS4 mRNA were injected 24 hrs prior to recording.

For the D2 dopamine receptor, receptor mRNA (4 - 25 ng for suppression experiments, 0.16 ng for wild type, and 1 ng for conventional mutagenesis), 10 ng each of GIRQ1 and GIRQ4, and ~25 ng tRNA (for nonsense suppression) were injected 48 hrs prior to recording. For low-expressing mutants generated by nonsense suppression, an additional ~25 ng receptor mRNA and ~25 ng tRNA were injected 24 hrs prior to recording.

As a negative control for all suppression experiments, unacylated full length tRNA was co-injected with mRNA in the same manner as charged tRNA. These control experiments yielded negligible responses for all sites studied.

3.5.3 Electrophysiology

Receptor function was assayed using the OpusXpress 6000A (Molecular Devices, Sunnyvale, CA) in two-electrode voltage clamp mode. The oocytes were clamped at a holding potential of -60 mV. For the muscle-type nAChR, acetylcholine doses in Ca^{2+} -free ND96 (96 mM NaCl, 2 mM KCl, 1 mM MgCl_2 , 5 mM HEPES, pH 7.5) were applied for 15 s followed by a 116 s wash with Ca^{2+} -free ND96. For the D2 dopamine receptor and M2 muscarinic acetylcholine receptor, cells were subjected to a ND96 (96 mM NaCl, 2 mM KCl, 1 mM MgCl_2 , 1.8 mM CaCl_2 , 5 mM HEPES, pH 7.5) pre-wash for 10 s, a high K^+ buffer (96 mM NaCl, 24 mM KCl, 1 mM MgCl_2 , 5 mM HEPES, 1.8 mM CaCl_2 , pH 7.5) application for 50 s to establish basal currents, and agonist application in high K^+

ringer for 25 s, followed by high K⁺ and ND96 washings for 45 s and 90 s in duration, respectively. Agonist-induced currents were measured over the basal K⁺ current as described previously.³⁹ Dopamine solutions in high K⁺ buffer were prepared immediately before recording by dilutions from a 1 M stock in water. The EC₅₀ and Hill coefficient (n_H) values for each condition were obtained by fitting the averaged, normalized dose-response data to the Hill equation.

3.5.4 Energy calculations

Using the Spartan '08 software package, molecular mechanics (MMFF) energies were calculated for the amino acids (R)-β-MeTrp, (S)-β-MeTrp, (R)-β-MePhe, and (S)-β-MePhe capped in the form: Ac-Xaa-NH-Me (where Xaa is the β-methyl amino acid). Energies were determined at all angles of χ^1 and χ^2 , in 10° increments. For Phe and β-MePhe, the backbone dihedrals were constrained to $\phi = -86^\circ$, $\psi = 120^\circ$ (β -sheet values observed for TrpD in the nicotine-bound *Ls*-AChBP crystal structure).³⁷ For Trp and β-MeTrp, the backbone dihedrals were constrained to either $\phi = -86^\circ$, $\psi = 120^\circ$ (β -sheet) or to $\phi = -48^\circ$, $\psi = -57^\circ$ (idealized α -helix). For all calculations, the backbone amide dihedrals were constrained to 180°. The resulting energies, relative to the global minimum for each condition, are plotted *versus* χ^1 and χ^2 in Figures 3.10 through 3.12. A cubic interpolation surface fit of each data set was constructed using MATLAB, from which energy values for a specific χ^1 , χ^2 were extracted. These values are shown in the tables in Figures 3.13 through 3.16,. The “methyl effect” plots (Figures 3.13 through 3.16) are generated by subtracting the relative energies for the parent amino acid (Trp or Phe) from the relative energies of the β-methyl analog.

3.5.5 Synthesis

Synthesis of Boc-5-aminomethyl indole (1). 5-aminomethyl indole (Aldrich, 500 mg, 3.42 mmol, 1 eq) was dissolved in a solution of H₂O (20 mL) and THF (20 mL). Boc₂O (Fluka, 0.864 mL, 3.76 mmol, 1.1 eq) was added with stirring, followed by NaOH (3.76 mL of a 1 M aqueous solution, 3.76 mmol, 1.1 eq), and stirred for 12 hrs. The THF was removed *in vacuo* and the aqueous layer extracted with dichloromethane (3x), washed with brine, dried over MgSO₄, and concentrated. The resulting crude product was purified by flash chromatography (2.5:1 hexanes/ethyl acetate). Compound **1** (786 mg, 93% yield) was recovered as a clear, colorless tar. ¹H NMR (300 MHz, CDCl₃) δ 8.51 (s, 1H), 7.55 (s, 1H), 7.33 (d, *J* = 8.3 Hz, 1H), 7.16 (m, 1H), 7.12 (d, *J* = 8.3 Hz, 1H), 6.51 (ddd, *J* = 3.0, 2.0, 0.9 Hz, 1H), 4.90 (s, 1H), 4.42 (d, *J* = 5.5 Hz, 2H), 1.50 (s, 9H).

Synthesis of hydroxyimine (2). Ethyl 3-bromo-2-hydroxyiminopropanoate³³ (298 mg, 1.42 mmol, 1 eq) was dissolved in 20 mL dichloromethane. Boc-5-aminomethyl indole **1** (700 mg, 2.84 mmol, 2 eq) followed by anhydrous Na₂CO₃ (226 mg, 2.13 mmol, 1.5 eq) were added, and the reaction suspension was stirred for 20 hrs under argon. Dichloromethane (25 mL) and H₂O (25 mL) were added, and the layers were partitioned. The aqueous layer was extracted (3x) with dichloromethane, the combined organics were washed with brine, dried over MgSO₄, and concentrated. The crude product was purified by flash chromatography (1.25:1 to 1:1.1 hexanes/ethyl acetate) to yield compound **2** (339 mg, 64% yield). ¹H NMR (300 MHz, CDCl₃) δ 10.34 (s, 1H), 8.32 (s, 1H), 7.64 (s, 1H), 7.22 (d, *J* = 8.2 Hz, 1H), 7.09 (s, 1H), 7.06 (s, 1H), 4.91 (s, 1H), 4.37 (d, *J* = 4.8 Hz, 2H), 4.20 (q, *J* = 7.2 Hz, 2H), 4.05 (s, 2H), 1.47 (s, 9H), 1.23 (t, *J* = 7 Hz, 3H).

Synthesis of Boc-5-aminomethyl-Trp ethyl ester (3). Hydroximine **2** (300 mg, 0.80 mmol) was dissolved in a solution of THF (27 mL) and H₂O (3 mL). Aluminum pellets (2 g) were treated with 10% NaOH (50 mL) for 3 min, washed (3x) with water, treated with 2% Hg₂Cl₂ (50 mL) for 5 min, washed (3x) with water, and dropped into the solution of hydroximine **2**. After 16 hrs stirring, the reaction was filtered through a short plug of silica, washing with ethyl acetate, then 5:2 ethyl acetate/methanol, and the combined organics were concentrated. The crude product (327 mg recovered) was carried on to the next step without further purification.

Synthesis of 5-aminomethyl-Trp ethyl ester (4). Crude amine **3** (100 mg, ~0.28 mmol) was dissolved in dichloromethane (1 mL). Trifluoroacetic acid was added (1 mL) and the reaction was stirred for 1 hr under argon, after which the reaction solution was concentrated *in vacuo*. The crude product (75 mg recovered) was carried on to the next step without further purification.

Synthesis of (NVOC)₂-5-aminomethyl-Trp ethyl ester (5). Crude diamine **4** (75 mg, ~0.29 mmol, 1 eq) was dissolved in H₂O (6 mL). 6-Nitroveratryloxycarbonyl (NVOC) chloride (158 mg, 0.574 mmol, 3 eq) dissolved in dioxane (6 mL) was added, and the reaction solution was stirred for 4 hrs. An additional portion of 6-nitroveratryloxycarbonyl (NVOC) chloride (39 mg, 0.191 mmol, 0.5 eq) dissolved in dioxane (1 mL) was added and the reaction solution was stirred for an additional 4 hrs. The reaction solution was poured into 75 mL H₂O, acidified to pH = 3 with 0.2 M aqueous HCl, and extracted (3x) with ethyl acetate. The combined organics were washed with brine, dried over Mg₂SO₄, and concentrated. The crude product was purified by flash chromatography (2.5:1 ethyl acetate/hexanes, followed by 100% ethyl acetate) to

yield compound **5** (48 mg, 20% yield over three steps from hydroximine **2**). ¹H NMR (500 MHz, DMSO-d₆) δ 10.84 (s, 1H), 8.01 (d, *J* = 7.8 Hz, 1H), 7.97 (t, *J* = 6.0 Hz, 1H), 7.69 (s, 2H), 7.42 (s, 1H), 7.29 (d, *J* = 8.3 Hz, 1H), 7.17 (s, 2H), 7.13 (s, 1H), 7.03 (dd, *J* = 8.3, 1.1 Hz, 1H), 5.37-5.26 (m, 4H), 4.29 (d, *J* = 5.1 Hz, 2H), 4.05 (dd, *J* = 7.0, 2.2 Hz, 1H), 3.86-3.74 (m, 14H), 3.14 (dd, *J* = 14.3, 5.2 Hz, 1H), 3.03 (dd, *J* = 14.5, 9.2 Hz, 1H), 1.09 (t, *J* = 7.1 Hz, 2H).

Synthesis of (NVOC)₂-5-aminomethyl-Trp (6). (NVOC)₂-5-aminomethyl-Trp ethyl ester **5** (43 mg, 0.058 mmol, 1 eq) was dissolved in a solution of H₂O (1 mL) and dioxane (5 mL). Aqueous 1M NaOH was added (0.5 mL) and the reaction was stirred for 20 hrs at room temperature. Additional 1M NaOH (1 mL) was added and the reaction was heated at 40°C for 1.5 hrs, after which the reaction was complete by TLC. The reaction solution was cooled to room temperature, diluted with H₂O, and aqueous KHSO₄ was added until the pH reached 2.5, causing the solution to turn cloudy. This suspension was extracted with dichloromethane (3x) and the combined organics were washed with brine, dried over Mg₂SO₄, and concentrated, to yield the crude product (42 mg recovered), which was carried on to the next step without further purification. LRMS (ESI-) calculated for [C₃₂H₃₂N₅O₁₄]⁻ ([M-H]⁻) 710.2, found 710.0.

Synthesis of (NVOC)₂-5-aminomethyl-Trp cyanomethyl ester (7). Crude (NVOC)₂-5-aminomethyl-Trp **6** (42 mg, ~0.058 mmol, 1 eq) was dissolved in a solution of DMF (1 mL) and chloroacetonitrile (1 mL, 16 mmol, 270 eq). Triethylamine (24 μL, 0.17 mmol, 3 eq) was added and the reaction was stirred at room temperature for 6 hrs. The reaction solution was concentrated *in vacuo* and the crude product was dissolved in dichloromethane. This solution was washed with 0.2 M aqueous HCl, 1 M aqueous

NaHCO_3 , and brine, dried over MgSO_4 , and concentrated. The crude product was recrystallized by dissolving in a minimal volume (~ 1 mL) dichloromethane, diluting with hexanes to precipitate the product, and cooling this suspension to 0°C . The precipitate was recovered by filtration, washing with cold hexanes, to yield compound **7** (21 mg, 47% yield over two steps). ^1H NMR (300 MHz, DMSO- d_6) δ 10.90 (s, 1H), 8.21 (d, $J = 7.5$ Hz, 1H), 7.97 (t, $J = 5.8$ Hz, 1H), 7.69 (s, 2H), 7.43 (s, 1H), 7.30 (d, $J = 8.3$ Hz, 1H), 7.19 (d, $J = 1.9$ Hz, 1H), 7.17 (s, 1H), 7.11 (s, 1H), 7.04 (d, $J = 8.3$ Hz, 1H), 5.40-5.27 (m, 4H), 4.99 (s, 2H), 4.42 (dd, $J = 14.1, 7.9$ Hz, 1H), 4.29 (d, $J = 5.7$ Hz, 2H), 3.86-3.79 (m, 12H), 3.23-3.05 (m, 2H). ^{13}C NMR (126 MHz, DMSO- d_6) δ 171.26, 155.78, 155.56, 153.40, 153.33, 147.67, 147.61, 139.15, 139.04, 135.36, 129.67, 128.07, 127.69, 126.75, 124.40, 121.13, 116.70, 115.66, 112.07, 111.42, 110.33, 110.13, 109.53, 108.81, 108.12, 62.67, 62.35, 56.13, 56.06, 54.60, 49.46, 44.62, 26.64.

Synthesis of $(\text{NVOC})_2\text{-5-aminomethyl-Trp-dCA}$ (8). dCA•2.2 TBA (10 mg, 8.6 μmol , 1 eq) and $(\text{NVOC})_2\text{-5-aminomethyl-Trp}$ cyanomethyl ester **7** (10 mg, 13 μmol , 1.5 eq) were dissolved in DMF (0.2 mL) and stirred at room temperature for 22 hrs under argon, then stirred at 50°C for 1 hr. The reaction was purified by HPLC to yield compound **8** (347 μg , 3% yield). MALDI-MS calculated for $[\text{C}_{51}\text{H}_{58}\text{N}_{13}\text{O}_{26}\text{P}_2]^+$ ($[\text{M}+\text{H}]^+$) 1330.31, found 1330.54.

NVOC-(2S,3S)- β -methylPhe cyanomethyl ester (9). Prepared from (2S,3S)- β -methylPhe (Chem-Impex) by standard methods as for compounds **22** and **23**. ^1H NMR (300 MHz, CDCl_3) δ 7.70 (s, 1H), 7.37-7.17 (m, 5H), 6.88 (s, 1H), 5.50 (dd, $J = 34.8, 15.0$ Hz, 2H), 5.12 (d, $J = 8.8$ Hz, 1H), 4.85-4.62 (m, 3H), 3.94 (s, 3H), 3.92 (s, 3H), 3.42 (m, 1H), 1.43 (d, $J = 7.1$ Hz, 3H). ^{13}C NMR (75 MHz, CDCl_3) δ 170.42, 155.76, 153.72,

148.22, 139.70, 129.19, 127.97, 127.83, 127.52, 113.81, 109.79, 108.23, 64.23, 59.17, 56.52, 48.94, 41.75, 17.88.

NVOC-(2S,3S)- β -methylPhe-dCA (10) Prepared from NVOC-(2S,3S)- β -methylPhe cyanomethyl ester (**9**) by standard methods as for compound **24**. MALDI-MS calculated for $[C_{39}H_{47}N_{10}O_{20}P_2]^+$ ($[M+H]^+$) 1037.24, found 1037.45.

NVOC-(2S,3R)- β -methylPhe cyanomethyl ester (11). Prepared from (2S,3R)- β -methylPhe (generous gift from Victor Hruby, University of Arizona) by standard methods as for compounds **22** and **23**. 1H NMR (300 MHz, $CDCl_3$) δ 7.70 (s, 1H), 7.35-7.19 (m, 5H), 6.93 (s, 1H), 5.50 (dd, J = 21, 15 Hz, 2H), 5.33 (d, J = 8.7 Hz, 1H), 4.64-4.56 (m, 3H), 3.95 (s, 6H), 3.32 (m, 1H), 1.43 (d, J = 7.2 Hz, 3H).

NVOC-(2S,3R)- β -methylPhe-dCA (12). Prepared from NVOC-(2S,3R)- β -methylPhe cyanomethyl ester (**11**) by standard methods as for compound **24**. MALDI-MS calculated for $[C_{39}H_{47}N_{10}O_{20}P_2]^+$ ($[M+H]^+$) 1037.24, found 1037.39.

NVOC-(2S,3S)- β -methylTrp cyanomethyl ester (13). Prepared from (2S,3S)- β -methylTrp (generous gift from Victor Hruby, University of Arizona) by standard methods as for compounds **22** and **23**. 1H NMR (300 MHz, $CDCl_3$) δ 8.17 (s, 1H), 7.70 (s, 1H), 7.62 (d, J = 7.9 Hz, 1H), 7.38 (d, J = 8.1 Hz, 1H), 7.22 (t, J = 7.6 Hz, 1H), 7.14 (t, J = 7.5 Hz, 1H), 7.09 (d, J = 2.5 Hz, 1H), 6.91 (s, 1H), 5.52 (dd, J = 15, 15 Hz, 2H), 5.35 (d, J = 8.7 Hz, 1H), 4.79-4.49 (m, 3H), 3.94 (s, 3H), 3.89 (s, 3H), 3.82 (m, 1H), 1.54 (d, J = 7.2 Hz, 4H). ^{13}C NMR ($CDCl_3$) δ 170.58, 155.90, 153.77, 148.31, 139.82, 136.56, 127.85, 126.41, 122.82, 122.13, 120.19, 118.94, 114.84, 113.93, 111.78, 110.08, 108.34, 64.30, 58.96, 56.60, 56.56, 48.95, 34.18, 18.10.

NVOC-(2S,3S)- β -methylTrp-dCA (14). Prepared from NVOC-(2S,3S)- β -methylTrp cyanomethyl ester (**11**) by standard methods as for compound **24**. MALDI-MS calculated for $[C_{41}H_{48}N_{11}O_{20}P_2]^+$ ($[M+H]^+$) 1076.25, found 1076.29.

Boc-indoleacrylic acid (15). *Trans*-3-indoleacrylic acid (2 g, 10.7 mmol, 1 eq) was added to a solution of acetonitrile (20 mL) and water (1.5 mL) in a 100 mL round bottom flask. Triethylamine (1.57 mL, 11.2 mmol, 1.05 eq) was added and all solids dissolved after several minutes of stirring. 4-Dimethylaminopyridine (131 mg, 1.07 mmol, 0.1 eq) was added, followed by Boc_2O (2.58 mL, 11.2 mmol, 1.05 eq), added dropwise over ~2 min, and the reaction solution was stirred at room temperature overnight. Additional Boc_2O (2.46 mL, 10.7 mmol, 1 eq) was added and the reaction was stirred at 45°C for 2 hrs, after which the reaction was complete by TLC. The reaction solution was diluted with 60 mL Et_2O and washed with 1M aqueous $KHSO_4$ (5x). The organic layer was extracted with 5% aqueous $NaHCO_3$ (5x) and the combined aqueous $NaHCO_3$ layers were acidified with aqueous HCl to pH 1.5, then extracted with Et_2O (5x) and these combined ether layers were washed with brine, dried over Na_2SO_4 , and concentrated. The resulting solid was purified by flash chromatography (5:1 to 1:1 dichloromethane/ethyl acetate), to give 2.15 g (~70% yield) of crude product, which was carried on to the next step without further purification. 1H NMR (300 MHz, $CDCl_3$) δ 8.21 (d, $J = 7.9$ Hz, 1H), 7.97-7.85 (m, 3H), 7.38 (m, 2H), 6.56 (d, $J = 16.1$ Hz, 1H), 1.70 (s, 9H).

Boc-indoleacrylic acid-oxazolidinone (16). Crude Boc-indoleacrylic acid **15** (1.5 g, ~5.2 mmol, 1.3 eq) was dissolved in dry THF (20.2 mL) in a 250 mL oven-dried Schlenk flask under argon. Triethylamine (1.41 mL, 10 mmol, 2.5 eq) was added, and the

reaction solution was cooled to ~-10°C. Trimethylacetyl chloride (0.595 mL, 4.8 mmol, 1.2 eq) was added dropwise, upon which a yellow precipitate formed, and the reaction suspension was stirred at -10°C for 1 hr. Dry LiBr (0.384 g, 4.4 mmol, 1.1 eq) was added, followed by (S)-4-phenyl-2-oxazolidinone (0.656 g, 4.0 mmol, 1.0 eq), the reaction was warmed to room temperature, and stirred at room temperature for 4 hrs. The reaction was quenched by addition of 0.2 M aqueous HCl (40 mL, 2 eq), and the THF was removed *in vacuo*, ethyl acetate was added, and this organic layer was washed with 0.2 M aqueous HCl, then 1M aqueous NaHCO₃ (2x), then brine, dried over Na₂SO₄, and concentrated. The crude product was purified by flash chromatography (4:1 hexanes/ethyl acetate) to yield compound **16** (1.51 g, 47% yield over 2 steps from *trans*-3-indoleacrylic acid). ¹H NMR (300 MHz, CDCl₃) δ 8.19 (dd, *J* = 5.9, 3.3 Hz, 1H), 8.08 (d, *J* = 15.8 Hz, 1H), 7.99-7.89 (m, 3H), 7.43-7.33 (m, 7H), 5.59 (dd, *J* = 8.7, 3.8 Hz, 1H), 4.76 (t, *J* = 8.8 Hz, 1H), 4.33 (dd, *J* = 8.8, 3.8 Hz, 1H), 1.68 (s, 9H).

(3R)-Boc-β-methylindolepropanoic acid-oxazolidinone (17). A solution of methylmagnesium bromide (3M in Et₂O, 1.75 mL, 5.24 mmol, 1.5 eq) in dry THF (18 mL) and dimethyl sulfide (5.4 mL) in an oven-dried Schlenk flask was subjected to three freeze-pump-thaw cycles, placed under an atmosphere of argon, and cooled to 0°C. CuBr•DMS (1.08g, 5.24 mmol, 1.5 eq) was added all at once and the solution was stirred for 30 min at 0°C. A solution of Boc-indoleacrylic acid-oxazolidinone (**16**) in THF (10 mL), which had also been subjected to three freeze-pump-thaw cycles, was added via cannula over 5 min. The reaction solution was stirred at 0°C for 2 hrs, then at room temperature for 45 min, quenched by the addition of 30 mL saturated aqueous NH₄Cl, and stirred at room temperature for 30 min. The layers were partitioned and the organic

layer was washed with saturated aqueous NH₄Cl (4x), then brine (2x), then dried over Mg₂SO₄ and concentrated. The major diastereomer was isolated from the crude product by flash chromatography (5:1 hexanes/ethyl acetate) to yield compound **17** (1.12 g, 72% yield). ¹H NMR (300 MHz, CDCl₃) δ 8.12 (d, *J* = 7.3 Hz, 1H), 7.60 (d, *J* = 7.3 Hz, 1H), 7.36-7.21 (m, 8H), 5.36 (dd, *J* = 8.7, 3.7 Hz, 1H), 4.58 (t, *J* = 8.8 Hz, 1H), 4.22 (dd, *J* = 8.9, 3.8 Hz, 1H), 3.61 (dd, *J* = 13.9, 7.0 Hz, 1H), 3.47 (dd, *J* = 16.5, 7.1 Hz, 1H), 3.25 (dd, *J* = 16.5, 7.2 Hz, 1H), 1.66 (s, 9H), 1.33 (d, *J* = 6.9 Hz, 3H). ¹³C NMR (75 MHz, CDCl₃) δ 171.51, 153.84, 139.05, 129.68, 129.23, 128.78, 125.94, 125.04, 124.42, 122.47, 121.80, 119.39, 115.44, 83.57, 70.05, 57.77, 42.24, 28.36, 26.97, 21.11.

(2S, 3R)-Boc-β-methyl-α-azido-indolepropanoic acid-oxazolidinone (18). (3R)-Boc-β-methylindolepropanoic acid-oxazolidinone **17** (600 mg, 1.34 mmol, 1 eq) was dissolved in THF (7 mL) under argon in a 50 mL oven-dried Schlenk flask. A solution of 0.5 M KHMDS in toluene (2.94 mL, 1.47 mmol, 1.1 eq) was added to THF (5 mL) in a 100 mL oven-dried Schlenk flask under argon. Both flasks were cooled to -78°C and the solution of compound **17** was transferred to the KHMDS solution by cannula. This solution was stirred at -78°C for 30 min. Trisyl azide^{46,47} was dissolved in THF (5 mL) in a 100 mL oven-dried Schlenk flask under argon and cooled to -78°C. The compound **17**/KHMDS solution was transferred to this flask via cannula transfer and the solution was stirred at -78°C for 5 min. The reaction was quenched by addition of glacial acetic acid (0.368 mL, 6.44 mmol, 4.8 eq), and the solution was warmed to room temperature, and stirred at room temperature for 4 hrs. This solution was diluted with Et₂O and 1M aqueous sodium chloride and mixed. The aqueous phase was extracted with 1:1 Et₂O/THF (3x) and the combined organics washed with 1M NaHCO₃ (2x) then brine

(2x), dried over MgSO₄, and concentrated. The crude product was purified by flash chromatography (5:1 hexanes/ethyl acetate) to yield compound **18** (455 mg, 69% yield).

¹H NMR (300 MHz, CDCl₃) δ 8.18 (d, *J* = 8.1 Hz, 1H), 7.65 (d, *J* = 7.4 Hz, 1H), 7.53 (s, 1H), 7.36-7.26 (m, 5H), 7.18 (dd, *J* = 7.6, 1.8 Hz, 2H), 5.36 (d, *J* = 9.4 Hz, 1H), 4.79 (dd, *J* = 8.3, 2.9 Hz, 1H), 4.02 (dd, *J* = 8.8, 3.0 Hz, 1H), 3.85 (t, *J* = 8.6 Hz, 1H), 3.64 (dq, *J* = 14.1, 7.0 Hz, 1H), 1.69 (s, 9H), 1.57 (d, *J* = 7.0 Hz, 3H). ¹³C NMR (75 MHz, CDCl₃) δ 169.63, 153.02, 149.58, 138.19, 135.25, 129.34, 129.26, 128.97, 125.77, 124.89, 124.11, 122.76, 120.30, 119.40, 115.34, 84.13, 70.22, 63.64, 58.02, 32.84, 28.31, 17.98.

(2S,3R)-Boc-β-methyl-α-azido-indolepropanoic acid (19). (2S,3R)-Boc-β-methyl-α-azido-indolepropanoic acid-oxazolidinone **18** (400 mg, 0.817 mmol, 1 eq) was dissolved in THF (10 mL) and H₂O (10 mL). This solution was cooled to 0°C and hydrogen peroxide (30% aqueous solution, 0.508 mL) was added dropwise over 1 min with stirring, then LiOH•H₂O (68 mg, 1.63 mmol, 2 eq) was added all at once, and the reaction solution was stirred at 0°C for 30 min, after which the reaction was complete by TLC. NaHSO₃ (512 mg in 0.6 mL H₂O, 4.92 mmol, 3 eq) was added at 0°C, followed by saturated aqueous NaHCO₃ (10 mL), and the mixture was stirred at room temperature for 30 min. THF was removed *in vacuo*, Et₂O (15 mL) was added and the layers were partitioned after mixing. The organic layer was extracted with saturated aqueous NaHCO₃ (3x) and the combined aqueous layers were acidified to pH = 1.5 with 1M HCl. The resulting suspension was extracted with ethyl acetate (4x) and these combined ethyl acetate layers were washed with H₂O (2x) and brine (2x), dried over MgSO₄, and concentrated to yield crude product 1. The original Et₂O organic layer was extracted again with saturated aqueous NaHCO₃ (3x), acidified to pH = 1, and this suspension was

extracted with ethyl acetate (4x). The combined organic layers were washed with brine (2x), dried over MgSO₄, and concentrated to yield crude product 2. Crude product 1 was partially purified by flash chromatography (1:1 ethyl acetate/hexanes, then 100% ethyl acetate, then 5% methanol and 1% acetic acid in ethyl acetate) to yield compound **19** (92 mg, 33% yield). ¹H NMR (300 MHz, CDCl₃) δ 9.62 (s, 1H), 8.16 (d, *J* = 8.0 Hz, 1H), 7.60 (d, *J* = 7.6 Hz, 1H), 7.54 (s, 1H), 7.31 (dt, *J* = 23.6, 7.0 Hz, 2H), 4.41 (d, *J* = 4.3 Hz, 1H), 3.79-3.71 (m, 1H), 1.69 (s, 9H), 1.44 (d, *J* = 7.0 Hz, 3H). ¹³C NMR (75 MHz, CDCl₃) δ 175.38, 149.84, 135.58, 129.21, 124.85, 123.65, 122.81, 121.07, 118.70, 115.70, 84.12, 66.28, 33.07, 28.34, 14.87. IR (NaCl) 2978 (m), 2928 (m), 2109 (s), 1733 (s), 1370 (s), 1157 (s) cm⁻¹.

(2S,3R)-Boc-β-methyltryptophan (20). (2S,3R)-Boc-β-methyl-α-azido-indolepropanoic acid **19** (81 mg, 0.235 mmol, 1 eq) was dissolved in THF (2 mL), trimethylphosphine (1M in THF, 0.47 mL, 0.47 mmol, 2 eq) was added, and the reaction solution was stirred at room temperature under argon for 1 hr. H₂O was added (0.1 mL, 5.6 mmol, 24 eq) and this solution was stirred at room temperature for 14 hrs, after which it was concentrated *in vacuo*. The resulting solid was partially purified by flash chromatography (1% acetic acid in ethyl acetate to 5% acetic acid in 1:1 ethyl acetate/methanol) to give 18 mg (~24% yield) of crude product, which was carried on to the next step without further purification. ¹H NMR (300 MHz, CD₃OD) δ 8.14 (d, *J* = 8.1 Hz, 1H), 7.81 (d, *J* = 7.9 Hz, 1H), 7.55 (s, 1H), 7.34-7.26 (m, 2H), 3.98-3.89 (m, 2H), 1.68 (s, 9H), 1.41 (d, *J* = 7.1 Hz, 3H). ¹³C NMR (126 MHz, CD₃OD) δ 178.44, 150.99, 130.48, 125.89, 124.69, 123.89, 121.97, 120.16, 116.39, 85.05, 32.49, 28.40, 22.81, 13.03. HRMS (APCI/ESI+) calculated for [C₁₇H₂₃N₂O₄]⁺ ([M+H]⁺) 319.1658, found 319.1663.

(2S,3R)- β -methyltryptophan (21). Crude (2S,3R)-Boc- β -methyltryptophan **20** (18 mg, ~0.058 mmol) was suspended in H₂O and heated to 170°C for 3 min by microwave irradiation. The resulting solution was lyophilized to give 15.2 mg crude compound **21**, which was carried on to the next step without further purification. ¹H NMR (300 MHz, CD₃OD) δ 7.74 (d, *J* = 7.8 Hz, 1H), 7.37 (d, *J* = 7.9 Hz, 1H), 7.18 (s, 1H), 7.13 (t, *J* = 7.5 Hz, 1H), 7.05 (t, *J* = 7.5 Hz, 1H), 4.01-3.95 (m, 2H), 1.39 (d, *J* = 6.6 Hz, 3H). HRMS (APCI/ESI+) calculated for [C₁₂H₁₅N₂O₂]⁺ ([M+H]⁺) 219.1128, found 219.1148.

NVOC-(2S,3R)- β -methyltryptophan (22). Crude (2S,3R)- β -methyltryptophan **21** (15.2 mg, ~0.07 mmol, 1 eq) and Na₂CO₃ (36.9 mg, 0.348 mmol, 5 eq) were dissolved in a solution of water (1 mL) and dioxane (1 mL). This solution was cooled to 0°C, 6-nitroveratryloxycarbonyl (NVOC) chloride (19.3 mg, 0.07 mmol, 1 eq) was added, and the reaction solution was stirred at room temperature for 3 hrs. The reaction solution was poured into H₂O (15 mL) and washed with Et₂O (3x). The aqueous layer was acidified to pH = 1.5 with 6M HCl, then extracted (4x) with Et₂O. These combined Et₂O layers were dried over MgSO₄ and concentrated. The resulting solid was purified by flash chromatography (1% acetic acid in 1.5:1 dichloromethane/ethyl acetate) to give 12.7 mg crude compound **22**, which was carried on to the next step without further purification. HRMS (APCI/ESI-) calculated for [C₂₂H₂₄N₃O₈]⁻ ([M-H]⁻) 458.1558, found 458.1616.

NVOC-(2S,3R)- β -methyltryptophan cyanomethyl ester (23). Crude NVOC-(2S,3R)- β -methyltryptophan **22** (12.7 mg, ~0.028 mmol, 1 eq) was dissolved in DMF (0.2 mL) and chloroacetonitrile (0.2 mL, 3.16 mmol, 113 eq) under argon. Triethylamine (11.6 μ L, 0.083 mmol, 3 eq) was added and the reaction was stirred at room temperature for 2 hrs, then concentrated *in vacuo*. The resulting solid was partially purified by flash

chromatography (15:1 to 2.5:1 dichloromethane/ethyl acetate), and further purified by additional flash chromatography (1:10 to 1:2 ethyl acetate/hexanes), to yield compound **23** (6.3 mg, 5% yield over 4 steps from compound **19**). ^1H NMR (300 MHz, CDCl_3) δ 8.17 (s, 1H), 7.70 (s, 1H), 7.60 (d, J = 7.8 Hz, 1H), 7.38 (d, J = 8.0 Hz, 1H), 7.22 (t, J = 7.2 Hz, 1H), 7.13 (t, J = 7.4 Hz, 1H), 7.08 (d, J = 2.4 Hz, 1H), 6.91 (s, 1H), 5.56-5.38 (m, 3H), 4.75 (dd, J = 8.7, 6.1 Hz, 1H), 4.56 (q, J = 15.6 Hz, 2H), 3.95 (s, 3H), 3.90 (s, 3H), 3.72-3.63 (m, 1H), 1.52 (d, J = 7.2 Hz, 3H). ^{13}C NMR (126 MHz, CDCl_3) δ 170.61, 155.58, 153.76, 148.31, 139.83, 136.37, 127.83, 126.55, 122.71, 122.03, 120.05, 118.66, 115.34, 113.88, 111.70, 110.13, 108.32, 64.23, 59.24, 56.60, 56.56, 48.75, 34.04, 17.18. HRMS (APCI/ESI+) calculated for $[\text{C}_{24}\text{H}_{25}\text{N}_4\text{O}_8]^+$ ($[\text{M}+\text{H}]^+$) 497.1667, found 497.1677.

NVOC-(2S,3R)- β -methylTrp-dCA (24). dCA•2.2 TBA (10 mg, 8.6 μmol , 1 eq) and NVOC-(2S,3R)- β -methyltryptophan cyanomethyl ester **23** were dissolved in DMF (0.135 mL) and stirred at room temperature for 40 hrs under argon. The reaction was purified by HPLC to yield compound **24** (283 μg , 3% yield). MALDI-MS calculated for $[\text{C}_{41}\text{H}_{48}\text{N}_{11}\text{O}_{20}\text{P}_2]^+$ ($[\text{M}+\text{H}]^+$) 1076.25, found 1076.65.

NVOC-*tert*-leucine cyanomethyl ester. *Tert*-leucine (Aldrich) was NVOC-protected and activated as a cyanomethyl ester by standard procedures. ^1H NMR (300 MHz, CDCl_3) δ 7.71 (s, 1H), 6.96 (s, 1H), 5.52 (d, J = 3.6 Hz, 2H), 5.41 (d, J = 9.4 Hz, 1H), 4.77 (dd, J = 53.3, 15.6 Hz, 2H), 4.25 (d, J = 9.4 Hz, 1H), 3.99 (s, 3H), 3.95 (s, 3H), 1.04 (s, 9H). ^{13}C NMR (126 MHz, CDCl_3) δ 170.63, 155.74, 153.71, 148.33, 139.89, 127.74, 113.89, 110.12, 108.31, 64.27, 62.18, 56.61, 56.55, 48.61, 34.94, 26.60.

NVOC-*tert*-leucine-dCA. Prepared from NVOC-*tert*-leucine cyanomethyl ester by standard methods as for compound **24**. MALDI-MS calculated for $[C_{35}H_{47}N_{10}O_{20}P_2]^+$ ($[M+H]^+$) 989.24, found 989.68.

3.6 References

1. Schwartz, T. W., Frimurer, T. M., Holst, B., Rosenkilde, M. M. & Elling, C. E. Molecular mechanism of 7TM receptor activation-a global toggle switch model. *Annu Rev Pharmacol Toxicol* **46**, 481–519 (2006).
2. Hubbell, W. L., Altenbach, C., Hubbell, C. M. & Khorana, H. G. Rhodopsin structure, dynamics, and activation: a perspective from crystallography, site-directed spin labeling, sulfhydryl reactivity, and disulfide cross-linking. *Adv Protein Chem* **63**, 243–290 (2003).
3. Wess, J., Han, S. J., Kim, S. K., Jacobson, K. A. & Li, J. H. Conformational changes involved in G-protein-coupled-receptor activation. *Trends Pharmacol Sci* **29**, 616–625 (2008).
4. Gether, U. *et al.* Agonists induce conformational changes in transmembrane domains III and VI of the beta2 adrenoceptor. *EMBO J* **16**, 6737–6747 (1997).
5. Palczewski, K. *et al.* Crystal structure of rhodopsin: A G protein-coupled receptor. *Science* **289**, 739–745 (2000).
6. Scheerer, P. *et al.* Crystal structure of opsin in its G-protein-interacting conformation. *Nature* **455**, 497–502 (2008).
7. Cherezov, V. *et al.* High-resolution crystal structure of an engineered human beta2-adrenergic G protein-coupled receptor. *Science* **318**, 1258–1265 (2007).
8. Rasmussen, S. G. *et al.* Crystal structure of the beta2 adrenergic receptor-Gs protein complex. *Nature* **477**, 549–555 (2011).
9. Ballesteros, J. A. & Weinstein, H. Integrated Methods for the Construction of Three-Dimensional Models and Computational Probing of Structure-Function Relations in G Protein-Coupled Receptors. *Methods in Neurosciences* **25**, 366–428 (1995).
10. Visiers, I., Ballesteros, J. A. & Weinstein, H. Three-dimensional representations of G protein-coupled receptor structures and mechanisms. *Meth. Enzymol.* **343**, 329–371 (2002).
11. Shi, L. *et al.* Beta2 adrenergic receptor activation. Modulation of the proline kink in transmembrane 6 by a rotamer toggle switch. *J. Biol. Chem.* **277**, 40989–40996 (2002).
12. Chabre, M. & Breton, J. Orientation of aromatic residues in rhodopsin. Rotation of one tryptophan upon the meta I to meta II transition after illumination. *Photochem Photobiol* **30**, 295–299 (1979).
13. Crocker, E. *et al.* Location of Trp265 in metarhodopsin II: implications for the activation mechanism of the visual receptor rhodopsin. *J Mol Biol* **357**, 163–172

- (2006).
14. Holst, B. *et al.* A conserved aromatic lock for the tryptophan rotameric switch in TM-VI of seven-transmembrane receptors. *J. Biol. Chem.* **285**, 3973–3985 (2010).
 15. Li, J., Jonsson, A. L., Beuming, T., Shelley, J. C. & Voth, G. A. Ligand-Dependent Activation and Deactivation of the Human Adenosine A2A Receptor. *J. Am. Chem. Soc.* **135**, 8749–8759 (2013).
 16. Choe, H. W. *et al.* Crystal structure of metarhodopsin II. *Nature* **471**, 651–655 (2011).
 17. Xu, F. *et al.* Structure of an agonist-bound human A2A adenosine receptor. *Science* **332**, 322–327 (2011).
 18. Haga, K. *et al.* Structure of the human M2 muscarinic acetylcholine receptor bound to an antagonist. *Nature* **482**, 547–551 (2012).
 19. Taly, A. *et al.* Normal mode analysis suggests a quaternary twist model for the nicotinic receptor gating mechanism. *Biophys J* **88**, 3954–3965 (2005).
 20. Hilf, R. J. C. & Dutzler, R. Structure of a potentially open state of a proton-activated pentameric ligand-gated ion channel. *Nature* **457**, 115–118 (2009).
 21. Bocquet, N. *et al.* X-ray structure of a pentameric ligand-gated ion channel in an apparently open conformation. *Nature* **457**, 111–114 (2009).
 22. Hilf, R. J. C. & Dutzler, R. X-ray structure of a prokaryotic pentameric ligand-gated ion channel. *Nature* **452**, 375–379 (2008).
 23. Dacosta, C. J. B. & Baenziger, J. E. Gating of pentameric ligand-gated ion channels: structural insights and ambiguities. *Structure* **21**, 1271–1283 (2013).
 24. Li, S. X. *et al.* Ligand-binding domain of an alpha7-nicotinic receptor chimera and its complex with agonist. *Nat Neurosci* **14**, 1253–1259 (2011).
 25. Unwin, N. & Fujiyoshi, Y. Gating movement of acetylcholine receptor caught by plunge-freezing. *J Mol Biol* **422**, 617–634 (2012).
 26. Unwin, N. Refined structure of the nicotinic acetylcholine receptor at 4 Å resolution. *Journal of Molecular Biology* **346**, 967–989 (2005).
 27. Hruby, V. J., Li, G., Haskell-Luevano, C. & Shenderovich, M. Design of peptides, proteins, and peptidomimetics in chi space. *Biopolymers* **43**, 219–266 (1997).
 28. Chien, E. Y. *et al.* Structure of the human dopamine D3 receptor in complex with a D2/D3 selective antagonist. *Science* **330**, 1091–1095 (2010).
 29. Chen, S., Lin, F., Xu, M., Riek, R. P. & Novotny, J. Mutation of a single TMVI residue, Phe282, in the β2-adrenergic receptor results in structurally distinct activated receptor conformations. *Biochemistry* (2002).
 30. Valentin-Hansen, L., Holst, B., Frimurer, T. M. & Schwartz, T. W. PheVI:09 (Phe6.44) as a Sliding Microswitch in Seven-transmembrane (7TM) G Protein-coupled Receptor Activation. *J. Biol. Chem.* **287**, 43516–43526 (2012).
 31. Spalding, T. A., Burstein, E. S., Henderson, S. C., Ducote, K. R. & Brann, M. R. Identification of a ligand-dependent switch within a muscarinic receptor. *J. Biol. Chem.* **273**, 21563–21568 (1998).
 32. Chen, S., Lin, F., Xu, M. & Graham, R. M. Phe(303) in TMVI of the alpha(1B)-adrenergic receptor is a key residue coupling TM helical movements to G-protein activation. *Biochemistry* **41**, 588–596 (2002).
 33. Gilchrist, T. L., Lingham, D. A. & Roberts, T. G. Ethyl 3-bromo-2-hydroxyiminopropanoate, a reagent for the preparation of ethyl esters of α-amino

- acids. *Journal of the Chemical Society, Chemical Communications* (1979).
34. Daeffler, K. N. M., Lester, H. A. & Dougherty, D. A. Functionally Important Aromatic–Aromatic and Sulfur–π Interactions in the D2 Dopamine Receptor. *J. Am. Chem. Soc.* **134**, 14890–14896 (2012).
 35. Boteju, L. W., Wegner, K., Qian, X. H. & Hruby, V. J. Asymmetric-Synthesis of Unusual Amino-Acids - Synthesis of Optically Pure Isomers of N-Indole-(2-Mesitylenesulfonyl)-Beta-Methyltryptophan. *Tetrahedron* **50**, 2391–2404 (1994).
 36. Han, G. X., Lewis, A. & Hruby, V. J. Synthesis of (2S,3S)-beta-methyltryptophan. *Tetrahedron Lett* **42**, 4601–4603 (2001).
 37. Celie, P. H. *et al.* Nicotine and carbamylcholine binding to nicotinic acetylcholine receptors as studied in AChBP crystal structures. *Neuron* **41**, 907–914 (2004).
 38. Shapovalov, M. V. & Dunbrack, R. L., Jr. A Smoothed Backbone-Dependent Rotamer Library for Proteins Derived from Adaptive Kernel Density Estimates and Regressions. *Structure* **19**, 844–858 (2011).
 39. Torrice, M. M., Bower, K. S., Lester, H. A. & Dougherty, D. A. Probing the role of the cation-pi interaction in the binding sites of GPCRs using unnatural amino acids. *Proc. Natl. Acad. Sci. U.S.A.* **106**, 11919–11924 (2009).
 40. Gleitsman, K. R. Chemical-Scale Studies of the Nicotinic Acetylcholine Receptor: Insights from Amide-to-Ester Backbone Mutagenesis. (2010).
 41. Bešker, N. & Gervasio, F. L. Using metadynamics and path collective variables to study ligand binding and induced conformational transitions. *Methods Mol. Biol.* **819**, 501–513 (2012).
 42. Saks, M. E. *et al.* An engineered Tetrahymena tRNAGln for in vivo incorporation of unnatural amino acids into proteins by nonsense suppression. *J. Biol. Chem.* **271**, 23169–23175 (1996).
 43. Rodriguez, E. A., Lester, H. A. & Dougherty, D. A. Improved amber and opal suppressor tRNAs for incorporation of unnatural amino acids in vivo. Part 1: Minimizing misacylation. *Rna* **13**, 1703–1714 (2007).
 44. Rodriguez, E. A., Lester, H. A. & Dougherty, D. A. Improved amber and opal suppressor tRNAs for incorporation of unnatural amino acids in vivo. Part 2: evaluating suppression efficiency. *Rna* **13**, 1715–1722 (2007).
 45. Nowak, M. W. *et al.* In vivo incorporation of unnatural amino acids into ion channels in Xenopus oocyte expression system. *Meth. Enzymol.* **293**, 504–529 (1998).
 46. Curphey, T. J. Preparation of p-toluenesulfonyl azide. A cautionary note. *Organic Preparations and Procedures International* 112–115 (1981).
 47. Harmon, R. E., Wellman, G. & Gupta, S. K. Reaction of arylsulfonyl azides with N-methylindole. *J Org Chem* **38**, 11–16 (1973).

Chapter 4: Binding interactions to the complementary subunit of the $\alpha 4\beta 4$ receptor*

4.1 Abstract

The agonist binding site of nicotinic acetylcholine receptors (nAChRs) spans an interface between two subunits of the pentameric receptor. The principal component of this binding site is contributed by an α subunit, and it binds the cationic moiety of the nicotinic pharmacophore. The other part of the pharmacophore – a hydrogen bond acceptor – has recently been shown to bind to the complementary, non- α subunit, via the backbone NH of a conserved Leu. This interaction was predicted by studies of acetylcholine binding proteins (AChBPs) and confirmed by functional studies of the neuronal (CNS) nAChR, $\alpha 4\beta 2$. The AChBP structures further suggested that the hydrogen bond to the backbone NH was mediated by a water molecule, and that a second hydrogen bonding interaction occurs between the water molecule and the backbone CO of a conserved Asn, also on the non- α subunit. Here we provide new insights into the nature of the interactions between the hydrogen bond acceptor of nicotinic agonists and the complementary subunit backbone. We have studied both the nAChR of the neuromuscular junction (muscle-type) and a neuronal subtype, $(\alpha 4)_2(\beta 4)_3$. In the muscle-type receptor, both acetylcholine (ACh) and nicotine show a strong interaction with the Leu NH, but the potent nicotine analog epibatidine does not. This interaction is much attenuated in the $\alpha 4\beta 4$ receptor. Surprisingly, we find no evidence for a functionally significant interaction with the backbone carbonyl of the relevant Asn in either receptor with an array of agonists.

*This chapter is adapted from research previously published in the *Journal of Biological Chemistry*: Blum, A. P., Van Arnam, E. B., German, L. A., Lester, H. A., and Dougherty, D. A. Binding interactions to the complementary subunit of nicotinic receptors. *J. Biol. Chem.* (2013) **288**, 6991–6997. © the American Society for Biochemistry and Molecular Biology. The work described in this chapter was done in collaboration with Angela P. Blum and Laurel A. German, who conducted all of the muscle-type receptor experiments.

4.2 Introduction

nAChRs are pentamers, composed of five subunits arranged symmetrically around a central ion-conducting pore. Nicotinic agonists bind at subunit interfaces, and a combination of structure-function studies and structural studies of the acetylcholine binding proteins (AChBPs), which share considerable sequence homology with the ligand binding domain of the nAChR, have established a detailed binding model.¹⁻³ The α subunits contribute the principal component of the agonist binding site, which binds to the cationic end of agonists. This binding site is well-characterized, consisting of a cation- π interaction to one of several conserved aromatic residues and typically a hydrogen bond from the N⁺H of the drug to a backbone carbonyl.⁴⁻⁶ The natural agonist acetylcholine (ACh), which lacks the crucial N⁺H, does not participate in the latter interaction.

The complementary component of the agonist binding site is formed by non- α subunits, and recent work has shown that it involves a hydrogen bonding interaction to the hydrogen bond acceptor of agonists (e.g., the C=O of ACh or the pyridine N of nicotine; Figures 4.1 and 4.2). Crystal structures of AChBPs with several drugs bound produced a binding model in which two backbone features – a CO and an NH from amino acids that are 12 residues apart – coordinate a water molecule, which in turn hydrogen bonds to the hydrogen bond acceptor of agonists (Figure 4.1).^{2,7,8} In nAChRs the particular residues are an Asn and a Leu, and they are conserved across the family (Figure 4.3; they are a Leu and a Met, respectively, in the AChBP structure of Figure 4.1A). Since residue numbering varies among different receptors, we will refer to them simply as the Asn and the Leu sites, the former contributing a CO, the latter an NH to the

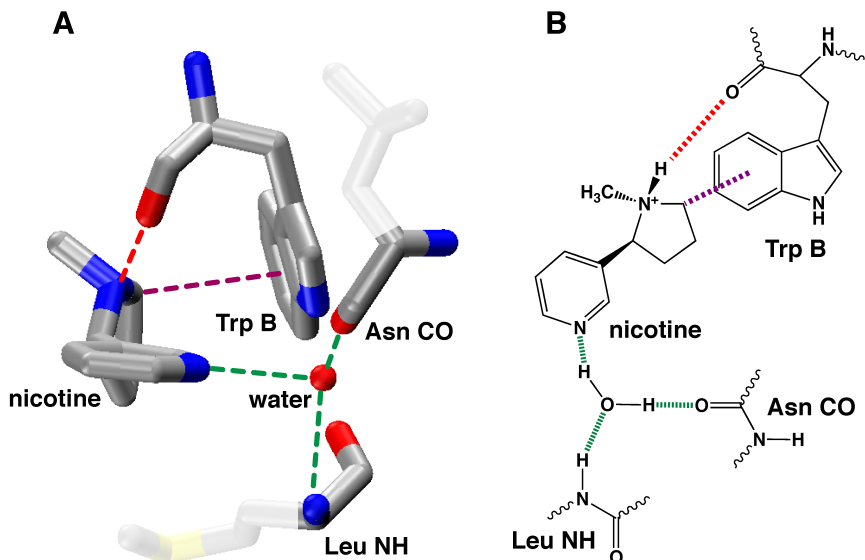


Figure 4.1. Proposed binding model for nicotine at nAChRs. **(A)** Crystal structure of nicotine bound to AChBP (1UW6). **(B)** Schematic of binding model, denoting key interactions probed here.

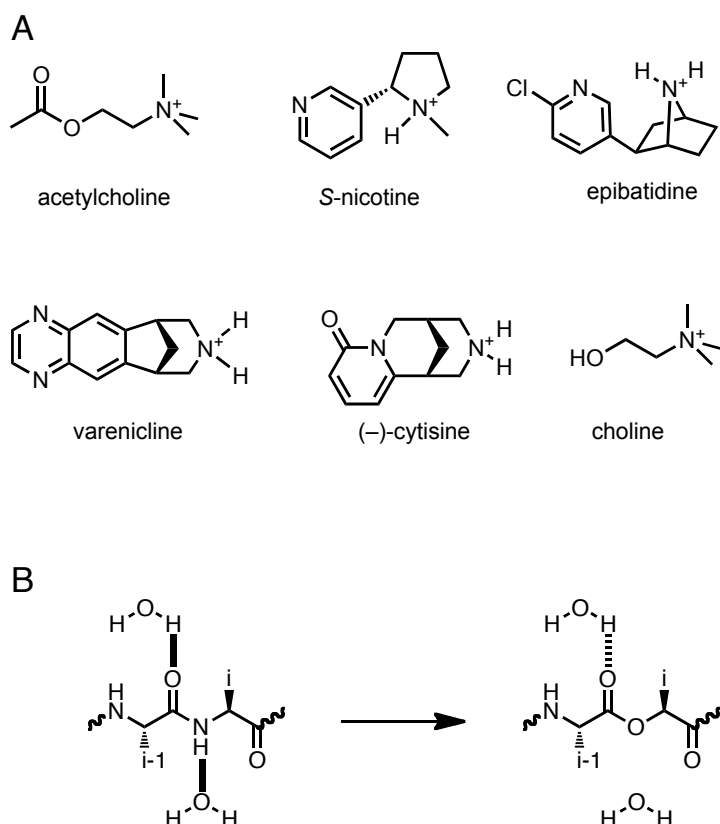


Figure 4.2. **(A)** Agonists used in this study. **(B)** Illustration of amide-to-ester mutation. Introduction of an α -hydroxy acid in place of an amino acid eliminates the hydrogen bond donor (backbone NH) of the i -residue and attenuates the hydrogen bond accepting ability of the i - β carbonyl. In this figure, the attenuated hydrogen bond is represented by a dashed line.

	104	123
rat $\beta 2$	F Y S <u>N</u> A V V S Y D G S I F W <u>L</u> P P A I	
human $\beta 4$	V Y T <u>N</u> L I V R S N G S V L W <u>L</u> P P A I	
mouse γ	L Y C <u>N</u> V L V S P D G C I Y W <u>L</u> P P A I	
mouse δ	Y A C <u>N</u> V L V Y D S G Y V T W <u>L</u> P P A I	
AChBP (<i>Lymnaea</i>)	T P Q L A R V V S D G E V L Y M P S I R	

Figure 4.3. Sequences of the complementary subunits considered here. The hydrogen bond-donating Leu and hydrogen bond-accepting Asn are highlighted. The key residues are highly conserved in other orthologs. Residue numbering is for the $\beta 2$ subunit.

proposed hydrogen bonding array; specific residue numbers are noted in the experimental section. Recent studies of the neuronal $\alpha 4\beta 2$ nAChR confirmed that the Leu NH of the $\beta 2$ subunit does hydrogen bond to the pyridine N of nicotine and to the carbonyl O of ACh.⁹

The present work expands these studies of hydrogen bonding interactions involving the complementary subunit in two ways. First, we consider two new receptor subtypes: a second neuronal form, $(\alpha 4)_2(\beta 4)_3$, henceforth referred to as $\alpha 4\beta 4$; and the form found at the neuromuscular junction of the peripheral nervous system, $(\alpha 1)_2\beta 1\gamma\delta$ (fetal form; in the adult variant the ϵ subunit replaces γ), which we will refer to as the muscle-type receptor. Note that the pharmacology of the muscle-type receptor is quite distinct from neuronal receptors such as $\alpha 4\beta 2$ and $\alpha 4\beta 4$, most importantly in the fact that nicotine is quite potent at these neuronal receptors but not at the receptors of the neuromuscular junction. This distinction allows smokers to become addicted to nicotine without adverse peripheral effects. Second, we evaluate the other component of the proposed hydrogen bonding model, the water-mediated hydrogen bond to the Asn carbonyl, in both the $\alpha 4\beta 4$ and the muscle-type receptors. Efforts to probe the Asn backbone carbonyl in the previously studied $\alpha 4\beta 2$ receptor were thwarted by technical

issues; the nonsense suppression methodology necessary for these studies was not selective/efficient enough for the present purposes.

Using unnatural amino acid mutagenesis we find key differences in the hydrogen bonding properties of specific drug-receptor combinations. Interestingly, we find no evidence for a functionally significant hydrogen bond to the Asn backbone carbonyl.

4.3 Results

4.3.1 General strategy

The two hydrogen bonding interactions being considered here both involve the protein backbone, and such interactions can be probed by incorporating α -hydroxy analogs of amino acids at appropriate locations (Figure 4.2B). As a probe of the Leu NH the strategy is straightforward: the backbone NH is replaced by an O. Concerning the backbone CO, α -hydroxy substitution attenuates the hydrogen bonding ability of the *i*-1 carbonyl by converting it to an ester carbonyl. It is well-established that the carbonyls of esters are much poorer hydrogen bond acceptors than those of amides. Interestingly, in many studies, both quantitative and qualitative, it has been shown that the two effects associated with backbone ester incorporation – removal of the NH hydrogen bond donor and attenuation of the CO hydrogen bond acceptor – can have similar energetic consequences.¹⁰⁻¹⁴ As such, to perturb the Asn CO we actually mutate the *i*+1 residue, which is Leu in the α 4 β 4 receptor and Val in the muscle-type receptor. Backbone ester mutations can be efficiently incorporated site-specifically into nAChRs expressed in *Xenopus* oocytes by nonsense suppression methodology.^{15,16} Typical experimental traces

and dose-response relations for unnatural amino acid mutagenesis experiments with these receptors have been reported previously.^{6,17}

These studies use EC₅₀, the effective agonist concentration needed to reach a half-maximal response, as a read-out of the functional impact of each mutation. It is well recognized that EC₅₀ is a composite measure, reflecting multiple equilibria that include both “binding” events – drug entering/exiting the agonist binding site – and “gating” events – the equilibria between open and closed states of the channel. It is typical in an EC₅₀ study to note an ambiguity as to whether a given mutation affects binding or gating. We would argue that in the present system, as in many similar previous studies from our lab, the ambiguity is of a different kind. Given the subtlety and precision of the modifications enabled by unnatural amino acid mutagenesis, combined with our structural knowledge of the binding site and the location of the mutations made, it is clear that we are perturbing a hydrogen bonding interaction between the drug and the receptor – a binding interaction. In order to see a change in EC₅₀, it must be true that the hydrogen bonding interaction is diminished (or enhanced) in one or more of the multiple equilibria noted above. In the studies presented here, the ambiguity in the EC₅₀ measurement concerns which *equilibrium* is perturbed, not the nature of the perturbation, which is clearly an attenuated binding interaction.

Detailed kinetic analyses, typically at the single channel level, can often determine which equilibrium step(s) is being perturbed. However, we consider EC₅₀ to be an appropriate metric here for two reasons. First, detailed, single-channel studies are not feasible for the large number of drug-receptor combinations that we have considered. This is especially so given the protein expression limitations that are sometimes seen with

unnatural amino acid mutagenesis. More importantly, our goal is to make pharmacological comparisons among closely related systems in response to subtle structural changes. We also wish to compare these results to those of previous studies on related systems. EC₅₀ is a good measure of pharmacological activity. Given our experience with these systems and unnatural amino acid mutagenesis in particular, we consider EC₅₀ differences of less than a factor of 2 to be not interpretable.

For studies of the muscle-type receptor we use the known L9'S mutation in the M2 transmembrane helix of the $\beta 1$ subunit (where 9' is the ninth amino acid from the cytoplasmic end of the M2 α -helix).^{18,19} This mutation is introduced to generically increase the sensitivity of the protein to agonists, and it results in a systematic ~40-fold decrease in EC₅₀. Given that the 9' position is ~60 Å away from the agonist binding site, this mutation is generally expected to primarily affect gating and not agonist binding, although complications can arise.²⁰ We have performed backbone ester mutagenesis of the Leu NH in the muscle-type receptor both in the absence and presence of the L9'S background mutation, and similar shifts in EC₅₀ were seen for ACh (Table 4.1). This confirms the viability of this strategy in the present system. The agonist concentrations that were required to obtain a dose-response relation for epibatidine, nicotine and choline in the absence of the L9'S mutation were high enough that channel block by the agonist became a problem with some mutants, so all comparisons for this receptor are done using the L9'S mutation. An analogous mutation was also used in the studies of $\alpha 4\beta 2$.⁵ No such modification was necessary for the $\alpha 4\beta 4$ receptor.

Table 4.1. Mutagenesis of the backbone NH (γ L119/ δ L121 mutations) and backbone CO (γ V108/ δ V110 mutations) of the muscle-type nAChR. EC₅₀ and Hill coefficient (n_H) are \pm SEM for goodness of fit to the Hill equation.

	Agonist	EC₅₀ (μM)	Fold Shift	n_H
wild type	ACh	16.0 \pm 0.3		1.3 \pm 0.1
γ L119Leu, δ L121Leu ^a	ACh	16.0 \pm 0.5		1.5 \pm 0.1
γ L119Lah, δ L121Lah	ACh	230 \pm 6	14	1.5 \pm 0.1
wild type ^b	ACh	0.61 \pm 0.04		1.4 \pm 0.1
γ L119Leu, δ L121Leu ^{a,b}	ACh	0.31 \pm 0.02		1.5 \pm 0.1
γ L119Lah, δ L121Lah ^b	ACh	9.1 \pm 0.7	29	1.6 \pm 0.2
wild type ^b	Choline	840 \pm 20		1.6 \pm 0.1
γ L119Leu, δ L121Leu ^{a,b}	Choline	780 \pm 30		1.7 \pm 0.1
γ L119Lah, δ L121Lah ^b	Choline	1000.00 \pm 0.05	1.3	1.8 \pm 0.1
wild type ^b	(\pm)-Epibatidine	0.32 \pm 0.02		1.5 \pm 0.1
γ L119Leu, δ L121Leu ^{a,b}	(\pm)-Epibatidine	0.40 \pm 0.02		1.5 \pm 0.1
γ L119Lah, δ L121Lah ^b	(\pm)-Epibatidine	0.52 \pm 0.03	1.3	1.6 \pm 0.1
wild type ^b	S-Nicotine	22.0 \pm 0.8		1.6 \pm 0.1
γ L119Leu, δ L121Leu ^{a,b}	S-Nicotine	23 \pm 0.7		1.7 \pm 0.1
γ L119Lah, δ L121Lah ^b	S-Nicotine	230 \pm 30	10	2.2 \pm 0.5
γ V108Val, δ V110Val ^{a,b}	ACh	0.29 \pm 0.01		1.3 \pm 0.1
γ V108Vah, δ V110Vah ^b	ACh	0.41 \pm 0.05	1.4	1.2 \pm 0.2
γ V108Val, δ V110Val ^{a,b}	Choline	620 \pm 20		1.4 \pm 0.1
γ V108Vah, δ V110Vah ^b	Choline	790 \pm 60	1.3	1.4 \pm 0.1
γ V108Val, δ V110Val ^{a,b}	(\pm)-Epibatidine	0.230 \pm 0.006		1.4 \pm 0.1
γ V108Vah, δ V110Vah ^b	(\pm)-Epibatidine	0.240 \pm 0.006	1.0	1.5 \pm 0.1
γ V108Val, δ V110Val ^{a,b}	S-Nicotine	15 \pm 1		1.2 \pm 0.1
γ V108Vah, δ V110Vah ^b	S-Nicotine	33 \pm 2	2.2	1.6 \pm 0.1

^aExpression of the wild type receptor with the natural amino acid incorporated by nonsense suppression

^bReceptor contains the β L9'S mutation

Table 4.2. Mutagenesis of the backbone NH (β L119 mutations) and backbone CO (β L108 mutations) of the $(\alpha 4)_2(\beta 4)_3$ nAChR. EC₅₀ and Hill coefficient (n_H) are \pm SEM for goodness of fit to the Hill equation.

	Drug	EC₅₀	Fold Shift	Hill
β 4L119Leu ^a	ACh	15.0 \pm 0.7		1.42 \pm 0.08
β 4L119Lah	ACh	43 \pm 4	2.9	1.5 \pm 0.2
β 4L119Leu ^a	S-Nicotine	2.1 \pm 0.2		1.3 \pm 0.1
β 4L119Lah	S-Nicotine	5.8 \pm 0.4	2.8	1.4 \pm 0.1
β 4L119Leu ^a	(\pm)-Epibatidine	0.0055 \pm 0.0001		1.80 \pm 0.05
β 4L119Lah	(\pm)-Epibatidine	0.01018 \pm 0.00009	1.9	1.63 \pm 0.02
β 4L119Leu ^a	Varenicline	0.133 \pm 0.002		1.37 \pm 0.02
β 4L119Lah	Varenicline	0.050 \pm 0.003	1 / 2.7	1.5 \pm 0.1
β 4L119Leu ^a	(-)-Cytisine	0.229 \pm 0.004		1.37 \pm 0.02
β 4L119Lah	(-)-Cytisine	3.1 \pm 0.1	14	1.37 \pm 0.05
β 4L119Leu ^a	Choline	1400 \pm 300		1.4 \pm 0.2
β 4L119Lah	Choline	2000 \pm 700	1.4	1.1 \pm 0.2
β 4L108Leu ^a	ACh	15.2 \pm 0.9		1.43 \pm 0.09
β 4L108Lah	ACh	13 \pm 2	1 / 1.2	1.2 \pm 0.2
β 4L108Leu ^a	S-Nicotine	1.9 \pm 0.2		1.3 \pm 0.1
β 4L108Lah	S-Nicotine	1.7 \pm 0.2	1 / 1.1	1.4 \pm 0.1
β 4L108Leu ^a	(\pm)-Epibatidine	0.0050 \pm 0.0002		1.70 \pm 0.08
β 4L108Lah	(\pm)-Epibatidine	0.0065 \pm 0.0002	1.3	1.71 \pm 0.08
β 4L108Leu ^a	Varenicline	0.120 \pm 0.004		1.38 \pm 0.05
β 4L108Lah	Varenicline	0.24 \pm 0.01	2.0	1.19 \pm 0.05
β 4L108Leu ^a	(-)-Cytisine	0.227 \pm 0.005		1.42 \pm 0.04
β 4L108Lah	(-)-Cytisine	0.139 \pm 0.007	1 / 1.6	1.40 \pm 0.08
β 4L108Leu ^a	Choline	1200 \pm 70		1.62 \pm 0.09
β 4L108Lah	Choline	1100 \pm 100	1 / 1.1	1.4 \pm 0.1

^aExpression of the wild type receptor with the natural amino acid incorporated by nonsense suppression

4.3.2 Mutagenesis studies of the Leu NH

To probe for the presumed hydrogen bond to the Leu backbone NH, the leucine (γ L119/ δ L121 in the muscle-type receptor, β L119 in the $\alpha 4\beta 4$ receptor) was replaced with its α -hydroxy acid analog (leucine, α -hydroxy; Lah). In the muscle-type receptor, ACh and nicotine both showed substantial increases in EC₅₀, (Table 4.1) confirming that the backbone NH is important for receptor activation by these agonists. Surprisingly, epibatidine, a nicotine analog that is quite potent at the muscle-type nAChR (although

~300-fold less so than at the $\alpha 4\beta 2$ subtype), was unresponsive to the backbone ester mutation. This contrasts the 5-fold increase in EC₅₀ seen in the $\alpha 4\beta 2$ receptor for the analogous mutation with epibatidine as agonist. As expected, choline, which lacks the CO that serves as the hydrogen bond acceptor, was unresponsive to the backbone mutation, giving no shift in EC₅₀ upon incorporation of the α -hydroxy acid.

Surprisingly, the analogous Leu to Lah mutation in $\alpha 4\beta 4$ showed small to negligible effects for ACh, nicotine, epibatidine, varenicline, and (as expected) choline (Table 4.2). Cytisine does show a large response, establishing that the Leu NH can function as a hydrogen bond donor to an agonist in the $\alpha 4\beta 4$ receptor.

4.3.3 Mutagenesis studies of the Asn CO

The second hydrogen bond predicted by the AChBP structures is to the backbone CO of a conserved Asn. To probe for a hydrogen bond to this backbone CO, the *i+1* residue, $\gamma V108/\delta V110$ in the muscle-type receptor and $\beta L108$ in $\alpha 4\beta 4$, is replaced with its α -hydroxy acid analog (valine, α -hydroxy; Vah for Val or Lah for Leu). As discussed above, this converts a backbone amide to a backbone ester, thereby attenuating the hydrogen bond-accepting ability of this moiety.

Early efforts to probe the CO of the relevant Asn residue in the $\alpha 4\beta 2$ receptor gave inconsistent results that led us to question whether we could reliably control the stoichiometry of the mutant receptor.²¹ Since the muscle-type receptor reliably assembles into just one stoichiometry (($\alpha 1$)₂ $\beta 1\gamma\delta$), we anticipated that comparable experiments would experience fewer complications, and, indeed, nonsense suppression studies at the

appropriate Val gave functional mutant receptors. However, ACh, nicotine, epibatidine, and choline were not significantly impacted by the backbone ester mutation (Table 4.1).

With the experience gained from the muscle-type receptor, we were able to probe the key Asn carbonyl in a neuronal receptor, $\alpha 4\beta 4$. Again, we find no evidence for a meaningful interaction with the carbonyl for the agonists ACh, nicotine, epibatidine, varenicline, cytisine, and choline (Table 4.2).

4.4 Discussion

In recent years, the well-studied nicotinic pharmacophore, comprised of a cationic N and a hydrogen bond acceptor,²² has been mapped onto specific binding interactions in the nAChR (Figure 4.1). The cationic N binds to the principal component of the agonist binding site in the α subunit, and the hydrogen bond acceptor binds to the complementary, non- α subunit. Guided by structures of AChBP, backbone mutagenesis studies established a hydrogen bond between the pharmacophore acceptor (pyridine N of nicotine; carbonyl O of ACh) and a Leu backbone NH in the $\alpha 4\beta 2$ neuronal nAChR. It is important to note that it is not just the rise in EC₅₀ resulting from backbone mutation that establishes a hydrogen bond. In all cases, choline, which lacks the hydrogen bond acceptor of the other agonists, is unaffected by the backbone mutation, proving a direct link between the mutation and the hydrogen bond acceptor of agonists. In our previous experiments with the $\alpha 4\beta 2$ subtype, we also studied the nicotine analog S-N-methyl-2-phenylpyrrolidine (S-MPP).⁹ In this structure, the pyridyl ring of nicotine is replaced with a phenyl ring, providing an alternative way to probe the hydrogen bond-accepting

pyridine N. This is a more subtle probe than the ACh/Ch comparison, and it provided a compelling link between the hydrogen bond acceptor of nicotine and the backbone NH in the $\alpha 4\beta 2$ receptor. In the present systems, we were unable to perform comparable studies with S-MPP, because the low potency of this compound at the receptors considered here required agonist concentrations that produced competing channel block of the receptor in dose-response studies. Nevertheless, the studies of the $\alpha 4\beta 2$ receptor provide support for the notion that mutations of the Leu NH are perturbing a hydrogen bond to the agonist.

It is worth emphasizing that, while we consider the present work to probe hydrogen bonding interactions, we are in fact probing the functional significance of particular hydrogen bonds. Thus, it is possible that a structural study could show the presence of a hydrogen bond, but if deleting/attenuating that hydrogen bond has no functional consequence, it would show up as no hydrogen bond in our assay. We first discuss our findings concerning the contribution of the Leu backbone NH.

ACh and nicotine both show a strong hydrogen bonding interaction with the Leu backbone NH in the muscle-type receptor. Nicotine shows very poor potency at the wild-type muscle receptor, and so we were surprised to find that nicotine is very sensitive to the Leu backbone ester mutation, more sensitive than it is to the corresponding mutation in $\alpha 4\beta 2$, where nicotine is a very potent agonist. This mutation also impacted ACh potency much more in the muscle-type receptor than in the $\alpha 4\beta 2$ receptor. We have performed similar backbone mutations at locations throughout the nAChR to probe for various hydrogen bonds, and we typically see informative, but modest increases in EC₅₀ of ~5-20-fold. The 29-fold increase in EC₅₀ seen for ACh in the muscle-type receptor is among the largest responses we have seen for a backbone ester mutation. It is also much

larger than the 7-fold increase that was seen for the equivalent mutation in the $\alpha 4\beta 2$ receptor.⁹ These results may suggest that the hydrogen bond to the Leu NH is stronger in the muscle-type receptor, and it is possible that ACh and nicotine sit more closely to this residue in the muscle-type receptor than they do in the $\alpha 4\beta 2$ subtype. As expected, choline as an agonist is unresponsive to this mutation.

Surprisingly, epibatidine, a potent agonist at the muscle-type receptor, is unresponsive to the Leu backbone NH mutation. In crystal structures of AChBP binding nicotine or epibatidine, the relative positioning of all relevant atoms – the pyridine N and the backbone NH and CO – are essentially identical. As such, it has been assumed that these two closely related molecules bind in the same way, even though the bridging water is not observable in the epibatidine structure, presumably because it is not ordered enough for the relatively low resolution structure.

One possible explanation for the lack of a functionally significant hydrogen bonding interaction with the pyridine N of epibatidine in the muscle-type receptor is that the N is a relatively poor hydrogen bond acceptor. When considering closely related systems, pKa is an excellent predictor of hydrogen bonding ability. Pyridine, a good model for nicotine, has a pKa of 5.2, but 2-chloropyridine, a model for epibatidine, has a much lower pKa of 0.5.²³ Thus, epibatidine is expected to be a poorer base than nicotine by ~5 orders of magnitude, and it is safe to conclude that epibatidine would also be a much poorer hydrogen bond acceptor. Recently we have showed that varenicline, the smoking cessation compound marketed as Chantix®, is similarly unresponsive to the analogous backbone NH mutation in the $\alpha 4\beta 2$ receptor.²⁴ The quinoxaline nitrogens of varenicline have a pKa of 0.8, quite similar to that for epibatidine. Thus, in these two

very potent nicotinic agonists – epibatidine and varenicline – the strength of the hydrogen bond acceptor is expected to be greatly attenuated, and our functional assay for this hydrogen bond appears to reflect this property.

When we probe the Leu backbone NH interaction in the $\alpha 4\beta 4$ receptor, we find a much smaller impact of the backbone mutation. ACh and nicotine show meaningful, but much smaller effects than is usual; in $\alpha 4\beta 2$ receptors the effect ranged from 5.6- to 8.5-fold for the same agonists. Again, epibatidine shows no meaningful effect and varenicline actually shows a small gain of function. Cytisine, another compound that is marketed for smoking cessation under the brand name Tabex®, shows a large effect. The hydrogen bond acceptor in cytisine is not a pyridine-type N, but is rather the O of an amide carbonyl. Amides are much stronger hydrogen bond acceptors, and, indeed, we saw very large effects for cytisine at the $\alpha 4\beta 2$ receptor. For the two stoichiometries of $\alpha 4\beta 2$ – 2:3 and 3:2 – the backbone NH mutation led to perturbations of 62- and 14-fold, respectively, with cytisine as the agonist.

The second component of the interaction with the hydrogen bond acceptor of nicotinic agonists predicted by AChBP structures is the water-mediated hydrogen bond to the Asn backbone CO. Using the backbone ester strategy to perturb this proposed interaction, we measured 9 different drug-receptor interactions involving two different receptors, and in no case do we see a meaningful interaction (not including choline, for which no effect is expected). The strongest effects are for varenicline at $\alpha 4\beta 4$, with a ratio of 2.0, and for nicotine at the muscle-type receptor, with a ratio of 2.2, barely what we consider to be meaningful. All other effects are less than a factor of two.

Note that the strategy employed here to probe a hydrogen bond to a backbone carbonyl can produce large effects. In nicotinic receptors when we use the strategy to probe the interaction of the N⁺H of the drug to the backbone carbonyl of the key Trp residue of the binding site (Figure 4.1), we see EC50 shifts ranging from 9- to 27-fold for potent drug-receptor combinations.

We thus conclude that the water-mediated interaction between the hydrogen bond acceptor of agonists and the Asn backbone CO seen in AChBP structures is not functionally significant in nAChRs in general. We note that there is a fundamental distinction between the two hydrogen bonds seen in AChBP. If the water molecule were not present, the Leu backbone NH could donate a hydrogen bond directly to the hydrogen bond acceptor of agonists. In contrast, the Asn backbone CO is itself a hydrogen bond acceptor, and so it can interact with the hydrogen bond acceptor of agonists only through an intermediary water. Our results thus open up the possibility that the water molecule that is seen in essentially all AChBP structures is not present in actual receptors. Whether the water molecule is or is not present, we find that perturbing its putative hydrogen bonding partner has little consequence on receptor function.

In the pharmacology of nicotinic receptors, it has often been suggested that the non- α , complementary subunit plays a key role in establishing subtype selectivity for various drugs. We have now probed the complementary binding site for four nicotinic subtypes (muscle-type, $\alpha 4\beta 4$, and both stoichiometries of $\alpha 4\beta 2$), and see interesting variations for particular drug-receptor combinations. We believe this information will be of value to efforts to develop more selective drugs that target nicotinic receptors.

We have shown that ACh and nicotine both engage in a functionally important hydrogen bond to the complementary subunit Leu backbone NH in the muscle-type nAChR, but the nicotine analog epibatidine does not. In the $\alpha 4\beta 4$ receptor, interactions with the Leu backbone NH are surprisingly weak. We also find no evidence for a functionally important water-mediated hydrogen bond to the Asn backbone CO. Our results highlight the necessity of functional studies on intact receptors to probe interactions suggested by structural studies of model systems.

4.5 Experimental

4.5.1 Mutagenesis

Nonsense suppression was performed using techniques described previously on the mouse muscle embryonic nAChR, $(\alpha 1)_2\beta 1\gamma\delta$, in the pAMV vector⁵ and human $(\alpha 4)_2(\beta 4)_3$ receptor in the pGEMhe vector. For nonsense suppression experiments, a TAG (for mutation at γ V108/8V110) or TGA stop codon (for mutation at γ L119/ δ L121, β 4L108, and β 4L119) was introduced at the site of interest by the standard Stratagene QuickChange protocol and verified through sequencing. The $\beta 1$ subunit contains a background mutation in the transmembrane M2 helix ($\beta 1$ L9'S) that is known to lower whole-cell EC₅₀ values. The $\alpha 1$ subunit contains a hemagglutinin epitope in the M3-M4 cytoplasmic loop that does not alter EC₅₀ values in control experiments. cDNA was linearized with the restriction enzyme NotI for muscle-type receptor subunits and NheI for $\alpha 4$ and $\beta 4$. mRNA was prepared by *in vitro* transcription using the mMessage Machine T7 kit (Ambion).

4.5.2 Microinjection

Stage V-VI *Xenopus laevis* oocytes were injected with mRNA in a 10:1:1:1 or 1:1:5:5 ratio of α 1: β 1: γ : δ for wild-type/conventional mutagenesis or nonsense suppression experiments, respectively, on the muscle-type receptor. An mRNA ratio of 1:20 (α 4: β 4) was used for nonsense suppression experiments on the $(\alpha$ 4)₂(β 4)₃ receptor. Control nonsense suppression experiments confirmed that this ratio ensures a 2:3 subunit stoichiometry. α -Hydroxy acids and amino acids were appended to the dinucleotide dCA and enzymatically ligated to the truncated 74-nucleotide amber suppressor tRNA THG73 or opal suppressor tRNA TQOpS' as previously described.⁵ For wild-type or conventional mutagenesis experiments on the muscle-type receptor, 1-2 ng of mRNA was injected per oocyte in a single 75 nL injection. For nonsense suppression experiments on the muscle-type receptor, each cell was injected with 75 nL of a 1:1 mixture of mRNA (20-25 ng of total mRNA) and tRNA (10-25 ng). For nonsense suppression experiments on the $(\alpha$ 4)₂(β 4)₃ receptor, each cell was injected with 50 nL of a 1:1 mixture of mRNA (50 ng total) and tRNA (~25 ng). Amino acids bearing a 6-nitroveratryloxycarbonyl protecting group were deprotected prior to injection via irradiation with a 500 W Hg/Xe arc lamp, filtered with WG-334 and UG-11 filters prior to injection. Oocytes were incubated at 18 °C for 16-20 or 24-48 hours after injection for the wild-type/conventional mutagenesis or nonsense suppression experiments, respectively, on the muscle-type receptor. Oocytes were incubated for 48 hours after injection for nonsense suppression experiments on the $(\alpha$ 4)₂(β 4)₃ receptor. Wild-type recovery control experiments (injection of tRNA appended to the natural amino acid) were performed to evaluate the fidelity of the nonsense suppression experiments. In additional control experiments on

the muscle-type receptor, injections of mRNA only and mRNA with 76-mer THG73 or TQOpS' gave minimal currents in electrophysiology experiments (~100 nA or less for controls compared to >>2 μ A for nonsense suppression experiments). For the $(\alpha 4)_2(\beta 4)_3$ receptor, injections of mRNA with 76-mer TQOpS' gave no detectable currents.

4.5.3 Electrophysiology

Two-electrode voltage clamp electrophysiology was used to measure the functional effects of each mutation. Electrophysiology recordings were performed after injection and incubation as described above using the OpusXpress 6000A (Axon Instruments) at a holding potential of -60 mV. The running buffer was a Ca^{2+} free ND96 solution (96 mM NaCl, 2 mM KCl, 1 mM MgCl_2 , and 5 mM HEPES, pH 7.5). Agonist doses in Ca^{2+} -free ND96 were applied for 15 s followed by a 116 s wash with the running buffer. Acetylcholine chloride, (-)-nicotine tartrate, and (-)-cytisine were purchased from Sigma-Aldrich/RBI, (\pm)-epibatidine was purchased from Tocris, and varenicline tartrate was a generous gift from Pfizer. Dose-response data were obtained for ≥ 8 agonist concentrations on ≥ 8 cells. Dose-response relations were fit to the Hill equation to obtain EC_{50} and Hill coefficient values, which are reported as averages \pm standard error of the fit.

4.6 References

1. Brejc, K. *et al.* Crystal structure of an ACh-binding protein reveals the ligand-binding domain of nicotinic receptors. *Nature* **411**, 269–276 (2001).
2. Celie, P. H. *et al.* Nicotine and carbamylcholine binding to nicotinic acetylcholine receptors as studied in AChBP crystal structures. *Neuron* **41**, 907–914 (2004).
3. Sixma, T. K. & Smit, A. B. Acetylcholine binding protein (AChBP): a secreted glial protein that provides a high-resolution model for the extracellular domain of

- pentameric ligand-gated ion channels. *Annu. Rev. Biophys. Biomol. Struct.* **32**, 311–334 (2003).
4. Cashin, A. L., Petersson, E. J., Lester, H. A. & Dougherty, D. A. Using physical chemistry to differentiate nicotinic from cholinergic agonists at the nicotinic acetylcholine receptor. *J. Am. Chem. Soc.* **127**, 350–356 (2005).
 5. Xiu, X., Puskar, N. L., Shanata, J. A., Lester, H. A. & Dougherty, D. A. Nicotine binding to brain receptors requires a strong cation-pi interaction. *Nature* **458**, 534–537 (2009).
 6. Zhong, W. *et al.* From ab initio quantum mechanics to molecular neurobiology: a cation-pi binding site in the nicotinic receptor. *Proc. Natl. Acad. Sci. U.S.A.* **95**, 12088–12093 (1998).
 7. Hansen, S. B. *et al.* Structures of Aplysia AChBP complexes with nicotinic agonists and antagonists reveal distinctive binding interfaces and conformations. *EMBO J* **24**, 3635–3646 (2005).
 8. Hansen, S. B. *et al.* Structural characterization of agonist and antagonist-bound acetylcholine-binding protein from Aplysia californica. *J. Mol. Neurosci.* **30**, 101–102 (2006).
 9. Blum, A. P., Lester, H. A. & Dougherty, D. A. Nicotinic pharmacophore: the pyridine N of nicotine and carbonyl of acetylcholine hydrogen bond across a subunit interface to a backbone NH. *Proc. Natl. Acad. Sci. U.S.A.* **107**, 13206–13211 (2010).
 10. Deechongkit, S. *et al.* Context-dependent contributions of backbone hydrogen bonding to beta-sheet folding energetics. *Nature* **430**, 101–105 (2004).
 11. Deechongkit, S., Dawson, P. E. & Kelly, J. W. Toward assessing the position-dependent contributions of backbone hydrogen bonding to beta-sheet folding thermodynamics employing amide-to-ester perturbations. *J. Am. Chem. Soc.* **126**, 16762–16771 (2004).
 12. England, P. M., Zhang, Y., Dougherty, D. A. & Lester, H. A. Backbone mutations in transmembrane domains of a ligand-gated ion channel: implications for the mechanism of gating. *Cell* **96**, 89–98 (1999).
 13. Gleitsman, K. R., Kedrowski, S. M., Lester, H. A. & Dougherty, D. A. An intersubunit hydrogen bond in the nicotinic acetylcholine receptor that contributes to channel gating. *J. Biol. Chem.* **283**, 35638–35643 (2008).
 14. Koh, J. T., Cornish, V. W. & Schultz, P. G. An experimental approach to evaluating the role of backbone interactions in proteins using unnatural amino acid mutagenesis. *Biochemistry* **36**, 11314–11322 (1997).
 15. Nowak, M. W. *et al.* In vivo incorporation of unnatural amino acids into ion channels in Xenopus oocyte expression system. *Meth. Enzymol.* **293**, 504–529 (1998).
 16. Nowak, M. W. *et al.* Nicotinic receptor binding site probed with unnatural amino acid incorporation in intact cells. *Science* **268**, 439–442 (1995).
 17. Puskar, N. L., Xiu, X., Lester, H. A. & Dougherty, D. A. Two neuronal nicotinic acetylcholine receptors, alpha4beta4 and alpha7, show differential agonist binding modes. *J. Biol. Chem.* **286**, 14618–14627 (2011).
 18. Labarca, C. *et al.* Channel gating governed symmetrically by conserved leucine residues in the M2 domain of nicotinic receptors. *Nature* **376**, 514–516 (1995).

19. Filatov, G. N. & White, M. M. The role of conserved leucines in the M2 domain of the acetylcholine receptor in channel gating. *Mol Pharmacol* **48**, 379–384 (1995).
20. Gleitsman, K. R., Shanata, J. A., Frazier, S. J., Lester, H. A. & Dougherty, D. A. Long-range coupling in an allosteric receptor revealed by mutant cycle analysis. *Biophys J* **96**, 3168–3178 (2009).
21. Blum, A. P. Structure-Function Studies of Nicotinic Acetylcholine Receptors Using Unnatural Amino Acid Analogs and Synthetic Agonist Analogs. (2011).
22. Beers, W. H. & Reich, E. Structure and activity of acetylcholine. *Nature* **228**, 917–922 (1970).
23. Linnell, R. Dissociation Constants of 2-Substituted Pyridines. *J Org Chem* **25**, 290 (1960).
24. Da Silva Tavares, X. *et al.* Variations in binding among several agonists at two stoichiometries of the neuronal, alpha4beta2 nicotinic receptor. *J. Am. Chem. Soc.* **134**, 11474–11480 (2012).

Chapter 5: An unusual pattern of ligand-receptor interactions for the $\alpha 7$ nicotinic acetylcholine receptor, with implications for the binding of varenicline*

5.1 Abstract

The $\alpha 7$ nicotinic acetylcholine receptor shows broad pharmacology, complicating the development of subtype-specific nicotinic receptor agonists. Here we use unnatural amino acid mutagenesis to characterize binding to $\alpha 7$ by the smoking cessation drug varenicline (Chantix), an $\alpha 4\beta 2$ -targeted agonist that shows full efficacy and modest potency at the $\alpha 7$ receptor. We find that unlike binding to its target receptor, varenicline does not form a cation- π interaction with TrpB, further supporting a unique binding mode for the cationic amine of nicotinic agonists at the $\alpha 7$ receptor. We also evaluate binding to the complementary face of the receptor's binding site by varenicline, the endogenous agonist acetylcholine, and the potent nicotine analog epibatidine. Interestingly, we find no evidence for functionally significant interactions involving backbone NH and CO groups thought to bind the canonical agonist hydrogen bond acceptor of the nicotinic pharmacophore, perhaps reflecting a lesser importance of this pharmacophore element for $\alpha 7$ binding. We also show that the Trp55 and Leu119 side chains of the binding site's complementary face are important for the binding of the larger agonists epibatidine and varenicline, but dispensable for binding of the smaller, endogenous agonist acetylcholine.

*This chapter is adapted from: Van Arnam, E. B., Blythe, E. E., Lester, H. A., and Dougherty, D. A. An unusual pattern of ligand-receptor interactions for the $\alpha 7$ nicotinic acetylcholine receptor, with implications for the binding of varenicline. *Mol Pharmacol* (2013) **84**, 201-207. Copyright © 2013 by the American Society for Pharmacology and Experimental Therapeutics. Reprinted with permission of the American Society for Pharmacology and Experimental Therapeutics. All rights reserved. The work described in this chapter was done in collaboration with Emily E. Blythe.

5.2 Introduction

The $\alpha 7$ nicotinic acetylcholine receptor (nAChR), a member of the Cys loop (pentameric) family of ligand-gated ion channels, is one of the principal mediators of synaptic transmission in the central nervous system. It has attracted significant interest as a therapeutic target for Alzheimer's disease, schizophrenia, and inflammation,¹⁻³ and a number of $\alpha 7$ -directed compounds are currently in the clinic for treatment of these disorders.⁴

Pharmacology of the $\alpha 7$ nAChR has revealed a wide range of structures capable of activating the receptor,⁵ contributing to the challenge of advancing selectivity among receptor subtypes in CNS drug development. Varenicline, a potent partial agonist of the $\alpha 4\beta 2$ receptor currently prescribed as a smoking cessation therapy (Chantix),⁶ has also been demonstrated to be a full agonist of $\alpha 7$ with modest potency.⁷ Adverse neuropsychiatric effects of this drug have led to speculation that varenicline therapy could have off-target activity on $\alpha 7$ receptors.⁸

Despite a large and growing body of pharmacological data, our knowledge of the functionally important ligand-receptor interactions of the $\alpha 7$ -binding site remains limited. The receptor has five identical agonist binding sites, located at each subunit-subunit interface. While no direct structural data yet exist for this receptor, a large number of crystal structures of snail acetylcholine binding proteins (AChBPs), homologous to the extracellular domain of nAChRs, provide a useful guide for the binding site.^{9,10} Two chimeras of the $\alpha 7$ extracellular domain and an AChBP have recently been reported, one with the *Aplysia californica* AChBP in complex with the antagonist MLA¹¹ and another

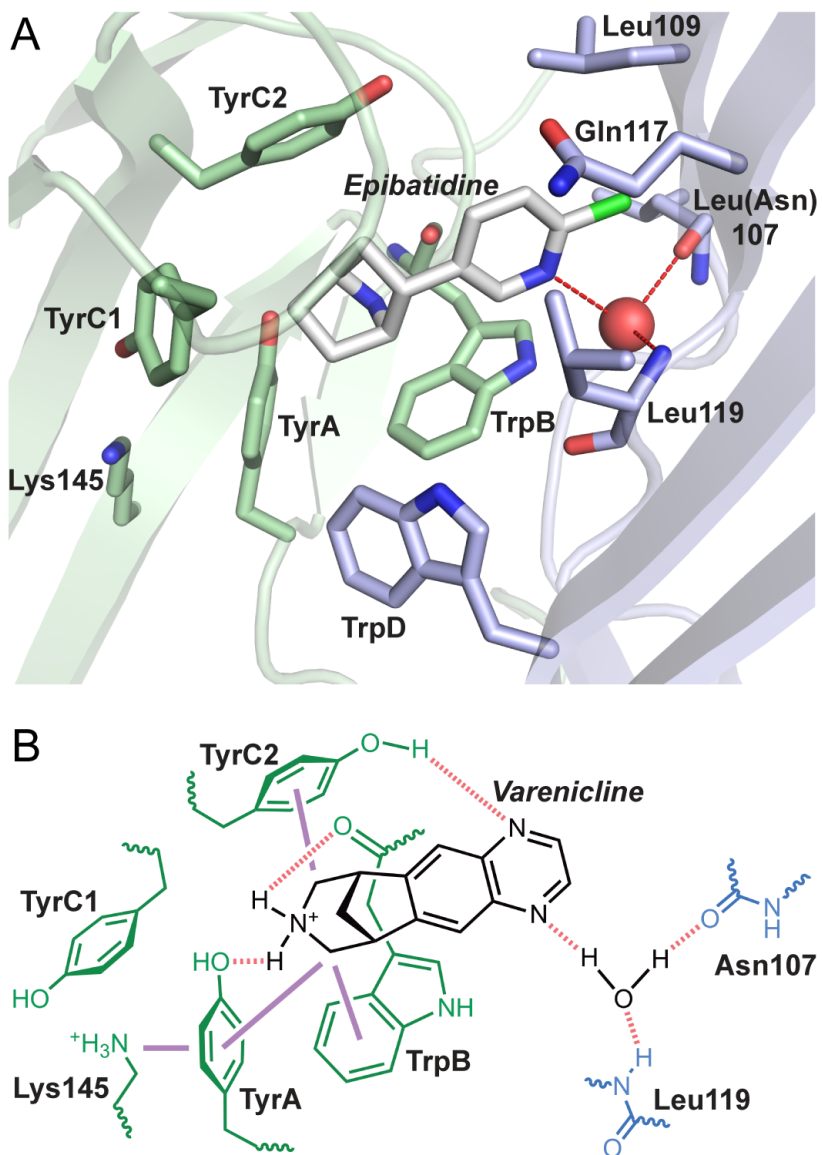


Figure 5.1. Two views of the nAChR agonist binding site. (A) Crystal structure of the *Ls*-AChBP/α7 chimera with epibatidine bound (3SQ6).¹² The water molecule shown (red sphere) is not seen in this particular structure, but has been placed in the position seen in other structures. All side chains shown in this structure are identical to the actual receptor residues studied except for Leu107, which instead is Asn. (B) Schematic of the agonist binding site, showing the key noncovalent interactions considered here. Varenicline is shown as the agonist so that all interactions considered in text can be illustrated. Solid purple lines: cation-π interactions; dashed red lines: hydrogen bonds. In both images, green residues are from the primary face; blue residues are from the complementary face.

with the *Lymnaea stagnalis* AChBP (*Ls*-AChBP) in complex with the agonist epibatidine.¹² Including all native $\alpha 7$ binding site residues and a bound agonist, the *Ls*-AChBP/ $\alpha 7$ chimera provides an excellent starting place to identify important agonist-receptor interactions (Figure 5.1A). Recent unmodified AChBP structures in complex with varenicline also suggest a ligand binding mode for this agonist.^{13,14} As for all other nicotinic receptors, the chief feature of the $\alpha 7$ binding site is an “aromatic box” defined by four residues (TyrA, TrpB, TyrC1, and TyrC2) contributed by its “principal” face and one (TrpD) contributed by its “complementary” face on the adjacent subunit (Figure 5.1).¹⁵ This motif accommodates the positive charge common to all orthosteric nicotinic agonists, the principal component of the classical nicotinic pharmacophore.¹⁶

The remainder of the binding site is contributed by the adjacent subunit. This complementary face of the binding site is thought to recognize the hydrogen bond acceptor moiety of the classical nicotinic pharmacophore. Various AChBP structures suggest that this hydrogen bonding partner is a water molecule held between the backbone NH of Leu119 and the backbone CO of Asn107.^{14,17-20} The proposed water molecule is not always evident in the structures, but the positioning of the key protein residues, including Leu119 and Asn107, is consistent in all structures, and so the water molecule is assumed to be present. As such, in Figure 5.1 we have added the proposed hydrogen bonding water molecule to the *Ls*-AChBP/ $\alpha 7$ chimera structure. In previous work, we have used unnatural amino acid mutagenesis to establish that the backbone NH of Leu119 does have a hydrogen bonding interaction with agonists in the $\alpha 4\beta 2$ and muscle-type nicotinic receptors, but the interaction is attenuated in the $\alpha 4\beta 4$ receptor.²¹

In contrast, similar evaluation of the Asn107 backbone CO in the muscle-type and $\alpha 4\beta 4$ receptors did not reveal a functionally significant hydrogen bonding interaction.²²

Several side chains on the complementary face of the binding site are also positioned to form possible ligand contacts. Recent crystal structures of AChBP in complex with varenicline have indicated that side chains corresponding to $\alpha 7$ residues Trp55, Leu109, Gln117, and Leu119 all contact this ligand (Figure 5.1A).^{13,14} Both the Trp55 and Leu119 side chains have recently been implicated in ligand binding for the $\alpha 7$ receptor.²³

We have previously characterized a unique binding mode for the endogenous agonist ACh and the potent nicotine analog epibatidine to the aromatic box residues of the $\alpha 7$ receptor.²⁴ As expected, the cationic moiety of the agonist binds *via* a cation- π interaction. Surprisingly, however, the residue involved was found to be either TyrA, for ACh, or TyrC2, for epibatidine – all other nicotinic receptor/agonist combinations we have examined involve a cation- π interaction to TrpB.²⁵⁻²⁷ Additionally, a strong hydrogen bond from TrpB's backbone carbonyl to the agonist N⁺-H (for agonists possessing this moiety), which has been seen in the $\alpha 4\beta 2$ and $\alpha 4\beta 4$ neuronal receptors^{24,26} and the muscle-type receptor,²⁸ appears to be weak or absent for epibatidine at the $\alpha 7$ receptor.

In the present work, we use unnatural amino acid mutagenesis to evaluate binding of the fully efficacious and moderately potent agonist varenicline to the aromatic box residues of the $\alpha 7$ receptor's principal face. We also evaluate interactions to the receptor's complementary face for the agonists ACh, epibatidine, and varenicline. Like

ACh and epibatidine, varenicline does not form a cation- π interaction to TrpB. This observation further supports a unique binding mode to the aromatic box for agonists in $\alpha 7$. We also find that these three agonists are largely insensitive to backbone mutations to both the NH and CO groups thought to recognize the hydrogen bond acceptor of the nicotinic pharmacophore. By conventional mutagenesis of complementary face residues proposed to contribute to the binding site, we have identified side chains that are functionally important for the agonists epibatidine and varenicline, but not for the smaller agonist ACh.

5.3 Results

5.3.1 Experimental design

Recently, we have shown that the $\alpha 7$ nAChR is amenable to unnatural amino acid mutagenesis by nonsense suppression in *Xenopus* oocytes – electrophysiology yields reproducible dose-response relationships when incorporating a wide panel of unnatural side chains (representative dose-response curves from this study are shown in Figure 5.2).²⁴ We coexpress the rat $\alpha 7$ nAChR with the human RIC-3 protein to overcome poor receptor expression. All mutant receptors studied include the T6'S background mutation in the transmembrane domain, which limits the rapid desensitization associated with the $\alpha 7$ receptor while minimally perturbing receptor pharmacology.²⁹

In the present study we measure the functional impact of each mutation using EC₅₀, the effective agonist concentration that gives a half-maximal response. EC₅₀ is a composite measure that reflects multiple equilibria: both “binding” events – drug

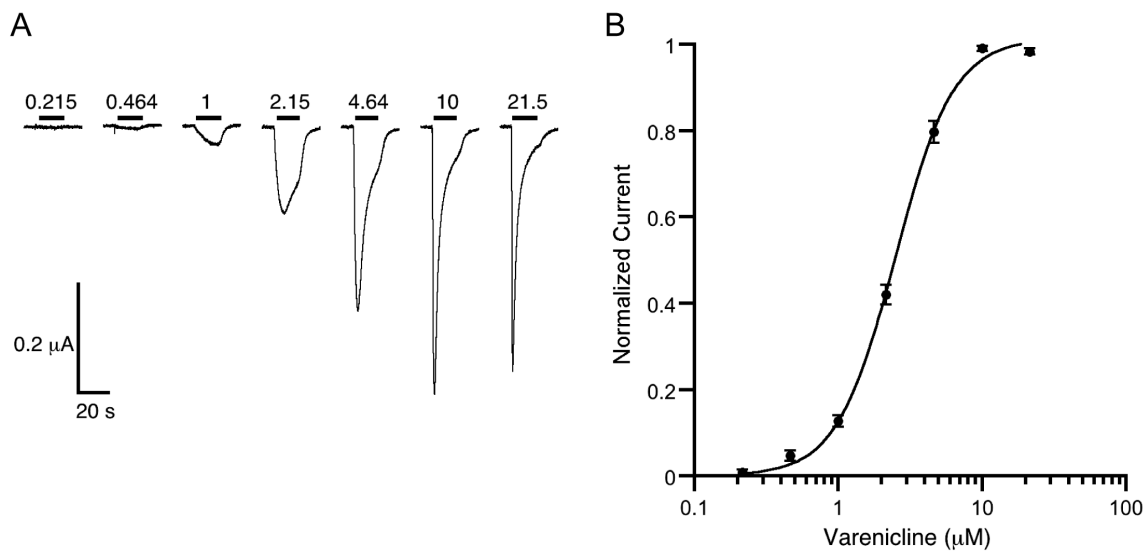


Figure 5.2. Representative traces and dose-response curves. (A) Representative current traces for incorporation of Trp by nonsense suppression at the TrpB (Trp149) site. Bars indicate application of varenicline (μM) at concentrations noted. (B) Dose-response curve and fit to the Hill equation for normalized varenicline responses for Trp incorporation at the TrpB site. Error bars indicate SEM ($n = 17$).

entering/exiting the agonist binding site – and “gating” events – the equilibria between open and closed states of the channel. Without detailed kinetic analyses, typically at the single channel level, it is not possible to parse which equilibria are perturbed by a given mutation. For example, a mutation affecting a binding interaction could affect a gating equilibrium if the drug binds more tightly to the open state of the channel than the closed state (or vice versa). The primary tool used here is unnatural amino acid mutagenesis, which allows precise, chemically well-defined modifications to the agonist binding site. We would argue that while the identity of the equilibrium step(s) being perturbed for each mutation in this study is unknown, we can confidently assign the nature of the perturbation: an attenuated ligand binding interaction. Our structural knowledge of the binding site has guided the location of mutations made, and previous studies on this and related systems demonstrate ligand-specific EC_{50} shifts consistent with specific binding interactions. Further, unnatural amino acid mutagenesis allows for subtle and precise

modifications to protein structure that target the interaction of interest. This argument is less compelling when more perturbing, conventional amino acid mutagenesis is employed, but studies of that kind reported here can provide guidance for further investigation.

We consider EC₅₀ to be the appropriate metric here for two reasons. First, detailed, single channel studies are not feasible for the large number of drug-receptor combinations that we have considered. This is especially so given the protein expression limitations that are sometimes seen with unnatural amino acid mutagenesis. Second and more importantly, our goal is to evaluate the pharmacology of the $\alpha 7$ receptor and compare these results to those of previous studies on related systems. EC₅₀ is a good measure of pharmacological activity. Given our experience with this system, we generally do not ascribe specific structural interactions to EC₅₀ differences that are less than a factor of 2.

5.3.2 Unnatural amino acid mutagenesis to probe cation-π interactions and hydrogen bonds to the protein backbone

To determine whether varenicline forms a cation-π interaction to one or more of the aromatic residues on the binding site's principal face, we incorporated unnatural aromatic amino acid analogs with attenuated cation-π binding ability and probed for a concomitant reduction in receptor function (Figure 5.3B). In particular, systematic fluorination of an aromatic side chain is diagnostic for a cation-π interaction. Comparing EC₅₀ shifts for the highly deactivating cyano (CN) substituent and the sterically similar but much less deactivating bromo (Br) substituent is also instructive.

We probe hydrogen bonding to the protein backbone with α -hydroxy acid mutagenesis, replacing the native amide peptide bond with an ester (Figure 5.3C). This mutation has two effects: most obviously, the hydrogen bond donor NH is deleted. Second, the ester carbonyl is well-established as a poorer hydrogen bond acceptor than the native amide carbonyl, so hydrogen bonds to this group will be attenuated. Note that a backbone carbonyl is modulated by mutating the $i+1$ residue to an α -hydroxy acid.

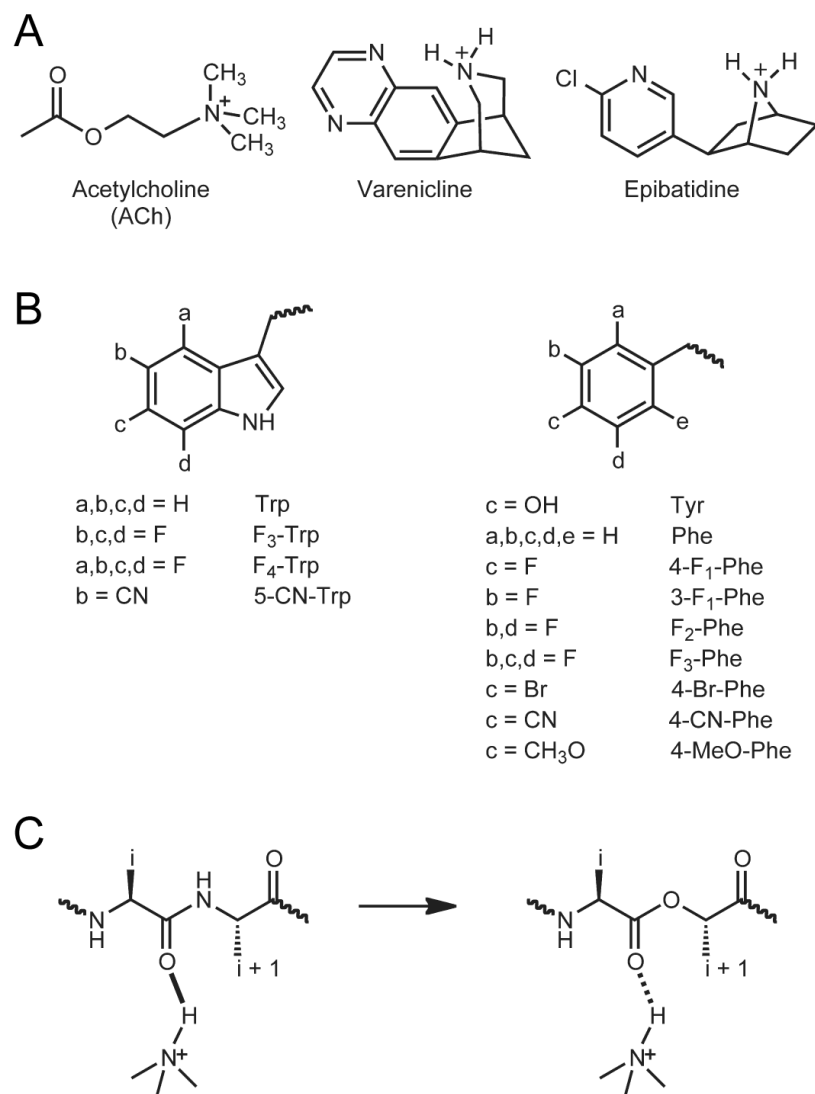


Figure 5.3. (A) Agonists considered here. (B) Aromatic unnatural amino acids employed here. (C) The α -hydroxy acid strategy for evaluating backbone hydrogen bonding. The hydrogen bond is stronger (solid line) on the left than on the right (dashed line).

5.3.3 Varenicline interactions with the binding site's principal face

At the TrpB site, the varenicline EC₅₀ for F₃-Trp is not significantly shifted from wild type, while F₄-Trp shows a modest 3.8-fold shift (Table 5.1), substantially smaller than we have observed for agonists forming a cation-π interaction with this side chain in other receptors. For comparison, a 16-20-fold shift was seen for the corresponding F₄-Trp mutation with varenicline at its targeted α4β2 receptor.²⁵ Further, for α7 we found that the highly deactivating cyano substituent has no functional effect, confirming that varenicline does not form a cation-π interaction to TrpB.

The remaining aromatic residues of the principal face, TyrA, TyrC1, and TyrC2, were also probed for cation-π binding to varenicline. Interrogation of tyrosine presents an additional challenge: fluorination of this aromatic system progressively lowers the pK_a of the hydroxyl group. This effect is substantial enough that tetrafluorotyrosine (pK_a~5.3 vs 10 for tyrosine) will likely be deprotonated under physiological conditions, confounding interpretation of EC₅₀ shifts.³⁰ We circumvent this complication by first evaluating the function of phenylalanine and then proceeding with fluorinated phenylalanine derivatives.

As we had previously observed for ACh and epibatidine, phenylalanine produces a substantial EC₅₀ shift at TyrA for varenicline, while 4-MeO-Phe produces a wild-type EC₅₀, possibly indicating the need for a hydrogen bond acceptor and/or steric placeholder at the 4-position (Table 5.1). F₂-Phe and F₃-Phe gave small, but detectable, responses at high varenicline doses. Full dose-response curves, however, were obscured by the response of naïve oocytes to varenicline at concentrations ≥ 1 mM. Without these data it is not possible to rule on a cation-π interaction at TyrA, although losses of function for 4-

Br-Phe and more so for 4-CN-Phe do suggest an important role for side chain electrostatics (Figure 5.4).

Table 5.1. Wild type and mutations to the binding site's principal face. EC₅₀ and Hill coefficient (n_H) are ± SEM for goodness of fit to the Hill equation.

Mutation	Agonist	EC ₅₀ (μM)	Fold Shift	n _H	n
wt	ACh	99 ± 3		2.7 ± 0.2	16
wt	Varenicline	1.99 ± 0.03		2.8 ± 0.1	15
wt	Epibatidine	0.34 ± 0.01		3.0 ± 0.2	13
TyrA					
Y93 Tyr ^a	Varenicline	2.21 ± 0.05		3.0 ± 0.2	7
Y93 Phe	Varenicline	126 ± 5	57	2.4 ± 0.2	9
Y93 4-F ₁ -Phe	Varenicline	34 ± 3	15	2.0 ± 0.3	11
Y93 F ₂ -Phe	Varenicline	>100 ^b			8
Y93 F ₃ -Phe	Varenicline	>100 ^b			8
Y93 4-Br-Phe	Varenicline	12 ± 1	5.4	3.1 ± 0.6	7
Y93 4-CN-Phe	Varenicline	33 ± 2	15	2.5 ± 0.4	10
Y93 4-MeO-Phe	Varenicline	2.19 ± 0.05	0.99	2.3 ± 0.1	6
TrpB					
W149 Trp ^a	Varenicline	2.5 ± 0.1		2.1 ± 0.1	17
W149 F ₃ -Trp	Varenicline	4.1 ± 0.1	1.6	2.3 ± 0.1	15
W149 F ₄ -Trp	Varenicline	9.6 ± 0.8	3.8	2.0 ± 0.2	15
W149 5-CN-Trp	Varenicline	2.1 ± 0.1	0.84	2.6 ± 0.4	12
TyrC1					
Y188 Tyr ^a	Varenicline	2.23 ± 0.08		2.4 ± 0.2	8
Y188 Phe	Varenicline	>100 ^b			6
TyrC2					
Y195 Tyr ^a	Varenicline	2.12 ± 0.02		2.76 ± 0.06	8
Y195 Phe	Varenicline	2.28 ± 0.09	1.1	3.1 ± 0.4	6
Y195 3-F ₁ -Phe	Varenicline	5.1 ± 0.07	2.4	1.9 ± 0.02	12
Y195 4-F ₁ -Phe	Varenicline	1.53 ± 0.05	0.72	3.4 ± 0.3	9
Y195 F ₂ -Phe	Varenicline	16.3 ± 0.7	7.7	2.4 ± 0.2	12
Y195 F ₃ -Phe	Varenicline	16 ± 1	7.5	2.6 ± 0.3	7
Y195 4-Br-Phe	Varenicline	3.48 ± 0.07	1.6	3.6 ± 0.2	5
Y195 4-CN-Phe	Varenicline	21 ± 1	9.9	3.8 ± 0.9	11
Y195 4-MeO-Phe	Varenicline	2.42 ± 0.09	1.1	2.8 ± 0.3	11
TrpB+1					
S150 Thr	Varenicline	0.81 ± 0.04		2.2 ± 0.2	11
S150 Tah	Varenicline	2.4 ± 0.1	3.0 from Thr	2.2 ± 0.2	15
Lys145					
K145A	ACh	N.R.			
K145Q	ACh	590 ± 20	6.0	2.5 ± 0.1	8
K145Q	Varenicline	9.4 ± 0.2	4.7	1.6 ± 0.2	7
K145R	ACh	1600 ± 100	16	2.6 ± 0.3	6
K145R	Varenicline	61.6 ± 0.2	31	3.19 ± 0.03	9

^aExpression of the wild type receptor with the natural amino acid incorporated by nonsense suppression

^bResponse of naïve oocytes to varenicline doses ≥ 1mM obscures complete dose-response data

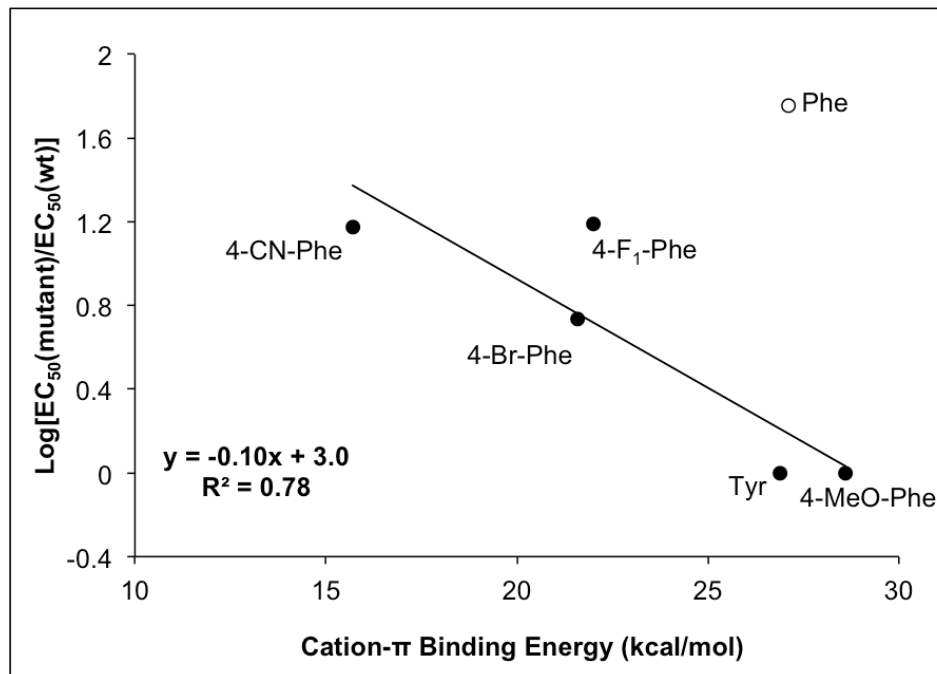


Figure 5.4. Cation- π binding plot for TyrA, in which $\log[\text{EC}_{50}(\text{mutant})/\text{EC}_{50}(\text{wt})]$ is plotted versus quantitative cation- π binding energies.^{27,31} a strong linear correlation would suggest a cation- π interaction. Phe (open circle) is not included in the fit.

In previous work on the $\alpha 7$ receptor, we assigned a cation- π interaction between ACh and TyrA.²⁴ However, a recent *Ls*-AChBP/ $\alpha 7$ chimera crystal structure suggests that TyrA may actually form an intra-protein cation- π interaction with the Lys145 side chain (Figure 5.1B).¹² We neutralized this Lys side chain to Gln and found only a modest 4-6-fold loss of function for Var and ACh (Table 5.1), suggesting that the much larger EC_{50} shifts for poor cation- π -binding Phe analogs at TyrA largely reflect a weakened ligand binding interaction instead.

At TyrC2 the Phe mutant and 4-MeO-Phe are essentially wild type. We do observe a loss of receptor function for varenicline with Phe analogs possessing attenuated cation- π binding ability (Table 5.1). However, EC₅₀ shifts are modest. For example, we see a 7.5-fold shift for the highly deactivating F₃-Phe mutation, while the same mutation for epibatidine (which does form a cation- π interaction with TyrC2) gave a nearly 50-fold shift.²⁴ Further, the EC₅₀s have only a weak linear dependence on cation- π binding energy (Figure 5.5). 4-F₁-Phe unexpectedly gave a gain of receptor function, though shifting the fluorine to the 3-position produces a modest loss of function. TyrC1 was too sensitive to phenylalanine substitution to even yield a measurable EC₅₀, preventing the study of this residue (Table 5.1).

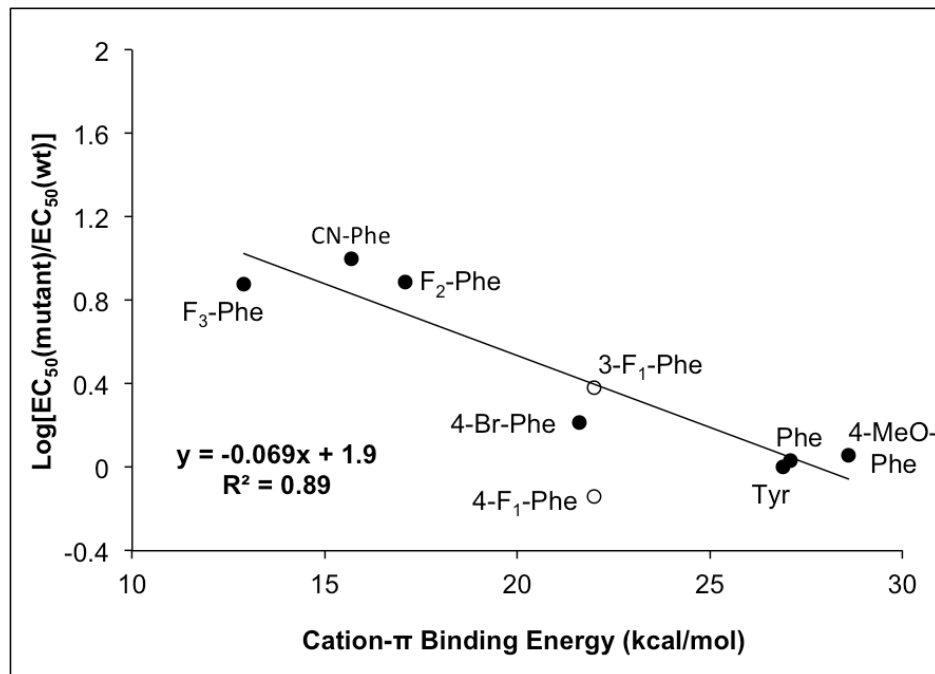


Figure 5.5. Cation- π binding plot for TyrA, in which log[EC₅₀(mutant)/EC₅₀(wt)] is plotted versus quantitative cation- π binding energies.^{27,31} A strong linear correlation would suggest a cation- π interaction. 3-F₁-Phe and 4-F₁-Phe (open circles) are not included in the fit.

Finally, we probed the TrpB backbone carbonyl for a functionally significant hydrogen bond to the agonist, as has been observed in other receptors with agonists possessing an N⁺-H group. We find that mutation of Ser150 (*i*+1 relative to TrpB) to threonine, α -hydroxy (Tah) produces a three-fold shift relative to the conservative mutation S150Thr, potentially indicating a weak hydrogen bond (Table 5.1).

5.3.4 Probing the canonical hydrogen bond of the nicotinic pharmacophore between agonists and the complementary subunit

To test for the functional importance of interactions with the hydrogen bond acceptor group on the agonist, we evaluated residues that contribute to the water-mediated hydrogen bonding array of Figure 5.1. The Leu119 backbone NH and the Asn107 backbone CO were evaluated by α -hydroxy acid mutagenesis. The L119Lah mutation, which deletes the Leu119 backbone NH, had little functional effect on the agonists ACh and varenicline, with EC₅₀ shifts less than 2-fold, and produced a 2.6-fold shift for epibatidine (Table 5.2). We probed the Asn107 CO by mutating its *i*+1 residue, Val108, to valine, α -hydroxy (Vah), attenuating the hydrogen bond accepting ability of the backbone CO of interest. We saw little functional effect for ACh and epibatidine, with EC₅₀ shifts less than 2-fold, and a modest 4.3-fold shift for varenicline.

5.3.5 Functional importance of side chains on the complementary face of the binding site

To complete our survey of ligand-receptor interactions, we tested the functional effect of alanine mutations on residues of the binding site's complementary face that are proposed to contact these agonists: Trp55, Leu109, Gln117, and Leu119.¹²⁻¹⁴ Of these mutations, L109A and Q117A produced modest shifts of 3.1-fold or less for all three agonists tested (Table 5.2). Interestingly, the mutants W55A and L119A showed little, if

any, effect on ACh, but large shifts of 9-fold or greater for the larger agonists epibatidine and varenicline.

Table 5.2. Mutations to the binding site's complementary face. EC₅₀ and Hill coefficient (n_H) are ± SEM for goodness of fit to the Hill equation.

Mutation	Agonist	EC ₅₀ (μM)	Fold Shift	n _H	n
V108 Val ^a	ACh	103 ± 2		2.9 ± 0.2	10
V108 Vah	ACh	184 ± 9	1.8	2.3 ± 0.2	10
V108 Val ^a	Varenicline	2.3 ± 0.1		4 ± 1	8
V108 Vah	Varenicline	10.0 ± 0.5	4.3	2.5 ± 0.3	9
V108 Val ^a	Epibatidine	0.396 ± 0.005		3.02 ± 0.09	7
V108 Vah	Epibatidine	0.64 ± 0.04	1.6	3.4 ± 0.5	11
L119 Leu ^a	ACh	120 ± 6		2.5 ± 0.3	9
L119 Lah	ACh	180 ± 8	1.5	2.4 ± 0.2	6
L119 Leu ^a	Varenicline	2.26 ± 0.02		2.76 ± 0.05	7
L119 Lah	Varenicline	3.15 ± 0.08	1.4	2.2 ± 0.1	9
L119 Leu ^a	Epibatidine	0.290 ± 0.005		3.3 ± 0.1	8
L119 Lah	Epibatidine	0.75 ± 0.01	2.6	3.4 ± 0.1	10
N107L	ACh	350 ± 3	3.5	2.48 ± 0.05	5
N107L	Varenicline	2.77 ± 0.05	1.4	2.6 ± 0.1	4
N107L	Epibatidine	1.37 ± 0.02	4.0	2.44 ± 0.06	4
W55A	ACh	134 ± 8	1.4	1.9 ± 0.2	8
W55A	Varenicline	67.6 ± 0.9	34	2.95 ± 0.09	11
W55A	Epibatidine	5.8 ± 0.3	17	2.2 ± 0.2	10
L109A	ACh	303 ± 7	3.1	2.4 ± 0.1	9
L109A	Varenicline	0.53 ± 0.01	0.27	3.3 ± 0.2	12
L109A	Epibatidine	0.282 ± 0.008	0.83	2.8 ± 0.2	9
Q117A	ACh	180 ± 4	1.8	2.7 ± 0.1	10
Q117A	Varenicline	4.85 ± 0.06	2.4	2.88 ± 0.09	12
Q117A	Epibatidine	0.90 ± 0.05	2.6	3.0 ± 0.4	11
L119A	ACh	210 ± 9	2.1	2.3 ± 0.2	11
L119A	Varenicline	41 ± 1	21	2.6 ± 0.2	11
L119A	Epibatidine	3.20 ± 0.09	9	3.0 ± 0.2	10

^aExpression of the wild type receptor with the natural amino acid incorporated by nonsense suppression

^bResponse of naïve oocytes to varenicline doses ≥ 1mM obscures complete dose-response data

5.4 Discussion

This work expands our survey of ligand-receptor interactions for ACh and epibatidine at the α7 nAChR and examines the yet-uncharacterized binding of varenicline. We have previously investigated binding of these ligands to other nAChRs, allowing for

comparisons to be drawn among these receptors with superficially similar binding sites, but distinct pharmacologies.

5.4.1 Cation-π interactions to the “aromatic box” residues of the principal face

The “aromatic box” is conserved across all nicotinic binding sites and is comprised of identical residues: three tyrosines (A, C1, and C2) and two tryptophans (B and D). The present study of varenicline’s interactions with these side chains corroborates our earlier findings for the binding of ACh and epibatidine to the $\alpha 7$ receptor: TrpB is not engaged in a cation- π interaction with the agonist.²⁴ This contrasts a large number of studies of other nAChRs, including the muscle-type receptor, the $\alpha 4\beta 4$ receptor, and both stoichiometries of the $\alpha 4\beta 2$ receptor, as well as other Cys-loop receptors such as the 5-HT_{3A} receptor, the glycine receptor, and the GABA_A receptor, all of which involve cation- π interactions to TrpB or another aromatic residue at that site.²⁴⁻

27,31-33

Instead, TyrA and TyrC2 of the $\alpha 7$ receptor form cation- π interactions with the agonists ACh and epibatidine, respectively.²⁴ We were able to evaluate a number of TyrC2 mutants. We find a modest effect when substituting poor cation- π binding side chains and only a weak correlation of cation- π binding energy with EC₅₀ (Figure 5.5). We conclude that TyrC2 does not form a strong cation- π interaction with varenicline. At the TyrA site we do observe a suggestive electrostatic trend with varenicline for the Phe analogs incorporated (Figure 5.4), but we lack data for F₂-Phe and F₃-Phe, hampered by EC₅₀ values beyond our measurable range. On the basis of the *Ls*-AChBP/ $\alpha 7$ chimera structure a cation- π interaction between TyrA and Lys145 has been proposed. However, we find that the K145Q produces a smaller effect than the 4-F and 4-CN mutations of

TyrA (Table 5.1), which is not consistent with this model. For $\alpha 7$, as for other nicotinic receptors we have investigated, extreme sensitivity of TyrC1 to mutagenesis has prevented further study of this residue.

5.4.2 Hydrogen bonding and steric effects on the principal face

It is worth emphasizing that, while we consider the present work to probe hydrogen bonding interactions, we are in fact probing the *functional significance* of particular hydrogen bonds. Thus, it is possible that a structural study could show the presence of a hydrogen bond, but if deleting/attenuating that hydrogen bond has no functional consequence, it would show up as no hydrogen bond in our assay.

We find evidence for only a weak hydrogen bond between the TrpB backbone carbonyl and the N⁺-H of varenicline, as we had observed for epibatidine (Table 5.1).²⁴ The hydroxy acid mutation that here produced a 3-fold EC₅₀ shift gave much larger 14-19-fold shifts for varenicline at its targeted $\alpha 4\beta 2$ receptor.²⁵ Indeed, comparably large shifts have been measured for all agonists bearing this N⁺-H that we have characterized to date at the $\alpha 4\beta 2$ and $\alpha 4\beta 4$ neuronal receptors, all of which also bind the TrpB side chain with a cation- π interaction.²⁴⁻²⁶ It is perhaps not surprising, then, that this hydrogen bond would be attenuated if the agonist has moved its cation- π interaction to other residues of the aromatic box.

Various AChBP crystal structures suggest a hydrogen bond between the side chain -OH of TyrA and the N⁺-H of agonists such as nicotine (1UW6), varenicline (4AFT), cytisine (4AFO), and epibatidine (2BYQ, 3SQ6), as shown in Figure 5.1.^{12,14,17,18} The large loss of function for deleting the -OH by mutation to Phe is

consistent with this model (Table 5.1). In addition, 4-MeO-Phe, which can serve as a hydrogen bond acceptor like Tyr, shows wild type behavior. 4-F₁-, 4-CN-, and 4-Br-Phe are all preferable to Phe, suggesting there could also be a steric component involving the 4 position of TyrA.

For TyrC2, mutation to Phe yields a receptor with wild type function for varenicline (Table 5.1): neither a steric nor a more specific hydrogen bonding role for this side chain –OH seems plausible. Recent AChBP-varenicline crystal structures show a potential hydrogen bond between the TyrC2 –OH and one of varenicline’s quinoxaline nitrogens.^{13,14} Our data indicate that any such interaction in the $\alpha 7$ receptor is not functionally important. Interestingly, the Phe mutant did have a significantly shifted EC₅₀ for ACh and for epibatidine (6-fold and 11-fold, respectively),²⁴ so varenicline evidently interacts with this side chain differently than these other agonists. Generally, mutations at this site do not strongly impact varenicline function, and there are no obvious trends in the data.

5.4.3 Hydrogen bonding to the complementary face

In addition to a cationic group, the classical nicotinic pharmacophore includes a hydrogen bond acceptor approximately 4-6 Å away,¹⁶ a feature shared by all three agonists tested in this study. AChBP crystal structures show agonist hydrogen bond acceptor groups directly contacting a water molecule, which in turn is held by a backbone NH and backbone CO of the complementary subunit (Figure 5.1). Mutant cycle analyses of the $\alpha 4\beta 2$ receptor confirm a hydrogen bonding role for the Leu119 backbone NH for both nicotine and ACh as agonists, consistent with the AChBP structures. In $\alpha 4\beta 2$, the L119Lah mutant (which removes this residue’s backbone NH) produced a 7-fold EC₅₀

shift for ACh and for nicotine.²¹ We now find that the corresponding backbone mutation of Leu119 in the $\alpha 7$ receptor has minimal functional effects on ACh and varenicline and only a 2.6-fold shift for epibatidine (Table 5.2). Evidently, the Leu119 NH does not form a functionally important interaction in the $\alpha 7$ receptor, perhaps reflecting either a reshaping of the binding site or a repositioning of agonists relative to their binding mode in the other receptors. A subtly different ligand binding mode might be expected given the use of TyrA and TyrC2 for cation- π interactions in $\alpha 7$, rather than TrpB. Functional importance of the Leu119 NH in other nicotinic receptors is mixed: it forms important contacts to ACh and nicotine for the muscle-type nAChR, but significantly weaker interactions in the neuronal $\alpha 4\beta 4$ receptor.²²

The other proposed hydrogen bonding partner of the binding site's complementary face is the Asn107 backbone CO, which accepts a hydrogen bond from the water molecule that also binds to the Leu119 NH and the drug hydrogen bond acceptor. We find that, in the $\alpha 7$ receptor, ACh and epibatidine are largely insensitive to the V108Vah mutation that attenuates the hydrogen bond acceptor ability of the Asn107 CO, with EC₅₀ shifts < 2-fold (Table 5.2). This group may have a modest functional relevance for varenicline, as we did record a 4.3-fold loss of function for that drug. Note that both the CO on the protein backbone and the quinoxaline N on varenicline can only act as hydrogen bond acceptors, so this hydrogen bond would need to be mediated by a water molecule, as observed in AChBP. Analogous hydroxy acid mutations modulating this CO in the muscle-type and $\alpha 4\beta 4$ receptors did not affect agonist EC₅₀.²² Note that α -hydroxy acid mutations probing backbone CO hydrogen bonding can produce large EC₅₀

shifts, an example being the TrpB backbone CO, where we have seen shifts as large as 20-30-fold in other receptors.^{25,26}

Taken together, it is possible that the $\alpha 7$ receptor either engages the agonist hydrogen bond acceptor with other groups or lacks energetically significant contacts with it. Regarding the former possibility, other candidate hydrogen bonding partners expected to lie near the agonist include the Gln117 and Asn107 side chains. Mutation of these to side chains without the potential to form hydrogen bonds has only modest functional effects of 4-fold or smaller, indicating that no critical interactions are present (Table 5.2). Without direct structural data for the $\alpha 7$ binding site, it is unclear exactly where these and other potential hydrogen bonding groups lie relative to the agonist.

Regarding the possibility that this hydrogen bond acceptor group does not form functionally important receptor contacts, it is worth remembering that tetramethylammonium (TMA), a much simpler structure that, of course, cannot participate in the hydrogen bonding interactions being probed here, has virtually the same potency and efficacy as ACh for the $\alpha 7$ receptor.^{5,34} Heteromeric neuronal nAChRs and the muscle-type receptor also respond to TMA, but with substantially elevated EC₅₀s and/or reduced efficacies.^{5,34} As such, it appears that the minimal requirements for agonist binding are more relaxed for $\alpha 7$. Indeed, the homomeric $\alpha 7$ receptor, which is phylogenetically more ancestral than the subunits of heteromeric receptors,³⁵ appears to have a less specialized binding site with broad pharmacology.⁵ While most characterized agonists for the $\alpha 7$ receptor do possess a hydrogen bond acceptor moiety consistent with the canonical nicotinic pharmacophore, some $\alpha 7$ -specific agonists lack this feature.⁵

Diminished importance of hydrogen bonding interactions for $\alpha 7$ relative to other nAChRs may underlie this specificity.

5.4.4 Interactions with complementary face side chains

With the critical positively charged “head group” of agonists buried within the aromatic box of the binding site’s principal face, the remaining features of larger ligands might be expected to make significant receptor contacts to side chains on the complementary face of the binding site. In crystal structures of varenicline bound to AChBP, the side chains corresponding to Trp55 (the sole complementary face contributor to the aromatic box), Leu109, Gln117, and Leu119 all contact the ligand.^{13,14} We find that the endogenous ligand ACh is minimally perturbed by alanine mutations to each of these residues (Table 5.2). The largest loss of function for ACh is observed for the L109A mutation (3.1-fold), which interestingly caused a modest gain of function (3.8-fold) for the larger varenicline ligand and a wild type EC₅₀ for epibatidine. Steric compensation between the ligand and side chain could explain this observation. The Q117A mutant had only a small effect on all three agonists, with EC₅₀ fold shifts of 1.8 to 2.6. The W55A and L119A mutations, however, were highly detrimental to epibatidine and varenicline, but unperturbing to ACh. These residues, more highly conserved than Leu109 and Gln117 among subunits forming the complementary face of nicotinic binding sites, could form hydrophobic interactions with larger ligands, but do not affect ACh.

The Trp55 and Leu119 side chains were previously shown to play an important functional role in the $\alpha 7$ receptor, with modifications to these side chains selectively affecting larger agonists.²³ Strikingly, the W55A mutation has only a small effect on

EC₅₀, but increases the relative efficacy of varenicline from 15% to 125% in the α4β2 receptor, this drug's intended target.¹³ The substantial increase in EC₅₀ we observe for W55A in the α7 receptor represents a dramatically different phenotype and indicates that this residue makes different contributions to receptor function for α7 *versus* α4β2. These findings suggest that avoiding agonist interactions with Trp55 could be a strategy to improve α4β2 selectivity over α7.

5.5 Conclusions

Our survey of potential agonist-receptor contacts for the α7 receptor reveals a unique pattern of interactions compared to other nAChRs. Differing roles for conserved binding site residues across nAChRs underscore the challenge of rationalizing subtype selectivity and the critical importance of functional evaluation of interactions suggested by structural models. Despite these challenges, the growing body of knowledge on subtype-specific drug-receptor interactions holds promise for advancing selectivity in drug design.

5.6 Experimental

5.6.1 Molecular biology

cDNA for the rat α7 T6'S receptor and for human RIC-3 were in the pAMV and pGEM plasmids, respectively. Site-directed mutagenesis was performed using the QuikChange protocol (Agilent Technologies, Santa Clara, CA). For nonsense

suppression experiments, the site of interest was mutated to the amber stop codon, with the exception of Val108 and Leu119, which were mutated to the opal stop codon. Circular α 7 and hRIC-3 DNA were linearized with NotI and Xhol restriction enzymes, respectively. After purification (Qiagen, Hilden, Germany), linearized DNA was used as a template for runoff *in vitro* transcription using the T7 mMessage mMachine kit (Life Technologies, Carlsbad, CA). The amber suppressor tRNA THG73³⁶ was used for nonsense suppression at all sites except Val108 and Leu119, for which the opal suppressor TQOpS^{37,38} was used.

α -Hydroxy or amino acids were appended to the dinucleotide dCA and enzymatically ligated to the appropriate truncated 74mer suppressor tRNA as previously described.^{39,40} Crude tRNA-amino acid or tRNA-hydroxy acid product was used without desalting, and the product was confirmed by MALDI-TOF MS on a 3-hydropicolinic acid matrix. tRNA-amino acids bearing a 6-nitroveratryloxycarbonyl protecting group were deprotected prior to injection *via* irradiation with a 500 W Hg/Xe arc lamp, filtered with WG-334 and UG-11 filters prior to injection.

5.6.2 Microinjection

Stage V–VI *Xenopus laevis* oocytes were harvested and injected with RNAs as described previously.⁴⁰ 5–25 ng of α 7 mRNA was co-injected with ~20 ng of RIC-3 mRNA per oocyte. For all of the suppression experiments, ~15 ng of tRNA per cell was used. Each oocyte was injected with 50 nL of RNA solution and incubated for 24–48 hrs before recording. In the case of low maximal currents sometimes observed in nonsense suppression experiments, presumably due to low expression, a second RNA injection was required 24 hrs after the first injection. As a negative control for suppression

experiments, unacylated full length tRNA was co-injected with mRNA in the same manner as charged tRNA. These control experiments yielded negligible responses for all sites studied.

5.6.3 Electrophysiology

Receptor function was assayed using the OpusXpress 6000A (Molecular Devices, Sunnyvale, CA) in two-electrode voltage clamp mode. The oocytes were clamped at a holding potential of -60 mV. 1 mL of each drug solution was applied for 15 s, followed by a 5-min wash step with ND96 buffer (96 mM NaCl, 2 mM KCl, 1 mM MgCl₂, 1.8 mM CaCl₂, 5 mM HEPES) between each concentration. Acetylcholine chloride was purchased from Sigma-Aldrich (St. Louis, MO), (±)-epibatidine was purchased from Tocris (Bristol, United Kingdom), and varenicline tartrate was a generous gift from Pfizer. Drug dilutions were prepared in ND96 buffer. Dose-response data were obtained for at least six concentrations of agonist and for a minimum of four oocytes. The EC₅₀ and Hill coefficient (n_H) values for each condition were obtained by fitting the averaged, normalized dose-response data to the Hill equation.

5.7 References

1. de Jonge, W. J. & Ulloa, L. The alpha7 nicotinic acetylcholine receptor as a pharmacological target for inflammation. *British journal of pharmacology* **151**, 915–929 (2007).
2. Hernandez, C. M. & Dineley, K. T. alpha7 nicotinic acetylcholine receptors in Alzheimer's disease: neuroprotective, neurotrophic or both? *Current drug targets* **13**, 613–622 (2012).
3. Martin, L. F., Kem, W. R. & Freedman, R. Alpha-7 nicotinic receptor agonists: potential new candidates for the treatment of schizophrenia. *Psychopharmacology* **174**, 54–64 (2004).
4. Mazurov, A. A., Speake, J. D. & Yohannes, D. Discovery and development of

- alpha7 nicotinic acetylcholine receptor modulators. *J Med Chem* **54**, 7943–7961 (2011).
5. Horenstein, N. A., Leonik, F. M. & Papke, R. L. Multiple pharmacophores for the selective activation of nicotinic alpha7-type acetylcholine receptors. *Mol Pharmacol* **74**, 1496–1511 (2008).
 6. Coe, J. W. *et al.* Varenicline: an alpha4beta2 nicotinic receptor partial agonist for smoking cessation. *J Med Chem* **48**, 3474–3477 (2005).
 7. Mihalak, K. B., Carroll, F. I. & Luetje, C. W. Varenicline is a partial agonist at alpha4beta2 and a full agonist at alpha7 neuronal nicotinic receptors. *Mol Pharmacol* **70**, 801–805 (2006).
 8. Papke, R. L., Trocme-Thibierge, C., Guendisch, D., Rubaiy, Al, S. A. & Bloom, S. A. Electrophysiological perspectives on the therapeutic use of nicotinic acetylcholine receptor partial agonists. *Journal of Pharmacology and Experimental Therapeutics* **337**, 367–379 (2011).
 9. Rucktooa, P., Smit, A. B. & Sixma, T. K. Insight in nAChR subtype selectivity from AChBP crystal structures. *Biochemical pharmacology* **78**, 777–787 (2009).
 10. Sixma, T. K. & Smit, A. B. Acetylcholine binding protein (AChBP): a secreted glial protein that provides a high-resolution model for the extracellular domain of pentameric ligand-gated ion channels. *Annu. Rev. Biophys. Biomol. Struct.* **32**, 311–334 (2003).
 11. Nemecz, A. & Taylor, P. Creating an alpha7 nicotinic acetylcholine recognition domain from the acetylcholine-binding protein: crystallographic and ligand selectivity analyses. *Journal of Biological Chemistry* **286**, 42555–42565 (2011).
 12. Li, S. X. *et al.* Ligand-binding domain of an alpha7-nicotinic receptor chimera and its complex with agonist. *Nat Neurosci* **14**, 1253–1259 (2011).
 13. Billen, B. *et al.* Molecular actions of smoking cessation drugs at alpha4beta2 nicotinic receptors defined in crystal structures of a homologous binding protein. *Proc. Natl. Acad. Sci. U.S.A.* **109**, 9173–9178 (2012).
 14. Rucktooa, P. *et al.* Structural characterization of binding mode of smoking cessation drugs to nicotinic acetylcholine receptors through study of ligand complexes with acetylcholine-binding protein. *Journal of Biological Chemistry* **287**, 23283–23293 (2012).
 15. Dougherty, D. A. Cys-loop neuroreceptors: Structure to the rescue? *Chem. Rev.* **108**, 1642–1653 (2008).
 16. Beers, W. H. & Reich, E. Structure and activity of acetylcholine. *Nature* **228**, 917–922 (1970).
 17. Celie, P. H. *et al.* Nicotine and carbamylcholine binding to nicotinic acetylcholine receptors as studied in AChBP crystal structures. *Neuron* **41**, 907–914 (2004).
 18. Hansen, S. B. *et al.* Structures of Aplysia AChBP complexes with nicotinic agonists and antagonists reveal distinctive binding interfaces and conformations. *EMBO J* **24**, 3635–3646 (2005).
 19. Rohde, L. A. *et al.* Intersubunit bridge formation governs agonist efficacy at nicotinic acetylcholine alpha4beta2 receptors: unique role of halogen bonding revealed. *Journal of Biological Chemistry* **287**, 4248–4259 (2012).
 20. Talley, T. T. *et al.* Atomic interactions of neonicotinoid agonists with AChBP: molecular recognition of the distinctive electronegative pharmacophore. *Proc. Natl.*

- Acad. Sci. U.S.A.* **105**, 7606–7611 (2008).
21. Blum, A. P., Lester, H. A. & Dougherty, D. A. Nicotinic pharmacophore: the pyridine N of nicotine and carbonyl of acetylcholine hydrogen bond across a subunit interface to a backbone NH. *Proc. Natl. Acad. Sci. U.S.A.* **107**, 13206–13211 (2010).
 22. Blum, A. P., Van Arnam, E. B., German, L. A., Lester, H. A. & Dougherty, D. A. Binding interactions to the complementary subunit of nicotinic receptors. *J. Biol. Chem.* (2013). doi:10.1074/jbc.M112.439968
 23. Papke, R. L., Stokes, C., Williams, D. K., Wang, J. & Horenstein, N. A. Cysteine accessibility analysis of the human alpha7 nicotinic acetylcholine receptor ligand-binding domain identifies L119 as a gatekeeper. *Neuropharmacology* **60**, 159–171 (2011).
 24. Puskar, N. L., Xiu, X., Lester, H. A. & Dougherty, D. A. Two neuronal nicotinic acetylcholine receptors, alpha4beta4 and alpha7, show differential agonist binding modes. *Journal of Biological Chemistry* **286**, 14618–14627 (2011).
 25. Da Silva Tavares, X. *et al.* Variations in binding among several agonists at two stoichiometries of the neuronal, alpha4beta2 nicotinic receptor. *J. Am. Chem. Soc.* **134**, 11474–11480 (2012).
 26. Xiu, X., Puskar, N. L., Shanata, J. A., Lester, H. A. & Dougherty, D. A. Nicotine binding to brain receptors requires a strong cation-pi interaction. *Nature* **458**, 534–537 (2009).
 27. Zhong, W. *et al.* From ab initio quantum mechanics to molecular neurobiology: a cation-pi binding site in the nicotinic receptor. *Proceedings of the National Academy of Sciences* **95**, 12088–12093 (1998).
 28. Cashin, A. L., Petersson, E. J., Lester, H. A. & Dougherty, D. A. Using physical chemistry to differentiate nicotinic from cholinergic agonists at the nicotinic acetylcholine receptor. *J. Am. Chem. Soc.* **127**, 350–356 (2005).
 29. Placzek, A. N., Grassi, F., Meyer, E. M. & Papke, R. L. An alpha7 nicotinic acetylcholine receptor gain-of-function mutant that retains pharmacological fidelity. *Mol Pharmacol* **68**, 1863–1876 (2005).
 30. Thorson, J. S., Chapman, E., Murphy, E. C., Schultz, P. G. & Judice, J. K. Linear Free-Energy Analysis of Hydrogen-Bonding in Proteins. *J. Am. Chem. Soc.* **117**, 1157–1158 (1995).
 31. Lummis, S. C., D, L. B., Harrison, N. J., Lester, H. A. & Dougherty, D. A. A cation-pi binding interaction with a tyrosine in the binding site of the GABAC receptor. *Chemistry & biology* **12**, 993–997 (2005).
 32. Beene, D. L. *et al.* Cation-pi interactions in ligand recognition by serotonergic (5-HT3A) and nicotinic acetylcholine receptors: the anomalous binding properties of nicotine. *Biochemistry* **41**, 10262–10269 (2002).
 33. Pless, S. A. *et al.* A cation-pi interaction in the binding site of the glycine receptor is mediated by a phenylalanine residue. *J. Neurosci.* **28**, 10937–10942 (2008).
 34. Papke, R. L., Bencherif, M. & Lippiello, P. An evaluation of neuronal nicotinic acetylcholine receptor activation by quaternary nitrogen compounds indicates that choline is selective for the alpha 7 subtype. *Neuroscience letters* **213**, 201–204 (1996).
 35. Le Novere, N., Corringer, P. J. & Changeux, J. P. The diversity of subunit

- composition in nAChRs: evolutionary origins, physiologic and pharmacologic consequences. *Journal of neurobiology* **53**, 447–456 (2002).
- 36. Saks, M. E. *et al.* An engineered Tetrahymena tRNAGln for in vivo incorporation of unnatural amino acids into proteins by nonsense suppression. *J. Biol. Chem.* **271**, 23169–23175 (1996).
 - 37. Rodriguez, E. A., Lester, H. A. & Dougherty, D. A. Improved amber and opal suppressor tRNAs for incorporation of unnatural amino acids in vivo. Part 1: minimizing misacylation. *Rna* **13**, 1703–1714 (2007).
 - 38. Rodriguez, E. A., Lester, H. A. & Dougherty, D. A. Improved amber and opal suppressor tRNAs for incorporation of unnatural amino acids in vivo. Part 2: evaluating suppression efficiency. *Rna* **13**, 1715–1722 (2007).
 - 39. England, P. M., Lester, H. A. & Dougherty, D. A. Incorporation of esters into proteins: Improved synthesis of hydroxyacyl tRNAs. *Tetrahedron Lett* **40**, 6189–6192 (1999).
 - 40. Nowak, M. W. *et al.* In vivo incorporation of unnatural amino acids into ion channels in Xenopus oocyte expression system. *Meth. Enzymol.* **293**, 504–529 (1998).

Chapter 6: Efforts toward single molecule fluorescence imaging of nAChRs

6.1 Abstract

Fluorescence studies probing conformational changes in nAChRs upon activation have the potential to bridge a wealth of functional data on these receptors from electrophysiology with emerging structural models for activation. Incorporation of fluorophores as unnatural amino acid side chains by nonsense suppression is an attractive option for selective labeling of these receptors for fluorescence studies. This chapter describes efforts to replicate and expand upon an earlier report from our group in which single nAChRs bearing a BODIPY fluorophore as an amino acid side chain were imaged in the membrane of *Xenopus laevis* oocytes. Progress was hampered by high levels of background fluorescence. Several approaches to circumvent this issue are described, including improved sample preparation, dye conjugation, and the use of a fluorescent tRNA with partially quenched fluorescence.

6.2 Introduction

Our understanding of nAChR gating motions lags far behind our functional understanding of these receptors from electrophysiology. Opening of the ion-conducting pore 60 Å away from the ligand binding site is thought to occur through closure of the C loop around the agonist and twisting of the entire extracellular domain coupled to tilting of TM2 and TM3.¹ Computational studies, x-ray crystallography of homologous bacterial channels, and cryo-EM structures of acetylcholine-bound and agonist-free

nAChRs corroborate some of these proposed gating motions.²⁻⁶ However, many questions remain: How large are the gating motions in the actual receptor? Are motions symmetric throughout the five subunits of the channel? What are the structures of desensitized and “uncoupled” states? Fluorescence studies on functional receptors in native cell membranes have the potential to address these questions.

To answer these sorts of detailed structural questions, small molecule fluorophores are highly preferred over fluorescent proteins due to their greater brightness, greater photostability, and most of all, small size. The tradeoff, of course, is the significant challenge of specific attachment of the fluorophore to the protein, especially *in vivo*. Incorporating the fluorophore as the side chain of an unnatural amino acid is an especially attractive option, and this approach has previously been used to incorporate single fluorophores into membrane proteins *in vivo*.^{7,8} This approach obviates the need for the attachment site to be solvent accessible, and also ensures site-selective labeling.

Previously, the Dougherty and Lester labs reported the successful incorporation of a BODIPY fluorophore into the nAChR by nonsense suppression in *Xenopus* oocytes, and single molecule imaging of these fluorescent receptors.⁹ The fluorophore used was BODIPYFL, which was conjugated to a lysine side chain (Figure 6.1A). This side chain was incorporated into the $\beta 19'$ site of the muscle-type nAChR, and the presence of functional receptors at the cell membrane was confirmed by electrophysiology. Fluorescence imaging was conducted on devitellinized oocytes using total internal reflection fluorescence (TIRF) microscopy. TIRF, in which only molecules less than ~100 nm from the glass surface the cell membrane is resting against are illuminated, was critical to enable fluorescent imaging at the membrane, given the high autofluorescence

of the oocyte interior¹⁰ and a large excess of fluorescent tRNA-Lys-BODIPY injected into the cell.

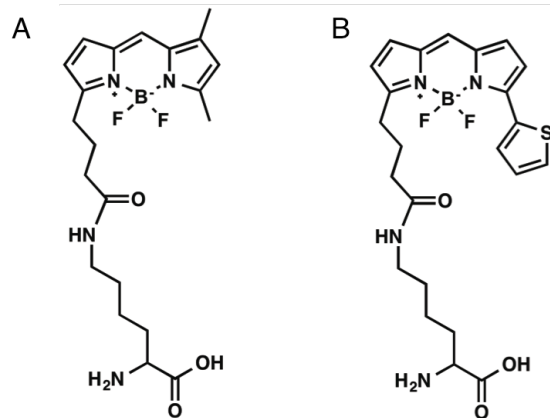


Figure 6.1. (A) Structure of Lys-BODIPYFL. (B) Structure of Lys-BODIPY558.

A logical extension of this work is the incorporation of two different fluorophores site-specifically into the nAChR to enable Förster resonance energy transfer (FRET) studies. A recently expanded toolkit of tRNAs for nonsense suppression in *Xenopus* oocytes enables the incorporation of multiple unnatural amino acids simultaneously.¹¹ Walrati Limapichat laid much of the groundwork for incorporation of multiple fluorophores into the nAChR, including the preparation of Lys-BODIPYFL and Lys-BODIPY558 (Figure 6.1) conjugated to dCA (which are used in the experiments described below), screening of sites for fluorophore incorporation, and preliminary imaging experiments.¹² These fluorophores have been incorporated into calmodulin as amino acid side chains by nonsense suppression *in vitro* and have a Förster radius (R_0) of 60 Å.¹³

This work aims to optimize the expression and TIRF imaging of fluorescent amino acids in nAChRs *in vivo* to enable two-color FRET experiments. Progress was

hampered by high background from fluorescent tRNA injected into the cell. Efforts are described to minimize this fluorescence background, including different membrane preparations and the preparation of a tRNA-Lys-BODIPYFL with partially quenched fluorescence. Analysis of single puncta simultaneously at two wavelengths is also discussed.

6.3 Results and Discussion

6.3.1 Background fluorescence from tRNA-BODIPY

As a starting point, visualization of receptors bearing a single Lys-BODIPYFL was attempted, under similar conditions to those used by Pantoja and co-workers in our lab's earlier report on receptor single molecule imaging.⁹ The β70 site was chosen for Lys-BODIPYFL incorporation, as this position is known to be permissive to the incorporation of large side chains.¹⁴ The amber suppressor tRNA TQAS was chosen for these experiments, as it shows low levels of reacylation in *Xenopus* oocytes.¹⁵ As a control, TQAS tRNA acylated with Lys-BODIPYFL (TQAS-BODIPYFL) was injected into cells alone to assess the level of background fluorescence from intracellular tRNA. High levels of fluorescence were seen for both β70 mRNA + TQAS-BODIPYFL and tRNA only conditions (Figure 6.2). Some cell-to-cell variability was seen for both conditions. Overall the two conditions were indistinguishable from each other, indicating that background fluorescence from tRNA-BODIPY was too high to permit visualization of fluorescent receptors. Conditions were not identical to those used by Pantoja⁹, but differences are not expected to affect the background fluorescence levels (conditions used here: 20 ng total of 2:5:1:1 α/β70TAG/γ/δ mRNA mix, 10 ng of TQAS-BODIPYFL

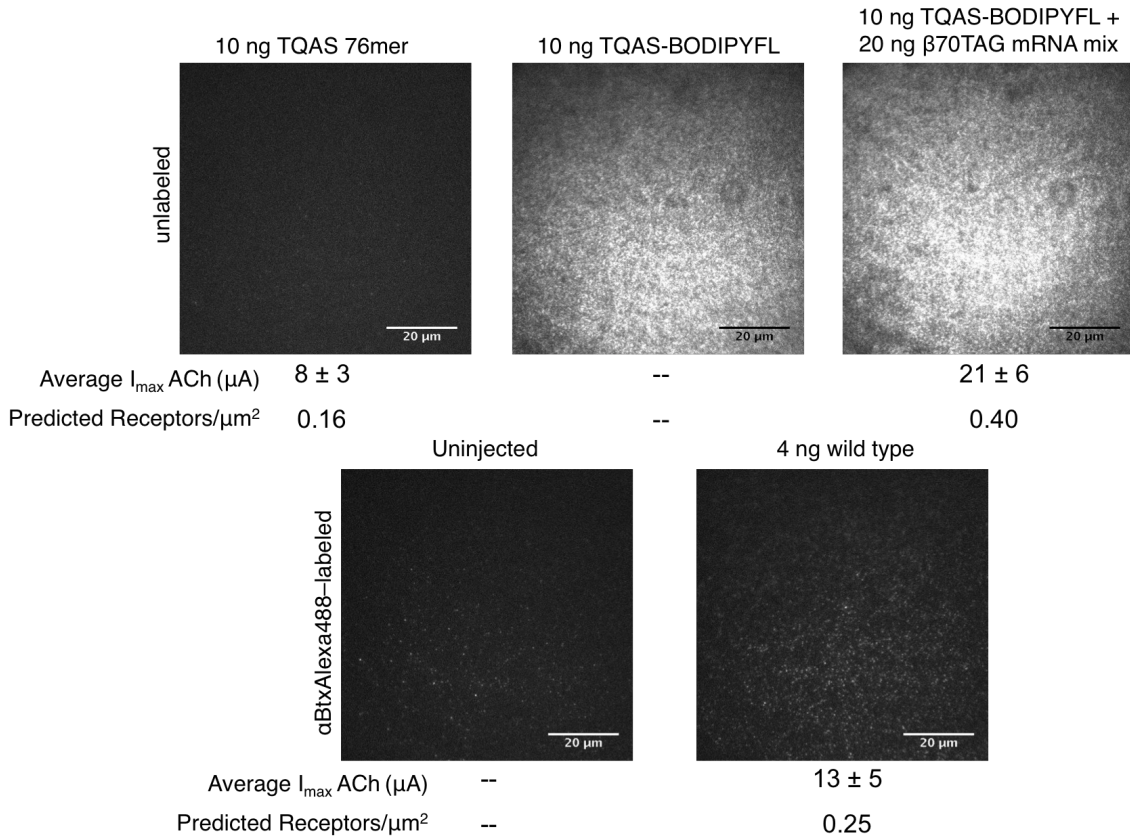


Figure 6.2. TIRF images and average whole cell currents from *Xenopus laevis* oocytes incubated for 24 hrs after the injection condition noted over each panel. Panels are representative images from the same cell batch that the electrophysiology recordings were made on. I_{max} values are for a saturating ACh concentration (1000 μ M). Receptor density on the cell surface is predicted from macroscopic currents observed from that cell batch, using previously reported assumptions.⁹ Brightness range for all panels is 100 counts (black) to 3000 counts (white).

tRNA, 24 hr incubation. Pantoja conditions: 25 ng total of 2:5:1:1 α/β 19'GGGU/ γ/δ

mRNA mix, 12.5 ng of YFaFS_{AAAC}-Lys-BODIPYFL tRNA, 24 hr incubation).

Subsequent imaging using the same tRNA employed by Pantoja (YFaFS_{AAAC}-Lys-BODIPYFL tRNA) gave similar background fluorescence levels.

The fluorescence observed has a relatively uniform, granular appearance (Figure 6.2) that is completely stationary, inconsistent with freely diffusing fluorophores within

the cytosol. We speculate that the fluorophores are most likely either embedded in the plasma membrane, with minimal lateral diffusion, or are adhered to the glass coverslip.

In the Pantoja and co-workers report, some background fluorescence was observed from cells injected with tRNA-BODIPYFL alone, but this was observed at significantly lower puncta densities than the mRNA + tRNA-BODIPYFL conditions ($0.007 \pm 0.002/\mu\text{m}^2$ for tRNA alone, compared with $0.021 \pm 0.003/\mu\text{m}^2$ for mRNA + tRNA).⁹ The fluorescence observed in the images obtained here (tRNA only and tRNA + mRNA conditions) was too dense for individual puncta to be counted.

Surface expression of receptors incorporating Lys-BODIPYFL was confirmed by electrophysiology (Figure 6.2). High levels of reacylation and/or readthrough are seen for nonsense suppression at this site, as indicated by a control in which unacylated 76mer tRNA is injected in place of tRNA-Lys-BODIPYFL. Assuming a typical average plasma membrane surface area of an oocyte and uniform membrane adhesion to the glass coverslip under imaging conditions, and using the known single channel conductance for this receptor, receptor density on the plasma membrane can be estimated from whole cell current magnitudes.⁹ These estimates (Figure 6.2) indicate that when currents from reacylation are subtracted, densities on the order of $0.2 \text{ receptors}/\mu\text{m}^2$ are expected for receptors bearing Lys-BODIPYFL under these conditions. While Pantoja only observed puncta at $\sim 1/3$ the density predicted by whole-cell currents, the larger currents observed here should still yield greater puncta densities than the $0.021 \pm 0.003/\mu\text{m}^2$ observed by Pantoja, with approximately the same amount of tRNA injected. While our failure to distinguish between tRNA only and tRNA + mRNA images is apparently due to high

background fluorescence from tRNA, we are not experiencing uniquely low levels of receptor expression relative to the quantity of fluorescent tRNA injected.

A more sensitive CCD camera was used for these experiments than in the Pantoja study, leading us to wonder whether the higher background fluorescence levels we observed were simply due to greater camera sensitivity, such that brighter punctate features were not visible over the high background observed. However, no new image features emerged (punctate or otherwise) when imaging at lower excitation laser intensities or shorter image integration times: we simply obtained dimmer images with the same uniform granular fluorescence pattern. To help reference the fluorescence intensities we observed, we labeled cells expressing wild type receptors with Alexa488-labeled α -bungarotoxin (α BtxAlexa488, from Life Technologies). This conjugate has approximately one dye per α -bungarotoxin molecule⁹, and there are two α -bungarotoxin binding sites per receptor. Alexa488 has a similar fluorescence emission profile as BODIPYFL and was reported to have approximately three times the brightness of BODIPYFL when each dye was conjugated to streptavidin.¹⁶ Some punctate α BtxAlexa488 background labeling was seen on uninjected cells (Figure 6.2), but more punctate fluorescence was seen for labeled cells expressing wild type receptors (Figure 6.2). These puncta are dimmer than the fluorescence background seen in cells injected with tRNA-Lys-BODIPYFL, indicating that imaging fluorescent receptors against this background will not be possible.

We wondered if optimizing the amount of mRNA and tRNA injected might yield conditions under which fluorescent receptors could be resolved above the background. As expected, the level of background fluorescence is dependent on the amount of tRNA

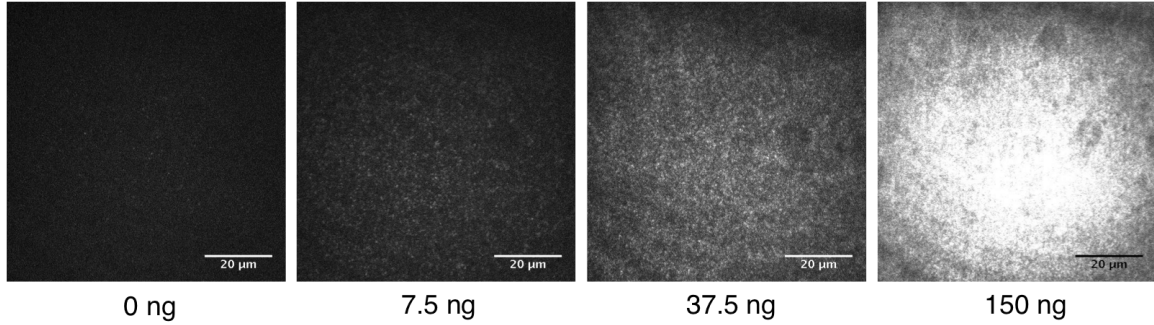


Figure 6.3. TIRF images from oocytes injected with varying amounts of TQAS-BODIPYFL. Brightness range for all panels is 100 counts (black) to 1500 counts (white).

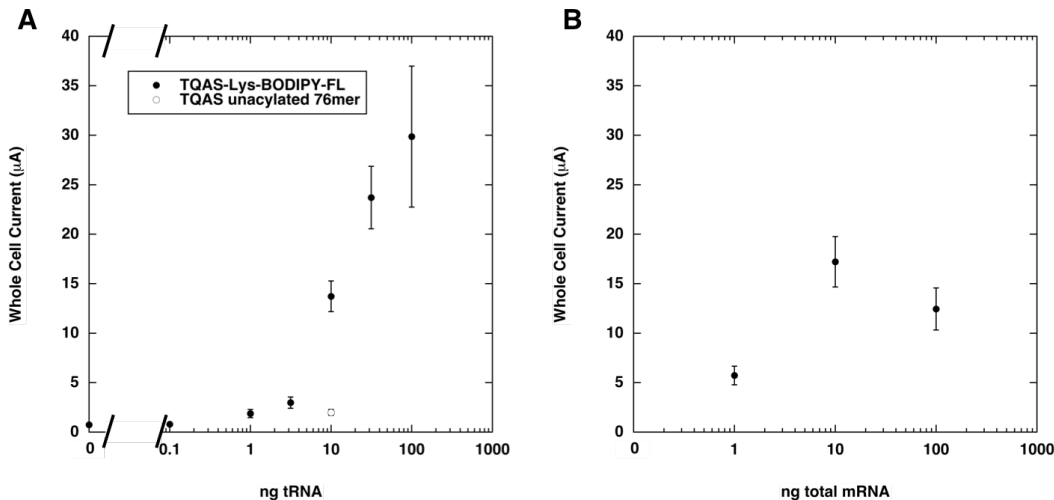


Figure 6.4. Whole cell currents from cells injected with various quantities of mRNA and tRNA. Incubation time is 24 hrs. **(A)** tRNA titration; all cells injected with 20 ng β 70TAG mRNA mix and the indicated quantity of tRNA. **(B)** mRNA titration; all cells injected with 37.5 ng TQAS-BODIPYFL and the indicated quantity of β 70TAG mRNA mix.

injected (Figure 6.3). Surface expression levels (judged by measuring whole-cell currents) increase when injecting 10 ng rather than 1 ng of mRNA, but do not get any larger with 100 ng of mRNA (Figure 6.4A). Expression levels continually increased over the entire range of tRNA injection amounts tested (Figure 6.4B). These data suggest that tRNA is the limiting factor for receptor expression, and unfortunately it must be supplied at an enormous excess: a rough estimate of surface expression levels from macroscopic currents suggest that 3×10^4 tRNA molecules were injected per receptor ultimately

present on the cell surface. This estimate is for 24 hrs after injection of 20 ng total β 70TAG mRNA and 10 ng TQAS-BODIPYFL tRNA. Comparison of absorbance values at 260 nm (λ_{max} for RNA) and 510 nm (λ_{max} for BODIPYFL) on TQAS-BODIPYFL tRNA using known molar absorptivity values indicate a 1:3 molar ratio of BODIPYFL to tRNA. This confirms that there is not an excess of BODIPY fluorophores in the tRNA solution and is consistent with the presence of some unacylated tRNA in the TQAS-BODIPYFL solution.

We wondered whether the background fluorescence we observed was from free BODIPY fluorophores, from Lys-BODIPY that had hydrolyzed off of the tRNA, or from fluorophores still attached to tRNA. The free backbone amine of Lys-BODIPY on the tRNA was protected with an NVOC group to minimize hydrolysis of the amino acid from the tRNA during preparation and storage, and was photolyzed immediately prior to oocyte injection. We compared fluorescence from oocytes injected under standard conditions to injection of tRNA-Lys-BODIPYFL-NVOC (i.e., the NVOC group was not photolyzed prior to injection) (Figure 6.5). Fluorescence was comparable for both

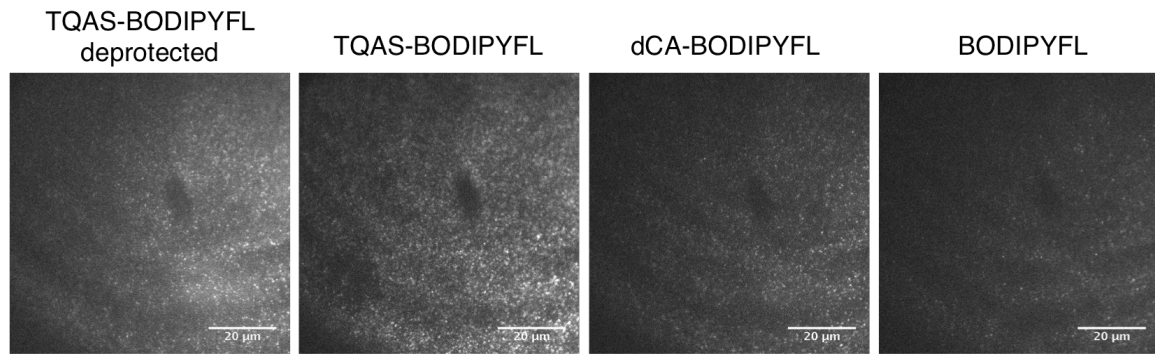


Figure 6.5. TIRF images from oocytes injected with various BODIPYFL species. All cells were injected with 0.1 pmol of the indicated species (= 2.5 ng TQAS-BODIPYFL). In the first panel TQAS-BODIPYFL was NVOC-deprotected by photolysis. All other samples were injected without photolysis. The common dark spot and interference pattern observed in all images is due to irregularities in the TIRF illumination field. Brightness range for all panels is 100 counts (black) to 3000 counts (white).

deprotected and NVOC-protected tRNA. We anticipate that much less of the Lys-BODIPYFL will hydrolyze from the tRNA in its NVOC-protected form, so background fluorescence from free Lys-BODIPYFL is not anticipated to be the issue.

To assess whether the nature of the moiety BODIPY is appended to changes the background signal, we also examined fluorescence from cells injected with the dinucleotide dCA appended to Lys-BODIPY (dCA-Lys-BODIPYFL-NVOC) and fluorescence from free BODIPYFL. Interestingly, somewhat less fluorescence was seen for dCA-BODIPY than for tRNA-BODIPY and less fluorescence still was seen for free BODIPY. It is possible that the hydrophobic BODIPY fluorophore partitions to the lipid-rich yolk of the oocyte unless tethered to a large hydrophilic moiety such as tRNA.

Cursory investigations using a different objective lens (100x, 1.65NA) and imaging on a different fluorescence microscope (Olympus IX81) also revealed similar images for tRNA-BODIPY only and for tRNA-BODIPY + mRNA conditions. These results suggest that optical issues (i.e., laser focusing, TIRF illumination, collection of fluorescence by the objective lens) were not likely to be the source of the background observed.

6.3.2 Optimization of vitelline membrane removal

Oocytes imaged by TIRF microscopy were first stripped of their vitelline membrane, a protein-rich layer of extracellular matrix surrounding the plasma membrane. Using a standard technique, this membrane was removed manually with forceps after osmotic shrinking of the oocyte. The plasma membrane of *Xenopus laevis* oocytes is heavily studded with microvilli extending through the extracellular matrix,¹⁷ and previous

studies imaging devitellinized oocytes have suggested that the microvilli may be sheared during the standard manual devitellinization protocol.¹⁸ We wondered whether the high fluorescent background observed could have been due to fluorophore leakage out of the oocyte via tears in the plasma membrane caused by devitellinization.

Other protocols have been reported for vitelline membrane removal that aim to preserve plasma membrane integrity. Two of these methods were investigated for their ability to reduce background fluorescence in this system. Both protocols were originally reported to improve the reliability of high-resistance seal formation for single channel patch clamp experiments. The first method aims to remove adhesions between the plasma membrane and vitelline membrane by enzymatic digestion.¹⁹ For 60 min, cells are exposed to 4 mg/mL collagenase and 4 mg/mL hyaluronidase, after which cells are shrunk by exposure to hypertonic media. Upon shrinking, the vitelline membrane (“detached,” though still intact) appears separated from the plasma membrane, while in the absence of enzymatic treatment the vitelline membrane wrinkles and shrinks together with the plasma membrane. This enzymatic treatment was conducted immediately prior to manual devitellinization and imaging.

In the second method, the vitelline membrane is completely digested enzymatically, so that manual stripping is unnecessary.²⁰ Digestion is achieved by protease treatment (0.05 mg/mL, Type VIII, Sigma) with gentle shaking. Swelling followed by disappearance of the vitelline membrane can be seen by light microscopy. While the literature report of this protocol cites complete digestion of the vitelline membrane within 3-4 min, we found that 30 min was required. To test whether membrane-expressed receptors are affected by the protease treatment, we performed

electrophysiology (2-electrode voltage clamp) immediately following digestion on oocytes expressing the wild-type muscle nAChR. We recorded an EC₅₀ for ACh ($17.4 \pm 0.7 \mu\text{M}$), only slightly shifted from untreated cells ($23.2 \pm 0.9 \mu\text{M}$, from the same cell batch), and observed similar current magnitudes, suggesting that receptors are still functional.

These two devitellinization conditions were compared with standard manual devitellinization by imaging cells injected with the small organic dye fluorescein (1 pmol/oocyte – we inject approximately this molar quantity of tRNA per oocyte in standard experiments). Fluorescence from standard devitellinization conditions and the collagenase/hyaluronidase reduced adhesion method gave similar, moderate levels of fluorescence (Figure 6.6A, B). The protease devitellinization condition, however, gave

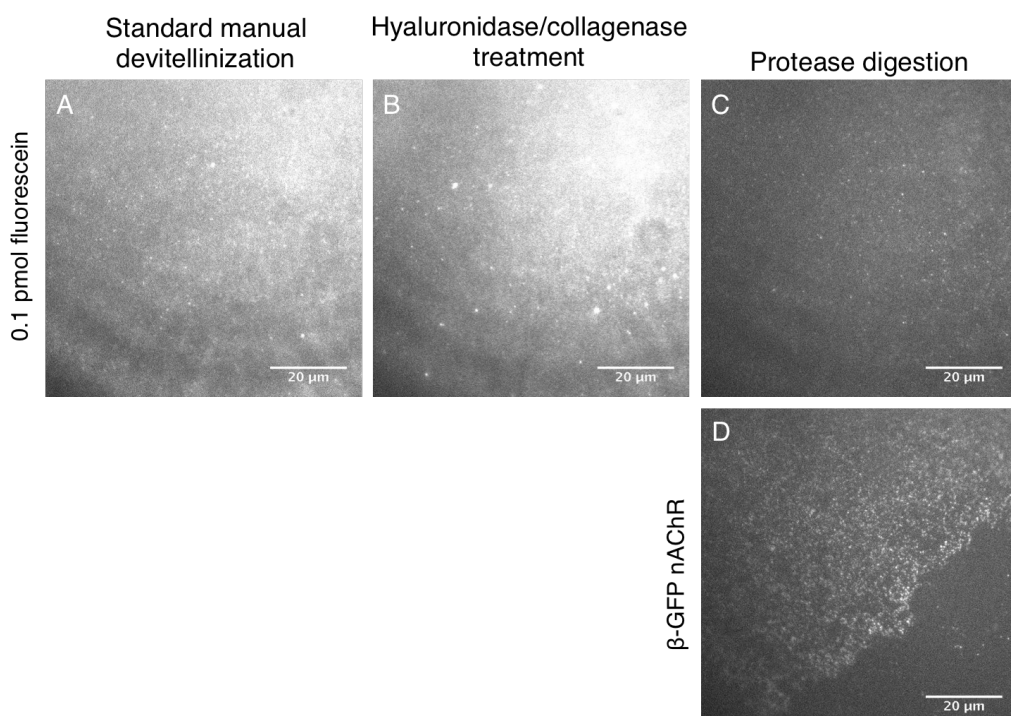


Figure 6.6. TIRF images from oocytes prepared under various devitellinization conditions. In top panels cells were injected with 0.1 pmol fluorescein and devitellinized by the method indicated. In the bottom panel the cell was injected with nAChR mRNA tagged with GFP on the β subunit. Brightness range for all panels is 100 counts (black) to 4000 counts (white).

very low fluorescence levels across many cells, consistent with less leakage of the dye from the oocyte (Figure 6.6C). To confirm that the plasma membrane was indeed exposed and adhered to the coverslip in the protease-digested cells, we imaged protease-treated cells expressing nAChRs with GFP appended to the $\beta 1$ subunit (Figure 6.6D). Indeed, we observed patches of fluorescence from these cells. Of note, inspection in brightfield mode (data not shown) suggested that these crisply delineated bright patches likely correspond with adhered sections of membrane.

With respect to delineated regions of fluorescence, the opposite result was observed in images from select oocytes prepared either by standard manual devitellinization or hyaluronidase/collagenase treatment prior to manual stripping. In isolated cases, regions where the plasma membrane did not appear tightly adhered to the glass coverslip (by inspection in brightfield mode) had higher fluorescence levels than adjacent regions that appeared to be adhered (Figure 6.7). The inverse is expected for TIRF imaging of the membrane, as only fluorophores within ~100 nm of the coverslip

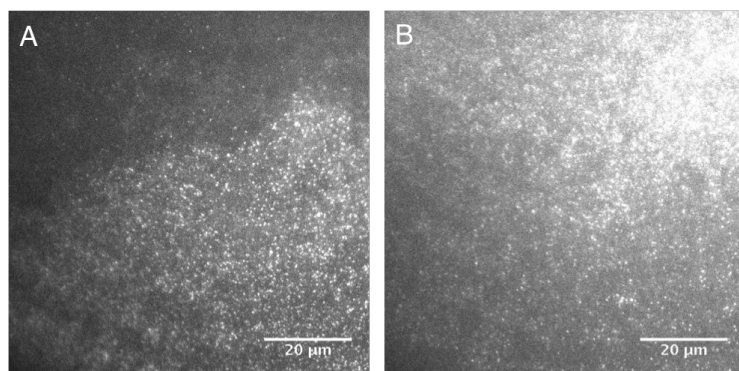


Figure 6.7. TIRF images from oocytes injected with 10 ng TQAS-BODIPYFL and 10 ng $\alpha 70$ TAG mRNA mix, imaged at apparent boundaries of plasma membrane adhesion to the glass coverslip. Adhesion to the coverslip is inferred from inspection under bright field illumination (not shown). **(A)** Oocyte devitellinized manually after hyaluronidase/collagenase treatment. Top of this field (dark region) appears adhered to the coverslip, while the bottom (brighter region) does not. **(B)** Oocyte devitellinized by standard manual technique without enzymatic treatment. Bottom of this field (darker region) appears adhered to the coverslip, while the top (brighter region) does not. Brightness range for both panels is 100 counts (black) to 4000 counts (white).

surface will be illuminated. This could be consistent with leakage of fluorophores from the cytosol into the space between the coverslip and plasma membrane, whereas diffusion of fluorophores into adhered regions is more restricted.

The protease condition seems promising for reducing background fluorescence. However, when imaging protease-treated cells injected with tRNA-BODIPY alone or with tRNA-BODIPY + mRNA, no difference was observed; both yielded comparable levels of punctate fluorescence (Figure 6.8), albeit with lower levels of background fluorescence than in earlier attempts (i.e., Figure 6.2).

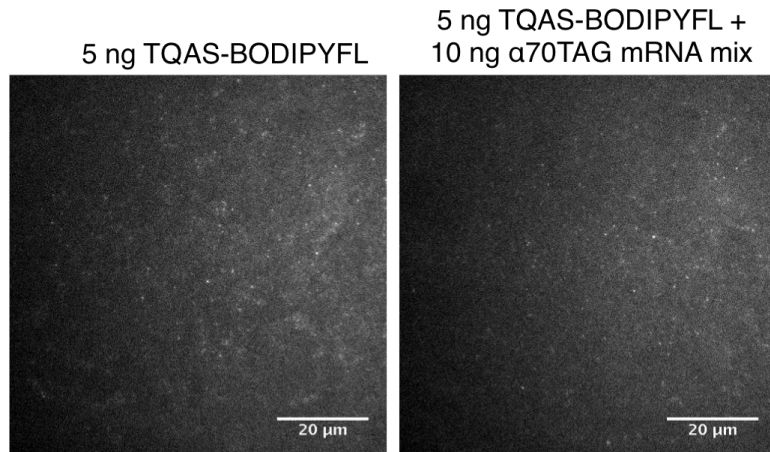


Figure 6.8. TIRF images from cells subjected to protease devitellinization conditions. Injection conditions are indicated above panels. Brightness range for both panels is 500 counts (black) to 3000 counts (white).

It should be noted that after significant practice at the standard technique using forceps to manually strip the vitelline membrane, low background fluorescence levels were sometimes obtained (Figure 6.9) – roughly at the same low background fluorescence levels seen in the protease digestion experiments. Good oocyte health may also be critical for this result, though this was not investigated systematically. With extremely precise technique, it is plausible that this method could yield satisfactorily low

levels of fluorescence, as were evidently obtained in the Pantoja et al. study.⁹ However, even at the low background fluorescence levels sometimes obtained in the experiments described here, no difference was ever observed between tRNA only and tRNA + mRNA conditions, as the Pantoja study describes.

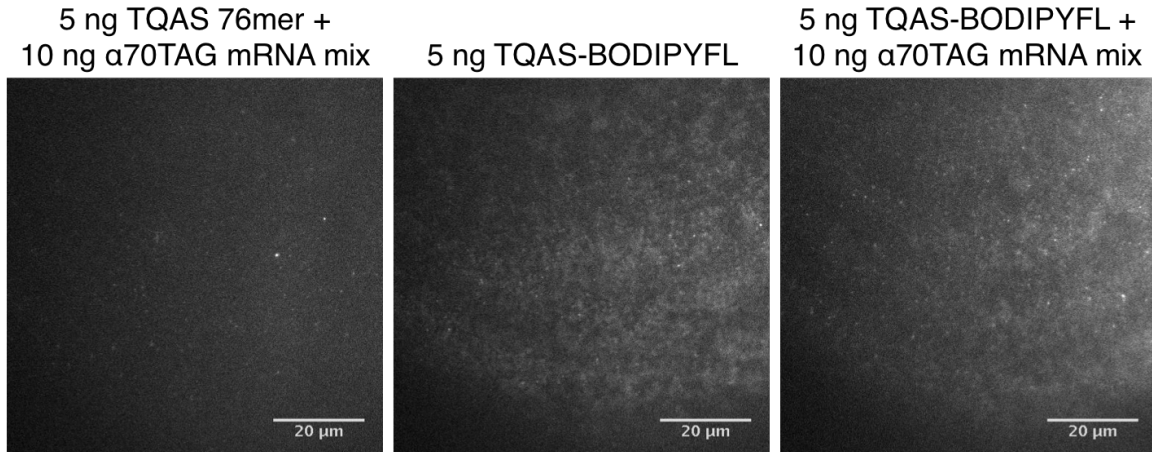


Figure 6.9. TIRF images showing low background from standard manual devitellinization conditions. Injection conditions are indicated above panels. Brightness range for all panels is 250 counts (black) to 3500 counts (white).

6.3.3 Two-color imaging and single puncta analysis

As receptors could not be convincingly visualized above fluorescent background in the single color imaging experiments described above, we turned to two-color FRET imaging. FRET should allow a means to distinguish receptors from background as it should only be observed from receptors bearing two fluorophores. In these experiments, we used Alexa488-labeled α -bungarotoxin to label receptors with this donor fluorophore, which could be excited by the same 488 nm laser used for the BODIPYFL experiments. The acceptor fluorophore used was BODIPY558 (Figure 6.1), incorporated as a Lys-BODIPY558 side chain at the γ 70 site. Here we used the opal suppressor tRNA TQOpS'.^{15,21} In these experiments, oocytes expressing γ 70Lys-BODIPY558 are labeled

with Alexa488- α -bungarotoxin immediately prior to imaging. It should be noted that there are two α -bungarotoxin binding sites on the muscle-type nAChR: at α/γ and α/δ interfaces. This leads to a complex FRET scenario with the potential for two donor fluorophores and a single acceptor. Based on rough modeling from the torpedo nAChR structure,²² these two donor-acceptor distances are expected to be roughly 40 Å and 60 Å. However, only 74% of α -bungarotoxin molecules are reported to be Alexa488-labeled in the supplied conjugate, and some of these donor fluorophores are likely bleached during sample handling and focus, such that 48% of Alexa488- α -bungarotoxin labeled receptors are reported to give only a single photobleaching step under similar conditions to those used here.⁹ Hence, some receptors will be expected to have two Alexa488 donor fluorophores, while many should have only one.

Two-color imaging is enabled by use of the OptoSplit II image splitter, which allows side-by-side imaging of the same field at two wavelengths. Excitation is identical to the experiments described above: a 488 nm laser is used to excite donor fluorophores. The fluorescence emission light path is split by a dichroic mirror and the two resulting light paths transit different bandpass filters, allowing for selection of the donor and acceptor emission wavelengths of interest, which are projected side-by-side onto the camera.

Corresponding puncta in the two channels were identified using IDL scripts written by Taekjip Ha's lab at the University of Illinois (details in Methods section), allowing the intensity of a given punctum in both channels to be determined as a function of time. Puncta with step-like fluorescence intensities were considered for further analysis. For all conditions, cells were labeled with Alexa488- α -bungarotoxin. For a

control in which cells are injected with γ 70TGA mRNA and unacylated 76mer tRNA, fluorescence in the donor channel is generally consistent with single step photobleaching, with little or no fluorescence in the corresponding acceptor channel (Figure 6.10). These donor fluorophores are likely the result of both nonspecific labeling of Alexa488- α -bungarotoxin and of labeling “background” receptors generated from nonsense suppression by tRNA acylated *in vivo*.

5 ng TQOpS' 76mer tRNA
+ 20 ng γ 70TGA mRNA mix

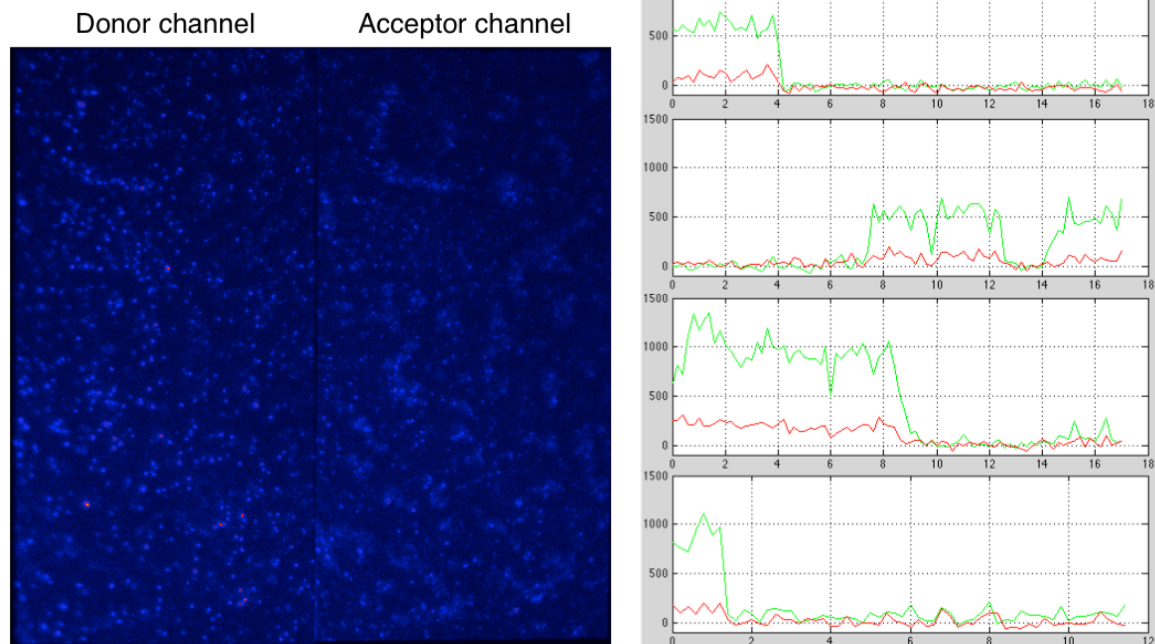


Figure 6.10. Two-color fluorescence image and fluorescence traces from selected puncta of a cell injected with unacylated TQOpS' 76mer tRNA and labeled with α BtxAlexa488. Entire fluorescence image is shown with the same “heatmap” false-color scheme. Donor channel and acceptor channel represent the same field of view imaged at different emission wavelengths. Fluorescence traces show donor channel intensity (green) and acceptor intensity (red) for the same punctum. Horizontal axis is time (s) and vertical axis is intensity (counts). Note the small degree of spectral bleedthrough of donor fluorescence into the acceptor channel (visible in both images and in traces).

Cells injected with γ 70TGA mRNA and tRNA-BODIPY558 do have puncta with fluorescence in both donor and acceptor channels, as would be expected for FRET (Figure 6.11). No clear hallmarks of single molecule FRET were observed however, such as anticorrelated donor and acceptor fluorescence intensities – specifically a jump in donor fluorescence intensity upon acceptor blinking or bleaching.

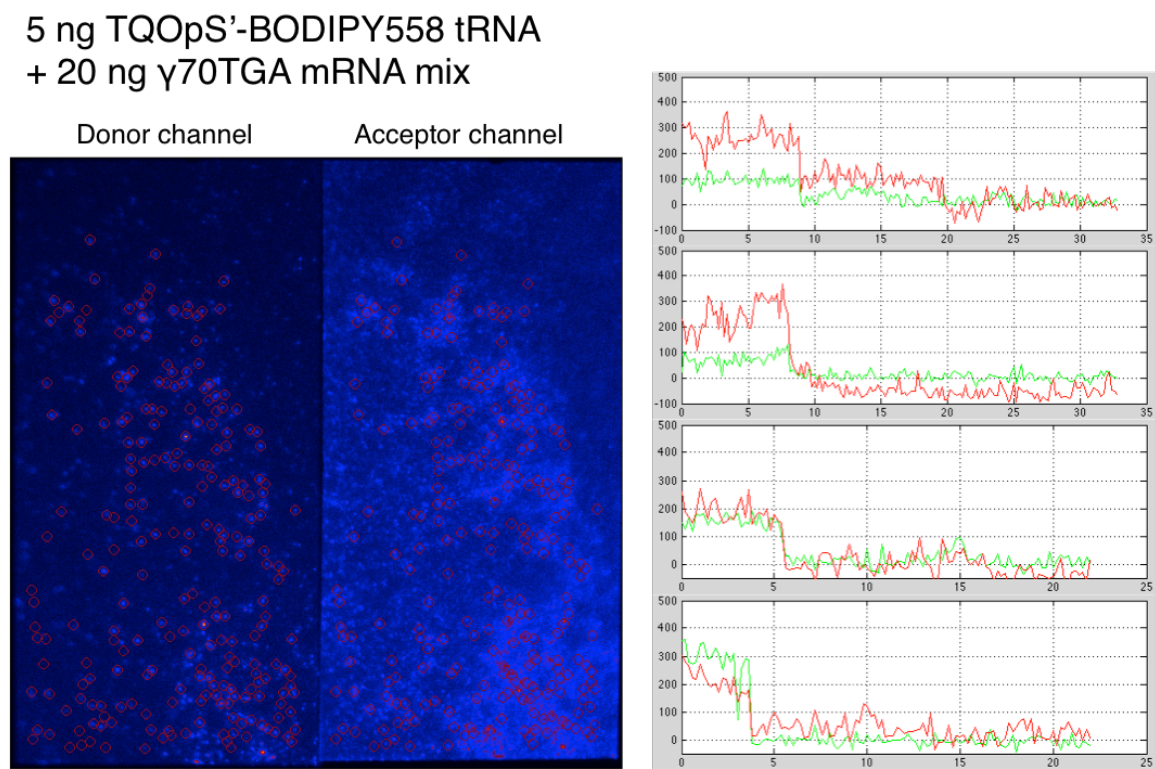


Figure 6.11. Two-color fluorescence image and fluorescence traces from selected puncta of a cell injected with TQOpS'-BODIPY558 tRNA and γ 70TGA mRNA mix and labeled with α BtxAlexa488. Puncta recognized by IDL scripts are surrounded by red circles in this image. Entire fluorescence image is shown with the same “heatmap” false-color scheme. Donor channel and acceptor channel represent the same field of view imaged at different emission wavelengths. Fluorescence traces show donor channel intensity (green) and acceptor intensity (red) for the same punctum. Horizontal axis is time (s) and vertical axis is intensity (counts).

Critically, very similar fluorescence traces were seen for puncta from control cells injected with tRNA-BODIPY558 only (no receptor mRNA) (Figure 6.12). For this condition, sparse Alexa488 donor fluorophores are likely present from nonspecific labeling by Alexa488- α -bungarotoxin. High background from BODIPY558 in the acceptor channel raises the possibility of nonspecific spatial overlap of fluorophores. However, fluorescence intensities in the donor and acceptor channels are correlated in many cases, suggesting either specific association of α -bungarotoxin and BODIPY558 (a

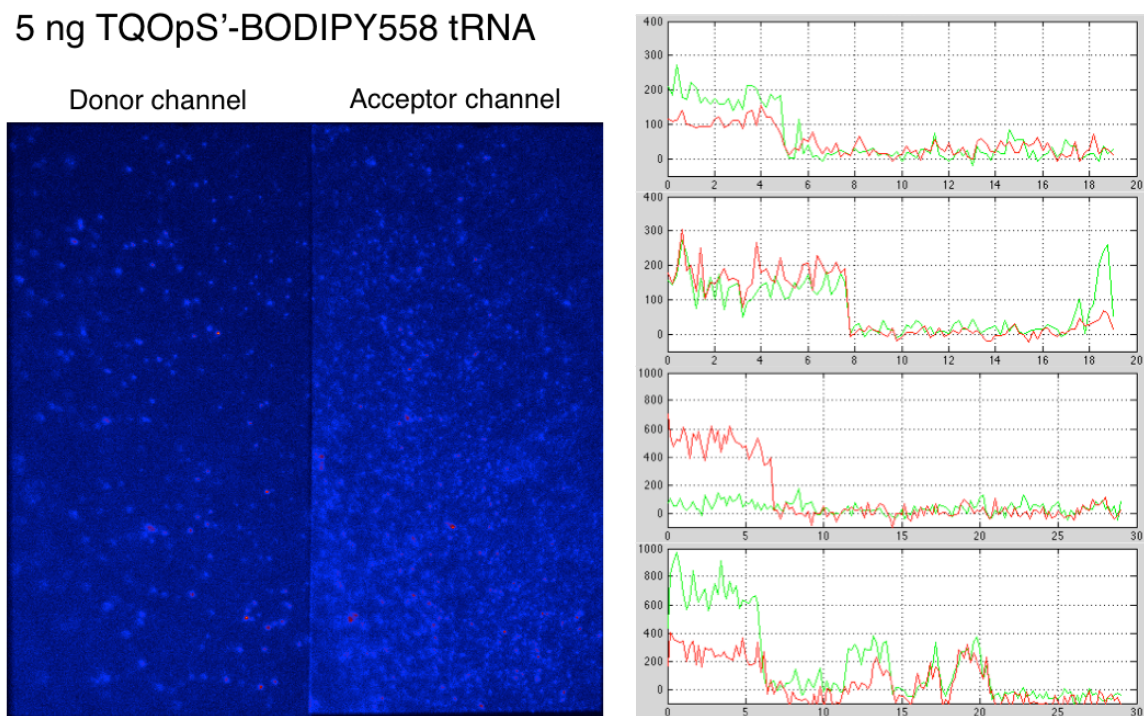


Figure 6.12. Two-color fluorescence image and fluorescence traces from selected puncta of a cell injected with TQOpS'-BODIPY558 tRNA and labeled with α BtxAlexa488. Entire fluorescence image is shown with the same “heatmap” false-color scheme. Donor channel and acceptor channel represent the same field of view imaged at different emission wavelengths. Fluorescence traces show donor channel intensity (green) and acceptor intensity (red) for the same punctum. Horizontal axis is time (s) and vertical axis is intensity (counts).

mechanism for this is unknown) or presence of another species with a broad fluorescence spectrum that spans both wavelength windows (inconsistent with either Alexa488 or BODIPY558). Local “breathing” of the plasma membrane in the vertical plane – in and out of TIRF illumination – is also plausible. Regardless of the origin of this effect, these control results suggest that the γ 70TGA mRNA + tRNA-BODIPY558 two-color fluorescence traces cannot be trusted as FRET. Presumably, “background” fluorescence from injected tRNA-BODIPY is once again the issue.

6.3.4 Attempts at fluorophore conjugation by azide-alkyne cycloaddition

In an effort to circumvent the high background fluorescence levels seen from injected tRNA-BODIPY, we attempted dye conjugation to surface-expressed receptors in a labeling step. The desired attributes of labeling were high specificity for the desired nAChR site and low nonspecific labeling of the cell surface. We selected copper-catalyzed azide-alkyne cycloaddition (“click chemistry”) as the ligation chemistry, which has extensive precedent for the labeling of biological samples.²³ In the envisioned ligation scheme, the alkyne is incorporated site-specifically into the nAChR as an unnatural amino acid side chain. Propargyl glycine (Pra), which is commercially available, (Figure 6.13A) was chosen and was ligated to tRNA by standard methods. This amino acid was effectively incorporated at the nAChR α 70 site (data not shown), which is known to be solvent-accessible.¹⁴

A principal concern when conducting copper-catalyzed click chemistry *in vivo* is the toxicity of copper to cells. We first sought to assess copper toxicity in our system before actually attempting the coupling reaction since, to our knowledge, copper-

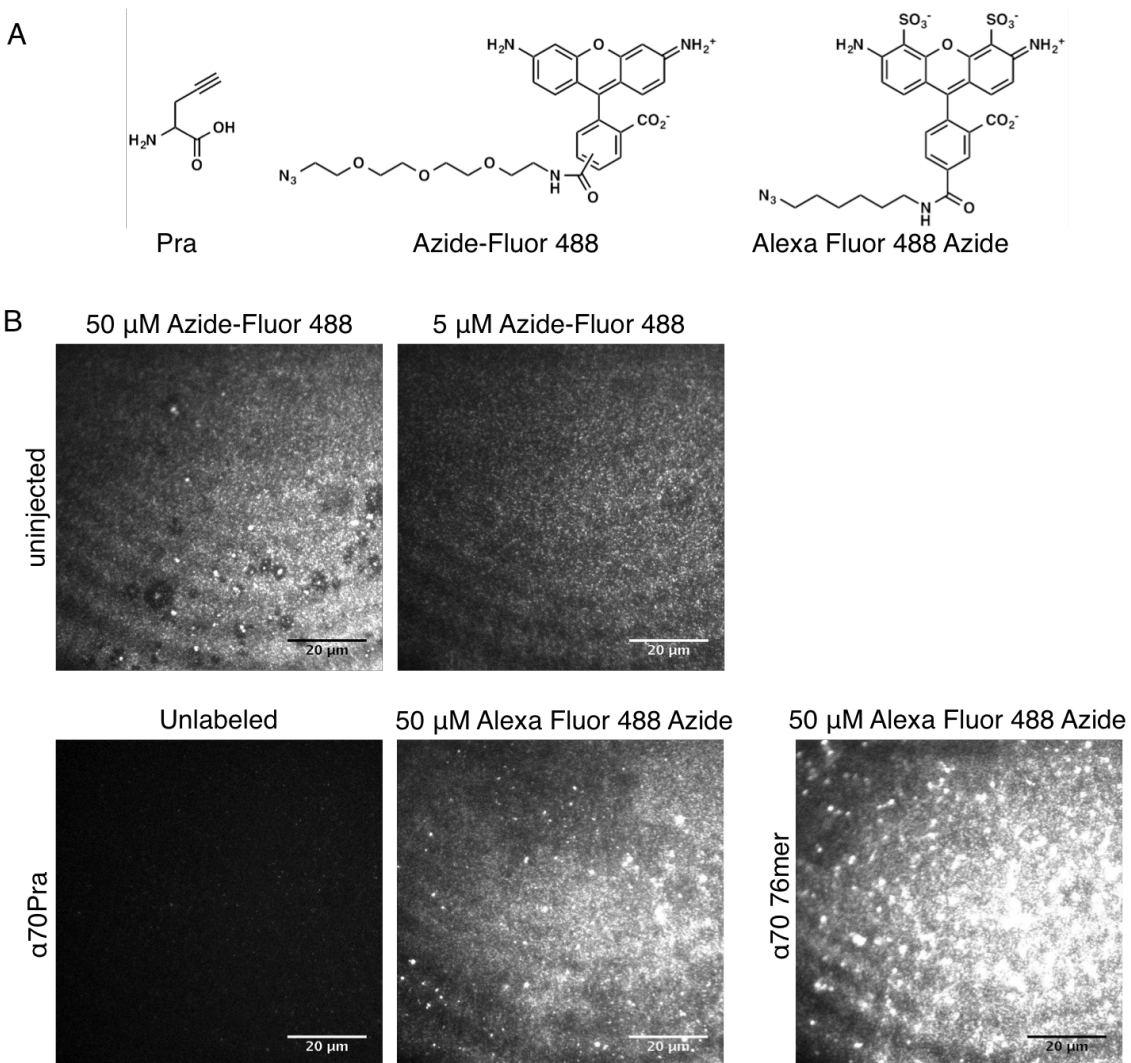


Figure 6.13. (A) Structures of propargyl glycine (Pra), Azide-Fluor 488, and Alexa Fluor 488 Azide. (B) TIRF images of oocytes labeled with azido dyes. In the top two panels, oocytes were simply incubated with the azido dye in ND96 solution. In the bottom three panels, oocytes were exposed to copper click conditions (Table 6.1 Condition 1) in the presence of azido dye in ND96.

Table 6.1. Analysis of cell health by whole cell electrophysiology after 1 hr exposure to copper-catalyzed azide-alkyne cycloaddition conditions.

	Untreated	Condition 1	Condition 2
Additives to ND96 incubation buffer		100 µM CuSO ₄ 500 µM THPTA 2.5 mM Na Ascorbate	1 mM CuSO ₄ 500 µM THPTA 2.5 mM Na Ascorbate
Resting potential (mV)	-68 ± 3	-27 ± 1	Cells appear swollen, ~1/3 ruptured after 1 hr
Leak Current (mA)	-0.008 ± 0.001	-0.13 ± 0.03	(not analyzed by electrophysiology)
EC ₅₀ (µM ACh)	23.9 ± 0.6	27.9 ± 0.6	

catalyzed click chemistry has not been reported on *Xenopus* oocytes. Oocytes expressing the wild type nAChR were exposed to standard click conditions for a typical reaction time of 1 hr (Table 6.1).²⁴ In these conditions, the copper is supplied as Cu(II), which is reduced to the active Cu(I) species *in situ* by ascorbate in the presence of the tris(3-hydroxypropyltriazolylmethyl)amine (THPTA) copper ligand.²⁴ While a reduction of the negative membrane resting potential and an increase in the leak current after incubation suggest some reduction in cell health, these cells survived a 40 min series of ACh applications to yield a dose-response curve with an EC₅₀ only modestly shifted from wild type. Tenfold higher concentrations of copper, however, result in cell death. These results suggest that cells could still be viable for *in vivo* imaging after exposure to standard copper click conditions, though some reduction in cell health is expected.

Next we assessed the viability of labeling by exposing oocytes to azide-conjugated dyes. We initially selected a commercially available rhodamine-derived azido dye, Azide-Fluor 488 (Figure 6.13A). High fluorescence levels were seen after exposing uninjected oocytes to a standard labeling concentration (50 µM) for 45 min, even after copious washes (5x) with buffer. A tenfold lower concentration of dye (lower than what is ideal for *in vivo* labeling) also gave appreciable levels of fluorescence (Figure 6.13B). We reasoned that a charged, more hydrophilic dye might give less nonspecific labeling, so we tested another commercially available azido dye, AlexaFluor 488-Azide (Figure 6.13B). Unfortunately we also observed high levels of background fluorescence for this dye. Indistinguishable fluorescence levels were seen for α70Pra-expressing cells treated with this dye in a labeling solution (Table 6.1, Condition 1) and for identically treated cells injected with α70TAG mRNA and unacylated 76mer tRNA

(Figure 6.13B). We conclude that these azido dyes give unacceptably high levels of nonspecific labeling to be viable in this system.

6.3.5 Design and synthesis of a fluorescence-quenched tRNA

Pursing the original scheme of fluorophore incorporation by nonsense suppression, we sought an alternative approach to reduce high background fluorescence from injected fluorescent tRNA. We reasoned that we might modify the tRNA-BODIPY in such a way that the BODIPY's fluorescence was quenched until the dye is incorporated into the protein of interest. Toward this end, we employed a “dark quencher” – a molecule that efficiently dissipates energy nonradiatively, and in this application acts as a FRET acceptor for a donor fluorophore.²⁵

Positioning of this quencher on the tRNA is expected to be critical: it must be in sufficiently close proximity to the BODIPY fluorophore at the tRNA’s 3’ terminus to efficiently quench its fluorescence, yet it must be in a position tolerated by the ribosome during translation. We reasoned that the 5’ terminus of the tRNA was a sensible site for quencher incorporation, allowing for relatively facile quencher incorporation and close proximity to BODIPY (Figure 6.14). Tolerance of a large structural modification to this region was largely unexplored, but at least modest changes are tolerated: removal of a native tRNA’s 5’ phosphate has a small effect on the rate of translation,²⁶ and we routinely use suppressor tRNAs bearing an unnatural 5’ triphosphate.²⁷

The Iowa Black FQ quencher, a dark quencher available from Integrated DNA Technologies, was selected for these experiments. The structure of this quencher has not been released by the manufacturer, but it is reported to have a molecular weight of 442.4

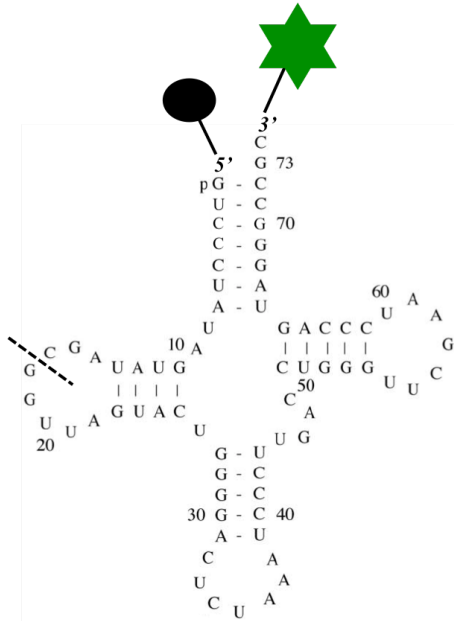


Figure 6.14. Schematic of Q-TQAS-BODIPYFL quenched fluorescent tRNA. Dashed line: disconnection of 16mer and 57mer component fragments. Black oval: Iowa Black FQ dark quencher. Green star: Lys-BODIPYFL.

g/mol and an absorbance maximum at 531 nm, which is appropriate for good spectral overlap with BODIPYFL fluorescence emission. To assemble a tRNA bearing this quencher group, we obtained a custom 16mer oligoribonucleotide corresponding to the first 16 bases of the TQAS suppressor tRNA's 5' terminus with the Iowa Black FQ quencher appended to its 5' end (Integrated DNA Technologies). This oligo was then ligated to a transcribed 57mer oligo comprising the remainder of TQAS, minus the final two 3' nucleotides, to yield the quencher-tagged "74mer." Prior to the ligation, the 57mer was treated with phosphatase to remove its 5' triphosphate, then treated with polynucleotide kinase to add a single 5' phosphate, rendering this oligo competent for ligation to the 16mer by T4 RNA ligase. The ligation product was purified by preparative polyacrylamide gel electrophoresis (PAGE). This "74mer" could then be ligated to aminoacylated dCA by standard methods.²⁷ In this fashion, full length "76mer"

TQAS tRNA bearing a 5' Iowa Black FQ quencher and acylated at its 3' end with Lys-BODIPYFL (Q-TQAS-BODIPYFL) was prepared, as was 76mer tRNA bearing a 5' quencher, but no 3' amino acid (Q-TQAS 76mer) for use in control experiments. Identity of the products was confirmed by MALDI-MS and also by UV-Vis absorption spectra (Figure 6.15). These spectra confirm that the Iowa Black FQ quencher absorbance should have good spectral overlap with BODIPYFL emission (~515 – 560 nm).

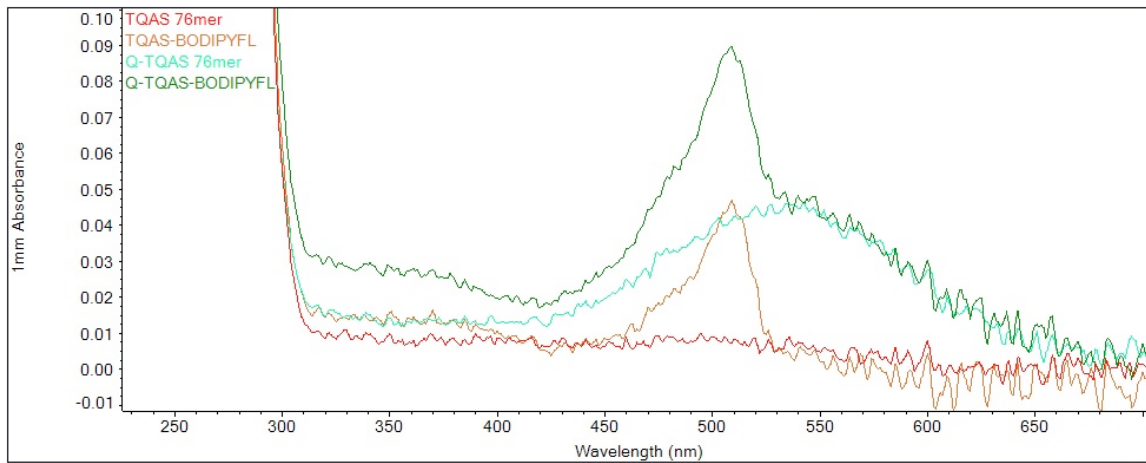


Figure 6.15. UV-Vis spectra of tRNAs

Next we sought to assess the translational competence of tRNA bearing a 5' quencher. Q-TQAS-BODIPYFL tRNA was evaluated for nonsense suppression at the β 70 site. Encouragingly, we observed appreciable expression of receptors by electrophysiology when using this tRNA, though the expression level was reduced relative to the condition for regular TQAS-BODIPYFL tRNA lacking the quencher (Figure 6.16). Q-TQAS 76mer conditions showed significantly less expression than those for acylated tRNA, suggesting that reacylation still low for tRNA with a 5'

quencher. In another experiment, we observed that Q-TQAS-Trp tRNA was competent for tryptophan incorporation by nonsense suppression at the α W149 site (data not shown).

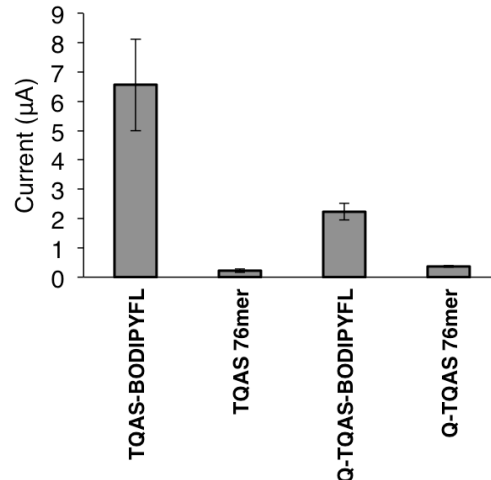


Figure 6.16. Maximal whole cell currents from cells injected with 10 ng β 70TAG nAChR mRNA mix and 10 ng of the specified tRNA. Cells were incubated for 24 hrs after injection and assayed with a saturating concentration of ACh (1000 μ M).

Table 6.2. tRNA fluorescence readings. All samples are 16 μ M in 1 mM NaOAc buffer (pH 4.5). Fluorescence readings were taken on 5 μ L samples using the Flexstation III fluorescent plate reader with excitation at 485 nm and emission filtered to 520 nm.

	520 nm fluorescence (RFU)
Buffer	0.413
TQAS-BODIPYFL	1840
Q-TQAS-BODIPYFL	512
TQAS 76mer	2.33
Q-TQAS 76mer	0.531

The efficiency of fluorescence quenching by Iowa Black FQ on the Q-TQAS-BODIPYFL tRNA was assessed using the Flexstation III fluorescent plate reader. We measured BODIPYFL fluorescence for tRNA samples and observed a 72% reduction in fluorescence for Q-TQAS-BODIPYFL relative to TQAS-BODIPYFL (Table 6.2). These

results do suggest fluorescence quenching of BODIPYFL by Iowa Black FQ on the tRNA, though appreciable fluorescence remains. To confirm that fluorescent impurities were not present (for example, RNAs with BODIPY but lacking the quencher), we performed fluorescence imaging of tRNA samples run out on a denaturing PAGE gel (Figure 6.17). For both TQAS-BODIPYFL and Q-TQAS-BODIPYFL tRNAs, we see only a single fluorescent species with emission at BODIPYFL wavelengths (515-545 nm), consistent with the anticipated tRNA species. Ethidium bromide staining allows for visualization of all nucleic acid species using a distinct fluorescence window (560-580 nm). This fluorescence window indicates multiple RNA species in both of these samples, which may account for hydrolysis of Lys-BODIPYFL off of the tRNA (this species is seen as a minor product by MALDI-MS). However, imaging of this gel suggests that there are not any other fluorescent species present in the sample that would account for “unquenched” fluorescence from Q-TQAS-BODIPYFL.

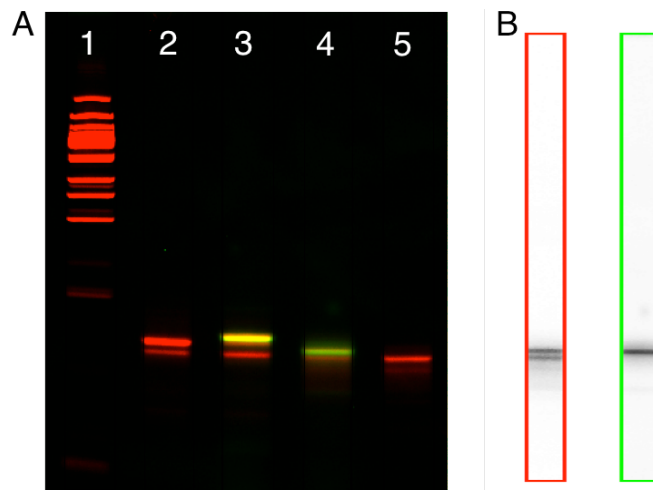


Figure 6.17. (A) Fluorescence image of an ethidium bromide-stained denaturing polyacrylamide gel of tRNA species. Lanes: (1) 50 bp DNA ladder; (2) TQAS 76mer; (3) TQAS-BODIPYFL; (4) Q-TQAS-BODIPYFL; (5) Q-TQAS 76mer. 0.2 µg RNA was loaded into each lane. Green false color is BODIPYFL fluorescence (515-545 nm) and red false color is ethidium bromide fluorescence (560-580 nm). (B) Ethidium bromide fluorescence channel (red border) and BODIPYFL fluorescence channel (green border) for Q-TQAS-BODIPYFL (Lane 4).

It is plausible that the quencher and BODIPY are too distant from each other on the tRNA for highly efficient quenching. In a representative tRNA (yeast Phe), the 5' phosphate and 3' hydroxyl groups are 24 Å distant from each other.²⁸ The 5' quencher and 3' BODIPY fluorophore will be more distant still – perhaps another 10 – 15 Å, if the Lys side chain and (unknown) quencher tether are included. The Förster radius of the BODIPYFL/Iowa Black FQ pair has not been reported, though it is plausible that at the ~25-40 Å separation of the BODIPY and Iowa Black on the tRNA, quenching by FRET may be in the 70% range suggested by our fluorescence measurements (Table 6.2).

Finally, we imaged oocytes injected with Q-TQAS-BODIPYFL. These oocytes were devitellinized by the standard manual method. At standard injection amounts (10 ng tRNA), we observed high levels of fluorescence for the tRNA-only condition and no discernible difference in fluorescence for tRNA + β70TAG mRNA (Figure 6.18A). Hence the original aim of the quenched tRNA to reduce background fluorescence levels to the extent that receptors can be distinguished from background has not been met. We also imaged cells injected with far less tRNA (0.2 ng) such that (background) fluorescence would be sparse and punctate. Again, we saw comparable levels of fluorescence (now punctate) for conditions with and without receptor mRNA (Figure 6.18B). Investigation of individual puncta brightness revealed similar values whether the cells were injected with Q-TQAS-BODIPYFL or TQAS-BODIPYFL (~3000 - 4000 counts). This is surprising, given the 72% reduction in bulk fluorescence measured for the quencher-bearing tRNA (Table 6.2). One explanation could be high levels of Lys-BODIPYFL hydrolysis off of the tRNA or some other form of tRNA degradation that liberates BODIPY from the quencher.

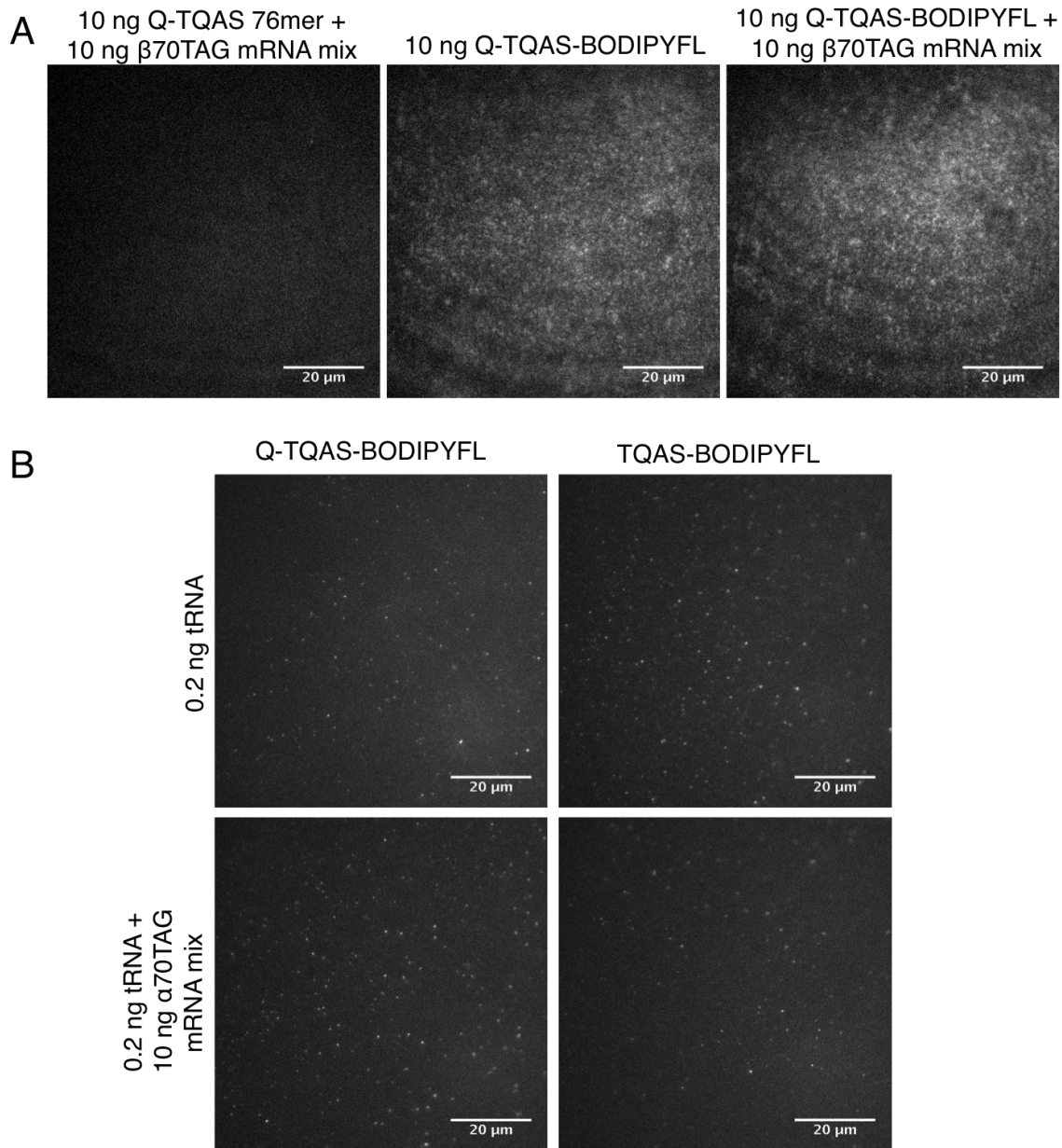


Figure 6.18. TIRF images of oocytes injected with fluorescence-quenched tRNA. **(A)** Q-TQAS-BODIPY tRNA still gives appreciable levels of background fluorescence. Brightness range: 400 counts (black) to 2000 counts (white). **(B)** TIRF images of cells injected with low amounts of tRNA. Puncta from all conditions have comparable brightness (~3000 – 4000 counts). Image brightness range: 100 counts (black) to 4500 counts (white).

6.4 Conclusions

Despite various efforts to circumvent background fluorescence from injected tRNA, we were unable to identify conditions in which fluorescent receptors could be visualized above background. Background fluorescence will be an inherent issue for *in vivo* imaging with fluorophore incorporation by nonsense suppression. TIRF microscopy offers a reduction of intracellular fluorescence seen, but in the experiments described in this chapter, background fluorescence, apparently at or near the glass surface, was still unmanageably high.

For future efforts on this project, several areas seem promising for improvements. First, clean plasma membrane preparation will likely be facilitated by only selecting cells of excellent health and by taking special care to use meticulous manual devitellinization technique. Second, dyes other than BODIPY that have greater photostability could be explored. A literature search revealed no studies using BODIPY dyes for single molecule FRET, likely due to the their limited photostability. Cy3 and Cy5 are the most widely used FRET pair for single molecule imaging,²⁹ and could be viable alternatives to BODIPY, though their slightly larger size could limit the efficiency of their incorporation into proteins by nonsense suppression. Finally, click chemistry conjugation of dyes could be viable using recently developed “turn on” fluorophores whose fluorescence intensity increases dramatically upon conjugation. This could offer a work-around for the high levels of nonspecific dye labeling observed in the fluorophore conjugation attempts described above.

6.5 Experimental

6.5.1 Molecular biology and in vivo expression

Nonsense suppression was performed using techniques described previously on the mouse muscle embryonic nAChR, ($\alpha 1$)₂ $\beta 1\gamma\delta$, in the pAMV vector.³⁰ Stage V-VI *Xenopus laevis* oocytes were injected with 1 ng total mRNA in a 2:1:1:1 ratio of $\alpha 1:\beta 1:\gamma:\delta$ for wild-type experiments. For nonsense suppression experiments, oocytes were typically injected with 10 ng tRNA and 10 ng total mRNA in a 10:1:1:1 ratio of $\alpha 1:\beta 1:\gamma:\delta$ for suppression in the α subunit, in a 2:5:1:1 ratio for suppression in the β subunit, or in a 2:1:5:1 ratio for suppression in the γ subunit. tRNAs bearing a 6-nitroveratryloxycarbonyl protecting group were deprotected prior to injection via irradiation with a 500 W Hg/Xe arc lamp, filtered with WG-334 and UG-11 filters prior to injection. Deprotection was carried out for 4 min only to limit the amount of BODIPY photobleaching.¹² Oocytes were injected for 24-48 hrs prior to imaging or electrophysiology.

6.5.2 Electrophysiology

Electrophysiology recordings were performed using the OpusXpress 6000A (Axon Instruments) at a holding potential of -60 mV. The running buffer was a Ca^{2+} free ND96 solution (96 mM NaCl, 2 mM KCl, 1 mM MgCl_2 , and 5 mM HEPES, pH 7.5). Agonist doses in Ca^{2+} -free ND96 were applied for 15 s followed by a 116 s wash with the running buffer. Dose-response relations were fit to the Hill equation to obtain EC_{50} and Hill coefficient values, which are reported as averages \pm standard error of the fit.

6.5.3 Oocyte membrane preparation

The oocyte vitelline membrane was removed prior to imaging. Under standard

conditions (used unless specified otherwise), oocytes were incubated in hypertonic media (220 mM Na aspartate, 10 mM EDTA, 2 mM MgCl₂, and 10 mM HEPES, pH 7.4) for 5–15 min. Under a dissecting microscope, the vitelline membrane, which was visible over the underlying plasma membrane, was manually removed using forceps. In one alternative condition,¹⁹ cells are incubated in ND96 solution containing 4 mg/mL collagenase (Sigma, Type IA) and 4 mg/mL hyaluronidase (Sigma, Type IV-S) for 60 min, after which cells are exposed to hypertonic media and manually stripped of their vitelline membrane, as described above. In another alternative condition,²⁰ complete digestion of the vitelline membrane is achieved by protease treatment (0.05 mg/mL in ND96, Type VIII, Sigma) with gentle shaking for 30 min. Digestion of the vitelline membrane is visualized under light microscopy. After any devitellinization procedure, the oocyte is immediately transferred to a glass-bottom petri dish (MatTek) for TIRF imaging. Oocytes were typically placed on the dish with their animal pole facing down, as the vegetal pole generally shows higher autofluorescence.

6.5.4 Total internal reflection fluorescence (TIRF) imaging

TIRF microscopy was conducted on an Olympus IX81 inverted microscope. A JDS Uniphase 2219 488 nm argon ion laser was coupled to the microscope via a fiber optic. Through-objective TIRF imaging was conducted using an Olympus 100x 1.45-NA objective lens. Images were captured using an Andor iXon 897 electron-multiplying charge coupled device (EMCCD) camera. Typical image integration time was 0.2 s. Andor iQ2 software was used to acquire the data, which were analyzed using ImageJ (National Institutes of Health). A region of interest on the cell was selected to establish

focus on the membrane and the TIRF condition. Imaging was conducted elsewhere on the cell, to limit the effect of photobleaching on measurements.

6.5.5 Azido dye labeling under copper-catalyzed click conditions

In tests to assess cell viability under conditions for copper-catalyzed azide-alkyne cycloaddition, *Xenopus* oocytes were exposed to a solution of ND96 buffer containing 100 μ M CuSO₄, 500 μ M tris(3-hydroxypropyltriazolylmethyl)amine ligand (a gift from Lan Ban, Hsieh-Wilson lab, Caltech), and 2.5 mM sodium ascorbate. For labeling attempts using an azido dye conjugate, oocytes were incubated in the above solution additionally containing 50 μ M azido dye (either Azide-Fluor 488 [Click Chemistry Tools] or AlexaFluor 488-Azide [Life Technologies]) for 45 – 60 min. Next cells were rinsed three times with ND96 buffer, incubated in ND96 for 15 min, rinsed again with ND96, and finally incubated another 15 min in ND96. Cells were then devitellinized using the standard manual devitellinization method and imaged.

6.5.6 Two-color TIRF imaging and image analysis

For all two-color TIRF imaging experiments, cells expressing the appropriate receptors of interest were labeled with Alexa488-labeled α -bungarotoxin (α BtxAlexa488, Life Technologies). Cells were incubated in 20 nM α BtxAlexa488 for 6.5 hrs at 18°C, then rinsed twice with ND96, incubated in 5 mg/mL BSA in ND96 for 10 min, then rinsed with ND96 and incubated for 30 min and rinsed again with ND96 and incubated for 30 min. Cells were then devitellinized using the standard manual devitellinization method and imaged.

For these experiments, an Optosplit II (Cairn Research) beam splitter was installed in the fluorescence emission light path directly in front of the camera. In our configuration of this device, incident light is split by a 560 nm dichroic mirror. Reflected light (“donor channel”) passes through a 500-550 nm bandpass filter and transmitted light (“acceptor channel”) passes through a 575-615 nm bandpass filter. These paths are focused side-by-side on the camera. In our experiments, intensity of the donor channel was significantly higher than intensity of the acceptor channel, so a neutral density filter was placed in the donor channel path.

IDL scripts written by Taekjip Ha’s lab at the University of Illinois were used for single puncta data analysis.³¹ Using a MATLAB script, TIFF files obtained from the Andor iQ2 acquisition software were converted to PMA files for further analysis. In order to correlate puncta in the donor channel to corresponding puncta in the acceptor channel, a mapping file was created using images of fluorescent beads collected on our TIRF microscope in two-color mode. The beads (Duke Scientific G100 green fluorescent beads) were sparsely distributed on a glass bottom dish identical to those used for oocyte imaging and a new mapping file was created for each imaging session, in case of variation in optical alignment of the two channels. This mapping file was applied to the actual movies of interest and fluorescence traces for each punctum identified by the script were extracted from both donor and acceptor channels. These traces were analyzed and plotted in MATLAB.

6.5.7 tRNA synthesis and characterization

TQAS-BODIPYFL and TQAS-BODIPY558 tRNAs were synthesized by standard methods, ligating dCA-Lys-BODIPYFL or dCA-Lys-BODIPY558 to 74mer TQAS.²⁷

dCA-Lys-BODIPYFL and dCA-Lys-BODIPY558 were prepared by Walrati Limapichat.¹²

Q-TQAS-BODIPYFL tRNA was synthesized by ligation of a transcribed 57mer oligoribonucleotide (3' portion) to a 16mer oligoribonucleotide (5' portion) to yield "74mer" TQAS tRNA. The 16mer oligoribonucleotide GUCCCUAUAGUAUAGC (all sequences are written 5' to 3') with a Iowa Black FQ quencher appended to its 5' terminus was purchased from Integrated DNA Technologies. The 57mer of the sequence GGUUAGUACUGGGGACUCUAAAUCUUUGACCUGGGUUCGAAUCCAGUA GGGCCGC was prepared by runoff transcription of a modified DNA oligonucleotide bearing 2' OMe groups on its two terminal 5' nucleotides. To render the 57mer competent for ligation to the 16mer, its 5' triphosphate was removed using calf intestinal alkaline phosphatase (New England Biolabs), with purification by PCI extraction. The resulting product was treated with T4 polynucleotide kinase (New England Biolabs), with purification by PCI extraction, to yield the desired 57mer with a 5' monophosphate. 16mer and 57mer were ligated to each other using T4 RNA ligase 1 (New England Biolabs). 16mer and 57mer were mixed in a 2:1 molar ratio, annealed by heating to 90°C for 2 min and then cooling to room temperature, and then subjected to standard T4 RNA ligase ligation conditions.²⁷ The crude product of the ligation reaction was isolated by PCI extraction. This product was purified by preparative acrylamide gel electrophoresis (PAGE) on a denaturing TBE 15% urea gel (Life Technologies). Finally, the "74mer" oligonucleotide was ligated to dCA-Lys-BODIPYFL by standard methods²⁷ to yield Q-TQAS-BODIPYFL tRNA. Control unacylated Q-TQAS 76mer tRNA was synthesized by ligating the 74mer to unacylated dCA. The identity of RNA products throughout the

synthesis was confirmed by matrix-assisted laser desorption-ionization time-of-flight mass spectrometry on a 3-hydroxypicolinic acid matrix. Final tRNA products were also characterized by UV-Vis on a Nanodrop 2000 spectrophotometer (Thermo Scientific).

Final tRNA products were also characterized by denaturing PAGE on a 15% TBE urea gel (Life Technologies). 0.2 µg of each tRNA was loaded onto the gel, which was stained with ethidium bromide after running. The gel was imaged on a Typhoon FLA 9000 imager (GE Healthcare Life Sciences) both at 473 nm excitation with a 515-545 nm bandpass emission filter and at 532 nm excitation with a 560-580 nm bandpass emission filter.

6.6 References

1. Dacosta, C. J. B. & Baenziger, J. E. Gating of pentameric ligand-gated ion channels: structural insights and ambiguities. *Structure* **21**, 1271–1283 (2013).
2. Taly, A. *et al.* Normal mode analysis suggests a quaternary twist model for the nicotinic receptor gating mechanism. *Biophys J* **88**, 3954–3965 (2005).
3. Hilf, R. J. C. & Dutzler, R. Structure of a potentially open state of a proton-activated pentameric ligand-gated ion channel. *Nature* **457**, 115–118 (2009).
4. Bocquet, N. *et al.* X-ray structure of a pentameric ligand-gated ion channel in an apparently open conformation. *Nature* **457**, 111–114 (2009).
5. Hilf, R. J. C. & Dutzler, R. X-ray structure of a prokaryotic pentameric ligand-gated ion channel. *Nature* **452**, 375–379 (2008).
6. Unwin, N. & Fujiyoshi, Y. Gating movement of acetylcholine receptor caught by plunge-freezing. *J Mol Biol* **422**, 617–634 (2012).
7. Kalstrup, T. & Blunck, R. Dynamics of internal pore opening in K(V) channels probed by a fluorescent unnatural amino acid. *Proc. Natl. Acad. Sci. U.S.A.* **110**, 8272–8277 (2013).
8. Turcatti, G. *et al.* Probing the structure and function of the tachykinin neurokinin-2 receptor through biosynthetic incorporation of fluorescent amino acids at specific sites. *J. Biol. Chem.* **271**, 19991–19998 (1996).
9. Pantoja, R., Rodriguez, E. A., Dibas, M. I., Dougherty, D. A. & Lester, H. A. Single-molecule imaging of a fluorescent unnatural amino acid incorporated into nicotinic receptors. *Biophys J* **96**, 226–237 (2009).
10. Ceriotti, A. & Colman, A. Protein transport from endoplasmic reticulum to the

- Golgi complex can occur during meiotic metaphase in *Xenopus* oocytes. *J. Cell Biol.* **109**, 1439–1444 (1989).
11. Rodriguez, E. A., Lester, H. A. & Dougherty, D. A. In vivo incorporation of multiple unnatural amino acids through nonsense and frameshift suppression. *Proceedings of the National Academy of Sciences* **103**, 8650–8655 (2006).
 12. Limapichat, W. in (Dougherty, D. A.) 1–220 (California Institute of Technology, 2012).
 13. Kajihara, D. *et al.* FRET analysis of protein conformational change through position-specific incorporation of fluorescent amino acids. *Nat Methods* **3**, 923–929 (2006).
 14. Gallivan, J. P., Lester, H. A. & Dougherty, D. A. Site-specific incorporation of biotinylated amino acids to identify surface-exposed residues in integral membrane proteins. *Chemistry & biology* **4**, 739–749 (1997).
 15. Rodriguez, E. A., Lester, H. A. & Dougherty, D. A. Improved amber and opal suppressor tRNAs for incorporation of unnatural amino acids in vivo. Part 1: Minimizing misacylation. *Rna* **13**, 1703–1714 (2007).
 16. Panchuk-Voloshina, N. *et al.* Alexa dyes, a series of new fluorescent dyes that yield exceptionally bright, photostable conjugates. *The journal of histochemistry and cytochemistry : official journal of the Histochemistry Society* **47**, 1179–1188 (1999).
 17. Larabell, C. A. & Chandler, D. E. The extracellular matrix of *Xenopus laevis* eggs: a quick-freeze, deep-etch analysis of its modification at fertilization. *J. Cell Biol.* **107**, 731–741 (1988).
 18. Sonnleitner, A., Mannuzzu, L. M., Terakawa, S. & Isacoff, E. Y. Structural rearrangements in single ion channels detected optically in living cells. *Proceedings of the National Academy of Sciences* **99**, 12759–12764 (2002).
 19. Choe, H. & Sackin, H. Improved preparation of *Xenopus* oocytes for patch-clamp recording. *Pflugers Arch* **433**, 648–652 (1997).
 20. Wang, M. H. A technical consideration concerning the removal of oocyte vitelline membranes for patch clamp recording. *Biochemical and Biophysical Research Communications* **324**, 971–972 (2004).
 21. Rodriguez, E. A., Lester, H. A. & Dougherty, D. A. Improved amber and opal suppressor tRNAs for incorporation of unnatural amino acids in vivo. Part 2: evaluating suppression efficiency. *Rna* **13**, 1715–1722 (2007).
 22. Unwin, N. Refined structure of the nicotinic acetylcholine receptor at 4A resolution. *Journal of Molecular Biology* **346**, 967–989 (2005).
 23. Sletten, E. M. & Bertozzi, C. R. Bioorthogonal Chemistry: Fishing for Selectivity in a Sea of Functionality. *Angew. Chem. Int. Ed.* **48**, 6974–6998 (2009).
 24. Hong, V., Presolski, S. I., Ma, C. & Finn, M. G. Analysis and optimization of copper-catalyzed azide-alkyne cycloaddition for bioconjugation. *Angew. Chem. Int. Ed. Engl.* **48**, 9879–9883 (2009).
 25. Silverman, A. P. & Kool, E. T. Quenched probes for highly specific detection of cellular RNAs. *Trends in Biotechnology* **23**, 225–230 (2005).
 26. Sprinzl, M. & Graeser, E. Role of the 5'-terminal phosphate of tRNA for its function during protein biosynthesis elongation cycle. *Nucleic Acids Res* **8**, 4737–4744 (1980).

27. Nowak, M. W. *et al.* In vivo incorporation of unnatural amino acids into ion channels in Xenopus oocyte expression system. *Meth. Enzymol.* **293**, 504–529 (1998).
28. Westhof, E. & Sundaralingam, M. Restrained refinement of the monoclinic form of yeast phenylalanine transfer RNA. Temperature factors and dynamics, coordinated waters, and base-pair propeller twist angles. *Biochemistry* **25**, 4868–4878 (1986).
29. Roy, R., Hohng, S. & Ha, T. A practical guide to single-molecule FRET. *Nat Meth* **5**, 507–516 (2008).
30. Xiu, X., Puskar, N. L., Shanata, J. A., Lester, H. A. & Dougherty, D. A. Nicotine binding to brain receptors requires a strong cation- π interaction. *Nature* **458**, 534–537 (2009).
31. Joo, C. & Ha, T. Single-molecule FRET with total internal reflection microscopy. *Cold Spring Harb Protoc* **2012**, (2012).

Chapter 7: Attempts to develop a FRET assay for the GPCR-G protein interaction

7.1 Abstract

The interaction between GPCRs and their cognate G proteins is the critical junction between sensing a stimulus from the extracellular environment and intracellular signaling. The atomic-level details of this interaction and the mechanism by which an active GPCR induces G protein activation are poorly understood. An assay was devised to probe this interaction by unnatural amino acid mutagenesis, which would allow detailed chemical-scale insights into the processes. The proposed assay is based on GTP-induced dissociation of a stable GPCR-G protein complex on isolated plasma membranes. A fluorescence readout was chosen drawing on precedent for detecting receptor-G protein interactions by FRET between fluorescent protein fusions. Fluorescent protein fusions were constructed of the $\beta 2$ adrenergic receptor, D2 dopamine receptor, and a variety of G protein subunits. When expressed in *Xenopus laevis* oocytes and assayed at the plasma membrane by fluorescence lifetime imaging microscopy (FLIM), no interaction between receptors and G proteins was detected, and the assay was not pursued further.

7.2 Introduction

While our knowledge of atomic-scale details of ligand binding to GPCRs is rapidly expanding, a similar understanding of the interaction between the receptor and the G protein lags far behind. The association of the active receptor with the G protein is the

key event relaying agonist binding to induction of a cellular response. The active receptor effectively catalyzes G protein activation – that is, the exchange of GDP for GTP that induces dissociation of $\text{G}\alpha$ from $\text{G}\beta\gamma$ (Figure 7.1).

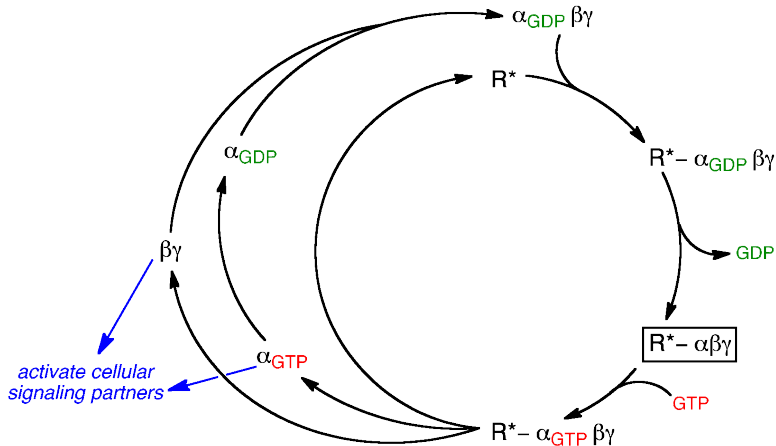
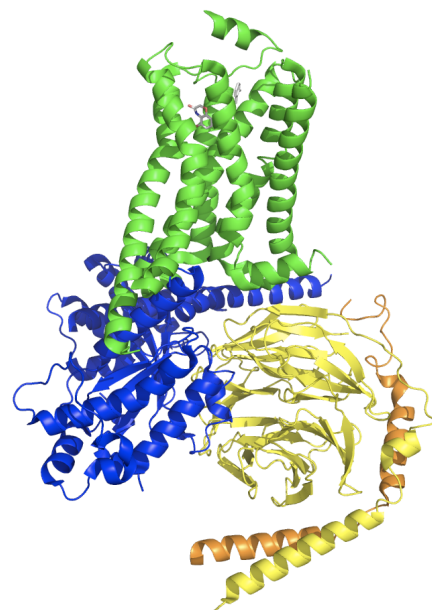


Figure 7.1. Cycle of G protein ($\alpha\beta\gamma$) activation by an activated GPCR (R^*)

In a landmark achievement, Kobilka and coworkers in 2011 obtained a crystal structure for the intermediate in this process: the complex of a nucleotide-free G protein (G_s) in complex with an active, agonist-bound GPCR (the $\beta 2$ adrenergic receptor, $\beta 2\text{AR}$) (Figure 7.2).¹ This structure should provide a starting point for well-informed structure-function studies of the receptor-G protein interface.

Figure 7.2. Crystal structure of the $\beta 2$ adrenergic receptor (green) in complex with $\text{G}\alpha$ (blue), $\text{G}\beta 1$ (yellow), and $\text{G}\gamma 2$ (orange)



Many intriguing questions remain with regard to G protein-receptor coupling.²

Most fundamentally, it is largely unknown which residues mediate functionally important interactions across the protein-protein interface. Second, the determinants of receptor specificity for a particular G protein are not well defined. A fascinating additional layer to this problem exists for receptors able to activate more than one type of G protein. In a principle known as signaling bias, different ligands can preferentially activate one signaling partner (G protein, arrestin, kinase, etc.) over another.³ Unnatural amino acid mutagenesis of the receptor-G protein interface would be a powerful tool to tackle these issues at a chemical scale, but an assay is not readily available to probe this interaction.

Assay considerations and proposed design

An ideal assay would isolate G protein activation from the larger signaling cascade of ligand binding, receptor activation, and G protein activation of cellular targets. An attractive in vitro system has been described involving a GPCR (the β2AR) and its cognate G protein (Gs) reconstituted into a nanodisc⁴ (a small protein-ringed patch of lipid bilayer).⁵ The receptor and G protein form a stable complex when all GDP and GTP is removed from the system by treatment with apyrase, a nonspecific nucleotide phosphatase.⁶ This complex (Figure 7.1, boxed species) essentially represents the “transition state” for G protein activation – GDP has been expelled from the G protein’s nucleotide binding site. This is the state that was captured in the β2AR-Gs crystal structure; apyrase digestion was required to form a stable receptor-G protein complex for crystallography.¹ In a cellular context this would be a transient intermediate: GTP binds next, inducing dissociation of the G protein from the receptor and the Gα subunit from Gβγ (Figure 7.1). In the nanodisc system, the G protein can be dissociated from the

receptor by addition of GDP or the nonhydrolyzable GTP analog GTP γ S in a dose-dependent fashion (Figure 7.3). In the general scheme envisioned for the desired assay, the GTP γ S EC₅₀ for dissociation of the nucleotide-free complex is measured: loss of function mutations destabilizing the complex will lower the EC₅₀, while mutations stabilizing the complex will raise it.

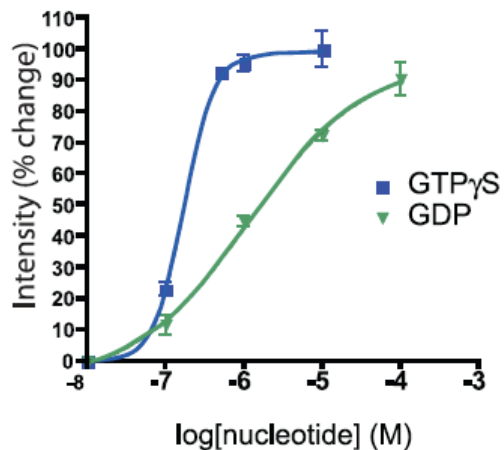


Figure 7.3. Dissociation of the nucleotide free nanobody-supported β 2AR-Gs complex by GDP or GTP γ S. Dissociation is monitored by fluorescence intensity of a bimane fluorophore on the β 2AR. Reproduced from Yao et al. (2009), copyright (2009) by the National Academy of Sciences.

An ideal assay for structure-function studies will allow for unnatural amino acid mutagenesis of the receptor and of the G protein. *In vivo* expression of both receptor and G protein in *Xenopus laevis* oocytes is attractive, as this system is well suited to GPCR unnatural amino acid mutagenesis by nonsense suppression.⁷⁻⁹ The assay proposed in this chapter involves GTP γ S dissociation of a receptor-G protein complex in plasma membranes derived from *Xenopus laevis* oocytes. FRET between fluorescent protein (FP) fusions of the receptor and the G protein could afford a readout for dissociation of the complex. Of course, the large size of FPs is undesirable, but FP fusions of both GPCRs and G proteins are well documented and several sites for FP incorporation are reported that permit receptor activation of the G protein.¹⁰⁻¹²

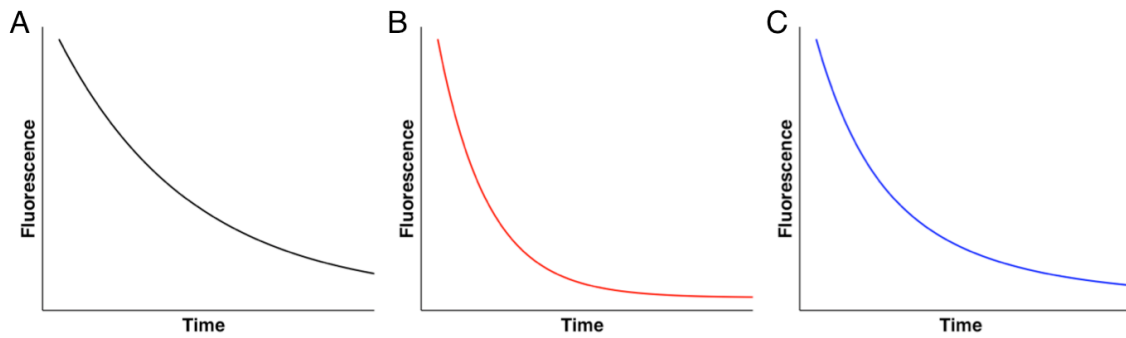


Figure 7.4. Hypothetical fluorescence decay traces. (A) Fluorescence decay of an isolated fluorophore. (B) Fluorescence lifetime shortened by the presence of a FRET acceptor. (C) Fluorescence decay of a mixed population of fluorophores A and B.

Fluorescence lifetime imaging microscopy (FLIM) will be the principle method used to probe for an association between FP-tagged receptors and G proteins. FLIM exploits the fact that a donor fluorophore participating in FRET has its fluorescence lifetime shortened relative to an isolated donor fluorophore (Figure 7.4).¹³ A fluorophore's fluorescence decay as a function of time, $F(t)$, is described by:

$$F(t) = Ae^{-\frac{t}{\tau}}$$

Where t is time, A is the fluorescence peak amplitude, and τ is the fluorescence lifetime. FRET will decrease the value of τ and the FRET efficiency is conventionally given by:

$$\text{FRET efficiency} = 1 - \frac{\tau_{\text{FRET}}}{\tau_D}$$

Where τ_{FRET} is the fluorescence lifetime corresponding to the FRET condition and τ_D is the fluorescence lifetime corresponding to a donor fluorophore in the absence of a FRET acceptor.

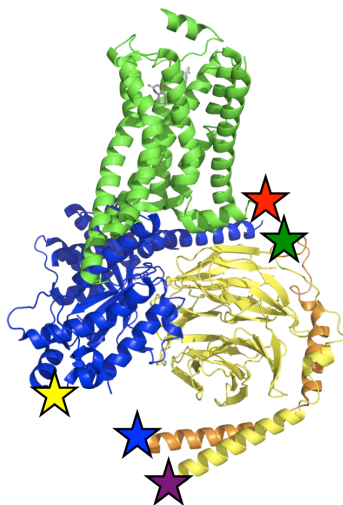
A significant advantage of the FLIM technique compared to other methods for FRET measurement is the ability to discriminate populations of donor fluorophores participating in FRET from non-interacting donors in a mixed population (and to determine the FRET efficiencies for each population).¹³ In a two-component sample (Figure 7.4 C) the fluorescence decay is simply fit to a double exponential and the size of each population is given by their relative peak amplitudes, A₁ and A₂. In the desired FRET assay for dissociation of a nucleotide-free G protein/receptor complex, most donor fluorophores will initially participate in FRET, and the interacting population will decrease as GTP γ S is added.

In the assay envisioned, plasma membrane sheets from oocytes expressing FP fusions of a receptor and a G protein are immobilized on a glass surface, exposing the intracellular side of the membrane to solution. The sheets are treated with apyrase to form stable receptor-G protein complexes, the initial FRET reading is established, and the sheets are subsequently treated with GTP γ S to dissociate the complexes. Such glass-immobilized sheets of *Xenopus laevis* membranes have previously been reported for fluorescence imaging of membrane proteins.^{14,15} FLIM imaging of the membrane sheets using a confocal fluorescence microscope can be used to detect the receptor-G protein interaction by FRET. The receptor-G protein system chosen for these experiments is the β 2 adrenergic receptor with G α s, G β 1, and G γ 2 – the same proteins crystallized in the β 2 adrenergic receptor-G protein structure.¹ The D2 dopamine receptor paired with G α i2 was also explored, as this receptor has been amenable to expression and characterization in *Xenopus* oocytes in our hands.^{8,16}

7.3 Results and Discussion

7.3.1 Construction of Fluorescent Protein Fusions

Sites for fluorescent protein fusion to the receptors and G proteins were selected based on literature reports of maintained function and of positioning that yields FRET *in vivo*.^{10,12} The chosen sites (Figure 7.5) have direct precedent for the β2 adrenergic receptor,¹⁰ D2 dopamine receptor,¹⁷ Gβ1,¹⁰ and Gγ2.^{10,12} For Gαi2 and Gαs, the FP was inserted into a site that yielded robust FRET with a GPCR, though for a different G



Construct	Protein	Insertion Site	Linker
β2AR-FP	human β2 adrenergic receptor	C terminus	-AGS-
D2DR-FP	human D2 dopamine receptor, long isoform	C terminus	-AGS-
Gαs-FP	human Gαs, short (isoform 3)	loop between helices A and B (residues 99 and 100)	-AGSG-, -GSGA-
Gαi2-FP	human Gαi2, isoform 1	loop between helices A and B (residues 91 and 92)	-AGSG-, -GSGA-
FP-Gβ1	bovine Gβ1	N terminus	-GSGA-
FP-Gγ2	human Gγ2	N terminus	-GSGA-
Gγ2-FP	human Gγ2	C terminus	-AGSG-

Figure 7.5. Fluorescent protein fusions created. Each fusion noted was made for EmGFP, EYFP, and mCherry. Approximate locations for fluorescent protein insertion are denoted by colored stars on the crystal structure of the β2AR-Gs complex.

protein (G α i1).¹¹ All genes were subcloned into the pGEMhe vector for optimal expression in *Xenopus laevis* oocytes.¹⁸ For a wide range of options for FRET pairs, every fusion was prepared with each of three different fluorescent proteins: engineered monomeric green fluorescent protein (EmGFP), engineered yellow fluorescent protein (EYFP), and monomeric Cherry (mCherry). Both EmGFP and EYFP can serve as FRET donors for mCherry.

Several previous studies provide guidance on which construct combinations should afford the most robust FRET signals. Michel Bouvier and co-workers have studied associations between FP-tagged G proteins and GPCRs by FRET, principally using the FRET pair of Luciferase (a protein yielding bioluminescence when supplied with the substrate coelenterazine) as the donor and GFP as the acceptor.^{10,11} This technique is termed bioluminescence resonance energy transfer (BRET) as donor emission occurs via bioluminescence. For each condition they quantify a BRET value: the ratio of GFP emission intensity to Luciferase emission intensity. All measurements were made *in vivo* in human embryonic kidney 293 cells. They quantified a modest BRET value of 0.15 for β 2AR-GFP coexpressed with G α i1-Luciferase (same insertion sites as in Figure 7.5),¹¹ and a more robust BRET value of 0.4 for β 2AR-Luciferase with GFP-G γ 2.¹⁰ Both measurements were made in the presence of agonist, but only modestly lower values were measured under ligand-free conditions. A strong BRET value of 0.4 was measured for both α 2A-adrenergic receptor-GFP/G α i1-Luciferase and α 2A-adrenergic receptor-Luciferase/GFP-G γ 2 combinations.¹¹ It should be noted that these BRET values *in vivo* likely encompass receptors and G proteins in a variety of states –

perhaps precoupled receptor-G protein(GDP) complexes, nucleotide free receptor-G protein complexes, and unassociated receptors and G proteins.

7.3.2 *Tests of construct function in vivo*

Several preliminary electrophysiology experiments were performed to confirm the function of these constructs when expressed in *Xenopus laevis* oocytes. These tests are by no means exhaustive, but do confirm the function of some of the constructs. The D2 dopamine receptor has routinely been expressed in this system and assayed via activation of coexpressed GIRK channels. Under standard expression conditions, the D2DR-EmGFP construct activated GIRK1/4 channels in response to dopamine and yielded a dose-response curve with an EC₅₀ of 55 nM, within the normal EC₅₀ range for the wild type D2 receptor.

In an established electrophysiology assay for the β2 adrenergic receptor in *Xenopus laevis* oocytes, the receptor can activate a coexpressed chloride channel, the cystic fibrosis transmembrane conductance regulator (CFTR).¹⁹ This assay was attempted for both wild type and FP-fusion constructs of the β2 adrenergic receptor coexpressed with the CFTR (subcloned into the pGEMhe vector for *Xenopus* expression), but no responses were detected. The reason for this assay's failure is unknown, though the function of the CFTR construct had not been validated. This assay was not pursued further. Another electrophysiology assay has been reported for the β2AR in *Xenopus* oocytes involving GIRK activation, which is enhanced by coexpression of Gas.^{20,21} While results were variable among cell batches, coexpression of β2AR, Gas, and GIRK1/4 gave large leak currents and gave very large basal currents upon exposure to high K⁺ buffer, and exposure to the β2AR agonist isoproterenol gave an induced current

above this basal current. Coexpression of Gas with GIRQ1/4 or β 2AR with GIRQ1/4 gave markedly smaller leak and basal currents, suggesting that β 2AR was signaling through expressed Gas. Large basal currents and a measurable induced current from isoproterenol were measured when β 2AR-EYFP and Gas-mCherry were coexpressed with GIRQ1/4, suggesting that these FP-tagged constructs are functional as well.

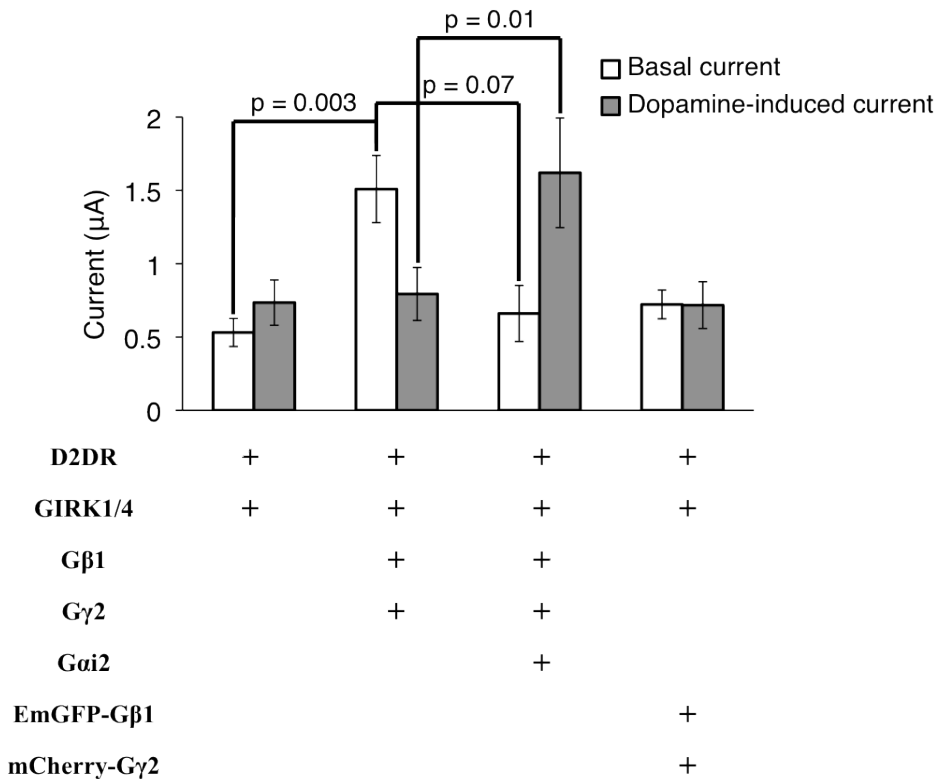


Figure 7.6. Average currents detected by electrophysiology from coexpression of G protein subunits with D2DR and GIRQ1/4 in *Xenopus laevis* oocytes. Equimolar amounts of each G protein mRNA were injected.

Preliminary electrophysiology data for D2DR coexpressed with GIRQ1/4 and various G protein subunits suggest that wild type G α i2, G β 1, and G γ 2 are likely functional in this expression system (Figure 7.6). Coexpression of wild type G β 1, and G γ 2 significantly increased basal currents in the D2DR/GIRQ1/4 system, though

elevation of basal currents was not significant when FP-tagged EmGFP-G β 1 and mCherry-G γ 2 were expressed instead. Also, coexpression of wild type Gai2 with G β 1 and G γ 2 significantly reduced basal currents and caused a borderline significant increase of dopamine-induced currents. While these data validate the function of the wild type G protein constructs in this system, they do not establish whether FP-G β 1 and FP-G γ 2 are functional.

7.3.3 Formation and fluorescence imaging of plasma membrane sheets

Several methods were investigated for the formation of glass-supported plasma membrane sheets.^{15,22} The cleanest and most reproducible was found to be the method of Singer-Lahat et al.,¹⁴ in which a devitellinized oocyte is laid on a glass cover slip in buffer, allowed to adhere, and then forcefully aspirated away. This yields a patch of plasma membrane with its intracellular face exposed to solution, which can be imaged by fluorescence microscopy.

All constructs tested (at least one FP fusion for each G protein or receptor) could be visualized in membrane patches by fluorescence microscopy, suggesting that they indeed express and are present in the plasma membrane. Representative images are shown in Figure 7.7.

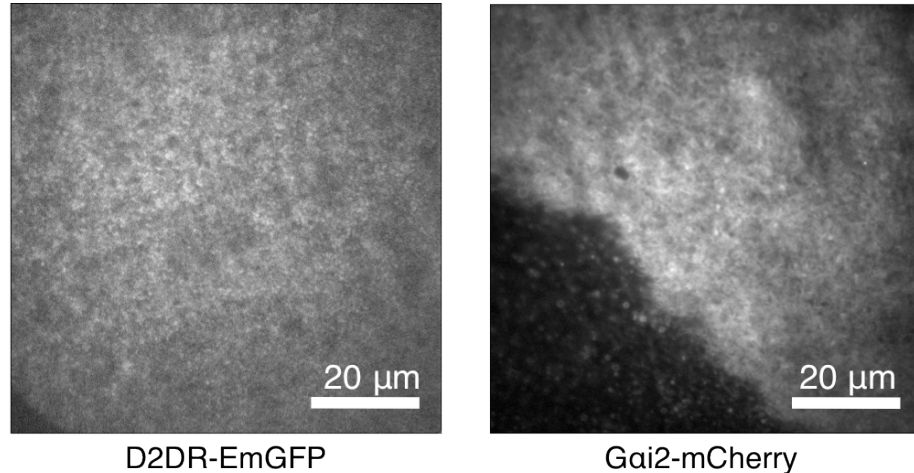


Figure 7.7. Fluorescence images of two different membrane patches, one expressing the D2DR-EmGFP construct and the other expressing the Gai2-mCherry construct. Membrane patch boundary is visible in the Gai2-mCherry image.

7.3.4 Attempts to measure FRET between G protein and receptor

Several control experiments suggested that FLIM should be a viable assay for this system. FLIM on membrane sheets from cells expressing the β 2AR-EmGFP construct generally gave a single-component fluorescence decay with a lifetime of approximately 2.5 ns (Table 7.1). A positive control in which mCherry was fused directly to EmGFP (via a -AGS- linker) on the β 2AR-EmGFP construct had an additional short component (approximately 1 ns) in its fluorescence decay, consistent with FRET between EmGFP and mCherry. The fact that this shorter component comprised only half of the fluorescence amplitude probably indicates that approximately half of the mCherry molecules are “dark” – either unfolded or do not have mature chromophores. This is consistent with an earlier report of a FLIM measurement in mammalian cells for this same FRET pair, which indicated that only 55% of mCherry chromophores were functional.²³ Thus, the actual fraction of interacting donors should be approximately double that suggested by FLIM.

Table 7.1. FLIM data from representative membrane sheets

Construct Expressed	Normalized A₁	τ₁ (ns)	Normalized A₂	τ₂ (ns)
β2AR-EmGFP	1	2.53	--	--
β2AR-EmGFP-mCherry	0.52	2.28	0.48	0.98

Inspired by the high BRET signals reported for coexpressed β2AR-luciferase and GFP-Gγ2 by Bouvier and coworkers, the constructs EmGFP-Gγ2 and β2AR-mCherry were explored for FRET in the *Xenopus* membrane sheet system. These constructs use the identical G protein and receptor as in the Bouvier system with fluorescent proteins appended at identical sites. EmGFP-Gγ2 expressed alone gave a single exponential fluorescence decay of approximately 2.5 ns (Table 7.2). Coexpression of β2AR-mCherry did not markedly change the fluorescence decay; no obvious second component was present. When the decay traces were fit to a single exponential, the condition in which the β2AR-mCherry FRET acceptor was present gave a very slightly shorter lifetime (Table 7.2), perhaps reflecting a small degree of FRET between the two proteins. If a shorter lifetime component was present at all it was too small to be reliably fit as a second component to the fluorescence lifetime, and thus not useful for a G protein-receptor assay. Note that for the oocytes from which these membrane sheets derived, a significant excess of the FRET acceptor β2AR-mCherry mRNA was injected, with the aim of minimizing the fraction of unpaired EmGFP-Gγ2 donor. These measurements were made in the presence of apyrase (2U/mL) and the β2AR agonist isoproterenol (100 μM), conditions that should promote formation of nucleotide free G protein-receptor complexes. For the cells used in these experiments, wild type Gαs and Gβ1 were also coexpressed with the FP constructs EmGFP-Gγ2 and β2AR-mCherry, which Bouvier and coworkers found to modestly increase BRET efficiency. A cursory attempt to measure

FRET by a ratiometric method instead (N_{FRET})²⁴ – comparing donor and acceptor fluorescence emission intensities – also did not indicate FRET between EmGFP-G γ 2 and β 2AR-mCherry.

Table 7.2. FLIM data for membrane sheets incubating in 2 U/mL apyrase and 100 μ M of the β 2AR agonist isoproterenol. mRNA injection amounts were 0.25 ng EmGFP-G γ 2 and 10 ng β 2AR-mCherry per oocyte. Every oocyte was also coinjected with 0.25 ng G α s and 0.25 ng G β 1 mRNA. All fluorescence decay traces were fit to a single exponential.

Construct(s) Expressed	τ (ns)	
EmGFP-G γ 2	2.49 ± 0.05	n = 9
EmGFP-G γ 2 + β 2AR-mCherry	2.37 ± 0.05	n = 9

Myriad other conditions were tested, none of which yielded fluorescence decay traces consistent with FRET. Similar traces were measured from intact cells imaged by FLIM: whole devitellinized oocytes were laid on glass coverslips and the portion of the cell directly contacting the coverslip was imaged. FLIM experiments were also conducted in the absence of apyrase or agonist, and in the presence of GTP γ S – none of which changed the fluorescence decays. EYFP was also tried as a donor fluorophore instead of GFP (the excitation wavelength and emission filters used in the FLIM experiments are suitable for both fluorophores). EYFP gave a slightly longer fluorescence lifetime than GFP (~2.8 ns), but no difference was observed between donor-only conditions and conditions in which the FRET acceptor was also present.

A second fluorescence lifetime component of small amplitude (often approximately 20% that of the principle component) and a shorter lifetime (1 - 1.6 ns) was occasionally detected. However, this feature was not associated with any particular sample type or conditions: it was found in donor-only samples as well as samples in which both donor and accepter were present and also seen with both GFP and YFP as

donors. The origin of this component is unknown; it is assumed to derive from background fluorescence in the membrane patch.

Finally, a wide array of other FP construct combinations were expressed and imaged by FLIM, though none of these yielded fluorescence decay traces consistent with FRET either. These combinations (Table 7.3), were not explored in as extensive detail as the EmGFP-G γ 2/ β 2AR-mCherry pair, but some conditions varied include ratios of mRNA injected and the presence of agonist, apyrase, or GTP γ S – none of which altered the FLIM traces. Additionally, a modified β 2AR-EYFP was tested in which the C terminus of the receptor (to which EYFP is appended) was truncated by 48 residues (everything after amino acid 365 was removed). This truncated version of the β 2AR is known to be functional and is the form in which the receptor was co-crystallized with its G protein.¹ It was hoped that having a shorter C terminus would position the appended YFP closer to the G protein, giving a higher FRET efficiency. Unfortunately, no FRET was observed for this construct either.

Table 7.3. Other construct combinations tested for FRET

Donor	Acceptor
β 2AR-EYFP	mCherry-G γ 2
γ 2-EYFP	β 2AR-mCherry
D2DR-EYFP	mCherry-G γ 2
γ 2-EYFP	D2DR-mCherry
D2DR-EYFP	G α i2-mCherry
G α i2-EYFP	D2DR-mCherry
β 2AR-EYFP	G α s-mCherry
β 2AR[truncated]-EYFP	mCherry-G γ 2

One possible reason for the failure of these experiments is that the distances between fluorescent proteins in these G protein/receptor complexes are beyond the working distance of the donor/acceptor pairs chosen. The Bouvier BRET experiments were conducted primarily using the *Renilla* luciferase/GFP10 BRET pair. The Förster distance (R_0) for this exact pair has not been reported in the literature, but luciferase paired with a related GFP analog (GFP2) has a R_0 of 75 Å.²⁵ In contrast, R_0 for EmGFP/mCherry and EYFP/mCherry are 51 Å and 57 Å, respectively. The shorter working distance of these pairs would result in lower FRET efficiencies, perhaps below the threshold of detection for this system.

7.4 Conclusions

As FRET was not convincingly observed between any receptor and G protein under any of the conditions tested, this assay for probing the interaction between GPCRs and their cognate G proteins was not pursued further. As no conditions tested yielded a measurable amount of FRET, no starting point was found for further optimization, we can only speculate about the reasons for the failure of the assay. FLIM, the method of FRET measurement, was validated by the positive control of EmGFP fused to mCherry, confirming that FRET can be detected by this experimental apparatus on fluorescent proteins expressed in these membrane patches. The electrophysiology experiments described above suggest that at least some of the FP constructs tested are functional in the *Xenopus* system, though not all (and very few in combination with each other) were evaluated. In literature reports, fluorescent protein fusions involving identical GPCRs and G proteins with (different) FPs placed at identical locations were functional and

yielded FRET in mammalian cells.^{10,11} Most likely, either the fusions of receptors and G proteins interact differently in the *Xenopus* system - they do not readily couple to one another or interact more transiently – or the working distances of the fluorescent protein donor/acceptor pairs investigated here are too short for the interactions probed.

7.5 Experimental

7.5.1 Molecular biology and *in vivo* expression

All constructs were in the pGEMhe vector. Fluorescent protein fusions were assembled by PCR subcloning with correct insertions verified by sequencing. cDNA was linearized with the appropriate restriction enzyme, purified (Qiagen), and used as a template for *in vitro* runoff transcription using the T7 mMessage mMachine Kit (Life Technologies). Stage V–VI *Xenopus laevis* oocytes were harvested and injected with RNAs as described previously.⁷ Each oocyte was injected with 0.5–20 ng of each appropriate mRNA 24–72 hrs before recording or imaging.

7.5.2 Electrophysiology

Oocyte recordings were made in two-electrode voltage clamp mode using the OpusXpress 6000A (Axon Instruments). Recording buffers were ND96 (96 mM NaCl, 2 mM KCl, 1 mM MgCl₂, 5 mM HEPES, 1.8 mM CaCl₂, pH 7.5) and high K⁺ ringer (96 mM NaCl, 24 mM KCl, 1 mM MgCl₂, 5 mM HEPES, 1.8 mM CaCl₂, pH 7.5). Solution flow rates were 2 mL min⁻¹ and drug application flow rates were 2.5 mL min⁻¹. Initial holding potential was -60 mV. Cells were subjected to a ND96 pre-wash for 10 s, a high K⁺ application for 50 s to establish basal currents, and agonist (dopamine for D2DR,

isoproterenol for β 2AR) application in high K⁺ ringer for 25 s, followed by high K⁺ and ND96 washings for 45 and 90 s in duration, respectively. Agonist-induced currents were measured over the basal K⁺ current as described previously.⁸

7.5.3 Membrane preparation:

Glass-supported plasma membrane sheets were prepared by the method of Singer-Lahat et al.¹⁴ A devitellinized oocyte is laid on a glass cover slip embedded in a plastic petri dish in ND96 buffer for approximately 15 min. The oocyte is forcefully aspirated into a Pasteur pipette, leaving behind a patch of membrane adhered to the cover slip, which is further aspirated and then forcefully rinsed with ND96 using a pipette.

7.5.4 FLIM imaging:

A commercial FLIM system (PicoQuant) was used, interfaced with a confocal fluorescence microscope (Nikon Eclipse TE 2000-U), and using a pulsed 488 nm excitation laser and a time-resolved single photon avalanche diode detector with filters suitable for both GFP and YFP emission. In a typical experiment, a *Xenopus* oocyte plasma membrane sheet from an oocyte expressing FP constructs was imaged at 60x magnification and a fluorescence decay profile was generated for a region of strong fluorescence.

7.6 References

1. Rasmussen, S. G. *et al.* Crystal structure of the beta2 adrenergic receptor-Gs protein complex. *Nature* **477**, 549–555 (2011).
2. Oldham, W. M. & Hamm, H. E. Heterotrimeric G protein activation by G-protein-coupled receptors. *Nat Rev Mol Cell Biol* **9**, 60–71 (2008).
3. Kenakin, T. & Christopoulos, A. Signalling bias in new drug discovery: detection, quantification and therapeutic impact. 1–12 (2012). doi:10.1038/nrd3954

4. Ritchie, T. K. *et al.* Chapter 11 - Reconstitution of membrane proteins in phospholipid bilayer nanodiscs. *Meth. Enzymol.* **464**, 211–231 (2009).
5. Whorton, M. R. *et al.* A monomeric G protein-coupled receptor isolated in a high-density lipoprotein particle efficiently activates its G protein. *Proceedings of the National Academy of Sciences* **104**, 7682–7687 (2007).
6. Yao, X. J. *et al.* The effect of ligand efficacy on the formation and stability of a GPCR-G protein complex. *Proc. Natl. Acad. Sci. U.S.A.* **106**, 9501–9506 (2009).
7. Nowak, M. W. *et al.* In vivo incorporation of unnatural amino acids into ion channels in Xenopus oocyte expression system. *Meth. Enzymol.* **293**, 504–529 (1998).
8. Torrice, M. M., Bower, K. S., Lester, H. A. & Dougherty, D. A. Probing the role of the cation-pi interaction in the binding sites of GPCRs using unnatural amino acids. *Proc. Natl. Acad. Sci. U.S.A.* **106**, 11919–11924 (2009).
9. Torrice, M. M. *Chemical-Scale Studies of the Nicotinic and Muscarinic Acetylcholine Receptors*. Division of Chemistry and Chemical Engineering (California Institute of Technology, 2009).
10. Gales, C. *et al.* Real-time monitoring of receptor and G-protein interactions in living cells. *Nat Methods* **2**, 177–184 (2005).
11. Gales, C. *et al.* Probing the activation-promoted structural rearrangements in preassembled receptor-G protein complexes. *Nat Struct Mol Biol* **13**, 778–786 (2006).
12. Bunemann, M., Frank, M. & Lohse, M. J. Gi protein activation in intact cells involves subunit rearrangement rather than dissociation. *Proceedings of the National Academy of Sciences* **100**, 16077–16082 (2003).
13. Morton, P. E. & Parsons, M. Measuring FRET Using Time-Resolved FLIM. *Methods Mol. Biol.* **769**, 403–413 (2011).
14. Singer-Lahat, D., Dascal, N., Mittelman, L., Peleg, S. & Lotan, I. Imaging plasma membrane proteins in large membrane patches of Xenopus oocytes. *Pflugers Arch* **440**, 627–633 (2000).
15. Ottolia, M., Philipson, K. D. & John, S. Xenopus oocyte plasma membrane sheets for FRET analysis. *Am J Physiol Cell Physiol* **292**, C1519–22 (2007).
16. Van Arnam, E. B., Lester, H. A. & Dougherty, D. A. Dissecting the functions of conserved prolines within transmembrane helices of the D2 dopamine receptor. *ACS Chem. Biol.* **6**, 1063–1068 (2011).
17. Wurch, T., Matsumoto, A. & Pauwels, P. J. Agonist-independent and -dependent oligomerization of dopamine D(2) receptors by fusion to fluorescent proteins. *FEBS Lett.* **507**, 109–113 (2001).
18. Liman, E. R., Tytgat, J. & Hess, P. Subunit stoichiometry of a mammalian K⁺ channel determined by construction of multimeric cDNAs. *Neuron* **9**, 861–871 (1992).
19. Riordan, J. R. The cystic fibrosis transmembrane conductance regulator. *Annu. Rev. Physiol.* **55**, 609–630 (1993).
20. Lim, N. F., Dascal, N., Labarca, C., Davidson, N. & Lester, H. A. A G protein-gated K channel is activated via beta 2-adrenergic receptors and G beta gamma subunits in Xenopus oocytes. *J Gen Physiol* **105**, 421–439 (1995).
21. Mullner, C. *et al.* Heterologous facilitation of G protein-activated K(+) channels

- by beta-adrenergic stimulation via cAMP-dependent protein kinase. *J Gen Physiol* **115**, 547–558 (2000).
- 22. Perez, J. B., Martinez, K. L., Segura, J. M. & Vogel, H. Supported cell-membrane sheets for functional fluorescence imaging of membrane proteins. *Adv Funct Mater* **16**, 306–312 (2006).
 - 23. Yasuda, R. *et al.* Supersensitive Ras activation in dendrites and spines revealed by two-photon fluorescence lifetime imaging. *Nat Neurosci* **9**, 283–291 (2006).
 - 24. Xia, Z. & Liu, Y. Reliable and global measurement of fluorescence resonance energy transfer using fluorescence microscopes. *Biophysj* **81**, 2395–2402 (2001).
 - 25. Dacres, H., Michie, M., Wang, J., Pfleger, K. D. G. & Trowell, S. C. Effect of enhanced Renilla luciferase and fluorescent protein variants on the Förster distance of Bioluminescence resonance energy transfer (BRET). *Biochemical and Biophysical Research Communications* **425**, 625–629 (2012).